

# YUCCA MOUNTAIN PROJECT

## GROUND MOTION MODELING of SCENARIO EARTHQUAKES at YUCCA MOUNTAIN

FINAL REPORT FOR ACTIVITY  
8.3.1.17.3.

May 30, 1996

John F. Schneider, Woodward Clyde Federal Services  
Norman A. Abrahamson, Consultant  
Thomas C. Hanks, U.S. Geological Survey

**WBS:**  
**1.2.3.2.8.3.3**  
**QA: L**

**Ground Motion Modeling of Scenario Earthquakes  
at Yucca Mountain:  
Final Report for Activity 8.3.1.17.3.3**

by

**John F. Schneider, Woodward-Clyde Federal Services  
Norman A. Abrahamson, Consultant  
Thomas C. Hanks, U.S. Geological Survey**

**Contributors**

**Byau-Heng Chin, University of Southern California  
William Joyner, U.S. Geological Survey  
Walter J. Silva, Pacific Engineering & Analysis  
Chandan Saikia and Paul G. Somerville, Woodward-Clyde Federal Services  
Yuehua Zeng and John G. Anderson, University of Nevada-Reno  
Joe Bennet and Jack Murphy, S-Cubed**

**Volume 1**

**May 30, 1996**

## Preface

Models for estimating ground motions are one of the three required inputs for a probabilistic seismic hazard analysis (PSHA). Such models permit a measure of ground motion (for example, peak ground acceleration or spectral acceleration at a given ground motion frequency) at a site to be estimated, given the magnitude of an earthquake and its distance from the site. It is most desirable to have ground motion (estimation models) established by a large enough data base of actual ground motion records to represent the full range of earthquake magnitudes, distances, and mechanisms for which motions are to be estimated. The reality of practice, however, is that this desirable situation generally is not realized. Even in geographic regions where large data bases of ground motion records have been obtained, new earthquake recordings often lead to significant revisions of the empirical-based ground motion attenuation relationships.

The basis for these observations is to be found in the large number of variables that influence ground motion. These include variables related to the earthquake source, the propagation of seismic waves from an earthquake source to a site, and the geological material properties beneath a site that impose site response effects on the ground motions. At distances close to an earthquake, source-source geometry and direction of rupture propagation contribute additional variability. Some variables significantly affect ground motion only in a limited distance range; others have a significant effect at all distances. A consequence of the large number of variables involved is that estimation of ground motion as a function of magnitude and distance involves significant uncertainty. The need for a state-of-the-art and well executed PSHA will require obtaining reasonable mean-centered estimates of ground motion attenuation and properly accounting for uncertainty.

There are very few recordings in the region of the Yucca Mountain site suitable for developing empirical relationships for input to a PSHA, mainly due to the low activity rates of faults in the region. Consequently, it will be necessary to expand the empirical data base to include recordings from other regions but in similar tectonic regimes and to make use of calibrated theoretical models to estimate ground motion for the Yucca Mountain PSHA. A separate report by Spudich and others (1995) evaluates the expanded empirical data base. In this report, we use theoretical models to predict the ground motion attenuation at Yucca Mountain.

Recent advances in ground motion modeling have led to the development of a number of credible theoretical models that have been calibrated using the large data set of recordings now available. By performing a broad range of ground motion simulations (for a range of earthquake magnitudes, distances, and source parameters) using a representative set of these well-calibrated theoretical models it is possible to obtain estimates of the mean and variability in ground motion estimates.

Six theoretical models representing the range of modeling approaches currently available were selected to simulate ground motions for the region of Yucca Mountain. These six models were calibrated for the Yucca Mountain region using available strong motion recordings from the 1992 Little Skull Mtn Earthquake. For each model, many hundreds of ground motion simulations were then performed using scenario earthquakes selected to represent a range of magnitudes and distances that are likely to contribute significantly to the seismic hazard at Yucca Mountain. The combined results of the six modeling simulations are considered to represent unbiased estimates of ground motion and its uncertainty (scientific uncertainty and randomness) in the region of the Yucca Mountain site. The results can be used to

supplement the sparse empirical ground motion data for the development of ground motion models appropriate for input to the Yucca Mountain PSHA.

# CONTENTS

Executive Summary

List of Figures

List of Tables

Introduction

Objectives

Tectonic setting of Yucca Mountain

Ground motion estimation issues

Related studies

Approach

Presentation of results

Selection of scenario earthquakes

Issues and geologic constraints

Candidate earthquakes

Consensus earthquakes

Background earthquake

Assignment of magnitudes

Ground-motion modeling methods

Selection of methods

Discussion of modeling methods

Source constraints and issues

Source rise-time

Near-surface slip

Slip distributions

Stress drop

Description of methods

$\omega$ -squared point-source model

Specific barrier method

Stochastic method with  $\omega^2$  sub-events

Stochastic slip function method

Composite fractal source method

Broadband Green's function method

Empirical method from nuclear explosion sources

Summary of model parameters

Modeling exercises and estimation of variability

Modeling exercises

Estimation of variability

Modeling variability

Parametric variability

Modeling and parametric aleatory variability

Epistemic and aleatory variability

Example

Complex versus simple models

Decomposition of variability for Yucca Mountain simulations

Yucca Mountain path and site properties

$V_p$  and  $V_s$  in the crust

$Q$  and geometrical spreading

Site constraints and issues

Base case velocity and Q profiles

Base case strain dependent shear modulus and damping

### Little Skull Mountain validation exercise

Source properties: results of previous work

Earthquake locations

Focal mechanisms and seismic moments

Best estimates of source parameters

Point-source inversion

Point-source inversion method

Point-source inversion analysis and results

Base case exercise specification

Input specification

Model-specific input parameters

Output specification

Base case exercise modeling results

Preferred case exercise and results

Preferred case (SM2) parameters

SM2 modeling results

Conclusion of Little Skull Mountain validation exercise

### Non-Linear Effects

Computational scheme

Site shear-wave velocity profile and non-linear response model

Development of smooth site response ratios

### Normal faulting exercises

## **Fault-site geometry and reciprocity**

### **Base case exercise (N01)**

**Multiple source realizations**

**Output specifications**

### **N01 modeling results**

**Parametric variability**

**Duration**

### **Point-source exercise and results**

### **Additional exercises and results**

**Preferred base case (N02)**

**Sensitivity to dip (N03 and N04)**

**Preliminary sensitivity to rupture area (N05 and N06)**

**Revised sensitivity to rupture area (N07 and N08)**

## **Strike-slip faulting exercises**

**Rock Valley fault**

**Furnace Creek fault**

**Results**

**Parametric Variability**

**Duration**

**Comparisons of results to empirical relations**

## **Scenario event ground motions**

**Scaling to scenario earthquake magnitudes**

**Estimation of median values and variability**

**Median ground motions**

**84th percentile ground motions**

## References

## Appendices

- A. Little Skull Mountain data
- B. Details of modeling methods and previous validations
  - Specific barrier method
  - Stochastic method with  $\omega^2$  sub-events
  - Stochastic slip function method
  - Composite fractal source method
  - Broadband Green's Function method
  - Empirical method from nuclear explosion sources
- C. Little Skull Mountain plots
- D. Plots of modeling results for normal events
- E. Plots of modeling results for strike-slip events
- F. Stress drops for normal faulting earthquakes
- G. Development of nonlinear site response scale factors
  - Randomization of near-surface  $V_s$  profile
  - Computation of nonlinear response
  - Model for site response factors

## EXECUTIVE SUMMARY

There are few recordings of strong earthquake ground motion in the Basin and Range Province, in which the proposed underground repository for high-level nuclear waste at Yucca Mountain is located. No recordings exist from earthquakes greater than magnitude (M) 6 at distances less than 20 kilometer (km). Due to this lack of strong motion data from the Yucca Mountain region, this project was organized to develop representative estimates of vibratory ground motion from realistic earthquake scenarios for Yucca Mountain. The focus of this project is the use of established numerical modeling methods for simulating ground motions applicable to the conditions at Yucca Mountain. A parallel study is being conducted by the United States Geological Survey (USGS) to examine empirical strong motion data from extensional regimes around the world. Together, these two studies will provide information for constraining attenuation relations (median values and variability) for earthquake magnitudes and source-to-site distances for which data are lacking in this region.

### Scenario Events

Based upon geologic constraints, six earthquake scenarios have been selected for evaluation (Table 1). These events were selected on the basis of geologic evidence for the likelihood of their seismic sources to have had significant earthquakes in the past, and to be capable of producing ground motion that would have potential impact on seismic hazard estimates at Yucca Mountain. The six selected scenarios include four normal faulting events (M 6.3 to 6.5) at source-to-site distances of 1 to 15 km and two strike-slip faulting events, M=6.7 and 7.0, at distances of 25 and 50 km, respectively.

— TABLE 1 NEAR HERE

The earthquake scenarios selected in this study are not dictated by the specific needs of a probabilistic seismic hazard analysis, nor for direct input to any other seismic analysis. However, these earthquakes could be among those that would play an important role in the seismic design of the repository.

### **Modeling Methods and Validation**

Six ground motion modeling groups were selected to apply their ground motion models to estimating the ground motions for the six earthquake scenarios. As part of the modeling exercises, estimates were made of both the median values and the variabilities in ground motions for each scenario. Most of the models had been previously calibrated against recordings from recent earthquakes. As part of this project, the modeling results of the six approaches were compared with the recordings from the 1992 M 5.7 Little Skull Mountain earthquake which occurred about 20 km from Yucca Mountain. The models produced ground motion estimates which were generally unbiased for periods less than 1 second.

## **Nonlinear Effects**

In preliminary evaluations, most of the ground motions models assumed linear response of the volcanic tuff at Yucca Mountain. In some cases, the resulting peak accelerations exceeded 1g for the closest sites. At these very high ground motion levels, the tuff is expected to be nonlinear based on laboratory testing of volcanic tuff at the Los Alamos National Laboratory (LANL). Therefore, in subsequent evaluations, the nonlinear response of the tuff was assumed to be similar to the tuff that had been tested at LANL. The simulated ground motions are modified to account for the expected nonlinear response of the top 40 meters of the tuff. The increase in damping from the nonlinear effects reduced the high-frequency ground motion by about a factor of 2 as compared to the ground motion computed assuming linear site response for the nearby normal faulting events. For the more distant strike-slip scenarios, the ground motions are much lower so the expected non-linear response of the tuff is not significant.

## **Computed Ground Motion**

The computed median spectral accelerations are shown in Figure 1. The ground motions from the nearby normal faulting events (Bow Ridge, Solitario Canyon, and Paintbrush Canyon) are large with 34 Hz spectral accelerations between 0.5 and 1.0 g for fault rupture distances of 1 to 3 km and magnitudes of 6.3 to 6.5. The Bare Mountain and Rock Valley events produce similar ground motions with 34 Hz spectral accelerations of 0.2 to 0.3 g. The distant Furnace Creek event produces the smallest high-frequency motions (less than 0.1 g at 34 Hz), but its long period motions are similar to the Bare Mountain and Rock Valley events due to the larger magnitude of the Furnace Creek event.

### **Comparisons with Attenuation Relations**

Comparisons of the model simulations were made with various empirical ground motion attenuation relations (Sadigh, 1993; Boore et al., 1994; Idriss, 1994; and Abrahamson and Silva, 1995). The simulated median ground motions for the four normal faulting events exceed those predicted by western United States (WUS) attenuation relations by about 60 percent at short distances (< 5 km) and by about 20 percent at a distance of 15 km. The differences between the results of the simulations and the empirical attenuation models are largest at the high-frequencies. At high-frequencies, the higher ground motions computed for Yucca Mountain as compared to standard WUS attenuation relations is partly attributed to the low damping ( $\kappa$ ) in the shallow rock at Yucca Mountain. At long periods, the increase is attributed to the larger crustal amplification and directivity.

For the more distant strike-slip faulting earthquakes, the simulated median ground motions exceed those predicted by WUS attenuation relations by about 30 percent at 25 km distance for the high-frequencies. This increase is also attributed to low  $\kappa$ . At 50 km distance, the simulated ground motions are consistent with WUS empirical attenuation relations.

The simulated higher ground motions at high-frequencies are consistent with the recordings of the 1992 Little Skull Mountain earthquake. The high-frequency ground motions from this event were significantly larger than predicted by WUS empirical attenuation relations.

In addition to the median ground motions, the variability of the simulated motions is also greater than the variability associated with the WUS empirical attenuation relations. The standard error is about 0.15 natural log units larger than found for empirical attenuation relations.

### **Implications for Probabilistic Hazard Calculations**

Based on the Exploratory Studies Facilities (ESF) study, at the  $10^{-3}$  to  $10^{-4}$  annual probability level, the dominant event is a M 5.5 to 6.0 at distances of 7 to 10 km. The scenario events considered in this study are of larger magnitude than the events that dominate the probabilistic hazard. However, based on the low kappa at Yucca Mountain (kappa  $\sim$  0.02 sec), the high-frequency ground motions are expected to be 10-20 percent larger than predicted by the attenuation relations used in the ESF study for the smaller events as well, consistent with the observations of the recordings of the 1992 Little Skull Mountain earthquake. At long periods ( $> 1$  second), the directivity effects for the smaller magnitude events are expected to be less than what was computed for the scenario events.

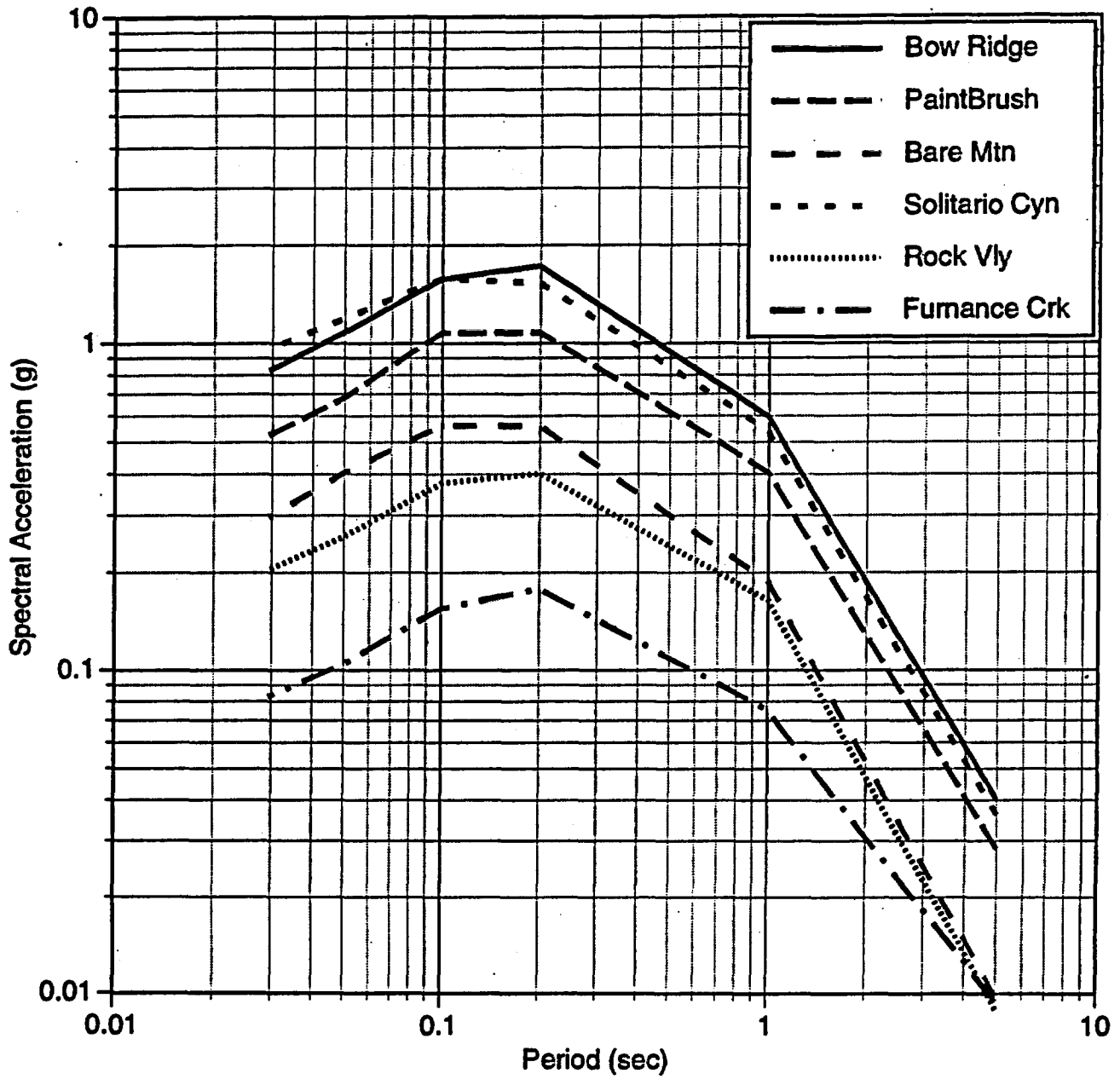
The ground motions from the simulations are based on an assumption that the stress-drop of events near Yucca Mountain have the same average value as the world-wide database of shallow crustal events. The world-wide database is dominated by earthquakes from active regions such as California. Recent studies have indicated that the median Brune stress-drop of events in the Basin and Range is lower than for events in California (EPRI, 1993). A lower median stress-drop would reduce the high frequency motions produced by the simulations and offset some of the effect of the lower kappa at Yucca Mountain. In contrast, there have also been studies that indicate that the median static stress-drop for low-slip-rate faults is larger than the world-wide average (Anderson, 1995). A higher median

high frequency motions above what is given in this report. The appropriate stress-drop for events in the Basin and Range is a key issue that needs to be resolved before these results are incorporated into a probabilistic hazard analysis.

**Table 1. Scenario Earthquakes**

| <b>Scenario</b> | <b>Fault</b>                                     | <b>M</b> | <b>Rupture Distance (km)</b>                    | <b>Mechanism</b> |
|-----------------|--|----------|---|------------------|
| 1               | Paintbrush Canyon-<br>Bow Ridge                  | 6.3      | Paintbrush branch: 4.5<br>Bow Ridge branch: 2.5 | Normal           |
| 2               | Solitario Canyon                                 | 6.5      | 1.0   | Normal           |
| 3               | Rock Valley                                      | 6.7      | 25  | Strike-Slip      |
| 4               | Bare Mountain                                    | 6.4      | 15.5  | Normal           |
| 5               | Furnace Creek                                    | 7.0      | 50  | Strike-Slip      |
| 6               | Solitario Canyon-<br>Fatigue Wash-<br>Windy Wash | 6.6      | 1.0   | Normal           |

Median SA values



## LIST OF FIGURES

Figure 2.1 Selected earthquake scenario strike-slip faults relative to Yucca Mountain and other mapped regional faults within 100 km of Yucca Mountain.

Figure 2.2 Selected earthquake scenario normal faults relative to Yucca Mountain and other mapped local faults within 15 km of Yucca Mountain.

Figure 2.3 Focal depth distribution of events in the SGB catalog.

Figure 5.1 Shear velocity as a function of depth in the vicinity of Yucca Mountain.

Figure 5.2 Compressional velocity as a function of depth in the vicinity of Yucca Mountain.

Figure 6.1 Locations of 29 June 1992 M 5.7 Little Skull Mountain earthquake, the Blume Strong Motion array and Yucca Mountain.

Figure 6.2 Estimated fault areas superimposed upon a vertical cross section of Little Skull Mountain aftershock locations.

Figure 6.3 Transfer function for Yucca Mountain shear-wave velocity profile.

Figure 6.4 Comparison of smoothed crustal amplification factors for Yucca Mountain and the Western United States (Boore, 1986).

**Figure 6.5a-e** Fourier acceleration amplitude spectra for the June 29, 1992 Little Skull Mountain mainshock for five stations used in the point-source inversion.

**Figure 6.6a-c** Fourier acceleration amplitude spectra for the July 5, 1992 Little Skull Mountain aftershock for three stations used in the point-source inversion.

**Figure 6.7a-b** Fourier acceleration amplitude spectra for the September 13, 1992 Little Skull Mountain aftershock for two stations used in the point-source inversion.

**Figure 6.8** Plan view of location of Little Skull Mountain earthquake and Blume Strong Motion recording stations used in this study.

**Figure 6.9** Plan view and fault-parallel and perpendicular cross sections of the Little Skull Mountain fault rupture area, with locations of test stations.

**Figure 6.10** Calculated versus observed 5 % damped acceleration response spectra for Station 1 (Lathrop Wells) for the Little Skull Mountain exercise SM1 (base case).

**Figure 6.11** Calculated versus observed 5 % damped acceleration response spectra for Station 2 (NTS Control Point 1) for SM1.

**Figure 6.12** Calculated versus observed 5 % damped acceleration response spectra for Station 3 (Beatty) for SM1.

**Figure 6.13** Calculated versus observed 5 % damped acceleration response spectra for Station 4 (Pahrump 2) for SM1.

**Figure 6.14** Calculated versus observed 5 % damped acceleration response spectra for Station 5 (Pahrump 1) for SM1.

**Figure 6.15** Standard error of observed versus calculated acceleration response spectra for SM1.

**Figure 6.16** Model bias of observed relative to calculated response spectra for SM1.

**Figure 6.17** Standard error of observed versus calculated acceleration duration for SM1.

**Figure 6.18** Model bias of observed relative to calculated acceleration duration for SM1.

**Figure 6.19** Calculated versus observed 5 % damped acceleration response spectra for Station 1 (Lathrop Wells) for the Little Skull Mountain exercise SM2 (preferred case).

**Figure 6.20** Calculated versus observed 5 % damped acceleration response spectra for Station 2 (NTS Control Point 1) for the Little Skull Mountain exercise SM2.

**Figure 6.21** Calculated versus observed 5 % damped acceleration response Spectra for Station 3 (Beatty) for the Little Skull Mountain exercise SM2.

**Figure 6.22** Calculated versus observed 5 % damped acceleration response Spectra for Station 4 (Pahrump 2) for the Little Skull Mountain exercise SM2.

**Figure 6.23** Calculated versus observed 5 % damped acceleration response Spectra for Station 5 (Pahrump 1) for the Little Skull Mountain exercise SM2.

**Figure 6.24** Standard error of observed versus calculated acceleration response spectra for the Little Skull Mountain exercise SM2.

**Figure 6.25** Model bias of observed relative to calculated response spectra for the Little Skull Mountain exercise SM2.

**Figure 6.26** Standard error of observed versus calculated acceleration duration for SM2.

**Figure 6.27** Model bias of observed relative to calculated acceleration duration for SM2.

**Figure 7.1** Top 100 m of the Yucca Mountain shear-wave velocity profile.

**Figure 7.2** Modulus reduction and damping curves based on laboratory dynamic testing of tuff samples taken at the Los Alamos National Laboratory.

**Figure 7.3** Comparison of computed linear and non-linear response of the tuff.

**Figure 7.4** Non-linear/linear site amplification factors.

**Figure 7.5** Comparison of smooth and raw site amplification factors for non-linear/linear response.

**Figure 7.6** Smoothed model for non-linear/linear site amplification factors.

**Figure 8.1** Reciprocal fault-site geometry.

**Figure 8.2** Station locations for the normal faulting exercises.

**Figure 8.3a** Median ground motions for N01 station 2 (Bow Ridge).

**Figure 8.3b** Median ground motions for N01 station 4 (Paintbrush Canyon).

**Figure 8.3c** Median ground motions for N01 station 5 (Bare Mountain).

**Figure 8.3d** Median ground motions for N01 station 7 (Solitario Canyon).

**Figure 8.4a** Comparison of ground motions with attenuation relations for N01 (34 Hz).

**Figure 8.4b** Comparison of ground motions with attenuation relations for N01 (20 Hz).

**Figure 8.4c** Comparison of ground motions with attenuation relations for N01 (10 Hz).

**Figure 8.4d** Comparison of ground motions with attenuation relations for N01 (5 Hz).

**Figure 8.4e** Comparison of ground motions with attenuation relations for N01 (1 Hz).

**Figure 8.4f** Comparison of ground motions with attenuation relations for N01 (0.2 Hz).

**Figure 8.5** Ratio of average simulated motion to average WUS attenuation relations.

**Figure 8.6** Parametric variability of spectral acceleration for N01 station 2 (Bow Ridge).

**Figure 8.7** Parametric variability of spectral acceleration for N01 station 4 (Paintbrush Canyon).

**Figure 8.8** Parametric variability of spectral acceleration for N01 station 5 (Bare Mountain).

**Figure 8.9** Parametric variability of spectral acceleration for N01 station 7 (Solitario Canyon).

**Figure 8.10** Comparison of median acceleration durations for N01.

**Figure 8.11** Parametric variability of acceleration duration for N01 station 2 (Bow Ridge).

**Figure 8.12** Parametric variability of acceleration duration for N01 station 4 (Paintbrush Canyon).

**Figure 8.13** Parametric variability of acceleration duration for N01 station 5 (Bare Mountain).

**Figure 8.14** Parametric variability of acceleration duration for N01 station 7 (Solitario Canyon).

**Figure 8.15** Parametric variability of velocity duration for N01 station 2 (Bow Ridge).

**Figure 8.16** Parametric variability of velocity duration for N01 station 4 (Paintbrush Canyon).

**Figure 8.17** Parametric variability of velocity duration for N01 station 5 (Bare Mountain).

**Figure 8.18** Parametric variability of velocity duration for N01 station 7 (Solitario Canyon).

**Figure 8.19a-f** Comparison of simulated ground motions with point source estimates for N01.

**Figure 8.20** Variation in dip for exercises N03 and N04.

**Figure 8.21** Effect of dip on computed response spectra for station 2 (Bow Ridge).

**Figure 8.22** Effect of dip on computed response spectra for station 4 (Paintbrush Canyon).

**Figure 8.23** Effect of dip on computed response spectra for station 5 (Bare Mountain).

**Figure 8.24** Effect of dip on computed response spectra for station 7 (Solitario Canyon).

**Figure 9.1** Station locations for RV1.

**Figure 9.2.** Station locations for FC1.

**Figure 9.3a.** Median ground motions for RV1 (station 3).

**Figure 9.3b.** Median ground motions for FC1 (station 3).

**Figure 9.4a.** Parametric variability of spectral acceleration for RV1.

**Figure 9.4b.** Parametric variability of spectral acceleration for FC1.

**Figure 9.5a.** Median acceleration duration for RV1.

Figure 9.5b. Median acceleration duration for FC1.

Figure 9.6a Parametric variability of acceleration duration for RV1.

Figure 9.6b Parametric variability of acceleration duration for FC1.

Figure 9.7a Parametric variability of velocity duration for RV1.

Figure 9.7b Parametric variability of velocity duration for FC1.

Figure 9.8a Comparison of ground motions with attenuation relations for RV1 (34 Hz).

Figure 9.8b Comparison of ground motions with attenuation relations for RV1 (20 Hz).

Figure 9.8c Comparison of ground motions with attenuation relations for RV1 (10 Hz).

Figure 9.8d Comparison of ground motions with attenuation relations for RV1 (5 Hz).

Figure 9.8e Comparison of ground motions with attenuation relations for RV1 (1 Hz).

Figure 9.8f Comparison of ground motions with attenuation relations for RV1 (0.2 Hz).

Figure 9.9 Ratio of average simulated motion to average WUS attenuation relations for RV1.

Figure 9.10a Comparison of ground motions with attenuation relations for FC1 (34 Hz).

Figure 9.10b Comparison of ground motions with attenuation relations for FC1 (20 Hz).

Figure 9.10c Comparison of ground motions with attenuation relations for FC1 (10 Hz).

Figure 9.10d Comparison of ground motions with attenuation relations for FC1 (5 Hz).

Figure 9.10e Comparison of ground motions with attenuation relations for FC1 (1 Hz).

Figure 9.10f Comparison of ground motions with attenuation relations for FC1 (0.2 Hz).

Figure 9.9 Ratio of average simulated motion to average WUS attenuation relations for FC1.

**Figure 10.1** Scale factors for magnitude scaling.

**Figure 10.2** Comparison of modeling standard errors for LSM validation exercise.

**Figure 10.3** Comparison of modeling standard errors for LSM with validations for other events.

**Figure 10.4** Variability due to differences in the median predictions of the methods.

**Figure 10.5a** Parametric variability due to multiple source realizations for Bow Ridge.

**Figure 10.5b** Parametric variability due to multiple source realizations for Paintbrush Canyon.

**Figure 10.5c** Parametric variability due to multiple source realizations for Bare Mountain.

**Figure 10.5d** Parametric variability due to multiple source realizations for Solitario Canyon.

**Figure 10.5e** Parametric variability due to multiple source realizations for Rock Valley.

**Figure 10.5f** Parametric variability due to multiple source realizations for Furnace Creek.

**Figure 10.6** Parametric variability due to dip uncertainty.

**Figure 10.7a** Components of variability for Bow Ridge.

**Figure 10.7b** Components of variability for Paintbrush Canyon.

**Figure 10.7c** Components of variability for Bare Mountain.

**Figure 10.7d** Components of variability for Solitario Canyon.

**Figure 10.7e** Components of variability for Rock Valley.

**Figure 10.7f** Components of variability for Furnace Creek.

**Figure 10.8** Components of variability for point source model.

**Figure 10.9a** Comparison of variability for Bow Ridge.

**Figure 10.9b** Comparison of variability for Paintbrush Canyon.

**Figure 10.9c** Comparison of variability for Bare Mountain.

**Figure 10.9d** Comparison of variability for Solitario Canyon.

**Figure 10.9e** Comparison of variability for Rock Valley.

**Figure 10.9f** Comparison of variability for Furnace Creek.

**Figure 10.10** Median response spectra for scenario events.

**Figure 10.11** 84th percentile response spectra for scenario events.

## LIST OF TABLES

- Table 1.1 Summary of faulting behavior in the vicinity of Yucca Mountain.
- Table 1.2 Selected key faults.
- Table 2.1 Participants and observers at the "Workshop to Characterize Scenario Earthquakes in the Yucca Mountain Region."
- Table 2.2 Proposed scenario faults.
- Table 2.3 Proposed scenario earthquakes.
- Table 2.4 Selected scenario earthquakes.
- Table 3.1 Prospective ground motion modelers.
- Table 3.2 Advisory panel for the selection of modelers.
- Table 3.3 Summary of physical modeling methods.
- Table 4.1 Components of variability for model 1.
- Table 4.2 Components of variability for model 2.
- Table 4.3 Source of variability considered in this study.
- Table 5.1 Summary of Q relations for southern basin and range.
- Table 5.2 Yucca Mountain velocity and Q profiles.
- Table 5.3 Modulus reduction and damping values as a function of shear strain.
- Table 6.1 Hypocenter locations.

|            |  |
|------------|--|
| Table 6.2  | Focal mechanisms and seismic moments.                                  |
| Table 6.3  | Source analysis methods and data.                                      |
| Table 6.4  | Fault plane coordinates.   |
| Table 6.5  | Little Skull Mountain fault plane coordinates.                         |
| Table 6.6  | Little Skull Mountain point-source inversion process.                  |
| Table 6.7  | Little Skull Mountain point-source inversion results.                  |
| Table 6.8  | Source parameters for Little Skull Mountain base case exercise (SM1).  |
| Table 6.9  | Little Skull Mountain strong motion station locations.                 |
| Table 6.10 | Model-specific parameters and values used in the SM1 exercise.         |
| Table 6.11 | Frequency points (Hz) specified for 5 percent damped response spectra. |
| Table 6.12 | Model-specific parameters and values used the SM2 exercise.            |
| Table 7.1  | Control motions magnitude and distances.                               |
| Table 7.2  | Coefficients for non-linear/linear ratio model.                        |
| Table 8.1  | Primary normal faulting scenario earthquakes.                          |
| Table 8.2  | Source parameters for N01 modeling exercise.                           |
| Table 8.3  | Model parameters used for N01.   |
| Table 8.4  | Fault coordinates for N01 modeling exercise.                           |
| Table 8.5  | Station locations for N01 modeling exercise.                           |

**Table 8.6** Source parameters for additional normal faulting exercise.

**Table 9.1** Strike-slip faulting scenarios exercises.

**Table 9.2** Rock Valley sites.

**Table 9.3** Furnace Creek sites.

# 1. INTRODUCTION

Yucca Mountain, Nevada is the proposed site of the mined geologic disposal system (MGDS). For this site to be approved as a repository, the Department of Energy (DOE) must demonstrate that the site complies with regulations designed to ensure the safety of the public. As a part of this process, DOE must perform extensive site characterization studies of the local and regional environment to establish the risk associated with various natural hazards associated with the site. Contributions to risk from hazards such as earthquakes, volcanoes, and climactic changes all must be considered in detail. This report specifically concerns a study of earthquake hazard based upon the analysis of predicted vibratory ground motion from several earthquake scenarios.

## Objectives

The main objective of this project is to obtain representative ground motions at Yucca Mountain, Nevada, from realistic earthquake scenarios. Realistic earthquakes are those earthquakes that have occurred sometime within the past several hundred thousand years in the vicinity of Yucca Mountain, as determined by a consensus of knowledgeable geologists. Representative ground motions are those that are generated from the range of earthquake magnitudes, distances, source spectra, and faulting scenarios that broadly sample the specified realistic earthquakes. We emphasize that the earthquakes of interest are not dictated by the specific needs of a probabilistic hazard analysis, nor for direct input to any other seismic analysis. However, given the constraints posed for "realistic earthquakes" and "representative ground motion", it is readily apparent that these earthquakes could be among those that would play an important role in the seismic design of the repository.

### **Tectonic Setting of Yucca Mountain**

Yucca Mountain is located within the Great Basin, which is a part of the Basin and Range Province (Figure 1-1). The Basin and Range Province is characterized by a series of north-trending mountain ranges and intervening basins or broad valleys. Yucca Mountain itself lies between Crater Flat to the west and Jackass Flats to the east (Figure 1-2). Yucca Mountain is located geologically within the Cordilleran mountain belt, a region of active deformation since the Paleozoic era, now located near the western boundary of the North American plate. The present-day evidence of significant extensional strain and volcanism in the vicinity of Yucca Mountain has occurred primarily in the past 10-20 million years (Carr, 1984; Eaton, 1982; Stewart, 1978). While the Great Basin was extending at a rate of 10-30 mm/year 5-15 Ma, it is currently deforming at a rate of 5-10 mm/yr, concentrated primarily to the west of Yucca Mountain. From 10 my to the present, the dominant tectonic deformation has been west of Death Valley. Yucca Mountain has been in an extensional regime, with ~East-West extension manifested in dip-slip and horizontal shear. Extension has occurred primarily along west-dipping normal faults and associated northeast and northwest trending strike-slip faults (Rogers et al., 1987; Scott, 1990).

FIGURE 1-1 and 1-2 NEAR HERE

There are some constraints that can be made on faulting behavior at Yucca Mountain based on modeling and geophysical data. Based on a boundary-element model (King, 1994; King and Janssen, 1994), fault dips can vary 45-80° (as a group or individually) without substantially changing the surface morphology (note: this result is based on an elastic model and may not be completely realistic). While it is apparent that some smaller faults are likely to converge with other, more steeply dipping, through-going faults, there are little to no constraints on fault geometries at depth. It is likely that one or a few (at most) Yucca Mountain faults are master faults, with the remainder coalescing at depth within the seismogenic portion of crust.

While the general behavior of faults in the vicinity of Yucca Mountain is reasonably well constrained in terms of tectonic trends and seismic budget, the details of individual fault behavior are not. However, some constraints do exist locally and regionally from observed Quaternary fault offsets, and regionally from historical earthquakes. In a recent summary of fault behavior by Pezzopane (1994), some 88 faults or fault combinations are identified that could play a role in an earthquake hazard or ground motion study. Tables 1.1 and 1.2 summarize this information.

TABLE 1.1, 1.2 – NEAR HERE

Table 1.1 provides an overview of the realistic earthquake scenarios available within the local and regional area for the purposes of this study. One can readily see that the scenario earthquakes will likely fall in the range  $5 \leq M \leq 8$  at distances less than 100 km. In addition, due to the nature of the repository facilities to be designed, the frequency band of interest to design is 0.5 to 35 Hz (R. Kennedy, oral communication, RPK Structural Mechanics Consulting, 1995). Because ground motion in this frequency band is by nature more stochastic than deterministic, complex details of the velocity structure will be less important to characterize than average seismic properties and associated variability.

There are numerous issues of interest for predicting ground motion from earthquakes in the vicinity of Yucca Mountain. First, given the moderate rate of seismicity and general lack of recordings of significant ground motion from local earthquakes, theoretical models will play a major role in estimating ground motions. The ground motion estimates from the theoretical models will be constrained by available information regarding seismic source, path and local site properties. Near-surface soil and rock properties will dictate the degree to which the Yucca Mountain site will exhibit nonlinear soil amplification effects. Some source properties such as mechanism, depth and fault orientation and geometry can be constrained to a degree by local geology and tectonics; however, rupture dynamics (for example, asperities, directivity, rupture velocity, and rise time) or stress drop for point-source models contribute to the overall variability of ground motion that must be considered as part of the ground motion characterization.

### **Ground Motion Estimation Issues**

There is very limited empirical strong motion data available from events in the Basin and Range Province. In particular, there are no recordings from events over M 6 within 10 km of the fault rupture. For an empirical study of strong motion data it is necessary to extend the study region beyond the Basin and Range Province. A study of empirical strong motion data from events in extensional regimes around the world has been conducted by Spudich and others (1996).

An important set of empirical data are the recordings of the 1992 M 5.7 Little Skull Mountain earthquake which occurred within 20 km of Yucca Mountain. The high-frequency ground motions from this event are much larger than predicted using standard "rock" empirical attenuation relations which are based primarily on California data. This difference has been attributed to lower damping in the shallow rock (lower kappa) at Yucca Mountain compared to typical "rock" sites in California (Spudich and others, 1996). Such differences in rock properties can be accounted for by using numerical simulation methods to estimate the ground motions as is done in this study. There are many methods that have been developed for computing ground motions via numerical simulation. To account for the range of models, multiple modeling methods are used in this study. Since the models use different parameters, care must be taken to keep the interpretations of the seismic source as consistent as possible for the different methods.

An important issue for ground motion simulation is the stress-drop of the events. The static stress-drop is related to the dimension of the rupture for a given magnitude. A higher stress-drop corresponds to a more compact source which tends to lead to larger ground motions, whereas a smaller stress-drop corresponds to a more extended source which tends to lead to smaller ground motions. In this study, we have used world-wide average values for the median stress-drop, however, there have been studies that indicate that the median stress-drop in the Basin and Range Province is lower than the world-wide average (EPRI, 1993).

Another issue in the use of numerical simulation methods is the treatment of site response. Due to the low damping, the predicted ground motions for near-fault locations will be very large at high-frequencies and the tuff at Yucca Mountain is not expected to remain linear at these shaking levels. Nonlinear response effects (strain dependent shear modulus and damping) need to be considered even for a rock site.

#### **Related Studies**

There have been two other major studies that have used multiple ground motion simulation methods to predict ground motions close to large earthquakes: the Electric Power Research Institute (EPRI) study in 1990 and the Southern California Earthquake Center (SCEC) study in 1995.

The objectives of the EPRI study were to assess the status of modeling methods for estimating ground motions close to large earthquakes; assess the utility of these methods in engineering design; and provide direction for improving the methods. Twelve teams applied their modeling methods to predict ground motions for one or both of two scenario earthquakes: a M 7.5 event on the San Andreas fault at distances from the fault of 5 and 10 km; and a M 5.8 event in Saguenay Quebec.

The objectives of the SCEC study were to develop a library of time histories for scenario earthquakes in Southern California. In this study, six modeling teams applied their numerical modeling methods to predict ground motions from one or more of five scenario events: M 6.75 and 7.25 events on the Palos Verdes fault, M 6.75 and 7.25 events on the Elysian Park Blind Thrust fault, and a M 7.9 event on the San Andreas fault. The ground motions for each of these five scenario earthquakes were computed at two sites: one in downtown Los Angeles and one near the Port of Los Angeles.

Several of the participants in this Yucca Mountain study were involved in one or both of these previous studies. The current study has built on the what was learned from these previous studies in terms of how to organize the exercises (what sort of constraints are needed), how to validate the models, and how to compare the results.

## Approach

The process of modeling earthquake scenarios requires a series of carefully choreographed steps to assure that the end result provides for both realistic earthquakes and representative ground motions. The first step of the process is to select the earthquake scenarios. These scenarios consist of geologic and seismologic constraints on fault geometry and dynamics based, at least in part, on local and regional studies of fault behavior. A broad consensus of scenarios of interest was obtained at an initial workshop attended by a group of about 30 geologists, seismologists, and tectonicists with extensive knowledge of Yucca Mountain.

The second step is to use these scenarios as guidance for developing a set of instructions or modeling exercises to form the basis for computational analyses. In this step it is necessary to specify values for a wide range of parameters that represent the earthquake process, specifically considering the generation of earthquake energy during fault rupture and the propagation of seismic waves through the earth's crust and near-surface soil and rock layers. A wide range of seismic, geologic and geotechnical data need to be evaluated in order to establish earthquake scenarios and to constrain parameter values for the modeling exercises.

The third step consists of the actual ground motion modeling or simulation process. To achieve relatively unbiased estimates of median values and variability (uncertainty and randomness) in ground motion estimates, it is important that both a variety of ground motion modeling methods as well as a broad range of simulations from each method are considered. In this way contributions to variability from modeling and parametric sources are adequately sampled. With each modeling method, many hundreds of realizations of possible ground motion time histories are produced for each earthquake scenario in order to achieve statistically stable and significant results. A part of this effort consists of a calibration/validation exercise for each ground motion modeling method to check model calibrations and test parameter sensitivities. Ground motion recordings from the Little Skull Mountain earthquake and its aftershocks are used in this exercise.

Finally, in the last step, the results of the different modeling methods are evaluated to determine median values and variabilities of ground motion. Selected initial results of each of these steps have been presented in preliminary reports by Schneider (1995) and Schneider and others (1995).

## **Presentation of Results**

The principal results of ground motion modeling are presented in terms of 5 percent damped response spectra for pseudo velocity and acceleration. Estimates of time history duration for acceleration and velocity are also presented in a compact format that will enable the reader to objectively compare waveform envelopes. Owing to the enormous quantity of data generated in the process of evaluating the scenario earthquakes, the composite plots of response spectra and duration values not only greatly facilitates data comparison, but also obviates the need to plot all but a few representative time histories.

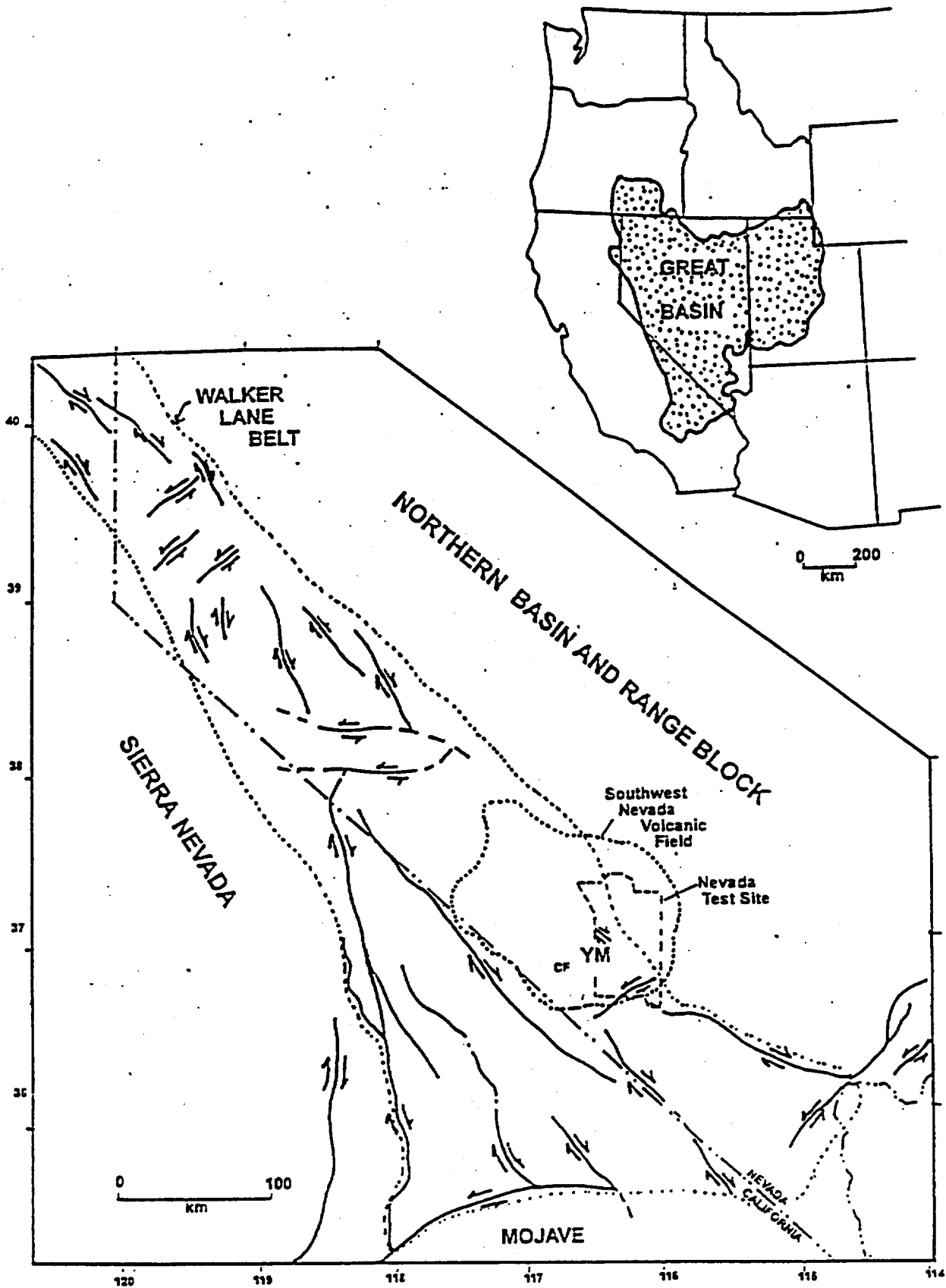
The frequency band of primary interest to the study is 0.5 to 30 Hz, but the computations are applicable from 0.1 Hz to 100 Hz (in response spectra). The focus of this study is on horizontal motions, for either two orthogonal components or a single average horizontal component. All motions are computed at the earth's free surface, with scenario ground motions specified for a location approximately at the center of the proposed repository at Yucca Mountain.

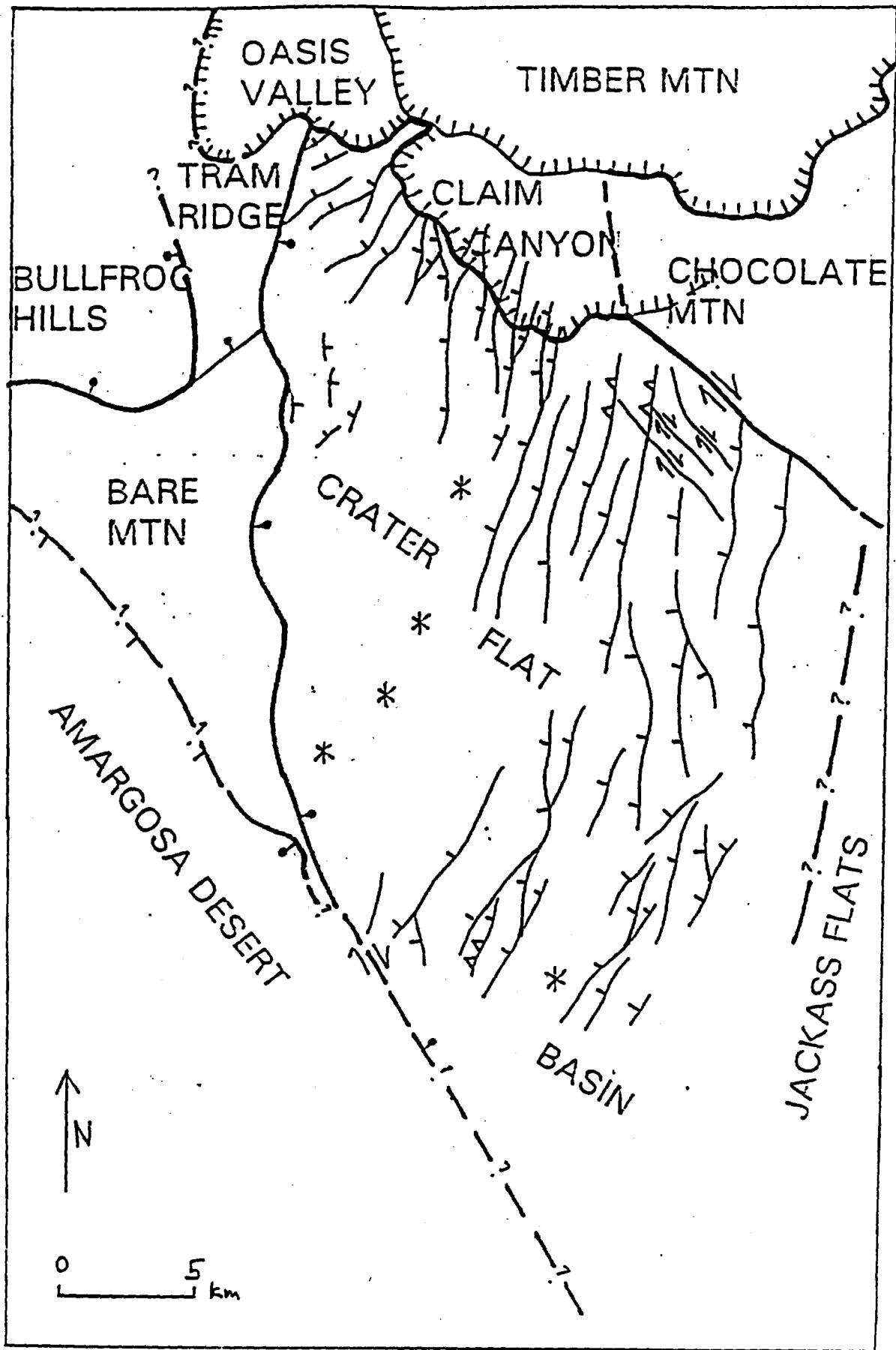
**Table 1.1 Summary of faulting behavior in the vicinity of Yucca Mountain.**

|  | <b>&lt;~10 km</b> | <b>10 - 100 km</b> | <b>100 - 300 km</b> |
|--|-------------------|--------------------|---------------------|
| <b>Number of faults<br/>or fault<br/>combinations</b>          | 17                | 65                 | 6                   |
| <b>Upper-bound<br/>magnitude</b>                               | 5.6 - 6.8         | 6.1 - 7.9          | 7.3 - 8.1           |
| <b>Recurrence<br/>interval (ka)</b>                            | 20 - 130          | 0.5 - 160          | 0.2 - 5             |
| <b>Faults with<br/>evidence of<br/>Quaternary<br/>faulting</b> | ~50%              | ~80%               | 100%                |

**Table 1.2 Selected key faults.**

| <b>Distance Range</b> | <b>Faults</b>   |
|-----------------------|---|
| 0-10 km               | Ghost Dance - Abandoned Wash<br>Solitario Canyon<br>Bow Ridge<br>Fatigue Wash<br>Paintbrush Canyon - Stage Coach Road<br>Windy Wash |
| 10-100 km             | Bare Mountain<br>Rock Valley<br>Death Valley - Furnace Creek - Fish Lake Valley<br>Pahrump - Stewart Valley                         |
| 100-300 km            | Owens Valley<br>Fish Lake Valley<br>Garlock<br>White Mountains - Cedar Mountain<br>San Andreas                                      |





## 2 SELECTION OF SCENARIO EARTHQUAKES

While the general behavior of faults in the vicinity of Yucca Mountain is reasonably well constrained in terms of tectonic trends and available strain energy, the details of individual fault behavior are not. However, some constraints do exist locally and regionally from observed Quaternary fault offsets, and regionally from historical earthquakes.

At the "Workshop to Characterize Scenario Earthquakes in the Yucca Mountain Region" (Workshop 1, February 28 to March 1, 1995), six earthquake scenarios were selected for this project (Schneider and Hanks, 1995). The events were selected on the basis of geologic evidence for the likelihood of their respective faults to have had significant earthquakes in the late Quaternary, and to be capable of producing ground motion that would have potential impact to seismic hazard estimates at Yucca Mountain. The selection process involved a group of about 30 geologists, seismologists, and tectonicists with knowledge of Yucca Mountain and the surrounding region. The workshop participants are listed in table 2.1.

TABLE 2.1 – NEAR HERE

The objectives of the workshop were to select approximately five scenario earthquakes and to specify geologic constraints and associated uncertainties for input to a set of ground motion modeling exercises pertinent to the potential nuclear waste repository at Yucca Mountain. Specifically, observable fault characteristics such as fault length, displacement and geometry were to be defined in order to constrain earthquake parameters such as magnitude, distance and focal mechanism. This information is used as input for the ground motion modeling exercises.

### **Issues and Geologic Constraints**

As a means of establishing a pool of candidate sources, Pezzopane (1995) reviewed relevant fault sources within 100 km of Yucca Mountain (figs. 2.1 and 2.2). He prepared a list of faults and associated earthquakes capable of producing 0.1 g peak ground acceleration (PGA) at the Yucca Mountain site. Other relevant constraints on the source characteristics for candidate events are as follows:

- PGA is determined from the average of several empirical ground motion attenuation relationships using 84th percentile ground motion values;
- local and regional faults are based upon compilations of Simonds and others (1995) and Piety (1995);
- magnitudes are based upon the relationships of Wells and Coppersmith (1994), with median magnitudes taken for the maximum lengths;
- all faults considered exhibit Quaternary displacement; and
- specified fault lengths are determined by the geomorphic expression of the fault (Mapped fault length)

**FIGURES 2.1, 2.2 -- NEAR HERE**

Based upon the above constraints, the most significant local candidate faults are Solitario Canyon, Paintbrush Canyon-Stage Coach Road, Bare Mountain and a distributed faulting scenario. The major regional earthquake sources are Rock Valley, Amargosa River-Pahrump-Stewart Valley, Furnace Creek-Fish Lake Valley (with or without Death Valley and Fish Lake).

After presenting this information to the Workshop 1 participants, the participants were subdivided into four groups and asked to submit a list of approximately five faults for consideration for development of scenario earthquakes. Considerations for the various candidate faults included style of faulting (for example, mechanism, hanging wall versus footwall, directivity), slip or recurrence rate, distance and magnitude. The resulting list of candidate faults is given in table 2.2. Generally speaking, there was wide agreement with respect to candidate faults between the four groups. After a brief presentation in plenary session by each of the group leaders, a single "proponent" or "expert" was assigned to develop proposed fault parameters for each of the scenarios.

TABLE 2.2 -- NEAR HERE

#### **Candidate earthquakes**

In the next phase of Workshop 1 the objective was to place some geologic and tectonic constraints for potential earthquakes on each of the proposed scenario faults. Observable constraints such as fault length, dip, strike, rake, seismogenic depth, and average displacement, however uncertain, comprise the basis for estimating magnitude and focal mechanism of a potential earthquake. Individuals with knowledge of each of the faults were asked to present their estimates of these parameters for review by the rest of the workshop participants. In this way, consensus values were derived. The results are presented in table 2.3.

TABLE 2.3 -- NEAR HERE

## **Consensus Earthquakes**

After placing geologic and tectonic constraints upon each of the proposed faults, the Workshop 1 participants were then asked to arrive at consensus scenario events. Scenarios 1 to 5 immediately came to the top of the list by virtue of their having been listed as candidates by all four break-out groups (see table 2.3): Paintbrush Canyon, Solitario Canyon, Rock Valley, Bare Mountain, and Furnace Creek. In addition, the geologic constraints for these events all indicate that they would produce significant, if not controlling, ground motions for consideration of the design of the repository. These scenarios are all modeled as a part of this study. Scenario 6 which is a volcanic-triggered event (or simultaneous rupture of the Solitario Canyon-Fatigue Wash-Windy Wash faults which are assumed to coalesce at a depth of a few km), was also a candidate of three of the groups, although details of this event certainly varied between groups. Its complexity and basis in an alternative tectonic model also make it of unique interest as a modeling exercise. However, since the modelers assume that the shallow rupture radiates little seismic energy, this scenario is not significantly different from the other normal faulting scenarios in terms of ground motion. Since this scenario would require substantially more effort than the other scenarios without providing much more information, it is treated only in an approximate manner.

The rest of the proposed scenarios did not receive consensus and are therefore outside the scope of this project. The Pahrump-Stewart Valley (scenario 7), Belted Range (scenario 11), and West Springs Mountain (scenario 12) events were eliminated from further consideration because the preferred fault lengths put them outside the possible controlling earthquake window (that is,  $PGA < 0.1 g$ ). The Mine Mountain (scenario 8) and Wahmonie Mountain (scenario 9) events could produce significant ground motions, but did not get sufficient support from the participants (only Group 4 had these events on its list of candidate events). Note also that Stagecoach Road was considered only as a possible southern extension of Paintbrush Canyon under Scenario 1. The "Scattered" Walker Lane event (scenario 10) engendered considerable discussion, but again, it appeared on only one break-out group's list. Although there are strong proponents of such an event, it did not receive the group consensus for inclusion as a realistic scenario.

### **Background Earthquake**

The background earthquake is essentially a floating event which represents the largest event that could occur not associated with a known fault. Geometrical constraints based on the depth of the seismogenic zone, range of fault dip, and estimates of fault area (S. Pezzopane, U.S.G.S., written communication, 1995) suggest an M 6.2 to 6.4 upper bound background event (using a seismogenic zone to 12 km depth). Empirical data from continental earthquakes also show that M 6.5 events have about a 2/3 chance of breaking the surface (K. Coppersmith, Geomatrix, written communication, 1995). Other data from Basin and Range Province events (dePolo, 1994) suggest that the largest event that would not exhibit any surface displacement would be approximately M 6.5. Given the small range in the size of potentially controlling earthquakes on known faults at very close distances and the upper bound size of a background earthquake, it was decided that a background earthquake would not be considered in the ground motion modeling exercises.

### **Assignment of Magnitudes**

Given geologic and tectonic constraints on fault dimensions and geometry, the earthquake magnitude can be estimated. Wells and Coppersmith (1994) have performed the most comprehensive statistical analysis of the problem. They found that the relationship between displacement alone or length alone to magnitude is much less stable than the relationship between rupture area and magnitude. They also found that, when averaged, measured fault displacements tend to be closer to average maximum displacements, not simply average displacements. Thus, the uncertainty in magnitude can be reduced by estimating magnitude directly from rupture area rather than from length alone or from length and displacement.

To constrain rupture area, an independent means to estimate the down-dip fault width is needed. The fault width can be expressed as a function of seismogenic thickness and the fault dip

$$\text{width} = \text{depth} / \sin(\text{dip}) \tag{2.1}$$

Although difficult to constrain for specific faults, fault dip and seismogenic thickness can be estimated generically. Based upon the consensus opinion of participants at Workshop 1, normal faults are assigned a range of dips from 45 to 70 degrees and strike-slip faults are at 90 degrees  $\pm$  5 degrees. Seismogenic thickness is limited to 12 km for all fault types based upon the observed distribution of seismicity in the vicinity of Yucca Mountain (fig. 2.3). For the larger earthquakes (that is, those that are of interest to this study), it is reasonable to assume that the fault plane will extend over the entire zone from 12 km depth to the surface. For normal faults, the fault width for the median dip (57.5°) is 14.2 km; for strike-slip faults, the fault width is simply fixed at 12 km.

FIGURE 2.3 -- NEAR HERE

Given estimates of fault length and width, the rupture area can be estimated. In order to do so, what is actually implied by the term "fault length" needs to be clarified. First, the surface lengths given by the Yucca Mountain geology experts are really not estimates of individual rupture lengths; they are best estimates of maximum (or total) fault lengths for fault segments (individual or combined) considered most likely to rupture in a single event. It is fair to assume that these lengths would represent upper bounds to surface ruptures for a suite of individual events occurring over a significant period of geologic time. On the other hand, surface rupture lengths (that is, for single events) are typically a lower bound estimate for the actual average subsurface length for a single earthquake, as demonstrated clearly by Wells and Coppersmith (1994). (For example, a normal fault with a surface rupture length of 18 km would correspond to a M 6.52 event with an average subsurface length of 24 km.) By this logic, to interpret the observed fault lengths as surface rupture lengths would yield unrealistically large magnitudes. Therefore, as a compromise, the rupture lengths are fixed to their surface fault lengths, which is equivalent to asserting that the observed fault lengths are more consistent with average subsurface rupture lengths.

With these definitions for length and width, the magnitude can be estimated from the rupture area. Since, Wells and Coppersmith (1994) find that there is not a statistically significant difference in the magnitude-rupture area regressions for strike-slip, reverse and normal faults, their relationship for all faults types is used.

$$M = 4.07 + 0.98 \log_{10} (RA). \quad (2.2)$$

where  $M$  is moment magnitude and  $RA$  is rupture area in  $\text{km}^2$ . The coefficient on the  $\log (RA)$  term is close to unity which would result if the average stress drop is independent of magnitude. Constraining the slope to unity yields the following relationship between  $M$  and  $RA$

$$M = 4.01 + 1.0 \log (RA). \quad (2.3)$$

This constrained relationship is preferred because it is both admissible by the data and corresponds to constant stress drop for the source scaling. The resulting fault areas and magnitudes for the various scenario earthquakes are given in table 2.4. Note that these magnitudes are based upon the areas taken from mean estimates of fault length (table 2.3) and widths of either 12 km (strike-slip) or 14.2 km (normal,  $57.5^\circ$  dip). The scenarios are for four normal faults in the magnitude range 6.3 to 6.6 within 15 km of Yucca Mountain (Scenarios 1, 2, 4 and 6), and two strike-slip faults with magnitudes of 6.7 and 7.0 at 25 and 50 km distance, respectively (Scenarios 3 and 5). Distances cited are closest distances from the center of the repository block to the fault trace (to the closest 0.5 km).

TABLE 2.4 -- NEAR HERE

**Table 2.1 Participants and observers at the "Workshop to Characterize Scenario Earthquakes in the Yucca Mountain Region."**

| <b>Participants</b> | <b>Affiliation</b>   |
|---------------------|----------------------|
| Allen, Clarence     | CalTech/NWTRB        |
| Anderson, Ernie     | USGS/ Golden         |
| Anderson, Larry     | USBurRecl/Denver     |
| Bell, John          | NevBurMinesGeol/Reno |
| Brocher, Tom        | USGS/Menlo Park      |
| Bucknam, Bob        | USGS/Golden          |
| Coppersmith, Kevin  | Geomatrix Conslt     |
| Crone, Tony         | USGS/Golden          |
| dePolo, Craig       | NevBurMinesGeol/Reno |
| Fridich, Chris      | USGS/YMPB/Denver     |
| Hanks, Tom          | USGS/Menlo Park      |
| Hamilton, Warren    | USGS/Denver          |
| Machette, Mike      | USGS/Golden          |
| Menges, Chris       | USGS/YMPB/Las Vegas  |
| O'Leary, Dennis     | USGS/YMPB/Denver     |
| Pezzopane, Silvio   | USGS/YMPB/Denver     |
| Ramelli, Alan       | NevBurMinesGeol/Reno |
| Schneider, John     | WCFS/USGS/Menlo Park |
| Schwartz, David     | USGS/Menlo Park      |
| Swan, Burt          | Geomatrix Conslt     |
| Wesling, John       | Geomatrix Conslt     |
| Wesnousky, Steve    | CentNeotect/UN-Reno  |
| Whitney, John       | USGS/YMPB/Denver     |

|                  |                    |
|------------------|--------------------|
| Wong, Ivan       | WCFS/Oakland       |
| Yount, Jim       | USGS/UN-Reno       |
| <b>Observers</b> | <b>Affiliation</b> |
| Ibrahim, Bakr    | NRC                |
| Abrahamson, Norm | Consultant         |
| Quittmeyer, Rich | WCFS/Las Vegas     |
| Reiter, Leon     | NWTRB              |
| Stepp, Carl      | WCFS/Consultant    |
| Sullivan, Tim    | DOE/Las Vegas      |

**Table 2.2 Proposed scenario faults.**

| <b>Scenario</b> | <b>Group 1, Leader:</b>                      | <b>Group 2, Leader:</b>                                     | <b>Group 3, Leader:</b>                                   | <b>Group 4, Leader:</b>   |
|-----------------|--|---|---|---|
|                 | <b>Bell</b>                                  | <b>Coppersmith</b>  | <b>Ramelli</b>  | <b>Wong</b>   |
| 1               | Paintbrush Canyon-<br>Stage Coach            | Paintbrush Canyon   | Paintbrush-Bow Ridge                                      | Paint Brush Canyon  |
| 2               | Solitario Canyon                             | Solitario Canyon  | see Scenario 6  | Solitario Canyon  |
| 3               | Rock Valley                                  | Rock Valley   | Rock Valley   | Rock Valley   |
| 4               | Bare Mountain                                | Bare Mountain   | Bare Mountain   | see Scenario 6  |
| 5               | Furnace Creek                                | Furnace Creek   | Furnace Creek   | Furnace Creek-Death<br>Valley   |
| 6               |  | Coalesced Windy<br>Wash-Solitario<br>Canyon-Fatigue<br>Wash | Coalesced Solitario<br>Canyon-Fatigue Wash-<br>Windy Wash | Solitario Canyon-<br>Fatigue Wash-<br>Windy Wash<br>coalesced to Bare<br>Mountain |
| 7               | Pahrump-Stewart<br>Valley-Amargosa<br>Valley |   | Pahrump-Stewart<br>Valley-Amargosa<br>Valley              |   |
| 8-12            | "Scattered"<br>Walker Lane (10)              | Stage Coach<br>(see Scenario 1)                             | Belted Range (11) or<br>West Springs Mountain<br>(12)     | Mine Mountain (8) or<br>Wahmonie Mountain<br>(9)                                  |

**Table 2.3 Proposed scenario earthquakes.**

| Scenario | Fault   | Length (km)          | Dip/Rake   | Strike (deg)                   | Max Disp. (m)                        |
|----------|---|----------------------|--|--------------------------------|--------------------------------------|
| 1        | Paintbrush Canyon-Bow Ridge                           | 14 - 15 <sup>1</sup> | 45 to 70 W / -70 (Normal/LL)   | 185 to 195                     | PC: 1.0 avg<br>BR: 0.4 avg           |
| 2        | Solitario Canyon                                      | 21 ± 7               | 58 ± 8 W / -65 ± 5 (Normal/LL)                                       | 185 ± 2                        | 0.8 ± 0.3 avg                        |
| 3        | Rock Valley   | 42                   | 90 ± 5 / 0 to -30 (LL/dip)   | 068 to 075                     | < 3                                  |
| 4        | Bare Mountain   | 18 ± 4               | 45 to 70 E / -90 (Normal)  | 000                            | 1 (avg)<br>1.5 (max)                 |
| 5        | Furnace Creek   | 90 ± 10              | 90 / 180 (RL)  | 310                            | 2 to 4 (max)                         |
| 6        | Solitario Canyon-Fatigue Wash-Windy Wash <sup>2</sup> | FW: 17<br>WW: 25     | FW: 80 to 90 / -80 to -90<br>WW: -50 to -60 / -70 to -90 (Normal/LL) | FW: 355 ± 10<br>WW: 183 to 211 | FW: 0.35, 0.50, 0.65<br>WW: 0.38 avg |
| 7        | Pahrump-Stewart Valley                                | 40                   | 90 / 180 (RL)  | 317                            | < 1.5 vertical                       |
| 8        | Mine Mountain   | 8 to 35              | 70 SE / -90 (normal)   | -045                           | unknown                              |
| 9        | Wahmonie Mountain                                     | 6 to 22              | 68 SE / -90 (normal)   | -045                           | unknown                              |
| 10       | "Scattered" Walker Lane <sup>3</sup>                  | 30 to 60             | 90 / 180 (RL)  | 315                            | 1 to 1.5                             |
| 11       | Belted Range  | 20                   |  | -020                           | 1 to 2                               |
| 12       | West Springs Mountain                                 | 38                   | 60 / -90 (normal)  | 342                            | -1.5                                 |

<sup>1</sup> with or without Bow Ridge.

<sup>2</sup> Volcanic triggered event with 120 cm displacement on Solitario Canyon, 50 cm on Fatigue Wash and 10 cm on Windy Wash, for a total slip of 180 cm.

<sup>3</sup> This event involves a right-lateral strike-slip event with NW strike buried to a depth of a few km, with distributed normal faulting in the upper crust.

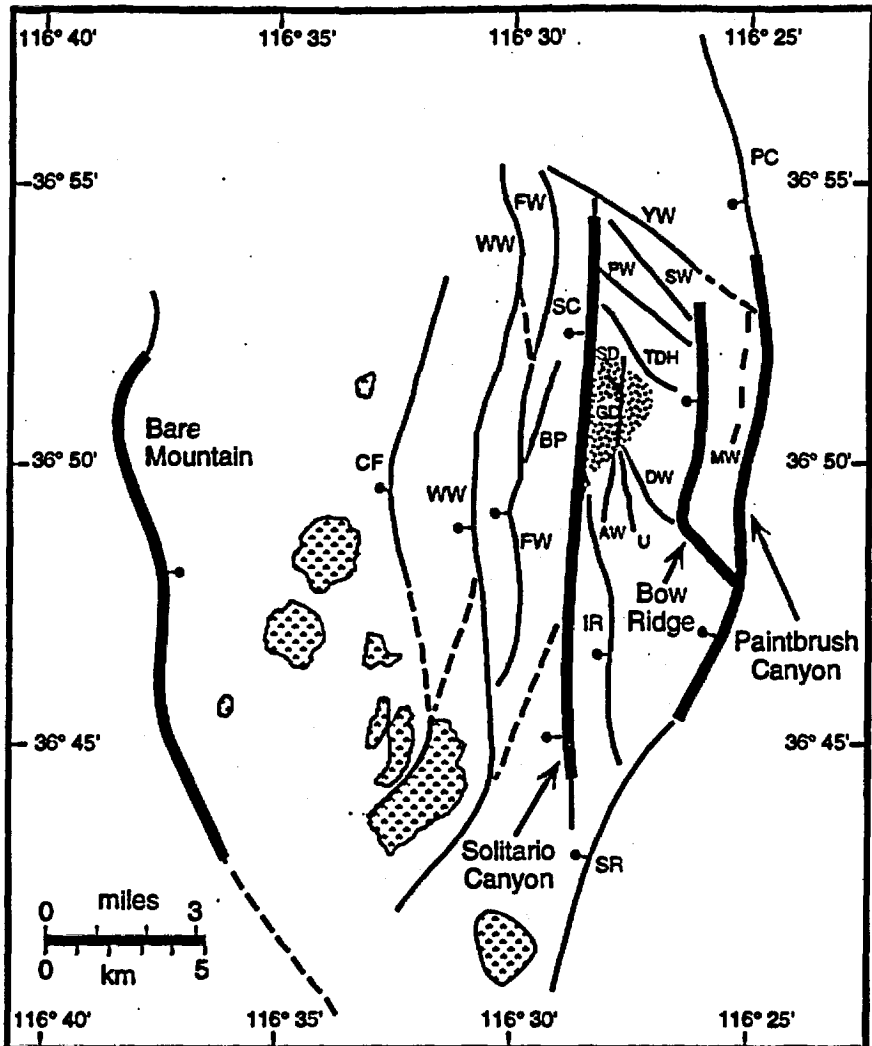
**Table 2.4 Selected scenario earthquakes.**

| Scenario | Fault   | Length<br>(km)   | Width<br>(km) | Dip                            | Rake  | M                 | Dist.<br>(km)      |
|----------|---|------------------|---------------|--------------------------------|---|-------------------|--------------------|
| 1        | Paintbrush Canyon-<br>Bow Ridge                               | 14 to 15         | 14.2          | 45 to 70 W                     | -70<br>(Normal/LL)                              | 6.31              | PC: 4.5<br>BR: 2.5 |
| 2        | Solitario Canyon  | 21 ± 7           | 14.2          | 58 ± 8 W                       | -65 ± 5<br>(Normal/LL)                          | 6.48              | 1.0                |
| 3        | Rock Valley   | 42               | 12            | 90 ± 5                         | 0 to -30<br>(LL/dip)                            | 6.71              | ~25                |
| 4        | Bare Mountain   | 18 ± 4           | 14.2          | 45 to 70 E                     | -90<br>(Normal)                                 | 6.42              | 15.5               |
| 5        | Furnace Creek   | 90 ± 10          | 12            | 90                             | 180 (RL)  | 7.04              | ~50                |
| 6        | Solitario Canyon-<br>Fatigue Wash-<br>Windy Wash <sup>1</sup> | FW: 17<br>WW: 25 | 14.2          | FW: 80 to 90<br>WW: -50 to -60 | FW: -80 to -90<br>WW: -70 to -90<br>(Normal/LL) | ~6.6 <sup>2</sup> | 1.0                |

<sup>1</sup>Volcanic triggered event with 2/3 displacement on Solitario Canyon, 1/3 on Fatigue Wash and Windy Wash.

<sup>2</sup> Based on an average fault rupture length of 25 km.



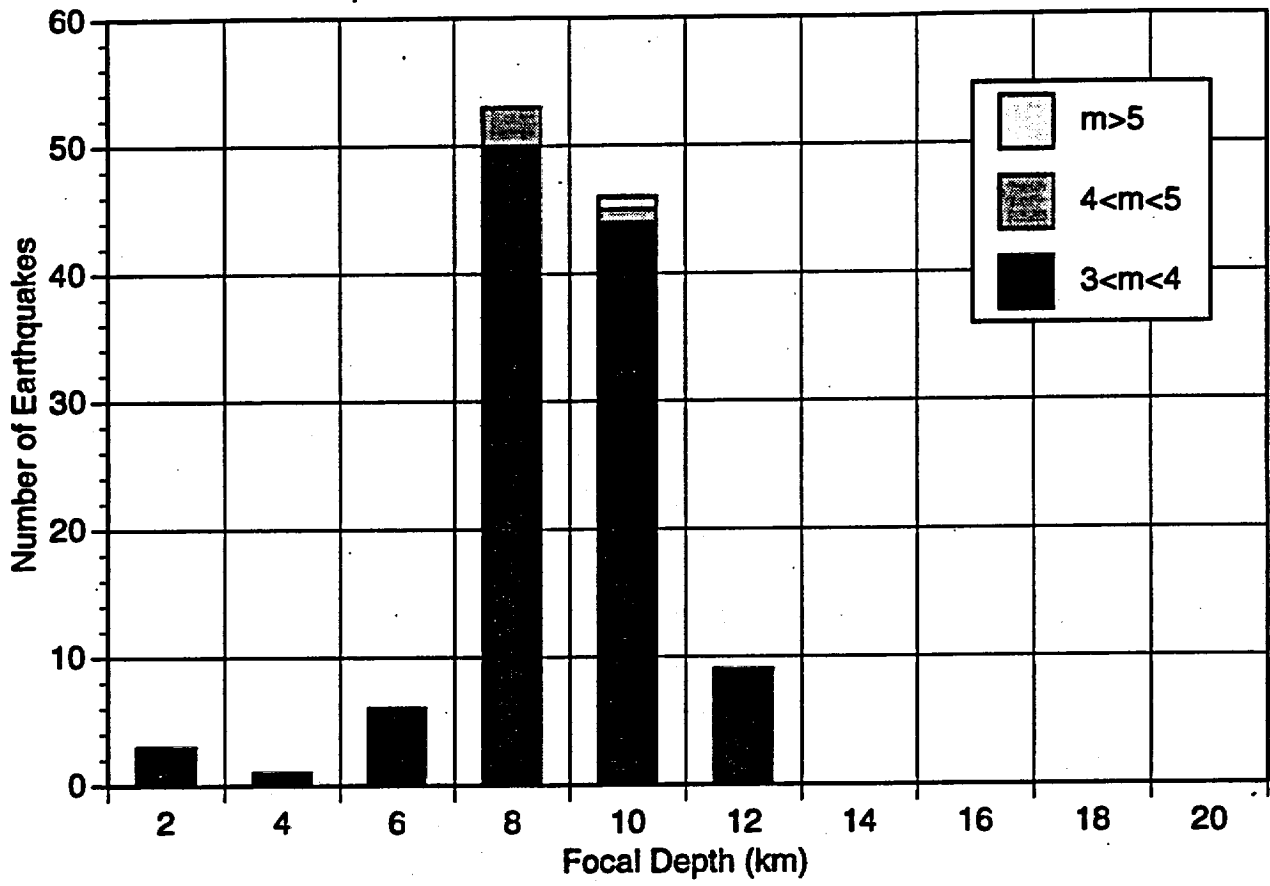


**EXPLANATION**

- Potential Repository Area
- Quaternary volcanic centers

**FAULT SYMBOLS**

| Abbreviation | Fault Name                   | Abbreviation | Fault Name             |
|--------------|------------------------------|--------------|------------------------|
| AW           | Abandoned Wash               | PC           | Paintbrush Canyon      |
| BM           | Bare Mountain                | PW           | Pagany Wash            |
| BP           | Boomerang Point              | SC           | Solitario Canyon       |
| BR           | Bow Ridge                    | SD           | Sundance               |
| CF           | Crater Flat                  | SR           | Stagecoach Road        |
| DW           | Dune Wash                    | SW           | Sever Wash             |
| FW           | Fatigue Wash                 | TDH          | Teacup-Drill Hole Wash |
| GD           | Ghost Dance                  | U            | unnamed                |
| IR           | Iron Ridge                   | WW           | Windy Wash             |
| MW           | Midway Valley (buried fault) | YW           | Yucca Wash             |



### **3. GROUND-MOTION MODELING METHODS**

In order to estimate representative ground motions for the selected Yucca Mountain earthquake scenarios, we need a set of criteria for determining what constitutes "representative" ground motions. The ground motions should be representative both from the perspective of the combination of physical parameters used in a given modeling method, as well as from the combination of methods used in the analysis. The purpose of this section is to discuss modeling methods. We discuss the criteria used to select an appropriate set of methods, as well as provide a brief discussion of each of the methods used in the study.

#### **Selection of Methods**

A set of criteria was developed to aid in the selection of modeling methods and modelers for the project. The criteria are as follows:

- methods are representative of the state-of-the-art;
- methods have been well calibrated against data;
- methods are amenable to evaluation of parameter sensitivity and ground motion uncertainty;
- methods are appropriate for application to Yucca Mountain;
- modelers are recognized experts in the field; and
- modelers are familiar with ground motion modeling for the western U.S., the Basin and Range Province, and/or Yucca Mountain.

In order to evaluate these criteria, a questionnaire was sent to a broad group of potential modelers (table 3-1). They were invited to answer the following questions.

- What are the most significant attributes of your model? What is unique about your approach? Include the frequency, magnitude and distance ranges of applicability of your model.
- How has your model been calibrated against data? What earthquakes and associated records have been modeled and compared to observations? What is the average uncertainty and bias for these events and how does it vary with frequency? Please provide copies of relevant published analyses.
- What parameters and their values need to be specified in your model? Of these parameters, which ones contribute greatest to the variation in predicted ground motion? Which parameter values are well-controlled by data and which ones are dominantly model dependent? What data would you like to consider for this application?
- What are the particular strengths and weaknesses of your model for application to Yucca Mountain? Do you require any special data or modifications to your model for this application?
- What is the greatest source of uncertainty in modeling ground motion at Yucca Mountain?

TABLE 3-1 -- NEAR HERE

An advisory panel of engineers and seismologists (table 3-2) then met to evaluate responses and to select methods and modelers for the modeling exercises. Of the 19 modelers sent questionnaires, 11 responded. From this group, six modelers were selected, with five representing physical modeling methods, and one representing an empirical method. The empirical method selected is based on ground-motion recordings from nuclear explosions in the vicinity of the Yucca Mountain site, calibrated against earthquake data. A seventh model based on the point-source stochastic model (Hanks and McGuire, 1981) is also considered in this study. Since the point source model is simple, the organizers applied this model rather than having a separate modeler apply the method.

TABLE 3-2 -- NEAR HERE

#### **Discussion of Modeling Methods**

In the physical modeling approaches, the ground motion at the site is built up by summing up the ground motions from a number of point-source sub-events distributed on the rupture plane. The assumptions and models of the sub-event ground motions and the manner in which the sub-events are combined to build up to the mainshock differ between the different modeling methods.

In the ground motion exercises, the seismic source is prescribed only by the rupture geometry (length, width, dip, and depth), seismic moment, and hypocenters (or a zone of allowable hypocenters). Other properties of the source are left to the modelers to determine based on their previous experience and calibrations of their respective numerical simulation procedures. The manner in which the seismic slip is distributed and released on the fault plane varies between methods. The methods also vary significantly in their assumptions of wave propagation, site response, and overall level of complexity, but all of the methods accommodate the essential aspects of seismic energy being generated at a finite source and propagated along the path to the site at the earth's surface. The key source parameters that are set by the modelers are discussed below. Not all of the source parameters listed are used in every model.

Together the six methods represent the state-of-the-art, and, as shall be demonstrated in a later section, the differences in resulting predictions can be used to capture a component of the uncertainty in scenario earthquake ground motions.

#### **Source Constraints and Issues**

There are some significant issues relative to the earthquake source that can have a large effect on the resulting ground motion predictions. Interpretations of parameters such as near-surface slip and source rise-time are not well constrained by data, yet the choices of values for these parameters can dominate the effects of most other parameter variations. Fortunately, this is where model calibrations and validations can play a very important role in restricting the range of admissible values. Some of the more important source issues are briefly discussed below.

## Source Rise-Time

Rise-time is the time it takes for slip to take place at a given point on the fault.

Some models assume that the rise-time is constant across the fault; while others assume that it is the slip velocity that is constant. In the former case, the slip velocity is then directly proportional to the slip; while in the latter, it is the rise time that is proportional to the slip. While the implications for actual ground motions can be dramatic, neither assumption can be positively accepted or rejected with our present-day modeling methods and data. Of course, it is quite possible, perhaps likely, that the truth lies somewhere in between. In addition, the resulting ground motion is sensitive to the choice of rise-time for any given model. Thus, it is important that this parameter be calibrated against ground motion observations for many different earthquakes.

## Near-Surface Slip

Finite-source numerical models of ground motion generally assume (either implicitly or explicitly) that the upper few kilometers of the earth's crust does not radiate significant amounts of seismic energy during major earthquakes. While this assumption is quite consistent with empirical ground motion attenuation models and also with the limited number of recordings of ground motion at very close distances to large fault ruptures, the ground motion evidence is apparently at odds with the fact that large earthquakes are often accompanied by very large slip at the surface. Seismic dislocation theory would predict that extremely large ground motions should accompany large surface displacements, unless some aspect of earth rheology is greatly different near the surface of the earth than it is at depth. From a numerical modeling perspective, the only viable ways to avoid this physical conundrum are to appeal to sufficiently slow rates of energy release or to very low shear strength in this part of the crust. The former can take the form of either a low rate of rupture (along the fault) or of slip (at a point on the fault), while the latter is manifested in the shear modulus. This issue is important to Yucca Mountain because of the clear evidence for large fault displacements within or very close to the proposed repository block.

In this study, we will address this issue only to the extent of comparing the ground motion values resulting from the two cases, one with seismogenic slip extending to the surface of the earth, and one with slip truncated at several kilometers depth. We do not attempt to address the larger issue of developing the physical understanding of the rheology and dynamics of the earth's near surface that is needed to validate the ground motion modeling results obtained here.

## Slip Distributions

The slip distribution describes the variation of the slip on the fault plane (for example, location of asperities). Information on the characteristics of the slip distribution have come from source inversions of strong motion data (as an example see Wald and Heaton, 1994). Most of the available source inversions for slip distributions on the fault are for strike-slip and reverse faults. For normal faults there is very little data. Somerville (1992) has summarized the results of several studies of source inversions and has shown that for strike-slip faults, the distribution of slip is not uniform with depth; it tends to be more heavily concentrated in the lower half of the fault. This trend does not appear to hold for reverse faults, where the slip distributions (for any given earthquake) are more consistent with uniform average slip with depth. For normal faults, it is not clear which model, if either, would be more appropriate.

## Stress Drop

Studies of stress drops for earthquakes in extensional regimes have yielded conflicting results. On the one hand, some data, especially from the Basin and Range Province, suggest a trend toward lower Brune or dynamic stress drops for earthquakes in extensional versus compressional regimes (for example, McGarr, 1984; Silva and others, 1992). On the other hand, studies such as those by Westaway and Smith (1989) and Wells and Coppersmith (1994) show that there are no statistically significant differences in ground motions and rupture areas between normal, strike-slip and reverse faulting earthquakes, implying that there is not a significant difference in stress-drop.

The stress drop can also be used as a benchmark for the variability of ground motion contributed by the various source parameters used in the physical modeling approaches. In the point-source model, the stress drop is the only source parameter, other than seismic moment. At some distance away from the source where the extended source effects are reduced effectively to a point, the variation in measured values of the stress drop, as defined by Brune (1970, 1971), should be comparable to the variations in stress drop produced by the extended source models. This issue is discussed further in Section 10.

### 3.4 Descriptions of Methods

Following is a brief description of each of the modeling methods. The purpose of these descriptions are to compare and contrast the main features of the models. More detailed descriptions of the modeling methods are given in Appendix B which also includes details of the approaches used for the ground motion modeling exercises in this study. As a prelude, we discuss the point-source  $\omega$ -squared model since it serves as a building block for most of the methods.

#### $\omega$ -Squared Point-Source

The  $\omega$ -squared point-source model is used as the model for the sub-events for most of the physical modeling methods. This model, developed by Hanks and McGuire (1981) has been refined by Boore (1983, 1986) and Silva (1991). In this model, the acceleration Fourier amplitude spectrum is given by

$$\text{FAS}(f) = C \frac{f^2}{1+(f/f_c)^2} \frac{M_0}{R} P(f) A(f) \exp\left\{-\frac{\pi f R}{\beta_0 Q(f)}\right\} \quad (3.1)$$

where FAS is the Fourier amplitude spectrum,  $f$  is frequency,  $M_0$  is the seismic moment,  $R$  is the distance,  $f_c$  is the corner frequency,  $\beta_0$  is the shear wave velocity at the source,  $Q(f)$  is the anelastic attenuation,  $A(f)$  is the amplification between the source depth and surface due to the crustal amplification,  $P(f)$  is a high-frequency cut-off filter, and  $C$  is a constant.

The corner frequency is related to the stress-drop by

$$f_c = \beta_0 \left( \frac{\Delta\sigma}{8.44M_0} \right)^{1/3} \quad (3-2)$$

The  $P(f)$  function is typically modeled by either an  $f_{\max}$  (Hanks, 1982) filter or a kappa (Anderson and Hough, 1984) filter:

$$\text{for } f_{\max}: \quad P(f) = \frac{1}{1 + (f/f_{\max})^{2n}} \quad (3.3)$$

$$\text{for kappa:} \quad P(f) = \exp(-\pi\kappa f) \quad (3.4)$$

Typically a value of  $n=4$  is used for the  $f_{\max}$  filter (equation 3.3). The kappa model is used in the applications of the point source model for the mainshock, but both models are used by the modelers for the sub-events.

The two source parameters for the  $\omega$ -squared model are the moment and the stress-drop. Since moment is specified by the earthquake of interest, the only remaining parameter is the stress drop. In using the  $\omega$ -squared model for the sub-events, the value used for the stress drop may be different for the different models because the models use different procedures for summing up the sub-events. Therefore, differences in the value of the stress drop used in a specific models does not in itself indicate incompatible models, because there may be offsetting assumptions. The values of the model parameters need to be consistent with the modeling method (as determined from the validation). This is why constraints are not put on this or other source parameters.

#### Specific Barrier Method

The Specific Barrier Method is applied in these exercises by Dr. Byau-Heng Chin and Prof. Keiiti Aki of the University of Southern California (denoted USC model). In this approach, the source spectrum is defined using the specific barrier model (Papageorgiou and Aki, 1983).

This source model uses a superposition of point sources in a line extending from the hypocenter to the edge of the fault in the direction of the site of interest. The  $\omega$ -squared model is used to represent the sub-event of the specific barrier model. Note that in this model, the seismic slip is not distributed over the 2-D rupture plane, but rather it is given by a line of point sources. For each site location, the line of point sources extends from the hypocenter toward the site. Therefore, this model will always result in forward directivity effects.

The propagation path effect is approximated by  $1/R$  geometrical spreading for distances less than 100 km. For distances greater than 100 km,  $1/R^{0.75}$  is used for the geometrical spreading. The amplitude attenuation due to absorption and scattering is included through  $Q(f)$ . The crustal amplification factor developed by Boore (1986) for western North America strong motion recordings on rock is assumed to apply to the Yucca Mountain region. The high frequency decay is modeled by an  $f_{\max}$  filter (but it is considered as part of the source rather than a site effect). Non-linear site effects are not considered.

The ground motions are estimated by applying the stochastic technique of Band-limited white noise (BLWN) and random vibration theory (RVT) of Boore (1983) to the Fourier amplitude spectrum determined from the source, path, and site parameters. For developing time histories, the following procedure is used for each barrier (sub-event). First, the Gaussian white noise with zero mean is generated with a random-number generator. The white noise is windowed by a shape function. The Fourier spectrum of the windowed time series is multiplied by the Fourier spectrum of the ground acceleration and an inverse Fourier transform yields the simulated time history for a single barrier. The time histories from the multiple barriers are then combined with appropriate time delays based on the rupture velocity. For estimating response spectral values, RVT is used to provide more stable estimates of the response spectra than the set of time histories.

#### Stochastic method with $\omega^2$ sub-events

The stochastic finite-fault method with  $\omega^2$  sub-events is applied in these exercises by Dr. Walter Silva of Pacific Engineering & Analysis (denoted PEA model). This method is an extension of the point-source stochastic method to the finite-fault case using the BLWN model with RVT.

The fault rupture plane is discretized into a number of equal size sub-fault regions. The radiation pattern is modeled by a constant which is the average factor for all of the sub-fault regions. The top 2 km of the crust is assumed to be non-seismogenic so the shallow extent of the slip is taken as 2 km. Different values of the slip are assigned to each sub-fault element to incorporate asperities into the model.

Empirical models are used to estimate the rise times of the mainshock and sub-events. Heterogeneity of the source process is modeled by randomizing the location of the sub-events within each sub-fault element as well as the sub-event rise-time.

The path effect is approximated using  $Q(f)$  and  $1/R$  geometrical spreading for distances less than 100 km and  $1/R^{0.5}$  for distances greater than 100 km. The crustal amplification is computed for the Yucca Mountain region specific crustal model.

The site effect is modeled by a kappa filter and an equivalent-linear model to accommodate non-linear site response effects (Silva and Lee, 1987).

RVT is used to estimate the response spectra to yield more stable results of the response spectra than the set of time histories. To generate time histories, the Fourier phase of the sub-event is represented empirically using a small ( $M=5$ ) Eastern North American (ENA) event. The sub-event time history is estimated using the empirical phase with the omega-squared amplitude spectrum for the particular sub-event. This is then convolved with a spike seismogram developed from the rupture times and amplitudes of each sub-event.

### Stochastic Slip Functions Method

The stochastic slip function method is applied in these exercises by Dr. Bill Joyner of the U.S. Geological Survey (denoted USGS model). This method is an extension of the point source stochastic method of Hanks and McGuire (1981) to spatially extended sources.

The method is based on a stochastic source function representing total slip at each point of a rectangular rupture surface. The source function has a spectrum in two-dimensional wavenumber space with amplitude prescribed such that the ground motion has an  $\omega$ -squared spectrum. The ground motion is calculated assuming rupture propagation at a uniform velocity from the hypocenter with a slip-velocity function of the Kostrov type (Kostrov, 1964) having a spectrum with a high-frequency falloff of  $\omega^{-0.5}$ . The path attenuation is computed using a  $1/R$  geometric spreading and  $Q(f)$ . The radiation pattern is modeled by a constant average factor for all points on the fault rupture plane. The site effects are incorporated by means of a frequency-dependent amplification factor as described in Boore (1986). The high-frequency decay is modeled by a kappa filter. Non-linear site response is not considered.

### Composite Fractal Source Method

The composite source model is applied in these exercises by Dr. Yuehua Zeng and Prof. John Anderson of the University of Nevada, Reno (denoted UNR model). The source model, developed by Zeng and others (1994), comprises a superposition of circular sub-events across a fault area, with the sub-event radii distribution following a power law distribution (Frankel, 1991). The sub-events are modeled as Brune pulses ( $\omega$ -squared spectra). The stress-drop of the sub-events is constant over the fault plane except at shallow depths. The stress drops decreases to zero at the surface. This tapering of the stress depth in the shallow depths is a mechanism for reducing the impact of the shallow slip on the computed ground motions.

Wave propagation is accommodated using synthetic Green functions generated using the generalized reflection and transmission coefficients method for a layered earth (Luco and Apsel, 1983) and wave scattering based on isotropic scattering theory. The site response is modeled using a kappa filter with crustal factors (Su and others, 1995) or by a site-specific velocity profile with Q.

### Broadband Green's Function Method

The Broadband Green's Function method is applied in these exercises by Drs. Paul Somerville and Chandan Saikia of Woodward-Clyde Federal Services (denoted WCC model). This method combines two different procedures for the low frequency ( $f < 1$  Hz) and high frequency ( $f > 1$  Hz) parts of the ground motion. At low frequency, theoretical source models are used including the radiation pattern; whereas at high frequencies, empirical source functions are used which include empirical estimates of the radiation pattern.

### Composite fractal source method

The composite source model is applied in these exercises by Dr. Yuehua Zeng and Prof. John Anderson of the University of Nevada, Reno (denoted UNR model). The source model, developed by Zeng and others (1994), comprises a superposition of circular sub-events across a fault area, with the sub-event radii distribution following a power law distribution (Frankel, 1991). The sub-events are modeled as Brune pulses ( $\omega$ -squared spectra). The stress-drop of the sub-events is constant over the fault plane except at shallow depths. The stress drops decreases to zero at the surface. This tapering of the stress depth in the shallow depths is a mechanism for reducing the impact of the shallow slip on the computed ground motions.

Wave propagation is accommodated using synthetic Green functions generated using the generalized reflection and transmission coefficients method for a layered earth (Luco and Apsel, 1983) and wave scattering based on isotropic scattering theory. The site response is modeled using a kappa filter with crustal factors (Su and others, 1995) or by a site-specific velocity profile with  $Q$ .

### Broadband Green's Function Method

The Broadband Green's Function method is applied in these exercises by Drs. Paul Somerville and Chandan Saikia of Woodward-Clyde Federal Services (denoted WCC model). This method combines two different procedures for the low frequency ( $f < 1$  Hz) and high frequency ( $f > 1$  Hz) parts of the ground motion. At low frequency, theoretical source models are used including the radiation pattern; whereas at high frequencies, empirical source functions are used which include empirical estimates of the radiation pattern.

**Table 3.1 Prospective ground motion modelers.**

| <b>Theoretical Modelers</b>             | <b>Responded</b> | <b>Selected</b> |
|---|------------------|-----------------|
| James Chin / Keiiti Aki                 | yes              | X               |
| Yuehua Zeng / John Anderson             | yes              | X               |
| Ralph Archuleta                         | no               |                 |
| Steve Day / Jeff Stevens                | yes              |                 |
| Larry Hutchings                         | yes              |                 |
| Bill Joyner                             | yes              | X               |
| Mehrdad Mahydiar                        | no               |                 |
| Walter Silva                            | yes              | X               |
| Paul Somerville                         | yes              | X               |
| Gabriel Toro                            | yes              |                 |
| Al Rodgers / Dave Perkins               | yes              |                 |
| David Wald / Tom Heaton                 | no               |                 |
| <br>                                    |                  |                 |
| <b>Empirical Modelers</b>               | <b>Responded</b> | <b>Selected</b> |
| Jack Murphy / Theron (Joe) Bennett      | yes              | X               |
| Dave Boore / Bill Joyner                | no               |                 |
| Ken Campbell                            | yes              |                 |
| I. M. Idriss / Ross Sadigh / Bob Youngs | no               |                 |
| M. Trifunac                             | no               |                 |
| Marianne Walck                          | no               |                 |

**Table 3.2 Advisory panel for the selection of modelers.**

**Norman Abrahamson**

**Allin Cornell**

**Tom Hanks**

**John Schneider**

**Table 3.3 Summary of physical modeling methods**

| Model   | Modeling Method  |   |  |
|---------|--|---|--|
|         | Source   | Path  | Site   |
| USC     | <ul style="list-style-type: none"> <li>• finite specific barrier model; Brune sub-event</li> <li>• BLWN RVT</li> <li>• <math>f_{max}</math></li> </ul>                                       | <ul style="list-style-type: none"> <li>• 1/R geometrical spreading and <math>Q(f)</math></li> </ul> | <ul style="list-style-type: none"> <li>• S-wave amplification factors (Boore, 1986) (high freq atten in source)</li> </ul> |
| USGS    | <ul style="list-style-type: none"> <li>• finite model with stochastic Brune source function; phase randomized over several realizations</li> <li>• Kostrov slip-velocity function</li> </ul> | <ul style="list-style-type: none"> <li>• 1/R geometric spreading and <math>Q(f)</math></li> </ul>   | <ul style="list-style-type: none"> <li>• 1-D crustal amplification factor and kappa</li> </ul>                             |
| S-cubed | <ul style="list-style-type: none"> <li>• empirical ground motion models based upon NTS data, modified to account for differences between earthquake and explosion sources</li> </ul>         | <ul style="list-style-type: none"> <li>• explosion-based attenuation functions</li> </ul>           | <ul style="list-style-type: none"> <li>• explosion-based site response</li> </ul>  |

**Table 3.3 (continued) Summary of physical modeling methods.**

| Model | Modeling Method   |   |  |
|-------|---|---|--|
|       | Source  | Path  | Site   |
| PEA   | <ul style="list-style-type: none"> <li>• finite with BLWN RVT</li> <li>• finite slip distrib. from f-k model</li> <li>• constant rupture velocity, randomized rise time, average radiation</li> </ul>   | <ul style="list-style-type: none"> <li>• 1/R geometrical spreading, or 1-D or 2-D</li> <li>Ou &amp; Herrmann</li> </ul>   | <ul style="list-style-type: none"> <li>• kappa/ equiv. linear for non-linear site-specific response</li> </ul>   |
| WCC   | <ul style="list-style-type: none"> <li>• finite with slip dist. from f-k model</li> <li>• variable rake angle, rise time, radiation</li> <li>• low f: continuous slip function w/ theoretical radiation pattern</li> <li>• high f: discretized grid w/ empirical source functions, corrected to the source</li> </ul> | <ul style="list-style-type: none"> <li>• low f: Green functions from f-k integration, complete response and Q for layered medium</li> <li>• high f: simplified Green functions from G-R theory, dominant rays and Q for layered medium</li> <li>• 2- and 3-D modeled with G-R for high f and finite diff. for low f.</li> </ul> | <ul style="list-style-type: none"> <li>• incorporated in empirical Green's functions, corrected for kappa.</li> <li>• normally elastic; equiv- lin. analysis possible</li> </ul> |

**Table 3.3 (continued) Summary of physical modeling methods.**

| <b>Model</b> | <b>Modeling Method</b>  |   |   |
|--------------|---|---|---|
|              | <b>Source</b>   | <b>Path</b>   | <b>Site</b>   |
| <b>UNR</b>   | <ul style="list-style-type: none"> <li>• composite finite model;</li> <li>superposition of circular</li> <li>sub-events with fractal</li> <li>distribution</li> </ul> | <ul style="list-style-type: none"> <li>• 1-D Green functions</li> <li>• scattering</li> </ul> | <ul style="list-style-type: none"> <li>• 2 approaches: elastic</li> <li>model of site-specific</li> <li>soil profile; or</li> <li>amplification factors</li> <li>and Kappa</li> </ul> |

---

## **4. MODELING EXERCISES AND ESTIMATION OF UNCERTAINTY**

The ground motion modeling exercises provide the ground rules within which estimates of ground motion can be made by each of the modelers. The exercises were developed by design to focus on general source, path, and site constraints for the physical modeling methods. The essential objective of the exercises is to capture median estimates of ground motion and associated uncertainty. This can be done in a systematic fashion by constructing modeling exercises such that the various components of uncertainty can be evaluated separately.

### **Modeling Exercises**

There are four types of exercises that are used in the course of obtaining the estimates of uncertainty.

1. **Validation exercise.** In this case, the modeler is asked to model ground motion from a previously recorded earthquake using (to the extent possible) source, path, and site parameters that have been determined independently. In this manner, we can determine the misfits of the models to data, which is an important piece of the uncertainty in estimating ground motion for future scenarios.

2. **Base case exercise (fixed parameters).** The source, path, and site properties of the scenario earthquake are prescribed or fixed in sufficient detail so as to limit the number of free choices of parameter values that can be used in any given model. Any differences in the resulting ground motion between models is attributed to differences in methods. The base case is also used to find systematic differences in output between methods that may be symptomatic of model bias or calibration error.
  
3. **Preferred case exercise (variable parameters).** The modeler is allowed to modify source, path and site properties relative to the base case to the degree that these changes can be justified by data or expert judgment. This case represents a refinement of the base case, because it allows the modeler to compensate for the effects of using different parameter values or assumptions in a given method that have been constrained by previous calibrations with observed ground motion data.
  
4. **Sensitivity exercise.** Within a given method or methods, specific parameter values are varied to determine their effect on the resulting ground motion. This type of analysis is used to assess the sensitivity of the ground motion to the source, path, and site characteristics specified for the scenario exercises.

### **Estimation of Uncertainty**

The uncertainty of the predicted ground motions are an important part of the ground motion characterization. In characterizing the uncertainty of ground motions from numerical simulations we need to be sure that we account for all of the sources of uncertainty without double counting uncertainty. To track the uncertainty, it is convenient to separate the total uncertainty into modeling uncertainty and parametric uncertainty which are discussed below.

### **Epistemic and Aleatory Uncertainty**

In seismic hazard analyses, two types of uncertainty are considered: aleatory and epistemic. Aleatory uncertainty is use to randomness and epistemic uncertainty is due to scientific uncertainty in a model or a set of alternative models.

It could be argued that all uncertainty in ground motion attenuation is epistemic. That is, if we had the right model (exact description of the source process, 3-D crustal structure, and site properties) then we could compute the ground motions exactly. The problem with this concept is that it does not consider the limitations of the information that is provided. Typically, the independent variables are simply magnitude, mechanism, distance, and site classification. Since these simple parameters are not sufficient to completely characterize the source, path, and site effects, we cannot develop an exact model of the ground motion. With an infinite number of recordings, we can reduce the uncertainty in the median ground motion to zero, but there will still be variability due to the range of source properties, crustal velocities, and site properties that all have the same magnitude, distance, and site class. This variability is the aleatory uncertainty.

As an example, consider an empirical attenuation relation. For a given magnitude and distance, the attenuation relation produces an estimate of the median ground motion  $a(\mu)$  and the standard deviation of a lognormal distribution ( $\sigma$ ). The lognormal distribution with standard deviation  $\sigma$  comprises the aleatory uncertainty. That is, the scatter of the recorded motions about the median attenuation curve is treated as randomness in the model. Due to the limited number of recordings in the data set used to develop the model, there is scientific uncertainty in the values of  $\mu$  and  $\sigma$ . There is a best value of  $m$  and  $s$  that could be found with an infinite number of recordings. The uncertainties in the values of  $\mu$  and  $\sigma$  are epistemic uncertainties denoted  $\sigma_\mu$  and  $\sigma_\sigma$ . Typically,  $\sigma_\mu$  and  $\sigma_\sigma$  are estimated by considering multiple attenuation relations.

#### **Uncertainties for Ground Motions from Numerical Simulations**

In numerical simulation procedures, there are typically more parameters to describe the seismic source and ray path than just magnitude and distance. Due to these additional model parameters, the treatment of uncertainty becomes more complicated than the simple case for empirical attenuation models described above. To properly account for the uncertainty for numerical simulations, the uncertainty is divided into two parts: modeling uncertainty and parametric uncertainty.

#### **Modeling uncertainty**

Modeling uncertainty represents the limitations of the ground motion model. That is, even when the model parameters are optimized for a particular past earthquake, there are still differences between the predicted motions and observed motions (for example, the residuals are not all zero). These differences are attributed to the use of a simplified model of a complicated process.

Since modeling uncertainty is a measure of the limitations of the ground motion model, the only way we can measure it is through comparisons with ground motions from previous earthquakes. The comparison of the model predictions with recordings from past earthquakes has been called model "validation", but it is more than that. It is also required for estimating the modeling uncertainty component of the total uncertainty of the ground motion predictions for future earthquakes.

There are two parts to the modeling uncertainty: the mean of the residuals and the standard error of the residuals. The mean residual is an estimate of the bias of the model. That is, does the model tend to systematically over-predict or under-predict the ground motion. If there is a large bias, then the model may not be acceptable. The evaluation of the model bias is really what is meant by the model "validation". If the bias is acceptably small, then the model is said to be validated. If there is a significant model bias, then the model could be revised (improved) in the future to correct for this bias. Because the bias is reducible with additional information, the bias is considered as part of the epistemic uncertainty (a component of  $\sigma_{\mu}$ ).

The standard error of the residual represents uncertainty of the ground motions that are not predictable by the simple model. This uncertainty is considered to be random variations (aleatory) for that particular model (as far as that particular model is concerned, these variations are random). When predicting ground motions for a future earthquake, we need to account for this random variation that is not captured by the model (part of aleatory  $\sigma$ ). There is also epistemic uncertainty due to the uncertainty in our estimation of the value of the standard error due to the limited number of recordings and earthquakes used in the validation exercise (component of  $\sigma_e$ ). In general, there is also uncertainty in the form of the probability distribution (e.g. other than lognormal), but that is outside the scope of this study).

Since modeling uncertainty is computed from comparisons to data, the modeling uncertainty is a catchall that in principal covers all of the shortcomings of the numerical simulation procedure. This is true only to the extent that the events used in the validation exercise are representative of future earthquakes. As the numerical models become more complete, the modeling uncertainty will be reduced, but the parametric uncertainty should then be increased as more event-specific parameters need to be randomized as described below.

### **Parametric Uncertainty**

The parametric uncertainty represents the uncertainty of ground motion due to variations of the parameters for future earthquakes. This variability comes from multiple realizations of the model with different values of the source parameters. Those source parameters that were optimized for individual events in the validation study are varied for future earthquakes. Parameters that are fixed in the model (either to constant value or constant scaling relations) are not varied because the effect of their variations are already captured as part of the modeling uncertainty if a sufficient number of events are used in the validation study. (The same goes for site and path parameters).

The uncertainty due to the variability of the ground motions from multiple realizations of the source generally leads to aleatory uncertainty; however, for some applications, some of the variability can be epistemic. For example, for predicting ground motions for a particular fault, the uncertainty in the dip of the fault is epistemic, but for predicting ground motions for a class of faults, the uncertainty in dip is aleatory. There is also epistemic uncertainty in the estimated distributions for the source parameters (mean and standard deviation of the source parameters) which contribute to  $\sigma_{\mu}$  and  $\sigma_{\sigma}$ .

The ground motions from the multiple realizations of the source generally lead to aleatory variability; however, geometrical variations in the source (for example, uncertainty in the dip of the fault) lead to epistemic uncertainty since the source geometry could be resolved with additional information. There is also epistemic uncertainty in the assumed distributions used for the source parameters (mean, standard deviation).

### **Total Uncertainty**

The total aleatory uncertainty is given by summing the modeling variance and parametric variance:

$$\sigma(\Gamma) = \sqrt{\sigma_{\text{model}}^2(\Gamma) + \sigma_{\text{param}}^2(\Gamma)} \quad (4.1)$$

This assumes that the covariance between the modeling and parametric terms is zero.

For the hazard analysis, the epistemic and aleatory components of the uncertainty are kept separate, however, for an 84th percentile ground motion estimate, the total uncertainty is given by summing the aleatory variance and the variance in the median:

$$\sigma_{\text{total}}(\Gamma) = \sqrt{\sigma_{\text{model}}^2(\Gamma) + \sigma_{\text{param}}^2(\Gamma) + \sigma_{\mu}^2(\Gamma)} \quad (4.2)$$

This total uncertainty is used to compute the 84th percentile ground motion.

### **Complex versus Simple Models**

As more complex models (and more accurate) as used, the modeling uncertainty is reduced, but there is a counter-acting increase in the parametric uncertainty. The total uncertainty cannot be reduced by using adding more event-specific parameters to the model.

The advantage of using a complex model with additional event- and site-specific parameters is that it does a better job of explaining past earthquakes. It provides a physical basis for the variations in the ground motion. We have more confidence in the model when we can explain the variations rather than just saying that they are random.

The disadvantage of using a more complex model is that we need to develop joint probability distributions for all of the event-specific parameters that are used in the model. It is hard enough to develop probability distributions for the parameters independently from the limited data available, but once we have multiple source parameters, we need to develop joint distributions because the source parameters may be correlated. If we ignore the correlation of the source parameters then we will probably over-estimate the variability.

#### **Uncertainty for this Scenario Earthquake Study**

The uncertainties considered in this study are shown in Table 4-1. In this study, the parametric aleatory uncertainty includes the source terms ( $\sigma_{\text{source}}$ ) which include variability in the hypocenter, sub-event stress drop, and slip distribution.

The focus of the uncertainty treatment in this study has been the estimation of the aleatory uncertainty ( $\sigma$ ) and the epistemic uncertainty in the median ( $\sigma_{\mu}$ ). A full treatment of the epistemic uncertainty in the standard deviation ( $\sigma_{\sigma}$ ) has not been made.

**Table 4.1 Source of Uncertainty**

|   | Aleatory<br>(randomness) | Epistemic<br>(scientific uncertainty)              |   |
|---|--------------------------|--|---|
|   | $\sigma$                 | $\sigma_{\mu}$                                     | $\sigma_{\sigma}$   |
| Modeling<br>(From comparisons<br>with data)                   | $\sigma_{\text{model}}$  | $\sigma_{\text{method}}$<br>$\sigma_{\text{bias}}$ | $\sigma_{\sigma \text{ method}}$<br>$\sigma_{\sigma \text{ model}}$ |
| Parametric<br>(From multiple<br>realizations of the<br>model) | $\sigma_{\text{source}}$ | $\sigma_{\text{dip}}$                              | Not<br>considered   |

## 5. YUCCA MOUNTAIN PATH AND SITE PROPERTIES

In this section, an overview of path and site properties and issues that are relevant to the estimation of vibratory ground motion at Yucca Mountain from local and regional earthquakes is presented. Based upon these considerations, best estimates for a Yucca Mountain one-dimensional crustal profile ( $V_p$ ,  $V_s$ , density,  $Q_p$  and  $Q_s$ ) and modulus reduction and damping curves are developed.

## **V<sub>p</sub> and V<sub>s</sub> in the Crust**

Overall, knowledge of the velocity structure of the crust in the vicinity of Yucca Mountain is moderately good for P waves in the upper 3-km of the crust, but very poor at greater depth, and generally poor at all depths for S waves. Below a few kilometers, the only direct information on S-wave and P-wave velocities comes from regional one-dimensional profiles developed for locating earthquakes (for example, Harmsen and Bufe, 1992; Harmsen, 1993). Available data indicate that the crustal structure in the vicinity of Yucca Mountain is strongly heterogeneous. Several two-dimensional profiles crossing the Nevada Test Site (and including Yucca Mountain) have been determined from analyses of ground-motion recordings of underground nuclear explosions (Walck and Phillips, 1988; 1990). Other constraints on P-wave velocities are available from seismic refraction and reflection studies (Ackerman and others, 1988; Hoffman and Mooney, 1983; Mooney and Schapper, 1994; and Pankratz, 1982) as well as from gravity profiles conducted primarily by the USGS (Snyder and Carr, 1982; 1984). In addition, sonic logs provide some one-dimensional control of P-wave velocities in the upper 1-2 km of the crust at a number of locations at Yucca Mountain and in Midway Valley (Nelson and others, 1991). These logs generally indicate significantly higher velocities than do the results of refraction studies. This conflict is apparently due to the highly fractured nature of the shallow crust, which tends to reduce velocities of waves at the longer periods sampled by the refraction studies (Mooney and Schapper, 1994).

S-wave data are not available for the crust from any of the above studies. At very shallow depths, there are some recent results of VSP profiles that provide control on both P- and S-wave velocities in the upper hundred meters or so below the surface at Yucca Mountain (Daley and Majers, 1995; Balch and others, 1994). These data are discussed below.

## **Q and Geometrical Spreading**

The attenuation properties for the Southern Great Basin (SGB) vary widely depending upon the data set and the analysis method. First, several studies have made observations of the ground-motion attenuation rate with distance, which includes the combined effects of geometrical spreading and Q. In a study of Modified Mercalli Intensity (MMI) for the Kern County 1952 earthquake, Evernden (1975) concluded that there was a slightly lower ground motion decay rate toward the SGB than in southern California. On the other hand, Chavez and Priestley (1985) found slightly greater attenuation in the SGB than in Southern California from an evaluation of the  $M_L$  scale. And in a most recent study, R. B. Herrmann (St. Louis University, written comm., 1995) has shown comparable rates of decay in normalized geometrical spreading curves from the SGB and New Madrid. Table 5.1 contains a summary of Q studies in the SGB, which show substantial differences in results. Some factors contributing to these differences are the influences of:

- assumptions about geometrical spreading and scattering;
- other source, path, and site effects;
- widely varying frequency bands, source-receiver distances, and regions of coverage;
- scattering versus anelastic Q;
- vertical versus horizontal component records; and
- earthquakes versus explosions.

Thus, while apparent differences in Q and attenuation can be quite large, it is likely that a significant portion of these differences has origins in one or more of these factors.

TABLE 5.1 -- NEAR HERE

Our interest is in selecting the appropriate  $Q$  for use in forward modeling of earthquake ground motion, with principal interest in modeling direct waves. In this context, there are a few key observations worthy of note. First, Samiezade (1993) has clearly demonstrated that coda  $Q$  values exhibit much stronger frequency dependence than  $Q$  from direct waves, implying differences between forward- and back-scattered waves. This factor should be considered when assigning or selecting  $Q$  for forward-modeling in our ground motion exercises. It is also generally observed that nuclear explosions are enriched in low frequencies and surface waves relative to earthquakes due to the shallow source depth. This observation will play a role in interpreting the results of the empirical ground motion modeling method used in this study. A final note of caution is that  $Q_{Lg}$  values, which are typically observed at low frequency and large distances, may not be appropriate for modeling higher frequency  $S$  waves at closer distances.

Fortunately, for our purposes in this study, uncertainty in attenuation has a relatively small impact on ground motion variability due to the dominance of close-in sources. However, this uncertainty is a factor at very high frequencies, for very low  $Q$  values, and for long travel paths (for example, at least 50-100 km).

## Site Constraints and Issues

Site issues are considered in the context of the geophysical and geotechnical data available to constrain site response estimation. The properties of interest are P- and S-wave velocities and damping (or Q), as discussed previously for wave propagation through the crust. An additional issue for the site, however, is the potential for motions to be modified at high strains in the near-surface layers, typically referred to as non-linear response. Here, the critical properties of interest are the dependence of shear-wave modulus and shear-wave damping as functions of strain. The change in modulus has the effect of increasing the amplification and shifting the peak response to lower frequency for larger strains. The change in damping has the effect of reducing motions for larger strains, with greatest impact at higher frequencies. The low-strain properties are generally resolvable from borehole seismic and geophysical surveys; whereas, high-strain properties of the shallow (upper 100 m) materials require dynamic testing under laboratory conditions (or direct measurements of earthquake strong motion).

To date, seismic, geophysical and geotechnical investigations of the site have focused on issues generally unrelated to the estimation of ground motion. Seismic reflection and refraction studies have been conducted primarily to determine crustal structure or to identify and characterize potentially seismogenic faults (as an example see Mooney and Schapper, 1995). Other geophysical and geotechnical studies have generated a broad range of log data from dozens of boreholes at and around Yucca Mountain (Nelson and others, 1991; Subramanian and others, 1990; and Gibson and others, 1992). Unfortunately, the results of these studies (especially sonic logs) do not constrain seismic velocities in the uppermost few hundred meters (that is, above the water table), which have the greatest impact on site response. The sonic velocities are also inconsistent with results of seismic refraction studies (Mooney and Schapper, 1995) or recent VSP logs (Daley and Majer, 1995; Balch and others, 1994). Previous geotechnical studies have focused on a broad range of static index properties and on a more limited number and range of dynamic properties (for example, Boyd and others, 1995 a, 1995b; Martin and others, 1994, 1995). The core velocities resulting from these tests are also inconsistent with lower-frequency, in situ measurements from VSP logs, as noted by Daley and Majer (1995) and Balch and others (1994).

There are, however, useful data for constraining velocity profiles at Yucca Mountain. The recent VSP logging studies mentioned earlier provide the most valuable constraints on low-strain P- and S-wave velocities at the frequencies of interest to strong ground motion. VSP logs in two boreholes (NRG-6 and WT-2) have been determined from a vertical and horizontal-shear vibroseis source by Daley and Majer (1995). Their data, while sparse, yields reasonable constraints on  $V_p$  and  $V_s$  to depths of 300 to 500 m. These data indicate that the Poisson's ratio increases from an average of  $\sim 0.27$  at 120 m, to  $\sim 0.45$  near the surface. This indicates that  $V_s$  decreases substantially more near the surface than would be obtained by assuming a constant Poisson ratio. Smoothed versions of these  $V_s$  profiles are shown in figure 5.1. Also shown for comparison is the  $V_s$  profile from the Exploratory Shaft Facility (DOE, 1994b), located approximately 1 km east of Yucca Mountain. Durrani and Walck (1995) have also recently developed a shallow two-dimensional P-wave profile through Yucca Mountain from borehole recordings of nuclear explosions (for example, Vortman and Long, 1982; Phillips, 1991).

FIGURE 5.1 -- NEAR HERE

Su and others (1995) and Anderson and Su (1995) have recently made estimates of low-strain damping from recordings of aftershocks of the Little Skull Mountain earthquake. Their work is based on estimates of the parameter kappa (Anderson and Hough, 1984), which represents either the whole-path damping ( $\kappa$ ), or damping in the uppermost 1-3 km beneath the site ( $\kappa_0$ ). Their average kappa ( $\kappa_0$ ) of 0.02 sec is between the average of 0.04 seconds appropriate for the western U.S. (Silva and Darragh, 1995), and 0.006 seconds for the eastern U.S. (EPRI, 1993).

Useful data on the high-strain behavior of materials are not available for Yucca Mountain. However, a laboratory-testing program was conducted recently on welded and nonwelded tuffs from Los Alamos, New Mexico, for the express purpose of deriving high-strain properties for input to earthquake site response analyses (Wong and others, 1995). While the samples tested do not necessarily reflect the exact properties of Yucca Mountain tuffs, sufficient similarities exist to warrant their evaluation. In fact, lacking any comparable data from Yucca Mountain samples, the Los Alamos tuff test results constitute a best estimate of shallow high-strain behavior at Yucca Mountain.

The impact of the limitations in available site-specific data is to increase the uncertainty in estimating ground motion. The impact is greatest at high strain, where potentially substantial reductions in motions above a few Hz must be offset by increased uncertainty in the magnitude of the effect.

#### **Base Case Velocity and Q Profiles**

Based upon the available data and previous work summarized above, one-dimensional P- and S-wave velocity and Q profiles for Yucca Mountain are assembled (table 5.2 and figs. 5.1 and 5.2).

**TABLE 5.2, FIGURE 5.2 -- NEAR HERE**

$V_s$  and  $V_p$  in Layers 1, 2 and 3 are controlled by measured  $V_s$  from VSP logs at WT-2 and NRG-6 by Daley and Majer (1995) (fig. 5.1). Below that,  $V_p$  is controlled in the upper 3 km largely by the refraction data (Mooney and Schapper, 1994), with  $V_s$  determined assuming a constant Poisson ratio of 0.25 (fig. 5.2). Below this depth, velocities are those developed for the earthquake location profile in the vicinity of Yucca Mountain (Harmsen, 1992). The densities are based upon a combination of density logs from Nelson and others (1991) in the upper 2 km and a gravity gradient of the Yucca Mountain region from Snyder and Carr (1982, 1984) which is correlated with seismic velocities by Ackerman (1988).

$Q_s$  values are specified so as to yield a  $\kappa_0$  of 0.02 seconds, as given by Su and others (1995) and Anderson and Su (1995), for the upper 3.1 km. This  $\kappa_0$  is equivalent to an average  $Q_s$  80 over that depth interval. The whole-path  $Q$  has an average value of 600, consistent with Sameigade (1993), and  $Q_s$  is specified as  $\sim 1/3 Q_p$  above 80 m, consistent with the higher Poisson ratio, and  $\sim 1/2 Q_p$  below that, approximately consistent with a Poisson solid (which would yield  $Q_s = 5/9 Q_p$ ). For modelers who prefer to use a frequency-dependent whole-path  $Q$ , the specified model is  $Q_s(f) = 250 f^{0.4}$  for Layers 7 to 10, which is consistent with many of the  $Q$  measurements given in table 5.2.

#### **Base Case Strain Dependent Shear Modulus and Damping**

The strain dependent shear modulus and damping "curves" are the basic input to an equivalent-linear analysis of strong motion site response (for example, Silva, 1987). The values listed in table 5.3 were developed from the results of torsional shear and resonant column tests on Los Alamos tuff samples (Wong and others, 1995). These values are comparable to those for a stiff-dry sand.

TABLE 5.3 -- NEAR HERE

**Table 5.1 Summary of Q relations for southern basin and range<sup>1</sup>.**

| Authors                 | Data                         | Source type | Method                           | Freq. range (Hz) | Result<br>$Q(f)=Q_0f^n$          |
|-------------------------|------------------------------|-------------|----------------------------------|------------------|----------------------------------|
| Singh & Herrmann 1983   | Lg coda, WWSSN and LRSM sta. | earthquake  | predom. freq. analysis           | 0.6 to 3.5       | Q <sub>0</sub> : 250<br>n: 0.45  |
| Peseckis & Pomeroy 1984 | Lg coda, WWSSN sta.          | explosion   | predom. freq. analysis           | 0.5 to 2.0       | Q <sub>0</sub> : 264<br>n: 0.30  |
| Chavez & Priestley 1986 | Lg, LLNL sta.                | explosion   | regression on source spectra & Q | 0.3 to 10.0      | Q <sub>lg</sub> : 214<br>n: 0.54 |
| Nuttli 1986             | Lg, WWSSN sta.               | explosion   | predom. freq. analysis           | 0.5 to 2.0       | Q <sub>0</sub> : 139<br>n: 0.60  |
| Rogers & others 1987    | S coda and Lg coda           | earthquake  | regression on amp. decay of coda | 1.0 to 10.0      | Q <sub>0</sub> : 143<br>n: 0.84  |
| Rogers & others 1987    | S coda and Lg coda           | explosion   | regression on amp. decay of coda | 1.0 to 3.0       | Q <sub>0</sub> : 188<br>n: 1.05  |

<sup>1</sup> first six entries after Xie and Mitchell, 1990

**Table 5.1 (continued) Summary of Q relations for southern basin and range.**

| Authors                 | Data                 | Source type | Method                                   | Freq.<br>range<br>(Hz) | Result<br>$Q(f)=Q_0 f^n$   |
|-------------------------|----------------------|-------------|--|------------------------|----------------------------|
| Rogers & others<br>1987 | peak displace.<br>Lg | earthquake  | regression on<br>source spectra and<br>Q | 1.0 to 10.0            | $Q_{lg}: 774$<br>n: 0.04   |
| Samiegade 1993          | SV, SGB network      | earthquake  | regression on<br>PSRV                    | 1.0 to 16.0            | $Q_{psrv}: 600$<br>n: 0.15 |
| Samiegade 1993          | SV, SGB network      | earthquake  | regression on amp<br>decay of coda       | 1.0 to 16.0            | $Q_0: 150$<br>n: 0.9       |

**Table 5.2 Yucca Mountain velocity and Q profiles.**

| Layer # | Depth to top<br>(km) | Thickness<br>(km) | V <sub>s</sub><br>(km/s) | V <sub>p</sub><br>(km/s) | density<br>(g/cm <sup>3</sup> ) | Q <sub>s</sub> | Q <sub>p</sub> |
|---------|----------------------|-------------------|--------------------------|--------------------------|---------------------------------|----------------|----------------|
| 1       | 0                    | 0.04              | 0.6                      | 1.8                      | 1.7                             | 25             | 80             |
| 2       | 0.04                 | 0.04              | 1.2                      | 2.5                      | 2.0                             | 40             | 120            |
| 3       | 0.08                 | 0.14              | 1.5                      | 2.9                      | 2.3                             | 40             | 120            |
| 4       | 0.22                 | 0.78              | 1.9                      | 3.2                      | 2.4                             | 70             | 150            |
| 5       | 1.00                 | 0.60              | 2.1                      | 3.6                      | 2.4                             | 100            | 200            |
| 6       | 1.60                 | 1.50              | 2.9                      | 5.0                      | 2.5                             | 150            | 300            |
| 7       | 3.10                 | 2.20              | 3.4                      | 5.8                      | 2.7                             | 400            | 800            |
| 8       | 5.30                 | 10.70             | 3.5                      | 6.2                      | 2.75                            | 400            | 800            |
| 9       | 16.00                | 16.00             | 3.8                      | 6.5                      | 2.9                             | 400            | 800            |
| 10      | 32.00                | —                 | 4.6                      | 7.8                      | 3.3                             | 400            | 800            |

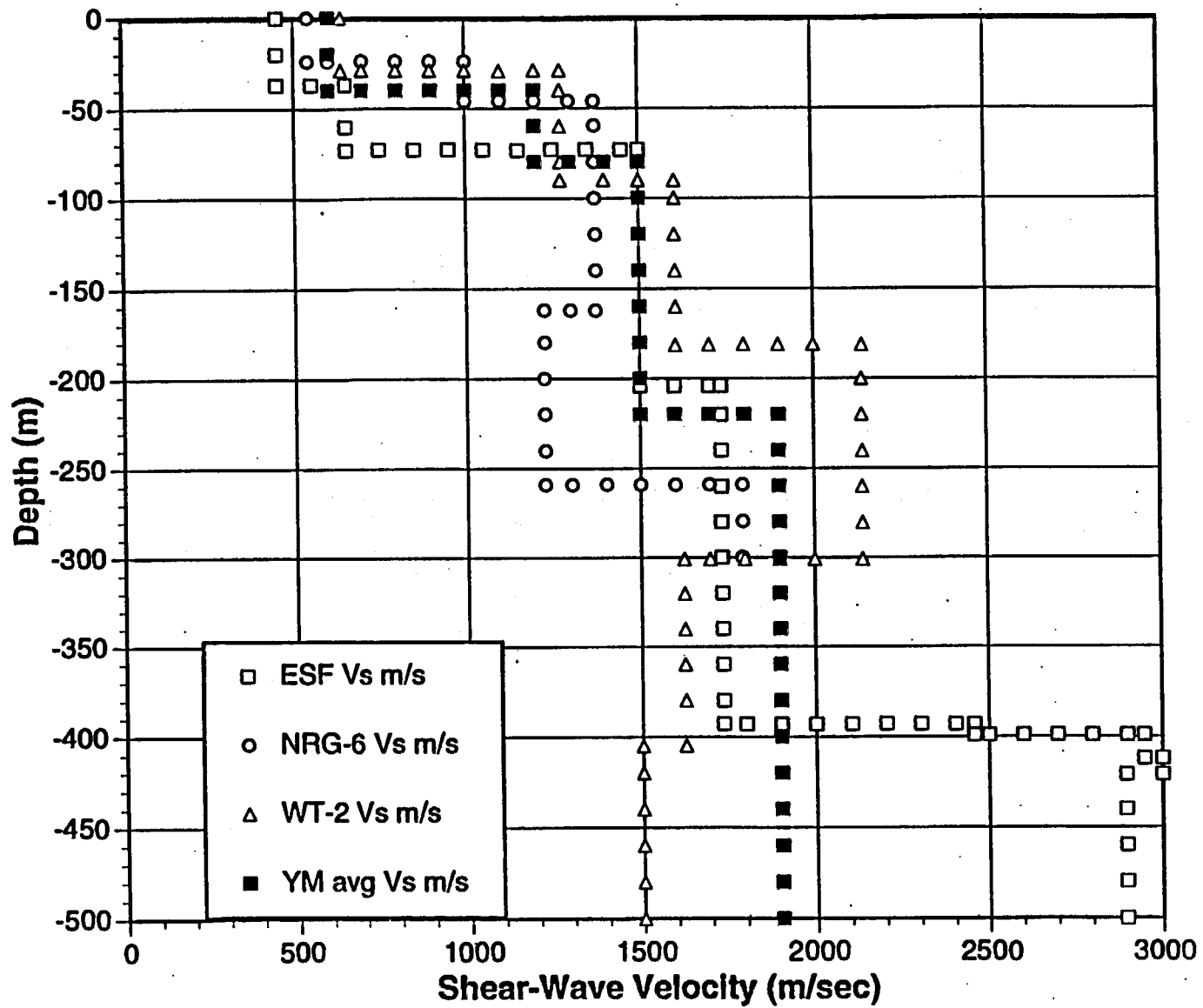
**Table 5.3 Modulus reduction and damping values as a function of shear strain.**

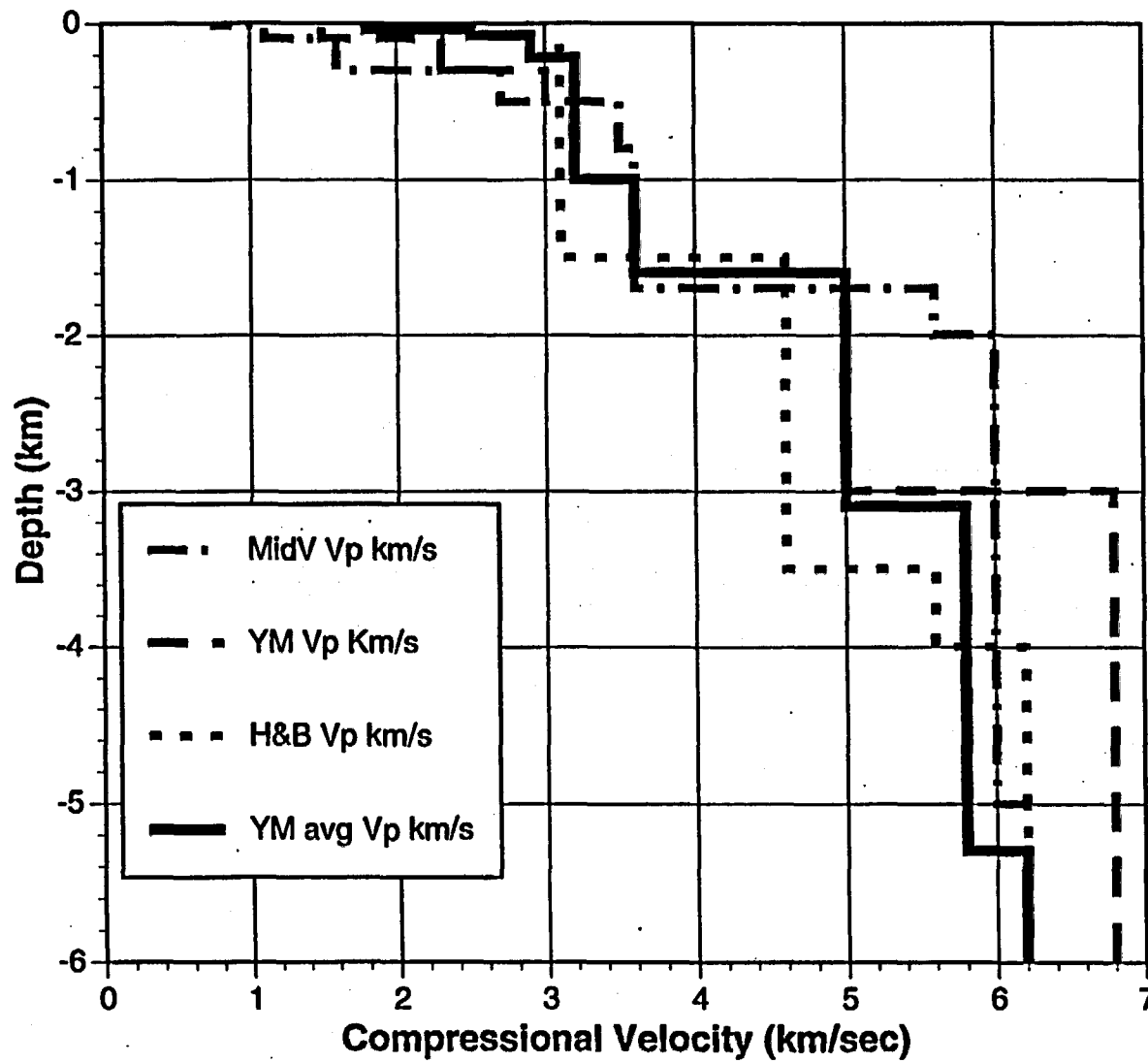
| <b>Log (Shear Strain)<br/>(Percent)</b> | <b>Shear Mod/<br/>Shear Mod<br/>at 10<sup>-4</sup>%</b> | <b>Shallow Tuff<br/>Damping Ratio<br/>(Percent)</b> | <b>Deep Tuff<br/>Damping Ratio<br/>(Percent)</b> |
|---|---|---|--|
| -4.0                                    | 1.0   | 0.8   | 0.4  |
| -3.5                                    | 1.0   | 0.8   | 0.4  |
| -3.0                                    | 1.0   | 1.0   | 0.6  |
| -2.5                                    | 0.95  | 1.4   | 1.0  |
| -2.0                                    | 0.85  | 2.4   | 2.0  |
| -1.5                                    | 0.66  | 4.8   | 4.0  |
| -1.0                                    | 0.44  | 9.1   | 6.3  |
| -0.5                                    | 0.22  | 14.7  | 10.7   |
| 0.0                                     | 0.09  | 21.0  | 16.0   |

## Figure Captions

Figure 5.1. Shear velocity as a function of depth in the vicinity of Yucca Mountain. "YM avg" is the composite "best-estimate" profile.

Figure 5.2. Compressional velocity as a function of depth in the vicinity of Yucca Mountain. "YM avg" is the composite "best-estimate" profile.





## 6. LITTLE SKULL MOUNTAIN VALIDATION EXERCISE

The June 29, 1992 M 5.7 Little Skull Mountain earthquake was recorded at the strong motion accelerograph array operated by Blume & Associates for the Department of Energy (Lum and Honda, 1993a, 1993b) (fig. 6.1). This is the largest earthquake to have been recorded within 20 km of Yucca Mountain. Moreover, it is the only earthquake in this vicinity (excluding aftershocks) for which significant recordings of strong motion are available. In this section, a ground motion modeling validation (or calibration) exercise is developed using the Blume strong motion data. This test exercise serves to calibrate the ground motion models as well as to refine values of source, path and site properties for estimating ground motion for scenarios specific to Yucca Mountain. The exercise is to model the observed strong motion records at the five stations closest to the Little Skull Mountain source, those that lie within about 60 km of the fault (fig. 6.1). In addition, ground motions are generated for a set of 10 test sites within 10 km of the fault for which no strong motion data exist. The motions at these test sites allow comparison of near fault ground motions for the different modeling methods when the source properties are constrained by more distant recordings.

FIGURE 6.1 – NEAR HERE

In this section, the source properties of the Little Skull Mountain event are documented and best estimates to be used as a starting point for the modeling exercise are developed. The results of a point-source inversion that was performed to serve as a guide to modelers for their forward-modeling analyses of the event are presented. Following this background analysis, the base-case and preferred-case modeling exercises and results are presented. Finally, the comparisons of the Little Skull Mountain recordings to various regional empirical attenuation relations are shown.

#### **Source Properties: Results of Previous Work**

Presented here is a summary of previous studies of the Little Skull Mountain earthquake from which best estimates are made of critical parameter values for input to the modeling exercise. Source parameters are discussed for the Little Skull Mountain mainshock (June 29, 1992) and two of the largest aftershocks (July 5 and September 13, 1992). Available information is given first on earthquake locations for these events, followed by information on focal mechanisms and seismic moments.

#### **Earthquake Locations**

Earthquake locations for the Little Skull Mountain mainshock and two largest aftershocks are given by Smith and others (1995) and Meremonte and others (1995) (table 6.1). Their analyses are based upon analyses of arrival times of body waves at stations of the Southern Great Basin (SGB) Network and at temporary, three-component stations installed to record aftershocks.

TABLE 6.1 -- NEAR HERE

### **Focal Mechanisms and Seismic Moments**

Focal mechanisms and seismic moments have been derived by a variety of investigators using several different analysis methods and data sets. Table 6.2 shows the analysis results, and table 6.3 provides additional information on the methods of analyses and data used. In general, the mainshock mechanism and moment are very-well constrained from all methods.

**TABLE 6.2, 6.3 – NEAR HERE**

### **Best Estimates of Source Parameters**

Based upon the information presented above, we can make best estimates of source parameter values. These best estimates provide constraints on the source parameters that are input to the modeling of strong motion records. We present best estimates of source parameter as follows:

- The best constrained hypocenters and origin times for all three events are given by Smith and others (1995). These values are constrained through a joint hypocenter location process in which the travel-time corrections for the SGB network stations were fixed (for all events) by minimizing the residuals for the best-recorded aftershocks at close distances. They also utilized a larger data set than Meremonte and others (1995) by incorporating all of the later aftershock recordings from the University of Nevada at Reno in the joint hypocenter location process.

- The mainshock focal mechanism is well constrained by a wide range of modeling approaches. Of the short-period, first-motion solutions (#1, 2 and 7), solution 1 is probably the best constrained. Of the wave-form analysis methods, solution #5 is probably the most robust because it takes into account a broad frequency band as well as observations from multiple stations. Solution 1 (60, 70, -70) is taken as the best estimate, with Solution 5 (45, 55, -60) as the alternate.
- For the aftershock focal mechanisms, short-period, first-motion solutions #11 (165, 70, -20) and #15 (110, 45, -80) from Smith and others (1995) are probably the best constrained. Surface-wave solution #12 for Aftershock 1 is poorly-constrained and is not in close agreement with the corresponding first-motion solutions #10 and 11.
- The seven independent mainshock moment estimates are all reasonably consistent, ranging across less than a factor of two. The mean (and best-estimate) seismic moment is  $3.66 \times 10^{24}$  dyne-cm. For the aftershocks, the Mayeda and Walter values (Solutions 14 and 17) are better constrained than Walter's (1993) solution for Aftershock 1 (W. Walter, LLNL, personal communication, 1995). Therefore, the seismic moments for Aftershocks 1 and 2 are taken to be  $3.5 \times 10^{22}$  and  $2.5 \times 10^{22}$  dyne-cm, respectively. These moments correspond to moment magnitudes M 5.7 (mainshock), M 4.3 (aftershock 1) and M 4.2 (aftershock 2).

- For mainshock fault radius, values range from 2.5 to 3.5 km from the distribution of early aftershocks (Solutions 1 and 2). The smaller radius of 2.5 - 3.0 km obtained by Smith and others (1995) is consistent with their hypocenter locations being more tightly constrained than those of Meremonte and others (1995). The 2.7 km radius (Solution 5) obtained by Zhao and Helmberger (1994) is based on their estimated source duration of 2.0 sec. Taking 2.7 km as the mean value yields a corresponding (static) stress drop of 70 bars and a fault area of 23 km.

Taking the mainshock fault area of 23 km and the aftershock distribution (Smith and others, 1995), the fault dimensions and location can be specified. For modeling purposes, to the nearest whole integer values, the fault rupture surface is 4 km along strike and 6 km down-dip, with the hypocenter near the lower southwest corner of the rectangle (fig. 6.2). Also consistent with the aftershocks, the bottom edge of the fault is placed at 12 km depth, which puts the top at 6.4 km depth. The best-estimate fault orientation determined previously are used: strike  $60^{\circ}$  and dip  $70^{\circ}$  SE. For this model, the coordinates of the corners of the fault plane and the hypocenter are given in table 6.4. Coordinates are given in terms of longitude, latitude and depth as well as rectangular coordinates, with the top of the fault along the y-axis.

TABLE 6.4, FIGURE 6.2 -- NEAR HERE

An alternative model of the fault plane is provided by using the average relationship of magnitude to rupture area given of Wells and Coppersmith (1994):  $M = 4.01 + \log_{10}(\text{rupture area})$ . In this case, the fault area is 46.3 km and the dimensions and location of the fault most consistent with the aftershock distribution yields a fault rupture surface 7 km along strike and 6.6 km down-dip. Again, the hypocenter is near the lower southwest corner of the rectangle. The bottom of the fault is placed at 12 km depth, which puts the top at 5.8 km depth ( $= 12 \text{ km} - 6.61 \text{ km} \times \sin 70^\circ$ ). The strike and dip are  $60^\circ$  and  $70^\circ$  SE., as before. For this model, the coordinates of the corners of the fault plane and the hypocenter are given in table 6.5. As with the previous model, the top of the fault is placed along the y-axis.

TABLE 6.5 -- NEAR HERE

#### **Point-Source Inversion**

An initial analysis of the Little Skull Mountain strong motion data using a simple point-source model provides initial constraints on source parameters for input to the more complex modeling methods. The results also provide a basis for comparing source properties of this event to those of other events in the Basin and Range Province. In particular, it is of interest to know whether the point-source stress drop (Brune 1970, 1971) for this event differs significantly from measured stress drops of other events in the region.

### Point-source Inversion Method

In the inversion scheme, earthquake source, path and site parameters are obtained by using a non-linear least-squares inversion of Fourier amplitude spectra for the stochastic model parameters given in equation 6.1 (Silva and Stark, 1992). The inversion scheme treats multiple earthquakes and sites simultaneously with a common crustal amplification,  $A(f)$ , and anelastic attenuation,  $Q(f)$ . The acceleration Fourier amplitude spectrum of the  $i^{\text{th}}$  earthquake at site  $j$  is modeled by

$$C \frac{f^2}{1 + \left(\frac{f}{f_c}\right)^2} \frac{M_0}{R} D \exp(-\pi\kappa f) \exp\left(\frac{-\pi\kappa R}{\beta_0 Q_0 f^\eta}\right) \quad (6.1)$$

where  $C$  is a constant given by

$$C = \frac{0.78\pi}{\rho_0 \beta_0^3} \quad (6.2)$$

Comparing with equation 3.1, there is an additional term in equation 6.1 ( $D_j$ ) which is a frequency independent site amplification which accounts for errors in the crustal amplification and allows broad-band adjustment of the modeled spectrum at each site. The six parameters which may be determined include: kappa ( $\kappa_j$ ) for each site,  $D_j$  for each site,  $Q_0$  and  $\eta$  for the region, seismic moment ( $M_i$ ) for each event, and corner frequency ( $f_{ci}$ ) for each event. Soil profile amplification can be accommodated in the inversion scheme by incorporating the appropriate transfer functions in the model spectra.

To reduce the non-uniqueness inherent in inversion schemes, a suite of starting models is employed. The final set of parameters is selected based upon visual inspection of the model fit to the Fourier amplitude spectrum as well as the least-square estimate of the error. Thus, this approach provides a consistent means by which to accommodate path  $Q(f)$  as well as  $\kappa$  and crustal amplification.

### Point-source Inversion Analysis and Results

The inversion procedure is applied to the Fourier spectra of the two horizontal-component accelerograms of the Little Skull Mountain mainshock and two large aftershocks. The initial data set consists of corrected horizontal-component accelerograms (Lum and Honda 1993a, 1993b) from a set of eight stations within about 100 km of the epicenter. In order to avoid having uncertainty in  $Q$  dominate the inversion results, the analysis is limited to the five closest stations which are within 60 km of the source. This constraint yields ten pairs of horizontal-component records: five from the mainshock, three from the July 5 aftershock and two from the September 13 aftershock. Fourier spectra are then computed for each record, then smoothed and band-limited to 0.1 to 25 Hz. In order to avoid low-frequency noise or contributions from surface waves, selected mainshock records are then high-pass filtered below either 0.15 or 0.2 Hz, and all aftershock records are high-pass filtered below either 0.2 or 0.3 Hz.

For the effect of crustal amplification, a transfer function is computed for the Yucca Mountain velocity profile developed previously (table 5-2). The transfer function, shown in figure 6.3, is for the amplification of the profile from Layer 8, the layer of dominant energy release (5.3 to 16.0 km depth), relative to a half-space model with the properties of Layer 8. In order to take into consideration the effect of variation in crustal properties, the transfer function is then smoothed (fig. 6.3) to yield a set of frequency-dependent amplification factors. For  $Q$ , the frequency-dependent  $Q$  model,  $Q(f) = 400 f^{0.4}$ , is used.

FIGURE 6.3 -- NEAR HERE

The high-frequency level of the amplification factors is given by the shear-wave impedance contrast between Layers 1 and 8, or  $\text{Sqrt}(V_8 \rho_8 / V_1 \rho_1) = 3.07$ . This value is within the range of amplifications for typical western U.S. crust (Boore and Joyner, 1996) but lower than given by Silva (written communication, 1996).

FIGURE 6.4 -- NEAR HERE

The best constraints on the parameter values are obtained through an iterative procedure by which each parameter can be constrained individually in order to evaluate the sensitivity of the inversion to correlations between parameters (table 6.6). In this manner, the first inversion is performed by fixing the magnitudes to the best estimates developed from previous studies discussed above. The results yield reasonable constraints on kappa values for each station, which are then fixed together with magnitudes for the next inversion run. The second run produces additional site amplification factors (D) averaging 1.03. These D factors allow the model to accommodate crustal amplification different from the assumed model. Since the average value is near 1, this indicates that the crustal amplification in the model is reasonable, on average. Thus, in the third and final iteration, we fix values for kappa and site amplification, and allow stress drop and magnitude to float to preferred values. Fourier amplitude spectra and best-fit curves from the final inversion are shown in figures 6.5 to 6.7. Final magnitude and stress drop values for the three events are given in table 6.7. Note that the median values of magnitude are 0.1 to 0.2 units smaller than the best estimates from other studies; and the resulting median values of stress drop are somewhat larger than those of the previous inversion run. Given the high negative-correlation between stress drop and magnitude, differences between results of the second and final runs are not statistically significant.

FIGURES 6.5, 6.6, 6.7 -- NEAR HERE

TABLES 6.6, 6.7 -- NEAR HERE

The stress drop values determined from this analysis indicate that the Little Skull Mountain earthquake and major aftershocks had stress drops that are consistent with those of other Basin and Range Province earthquake sequences (Appendix F).

### **Base Case Exercise Specifications**

The Little Skull Mountain earthquake ground motion modeling exercise is divided into two parts, a base case and preferred case. In the base case exercise, values of source, path, and site parameters are prescribed as much as possible from other data or results of previous analyses. Within this framework, the slip distribution and other aspects of fault dynamics are not known, and are therefore unspecified.

Modelers are free, for instance, to run several different slip distributions and source rise times in order to achieve the best fit to the data. In any case, if modelers choose to use source or path parameters that are not otherwise specified, the parameter values used must be consistent with those parameter values that are specified.

### **Input specifications**

Source parameter values and station coordinates for the base case exercise (SM1) are given in tables 6.8 and 6.9, respectively. In table 6.9, locations are given for the eight strong motion recording stations within 100 km of the source. Modeling of the horizontal-component records for the five closest sites (stations 1-5) is required as part of the exercise, while the remaining three sites (stations 6-8) are optional. In addition, locations are given for ten hypothetical test sites, also an optional part of the exercise. Figures 6.8 and 6.9 show the locations of the Little Skull Mountain fault area and hypocenter relative to the station locations of table 6.9. Refer to table 6.5 for coordinates of the 4 x 6 km (base case) fault plane and hypocenter.

**TABLES 6.8, 6.9 – NEAR HERE**

**FIGURES 6.8, 6.9 – NEAR HERE**

The crustal structure and shear modulus and reduction and damping values for the SM1 exercise are given in tables 5.2 and 5.3, respectively. Modelers have a choice of using these parameters or using empirical Green functions from recordings of Little Skull Mountain aftershocks. Records from the July 5 and September 13 aftershocks recorded within 25 km of the source (including on Yucca Mountain) are described in Appendix A.

#### Model-Specific Input Parameters

As noted above, properties of the source that are model-specific can not be prescribed generically. The values of model-specific parameters are identified in table 6.10, including any model-specific deviations from the SM1 exercise, as stated above. Unless otherwise noted, the SM1 specified parameter values for source, path and site properties are used.

TABLE 6.10 -- NEAR HERE

#### Output Specifications

The output specifications for all of the modeling exercises are standardized in order to facilitate comparison of results and statistical analyses which are developed in a later section. All ground motion estimates are presented in terms of 5 percent damped PSV response spectra for the geometric mean of horizontal components. The response spectra are computed at 89 frequency points from 0.1 to 100 Hz and are given in table 6.11. The 13 highest frequency points (above 34 Hz) are optional.

TABLE 6.11 -- NEAR HERE

Corresponding time history records (velocity and acceleration) are output for either two horizontal components (fault parallel and perpendicular) or one average horizontal component. Durations of velocity and acceleration time histories are also computed. The duration is defined in terms of the normalized Arias intensity for the vector sum of the two horizontal components (or one average horizontal component).

### Base Case Exercise Modeling Results

Figures 6.10 to 6.16 show comparisons of ground motion modeling results with observations at five stations for the SM1 base case. Figures 6.10 to 6.14 show calculated versus observed 5 percent damped acceleration response spectra for each station. It can be seen that the differences between observed and calculated spectra are site dependent. This is expected given that no site-specific properties are known; so, only average properties (velocity structure,  $Q$  and damping) are specified for all sites. Figures 6.15 and 6.16 show the goodness of fit of the model response spectra calculations in terms of standard error about the mean and model bias (Abrahamson and others, 1990), respectively. The standard error (natural log units) averages 0.3 to 0.8 at short period ( $< 0.5$  seconds), increases to 0.7 to 1.2 at 1 to 2 seconds, and decreases again to 0.3 to 1.0 from 2 to 10 sec. The model bias is strongly negative (implies overprediction of ground motion) and broadband for the PEA and USC models, but essentially unbiased for the UNR, WCC, and USGS results. The S-cubed empirical model shows a strong period dependence to the model bias with significant overprediction at long periods.

FIGURES 6.10 to 6.16 -- NEAR HERE

Figures 6.17 and 6.18 show the goodness of fit of the modeled acceleration time history duration in terms of the same standard error and bias. In this case, most of the modeled results exhibit significant underprediction of the recorded duration, particularly for the more distant stations. The UNR and USC models generally match the recorded durations quite well. The UNR model includes a scattering function and USC model as the duration as a adjustable parameter.

FIGURES 6.17, 6.18 -- NEAR HERE

### Preferred Case Exercise and Results

Based upon the SM1 modeling results, modelers are free to modify parameter values within the constraint that they be consistent with the observations and the results of previous work. For instance, modelers may get a better fit to the observed strong motion records using a moment of  $4.0 \times 10^{24}$  dyne-cm or a 6 x 6 km fault. Given that these values for moment and fault dimensions are well within the range of uncertainty of the observations, such adjustments would be considered reasonable and acceptable. On the other hand, it would not be acceptable to place the hypocenter in the top half of the fault, or even in the middle of the fault, as this would not be consistent with observation. Again, the slip distribution and other aspects of fault dynamics are unspecified.

### Preferred Case (SM2) Parameters

Some of the parameter values used in the SM1 case are modified to achieve a better fit to the observed data. Parameters used are the same as in SM1 unless otherwise specified in table 6.12.

TABLE 6.12 -- NEAR HERE

## SM2 Modeling Results

Figures 6.19 to 6.25 compare ground motion modeling results for the SM2 preferred case with recorded ground motions for the five stations closest to the Little Skull Mountain source. The same response spectral comparisons as well as standard error and bias plots are shown as before for SM1 modeling results. The SM2 results show significant improvement in the standard errors for the UNR and USGS models (fig. 6.24). There is substantial improvement in the model bias (fig. 6.25), especially for the PEA and USC models. The improvement in the model bias for the PEA model was obtained by using a larger fault area (for the same moment), which produced a broadband positive shift in the bias (reduced spectral amplitudes) of about 0.5 (natural log units) or a factor of about 1.6. For the USC model, the improvement in bias was obtained by reducing the local stress drop from 76 to 40 bar, which shifted the bias upward by about 0.4, or a factor of about 1.5. The USGS model also shows substantial improvement at short period due to using a site-specific kappa (estimated from the strong motion data), but it also shows a larger (negative) bias (overprediction) at long period due to using a soil amplification factor for stations 1, 4, and 5.

### FIGURES 6.19 to 6.25

The standard error and model bias plots for SM2 duration (figs. 6.26 and 6.27) show minimal improvement in the model fits. The most notable change is the reduction of the modal bias for PEA model by about 0.6 natural log units resulting from changing the selected sub-event time history to one that had a longer duration. The UNR model shows a significant decrease in the standard error of the duration of about 0.2 natural log units.

### FIGURE 6.26, 6.27 – NEAR HERE

### **Conclusion of Little Skull Mountain Validation Exercise**

Based on the model bias estimates for the preferred case (SM2) shown in figure 6.25, in general, the numerical simulation models have an acceptably small model bias for response spectral values at periods less than 1 second, indicating that they are applicable to estimating ground motions in the Basin and Range Province. The USGS model has a significant overprediction at period of 0.7 to 3.0 seconds. The empirical method also produces an acceptably small bias for period less than 0.8 seconds, but it should not be used for longer periods.

The USC and UNR models produce acceptably small bias for duration, but the WCC and USGS models significantly underestimate the duration. The PEA model also underestimates the duration, but the underestimation is not statistically significant. Some of the underestimation of the duration is a result of using more distant stations. Therefore, this underestimation will be of most concern for the Rock Valley and Furnace Creek scenario events (distances of 25 and 50 km, respectively).

**Table 6.1 Hypocenter locations.**

| <b>Event</b> | <b>Origin<br/>Date</b> | <b>Time</b> | <b>Lat</b> | <b>Lon</b> | <b>Depth<br/>(km)</b> | <b>Data<sup>1</sup></b> | <b>Reference</b>              |
|--------------|------------------------|-------------|------------|------------|-----------------------|-------------------------|-------------------------------|
| Main         | 06/29/92               | 1014        | 36.72      | -116.29    | 11.8                  | SGB                     | Smith and others,<br>1995     |
| Main         | 06/29/92               | 1014        | 36.72      | -116.29    | 9.6                   | SGB                     | Meremonte and<br>others, 1995 |
| AS1          | 07/05/92               | 0654        | 36.73      | -116.27    | 9.4                   | SGB, temp               | Smith and others,<br>1995     |
| AS1          | 07/05/92               | 0654        | 36.73      | -116.27    | 6.5                   | SGB, temp               | Meremonte and<br>others, 1995 |
| AS2          | 09/13/92               | 1146        | 36.72      | -116.30    | 8.9                   | SGB, temp               | Smith and others,<br>1995     |
| AS2          | 09/13/92               | 1146        | 36.73      | -116.30    | 7.0                   | SGB, temp               | Meremonte and<br>others, 1995 |

<sup>1</sup> SGB is the Southern Great Basin Network, temp is a temporary 3-component network installed to record aftershocks of the Little Skull Mountain earthquake

**Table 6.2 Focal mechanisms and seismic moments.**

| #  | Event | Fault Plane |     |      | Auxiliary Plane |     |      | $M_0$<br>(dyne-cm<br>$\times 10^{24}$ ) | Radius<br>(km) | Reference                   |
|----|-------|-------------|-----|------|-----------------|-----|------|---|----------------|-----------------------------|
|    |       | Strike      | Dip | Rake | Strike          | Dip | Rake |   |                |                             |
| 1  | Main  | 60          | 70  | -70  |                 |     |      |   | 2.5 to 3.0     | Smith and others, 1995      |
| 2  | Main  | 55          | 56  | -72  |                 |     |      |   | 3.5            | Meremonte and others, 1995  |
| 3  | Main  | 43          | 66  | -73  |                 |     |      | 3.5                                     |                | Romanowicz and others, 1993 |
| 4  | Main  | 34          | 44  | -70  |                 |     |      | 2.6                                     |                | Romanowicz and others, 1993 |
| 5  | Main  | 45          | 55  | -60  | 180             | 45  | -125 | 3.0                                     | 2.7            | Zhao and Helmberger, 1994   |
| 6  | Main  | 35          | 54  | -87  |                 |     |      | 4.1                                     |                | Walter, 1993                |
| 7  | Main  | 55          | 56  | -72  | 205             | 38  |      |   |                | Harmsen, 1994               |
| 8  | Main  | 54          | 51  | -65  | 197             | 45  |      | 4.8                                     |                | Dziewonski                  |
| 9  | Main  |             |     |      |                 |     |      | 3.7                                     |                | Mayeda & Walter, unpub.     |
| 10 | Main  |             |     |      |                 |     |      | 3.9                                     |                | Ritsema and others, 1993    |
| 11 | AS1   | 165         | 70  | -20  | 262             | 71  | -159 |   |                | Smith and others, 1995      |
| 12 | AS1   | 358         | 36  | -177 |                 |     |      | 0.043                                   |                | Walter 1993                 |
| 13 | AS1   | 5           | 85  | 12   | 95              | 88  | 6    |   |                | Harmsen, 1994               |
| 14 | AS1   |             |     |      |                 |     |      | 0.035                                   |                | Mayeda & Walter, unpub.     |
| 15 | AS2   | 110         | 45  | -80  | 276             | 46  | -100 |   |                | Smith and others, 1995      |
| 16 | AS2   | 186         | 50  | 8    | 16              | 40  | 27   |   |                | Harmsen, 1994               |
| 17 | AS2   |             |     |      |                 |     |      | 0.025                                   |                | Mayeda & Walter, unpub.     |

**Table 6.3 Source analysis methods and data.**

| # | Method  | Data                | Comments   |
|---|---|---------------------|--|
| 1 | short-period P-wave polarities;<br>radius from aftershock<br>distribution | SGB net             | good azimuthal coverage from SGB<br>net, better constrained than other<br>polarity methods due to improved<br>hypocentral location |
| 2 | short-period P-wave polarities  | SGB net             | similar to #1, but used different<br>hypocentral location  |
| 3 | surface wave moment tensor<br>inversion, T=15 to 50 sec                   | U.C. Berkeley       | automated inversion technique  |
| 4 | body waveform modeling  | UC Berkeley         | automated inversion technique  |
| 5 | broadband inversion   | So. Cal. Terrascope | optimizes solution for short and long-<br>period waveform  |
| 6 | body-wave and surface wave<br>inversion, T=15 to 50 sec                   | Kanab, Utah         | moment estimation for this path well-<br>calibrated from nuclear explosion<br>data   |
| 7 | short-period P-wave polarities  | SGB net             | good azimuthal coverage from SGB<br>net  |

**Table 6.3 Source analysis methods and data (cont)**

| #  | Method                                   | Data                                       | Comments  |
|----|--|--|---|
| 8  | Harvard centroid moment tensor inversion | teleseismic surface waves                  | rapid, automated algorithm  |
| 9  | surface wave inversion                   | surface waves from LLNL stations in Nevada | moment estimation for these paths well-calibrated from nuclear explosion data                             |
| 10 | centroid moment tensor inversion         | complete long-period motions               | rapid source inversion technique  |
| 11 | short-period P-wave polarities           | SGB net, temp stations from LLNL and USGS  | good azimuthal coverage from SGB net and temp stations, uses all available temporary stations             |
| 12 | body-wave and surface wave inversion     | regional distance; Kanab, Utah             | moment less well-constrained than for mainshock and mechanism poorly constrained due to low signal:noise. |
| 13 | short-period P-wave polarities           | SGB net, temp stations from USGS           | good azimuthal coverage from SGB net and temp stations  |

**Table 6.3 Source analysis methods and data. (cont)**

| <b>#</b> | <b>Method</b>                  | <b>Data</b>                                | <b>Comments</b>   |
|----------|--------------------------------|--|---|
| 15       | short-period P-wave polarities | SGB net, temp stations UNR                 | good azimuthal coverage from SGB net and temp stations                        |
| 16       | short-period P-wave polarities | SGB net                                    | mechanism not well-constrained from SGB net only                              |
| 17       | surface wave inversion         | surface waves from LLNL stations in Nevada | moment estimation for these paths well-calibrated from nuclear explosion data |

**Table 6.4 Little Skull Mountain fault plane coordinates.**

| <b>Point</b> | <b>Longitude</b> | <b>Latitude</b> | <b>x</b><br><b>(km)</b> | <b>y</b><br><b>(km)</b> | <b>z</b><br><b>(km)</b> | <b>Description</b> |
|--------------|------------------|-----------------|-------------------------|-------------------------|-------------------------|--------------------|
| C1           | -116.30          | 36.73           | 0.00                    | 0.00                    | 6.36                    | Origin             |
| C2           | -116.26          | 36.75           | 0.00                    | 4.00                    | 6.36                    | Az=60 from C1      |
| C3           | -116.29          | 36.72           | 2.05                    | 0.00                    | 12.00                   | downdip from C1    |
| C4           | -116.25          | 36.73           | 2.05                    | 4.00                    | 12.00                   | downdip from C2    |
| H            | -116.29          | 36.72           | 1.97                    | 0.50                    | 11.77                   | Hypocenter         |

**Table 6.5 Little Skull Mountain alternate fault plane coordinates.**

| <b>Point</b> | <b>Longitude</b> | <b>Latitude</b> | <b>x</b><br><b>(km)</b> | <b>y</b><br><b>(km)</b> | <b>z</b><br><b>(km)</b> | <b>Description</b> |
|--------------|------------------|-----------------|-------------------------|-------------------------|-------------------------|--------------------|
| C1           | -116.32          | 36.73           | 0.00                    | 0.00                    | 5.78                    | Origin             |
| C2           | -116.25          | 36.76           | 0.00                    | 7.00                    | 5.78                    | Az=60 from C1      |
| C3           | -116.30          | 36.71           | 2.26                    | 0.00                    | 12.00                   | downdip from C1    |
| C4           | -116.24          | 36.74           | 2.26                    | 7.00                    | 12.00                   | downdip from C2    |
| H            | -116.29          | 36.72           | 2.18                    | 2.00                    | 11.77                   | Hypocenter         |

**Table 6.6 Little Skull Mountain point-source inversion process.**

| Run # | Input                    |                |                         |               | Output                    |                           |                   |                                 |
|-------|--------------------------|----------------|-------------------------|---------------|---------------------------|---------------------------|-------------------|---------------------------------|
|       | M                        | Kappa<br>(sec) | Stress<br>Drop<br>(bar) | D             | Average<br>Kappa<br>(sec) | Stress<br>Drop**<br>(bar) | Average<br>D      | Standard<br>Error<br>(ln units) |
| 1     | fixed<br><br>(best est.) | free*          | free                    | free          | 0.018                     | 27, 11, 19                | 1.10              | 0.72                            |
| 2     | fixed<br><br>(best est.) | fixed (run 1)  | free                    | free          | 0.018 <sup>†</sup>        | 33, 14, 24                | 1.03              | 0.67                            |
| 3     | free                     | fixed (run 1)  | free                    | fixed (run 2) | 0.018 <sup>†</sup>        | 37, 23, 34                | 1.03 <sup>†</sup> | 0.64                            |

\*Kappa for Station 3 (Beatty) fixed to 0.001

\*\* for mainshock, July 5, and September 13 aftershocks, respectively

† fixed value from previous run

**Table 6.7 Little Skull Mountain point-source inversion results.**

| <b>Event</b>                       | <b>M</b>                          | <b>Stress Drop<br/>(bar)</b>  |
|------------------------------------|-----------------------------------|-------------------------------|
| <b>Mainshock</b>                   | <b><math>5.62 \pm 0.05</math></b> | <b><math>37 \pm 11</math></b> |
| <b>5 July<br/>Aftershock</b>       | <b><math>4.15 \pm 0.04</math></b> | <b><math>23 \pm 8</math></b>  |
| <b>13 September<br/>Aftershock</b> | <b><math>4.10 \pm 0.05</math></b> | <b><math>34 \pm 14</math></b> |

**Table 6-8. Source parameters for Little Skull Mountain base case exercise (SM1).**

| Source parameter                              | Value  |
|---|--|
| Fault Length (L)                              | 4 km   |
| Fault Width (W)                               | 6 km   |
| Fault Area (A) (L x W)                        | 24 km <sup>2</sup>                           |
| Magnitude (M)                                 | 5.68   |
| Average static stress drop ( $\Delta\sigma$ ) | 76 bars                                      |
| Average shear stress ( $\mu$ )*               | $3.37 \times 10^{11}$ dyne/cm <sup>2</sup> * |
| Average slip (D)                              | 45.2 cm                                      |
| Moment ( $M_0$ ) ( $\mu DA$ )                 | $3.66 \times 10^{24}$ dyne cm                |
| Fault strike                                  | 60 degrees ( $x = 0$ )                       |
| Fault dip                                     | 70 degrees to southeast ( $Az = 150$ )       |
| Fault rake                                    | -70 degrees (normal w/ left-lateral oblique) |

\* $\mu = \rho V_s^2$ , with  $\rho = 2.75$ ,  $V_s = 3.5$  km/s from Layer 8 of table 5.3

**Table 6-9. Little Skull Mountain strong motion station locations.**

| Site # | Site Name             | Long    | Lat   | x<br>(km) | y<br>(km) | Distance*<br>(km) |
|--------|-----------------------|---------|-------|-----------|-----------|-------------------|
| 01     | Lathrop Wells         | -116.40 | 36.64 | 4.5       | -12.7     | 12.9              |
| 02     | NTS Control Point 1   | -116.06 | 36.93 | -8.2      | 29.6      | 26.9              |
| 03     | Beatty                | -116.76 | 36.91 | -37.4     | -25.5     | 45.3              |
| 04     | Pahrump 2             | -116.07 | 36.23 | 58.6      | -10.0     | 57.5              |
| 05     | Pahrump 1             | -115.98 | 36.21 | 64.6      | -4.1      | 62.7              |
| 06     | Las Vegas -Calico Bsn | -115.41 | 36.15 | 95.7      | 36.4      | 99.1              |
| 07     | Las Vegas - Ann Road  | -115.31 | 36.26 | 89.6      | 50.2      | 99.0              |
| 08     | Death Valley - SC2    | -117.34 | 37.03 | -74.8     | -63.5     | 98.1              |
| 51     | Test Site             |         |       | 1.0       | 2.0       | 0.0               |
| 52     | Test Site             |         |       | 5.0       | 2.0       | 2.9               |
| 53     | Test Site             |         |       | 10.0      | 2.0       | 7.9               |
| 54     | Test Site             |         |       | 1.0       | 4.0       | 0.0               |
| 55     | Test Site             |         |       | 5.0       | 4.0       | 2.9               |
| 56     | Test Site             |         |       | -1.0      | 2.0       | 1.0               |
| 57     | Test Site             |         |       | -5.0      | 2.0       | 5.0               |
| 58     | Test Site             |         |       | -10.0     | 2.0       | 10.0              |
| 59     | Test Site             |         |       | -1.0      | 4.0       | 1.0               |
| 60     | Test Site             |         |       | -5.0      | 4.0       | 5.0               |

\*Distance is to surface projection of fault

**Table 6.10 Model-specific parameters and values used in the SM1 exercise.**

| Model | Source  | Path and Site  |
|-------|---|--|
| PEA   | <ul style="list-style-type: none"> <li>- Uniform slip over specified 4 x 6 km<sup>2</sup> area</li> <li>- Sub-event area 2 x 2 km<sup>2</sup></li> <li>- Sub-event Brune stress drop = 30 bar</li> <li>- Total rise time = 0.306 sec</li> <li>- Sub-event rise time =</li> <li>- Rupture velocity = 2.8 km/sec</li> </ul> | <ul style="list-style-type: none"> <li>- Layered velocity and Q model as provided</li> </ul>   |
| UNR   | <ul style="list-style-type: none"> <li>- D (fractal dimension) = 1.7</li> <li>- Dynamic stress drop = 50 bars</li> <li>- Maximum sub-events radius = 1.5 km</li> <li>- Rupture velocity = 2.8 km/sec</li> </ul>   | <ul style="list-style-type: none"> <li>- Layered velocity model as provided</li> <li>- Scattering parameters : scattering mean free path = 100 km</li> <li>- Intrinsic attenuation = <math>240 \cdot f^{0.5}</math></li> <li>- Shallow 1-D alternating layer 0.9 km thick with</li> <li>- 10 percent mean velocity variation</li> <li>- 10 percent mean density variation</li> </ul> |

**Table 6.10 Model-specific parameters and values used in the SM1 exercise. (cont)**

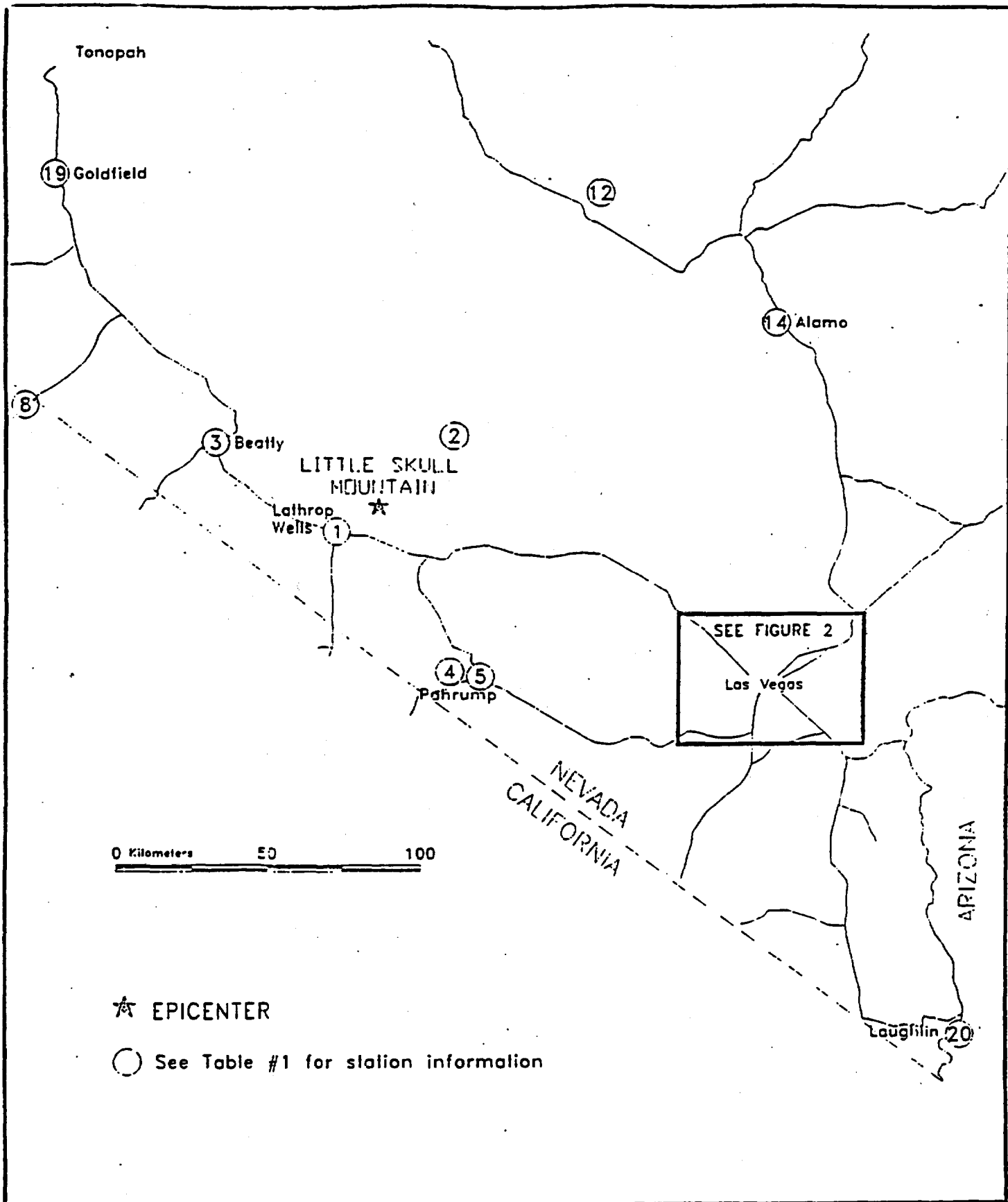
| Model | Source  | Path and Site   |
|-------|---|---|
| USC   | <ul style="list-style-type: none"> <li>- Specific Barrier model with barrier interval = 3 km =&gt; three sub-events, each with <math>M_0 = 1.22 \times 10^{24}</math> dyne-cm.</li> <li>- Local stress drop = 76 bars.</li> <li>- <math>f_{max} = 10</math> Hz, with high-cut filter<br/><math>P(f) = [1+(f/f_{max})^8]^{-0.5}</math>.</li> <li>- Rupture velocity = 2.8 km/sec.</li> </ul> | <ul style="list-style-type: none"> <li>- Geometric spreading factor = <math>1/R</math>.</li> <li>- WNA amplification factors (Boore, 1986)</li> <li>- <math>Q(f) = Q_0 f^h</math>, <math>Q_0 = 250</math>, <math>h = 0.4</math> (assigned values).</li> </ul> |
| WCC   | <ul style="list-style-type: none"> <li>- Fault dimensions: Length modified to 4.5 km to enable use of 1.5 x 1.5 km area needed for available sub-event source function.</li> <li>- Rise time: 0.265 sec</li> </ul>  | <ul style="list-style-type: none"> <li>- crustal structure and layered Q model as provided</li> </ul>   |
| USGS  | <p>fault dimension increased so that specified fault area boundaries correspond to half-max points on the tapered window function</p> <p><math>V_s = 2.8</math> km/s</p> <p><math>\Delta\sigma = 26</math> bars</p>   | <ul style="list-style-type: none"> <li>- Layered velocity and Q model as provided</li> </ul>  |
| SC3   | <ul style="list-style-type: none"> <li>- Spectral shape derived from explosion source model</li> </ul>  | <ul style="list-style-type: none"> <li>- Empirical attenuation developed from explosion source model</li> </ul>   |

**Table 6.11 Frequency points (Hz) specified for 5 percent damped response spectra.**

|       |       |       |       |       |       |       |       |        |       |
|-------|-------|-------|-------|-------|-------|-------|-------|--------|-------|
| 0.10  | 0.20  | 0.30  | 0.40  | 0.50  | 0.60  | 0.70  | 0.80  | 0.90   | 1.00  |
| 1.10  | 1.20  | 1.30  | 1.40  | 1.50  | 1.60  | 1.70  | 1.80  | 1.90   | 2.00  |
| 2.10  | 2.20  | 2.30  | 2.40  | 2.50  | 2.60  | 2.70  | 2.80  | 2.90   | 3.00  |
| 3.15  | 3.30  | 3.45  | 3.60  | 3.80  | 4.00  | 4.20  | 4.40  | 4.60   | 4.80  |
| 5.00  | 5.25  | 5.50  | 5.75  | 6.00  | 6.25  | 6.50  | 6.75  | 7.00   | 7.25  |
| 7.50  | 7.75  | 8.00  | 8.50  | 9.00  | 9.50  | 10.00 | 10.50 | 11.00  | 11.50 |
| 12.00 | 12.50 | 13.00 | 13.50 | 14.00 | 14.50 | 15.00 | 16.00 | 17.00  | 18.00 |
| 20.00 | 22.00 | 25.00 | 28.00 | 31.00 | 34.00 | 40.00 | 45.00 | 50.00  | 55.00 |
| 60.00 | 65.00 | 70.00 | 75.00 | 80.00 | 85.00 | 90.00 | 95.00 | 100.00 |       |

**Table 6.12 Model-specific parameters and values used the SM2 exercise.**

| Model | Source   | Path and Site  |
|-------|--|--|
| PEA   | <ul style="list-style-type: none"> <li>- Uniform slip over alternative 6 x 8 km<sup>2</sup> area</li> <li>- Sub-event area 3 x 3 km<sup>2</sup></li> <li>- Sub-event moment = 3.55 x 10<sup>23</sup> dyne-cm (M = 5.0)</li> <li>- Sub-event rise time = 0.142 sec</li> <li>- Different sub-event time history</li> </ul> | no change  |
| UNR   | <ul style="list-style-type: none"> <li>- source dimension = 6 km x 6 km</li> <li>- strike, dip and rake = 45<sup>0</sup>, 55<sup>0</sup> and -60<sup>0</sup>, respectively (Zhao and Helmberger, 1994)</li> </ul>  | <ul style="list-style-type: none"> <li>- Q<sub>s</sub> = 400 and a Q<sub>p</sub> = 800 for the first 6 shallow layers at CPT1 and BTYA</li> <li>- Kappa values: CPT1 = 0.01, BTYA = 0.001</li> </ul> |
| USC   | <ul style="list-style-type: none"> <li>- local stress drop = 40 bars</li> </ul>  | no change  |
| WCC   | no change  | no change  |
| USGS  | no change  | <ul style="list-style-type: none"> <li>- site specific kappa (measured from strong motion data)</li> <li>- modified amplification factor for alluvium sites (stations 1, 4, 5)</li> </ul>            |
| SC3   | no change  | no change  |

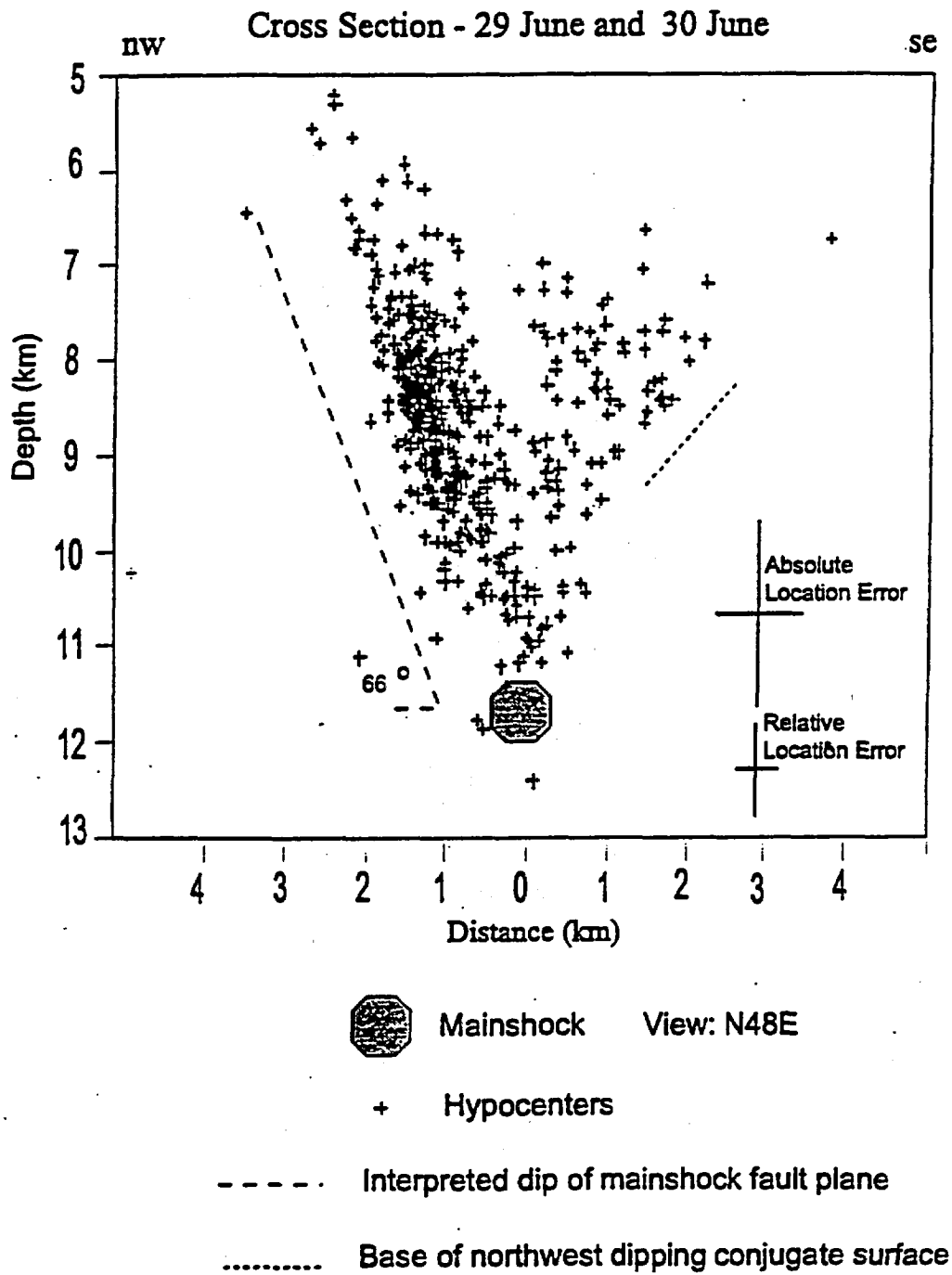


**URS/BLUME**  
 100 CALIFORNIA STREET  
 SAN FRANCISCO, CA 94111

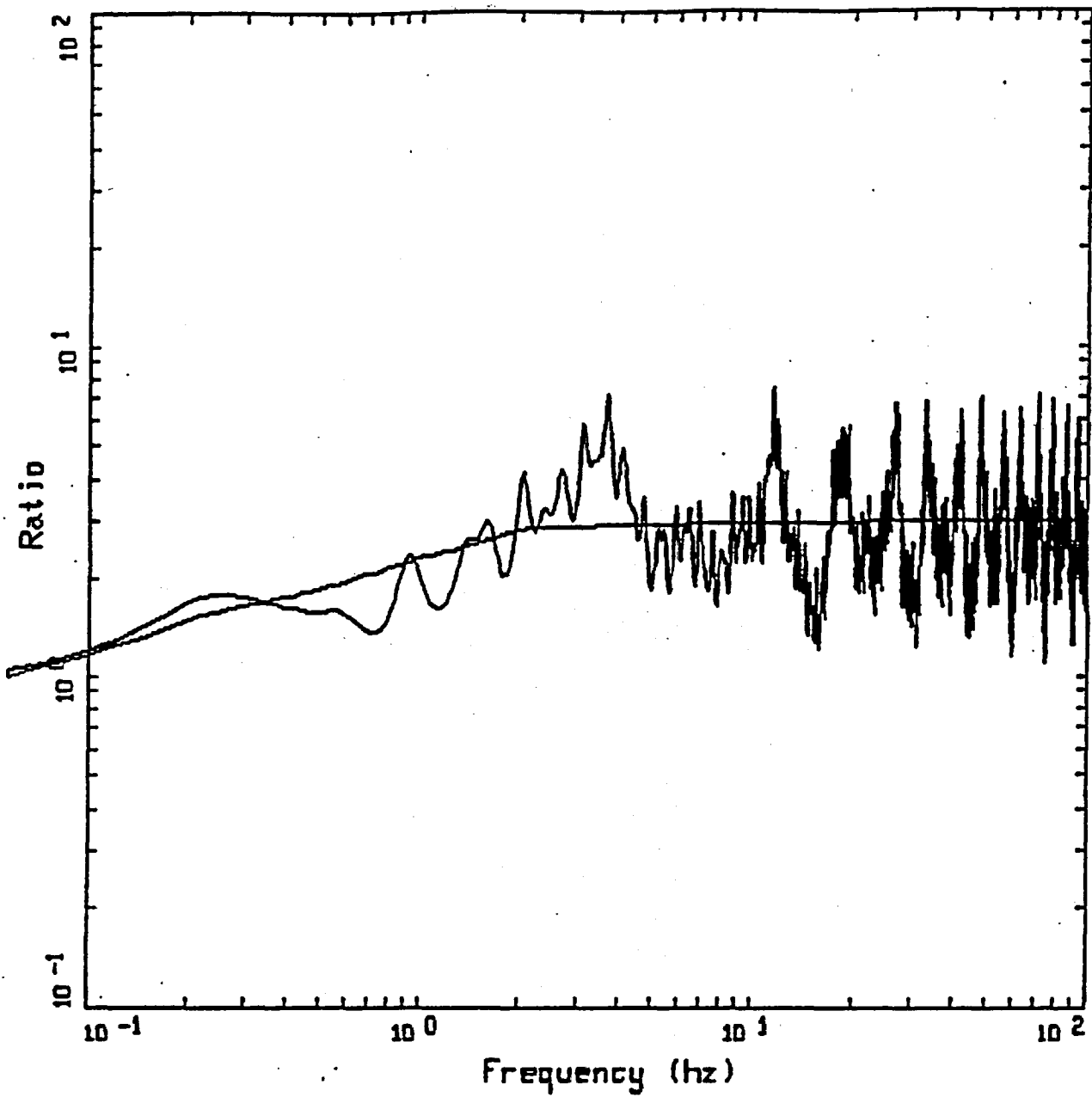
**FIGURE 1: STATIONS RECORDING THE LITTLE SKULL MT., NEVADA EARTHQUAKE OF 6/29/92 IN SOUTHERN NEVADA**



Figure 6.1. Locations of 29 June 1992 M 5.7 Little Skull Mountain earthquake, the Blume strong motion array and Yucca Mountain.



**Figure 6.2. Estimated fault areas superimposed upon a vertical cross section of Little Skull Mountain aftershock locations.**



YUCCA MTN TRANSFER FUNCTION

**LEGEND**  
 — smoothed transfer function  
 — unsmoothed transfer function

Figure 6.3 Transfer function for Yucca Mountain shear-wave velocity profile (Table 5.3). The smooth curve approximates the average effect of crustal amplification.

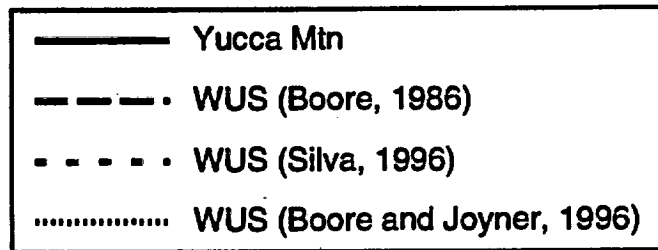
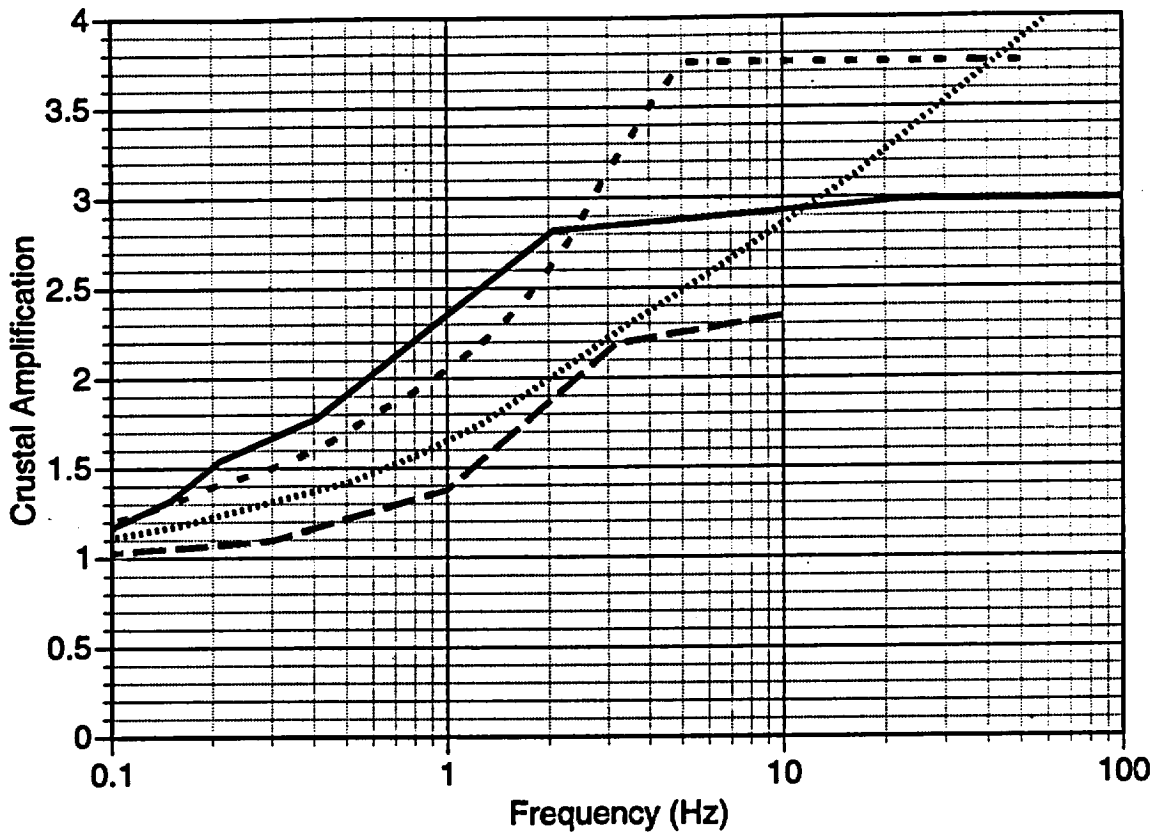
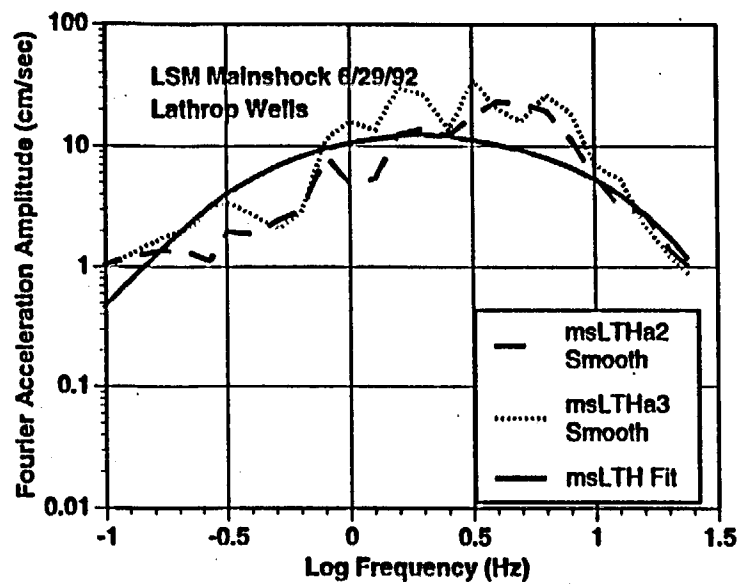
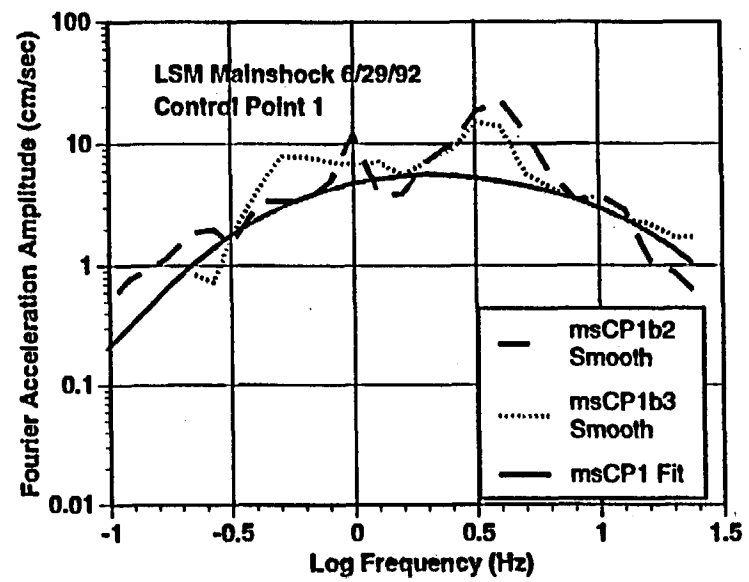


Figure 6.4. Comparison of smoothed crustal amplification factors for Yucca Mountain and typical Western United States.

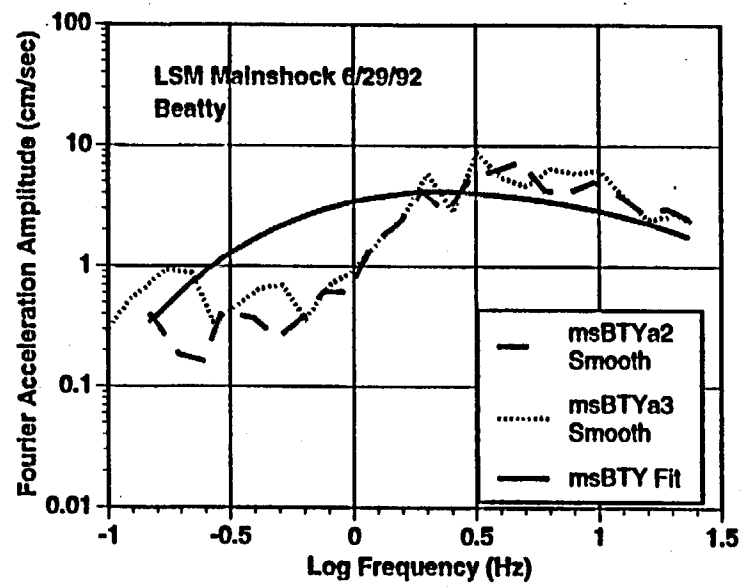


(a)

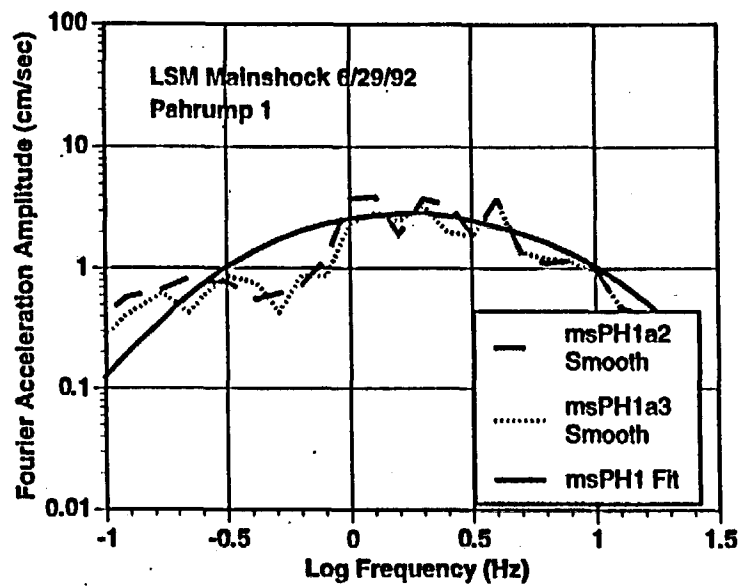
Figure 6.7a-e. Fourier acceleration amplitude spectra for the 6/29/92 Little Skull Mountain mainshock for five stations used in the point-source inversion. Best-fit curves are solid lines.



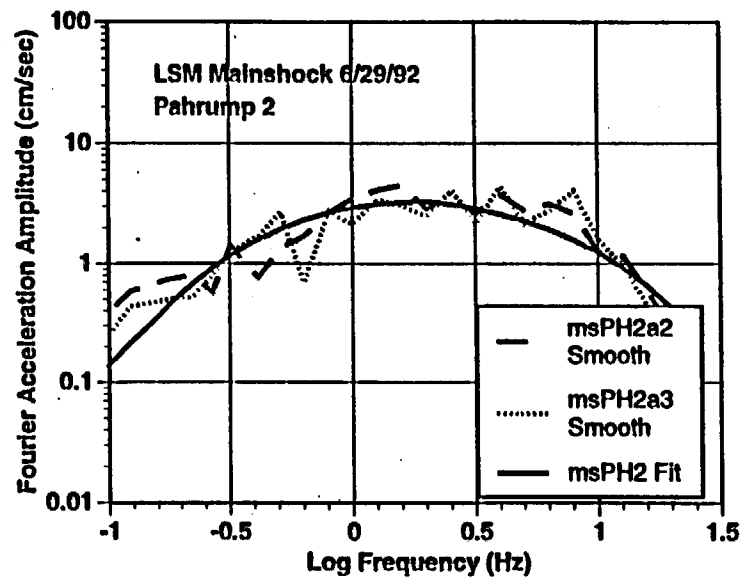
(b)



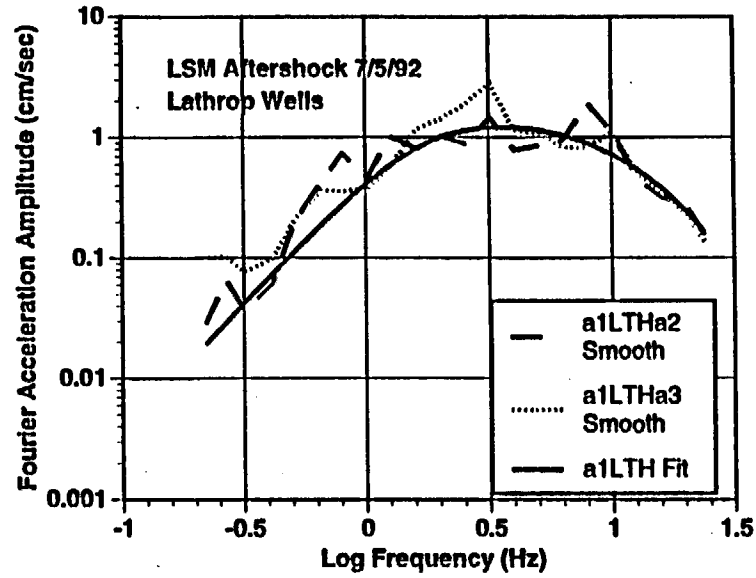
(c)



(d)



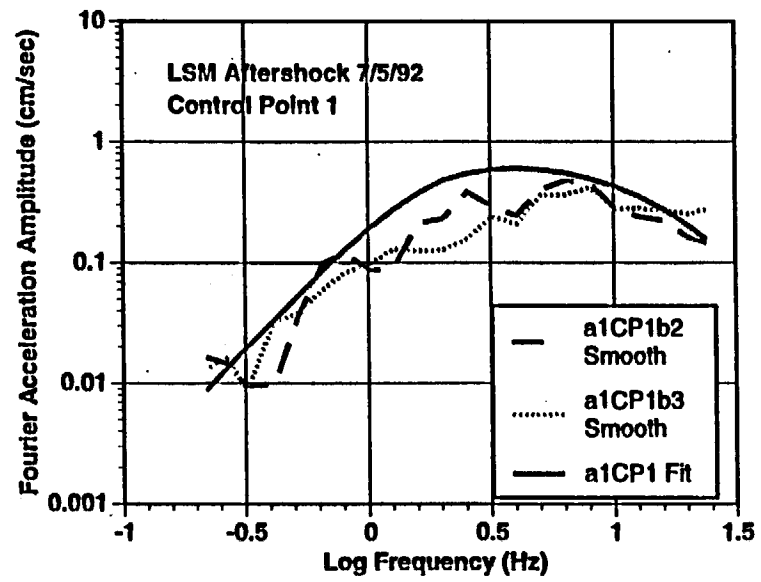
(e)



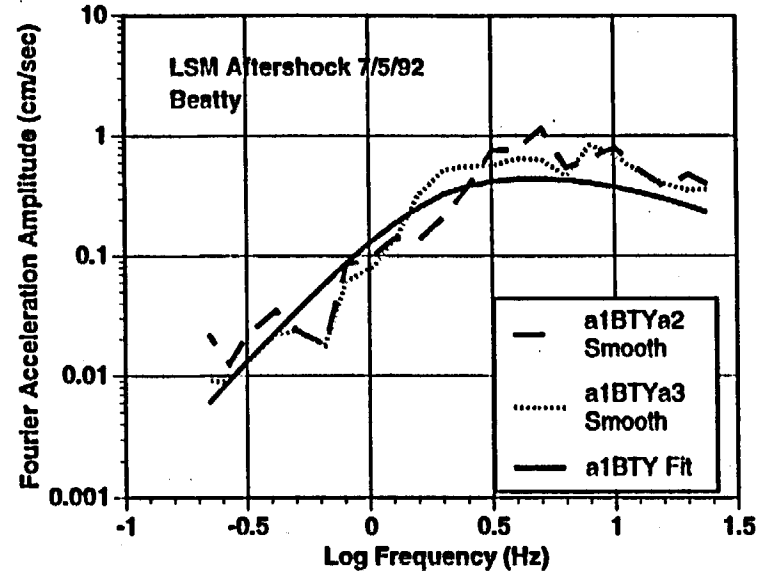
(a)

6-6a-c

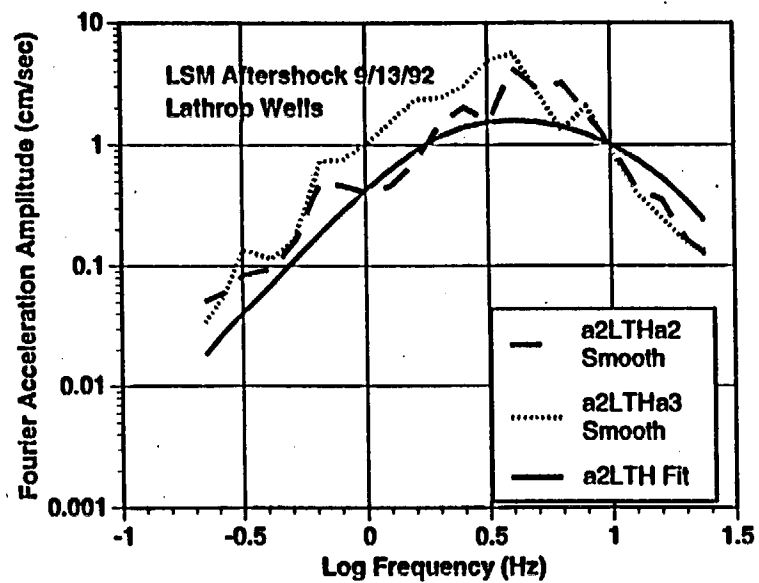
Figure 6-6a-c. Fourier acceleration amplitude spectra for the 7/5/92 Little Skull Mountain aftershock for three stations used in the point-source inversion.



(b)

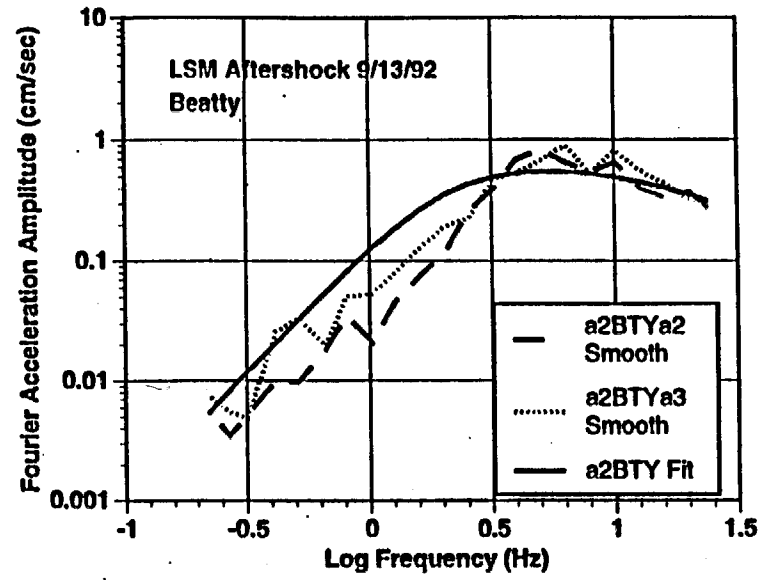


(c)



(a)

6-7  
 Figure 6-7a-b. Fourier acceleration amplitude spectra for the 9/13/92 Little Skull Mountain aftershock for two stations used in the point-source inversion.



(b)

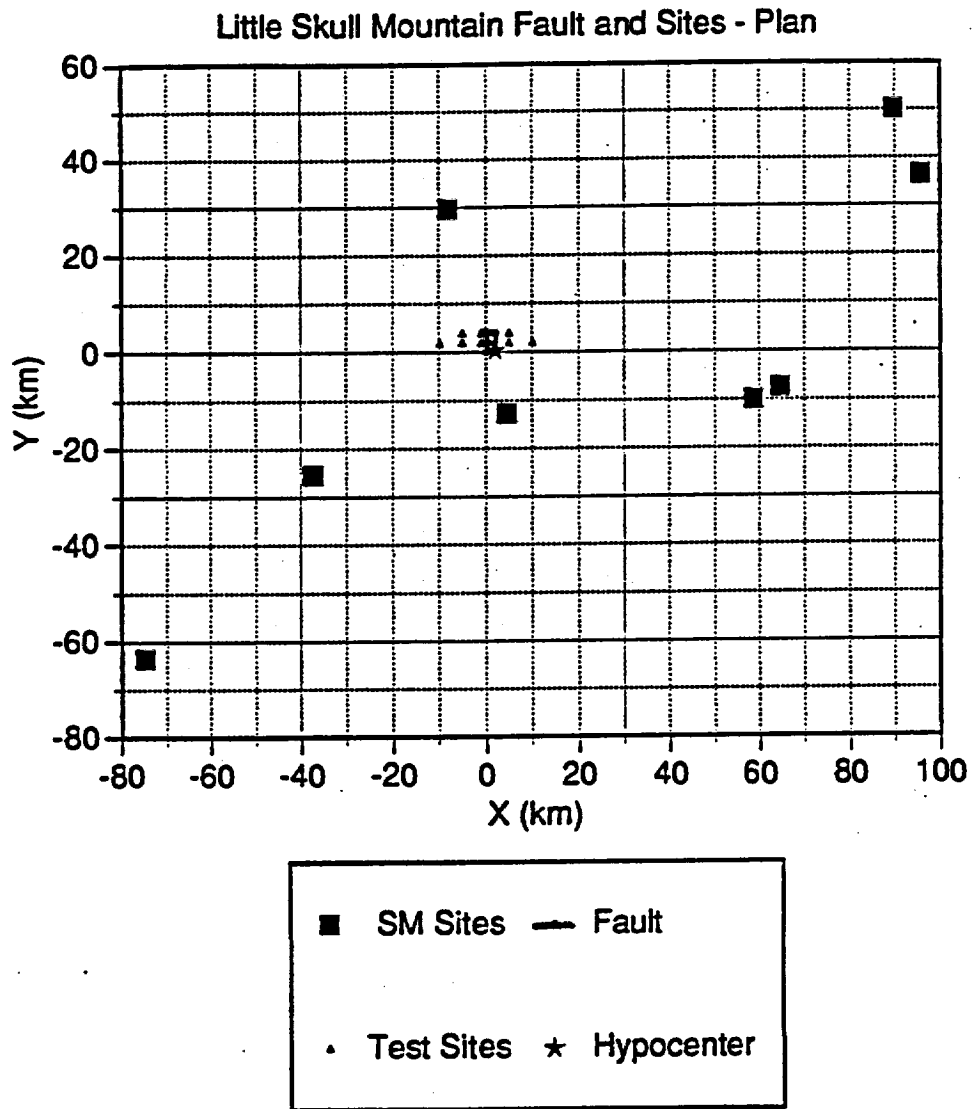


Figure 6.8. Plan view of location of Little Skull Mountain earthquake and Blume strong motion recording stations used in this study. The Y axis is oriented parallel to the strike of the fault, with positive direction at azimuth N60E.

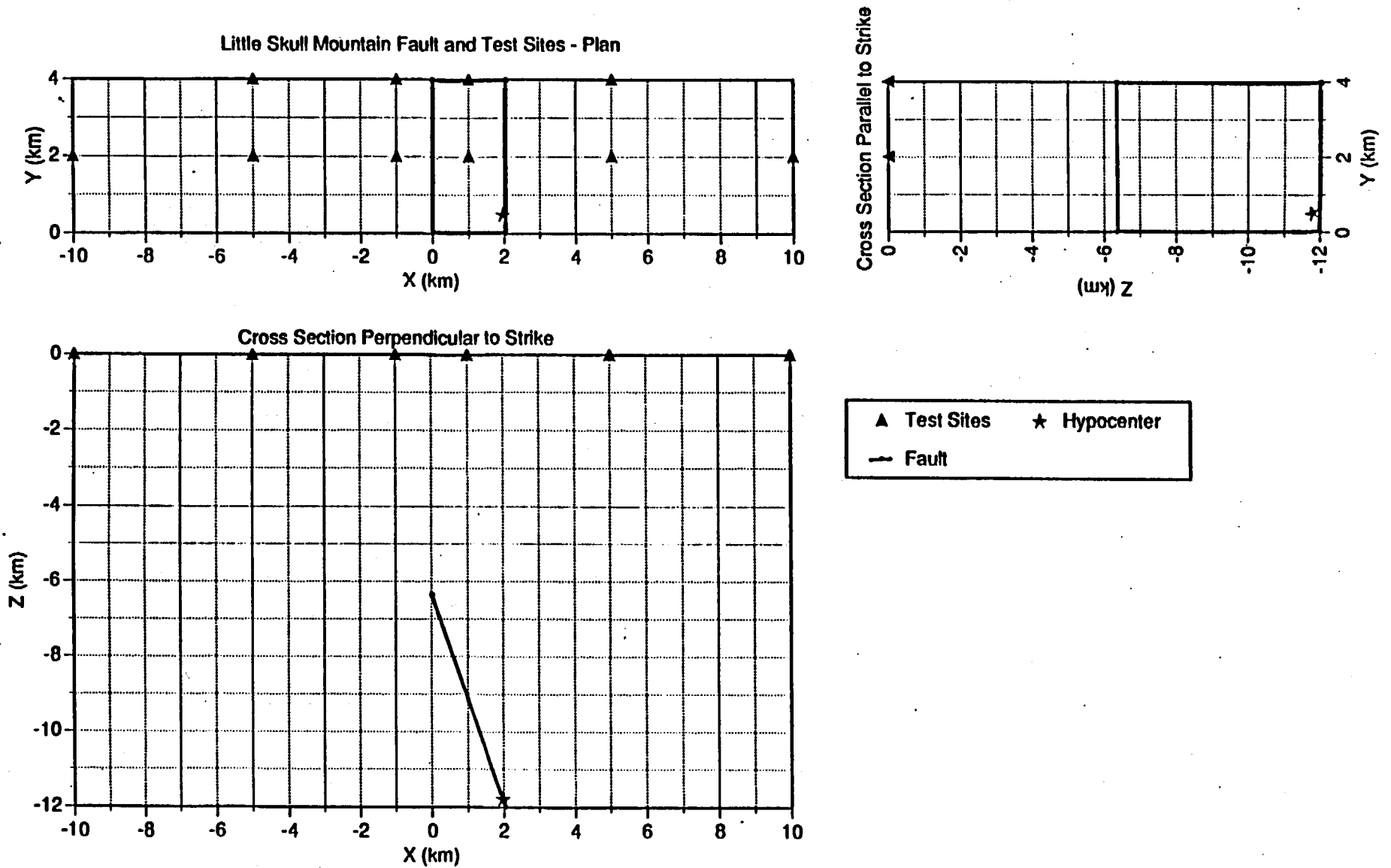


Figure 6.9: Plan view and fault-parallel and perpendicular cross sections of the Little Skull Mountain fault rupture area, with locations of test stations.

# SM1, STATION # 1 : Lathrop Wells

- : OBS
- : PEA
- - - - - : USC
- · - · - : UNR
- : WCC
- - - - - : USGS
- : S-CUBED

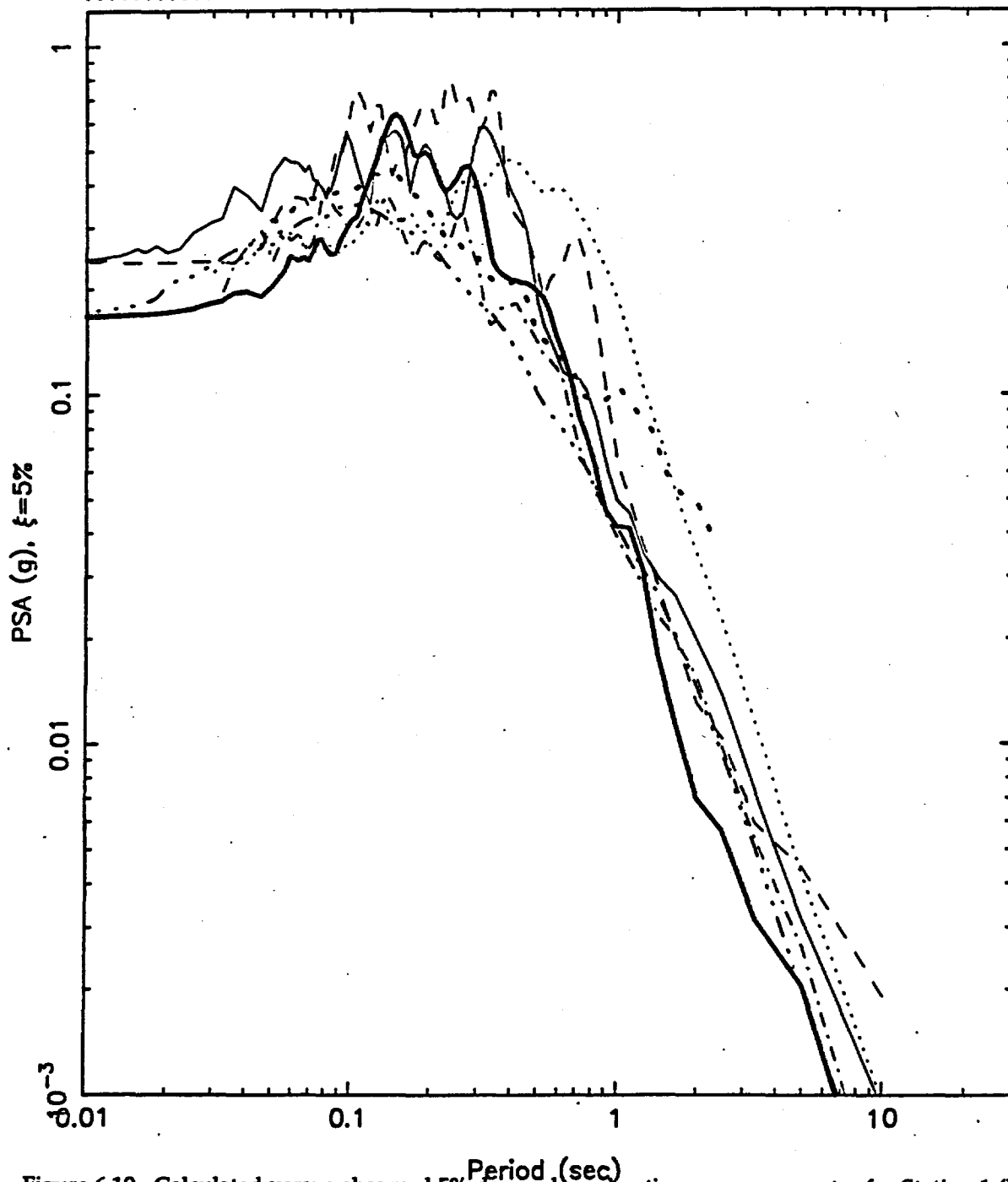


Figure 6.10. Calculated versus observed 5% damped acceleration response spectra for Station 1 (Lathrop Wells) for the Little Skull Mountain Exercise SM1 (base case).

# SM1, STATION # 2 : NTS Control Point 1

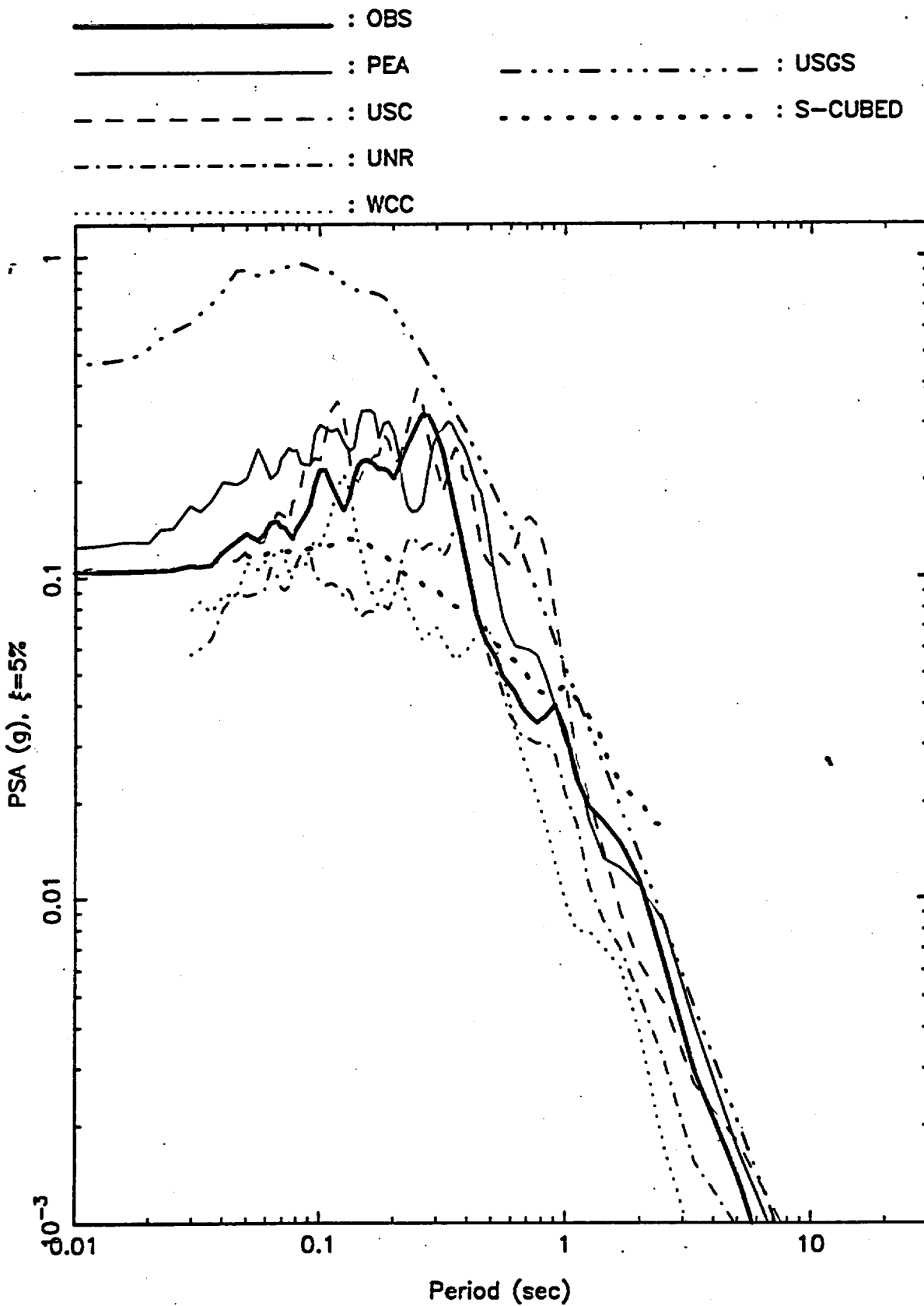


Figure 6.11. Calculated versus observed 5% damped acceleration response spectra for Station 2 (NTS Control Point 1) for SM1.

# SM1, STATION # 3 : Beatty

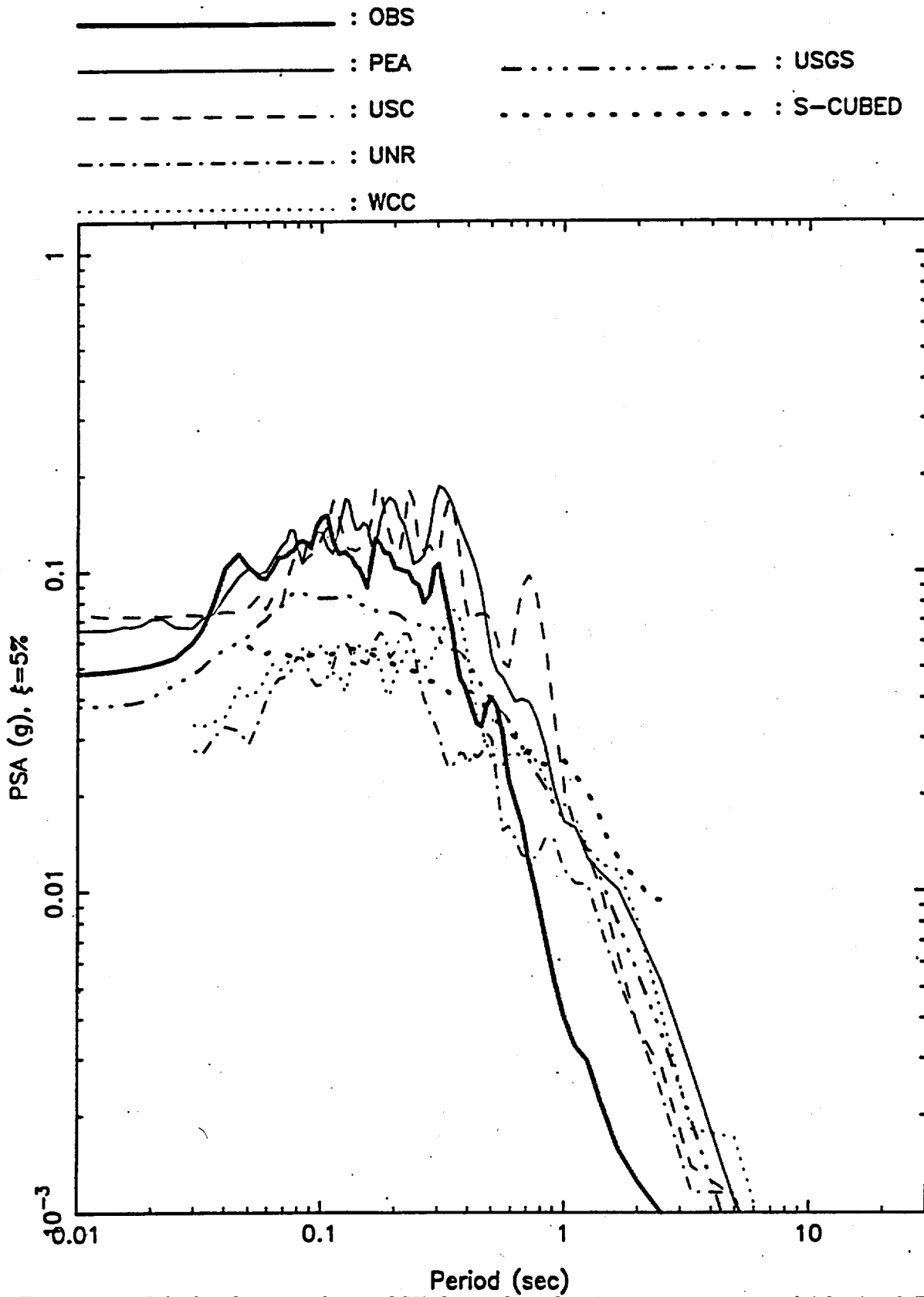


Figure 6.12. Calculated versus observed 5% damped acceleration response spectra for Station 3 (Beatty) for SM1.

SM1, STATION # 4 : Pahrump 2

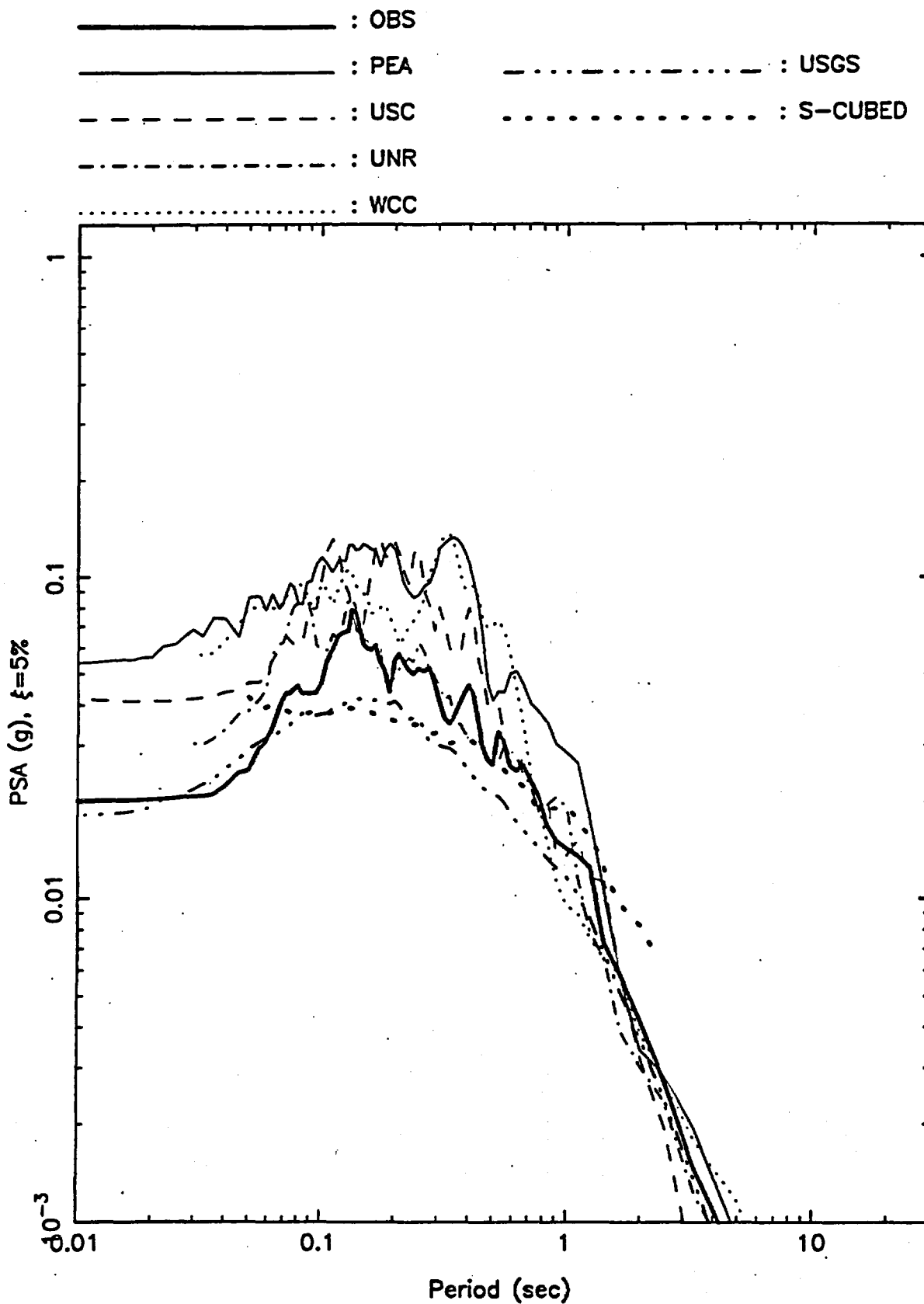


Figure 6.13. Calculated versus observed 5% damped acceleration response spectra for Station 4 (Pahrump 2) for SM1.

# SM1, STATION # 5 : Pahrump 1

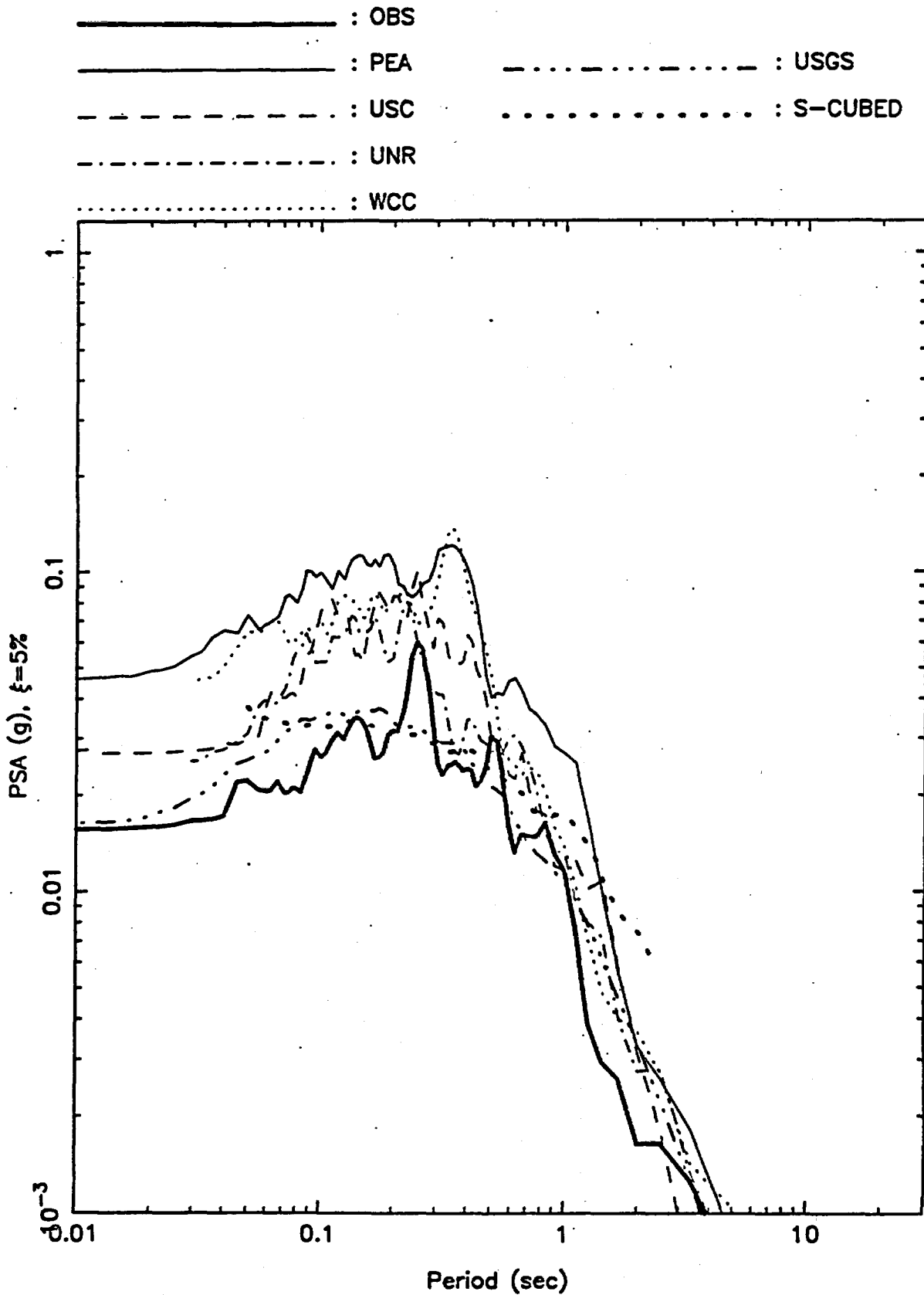


Figure 6.14. Calculated versus observed 5% damped acceleration response spectra for Station 5 (Pahrump 1) for SM1.

# SM1: 1-5 Sites, for Response Spectra

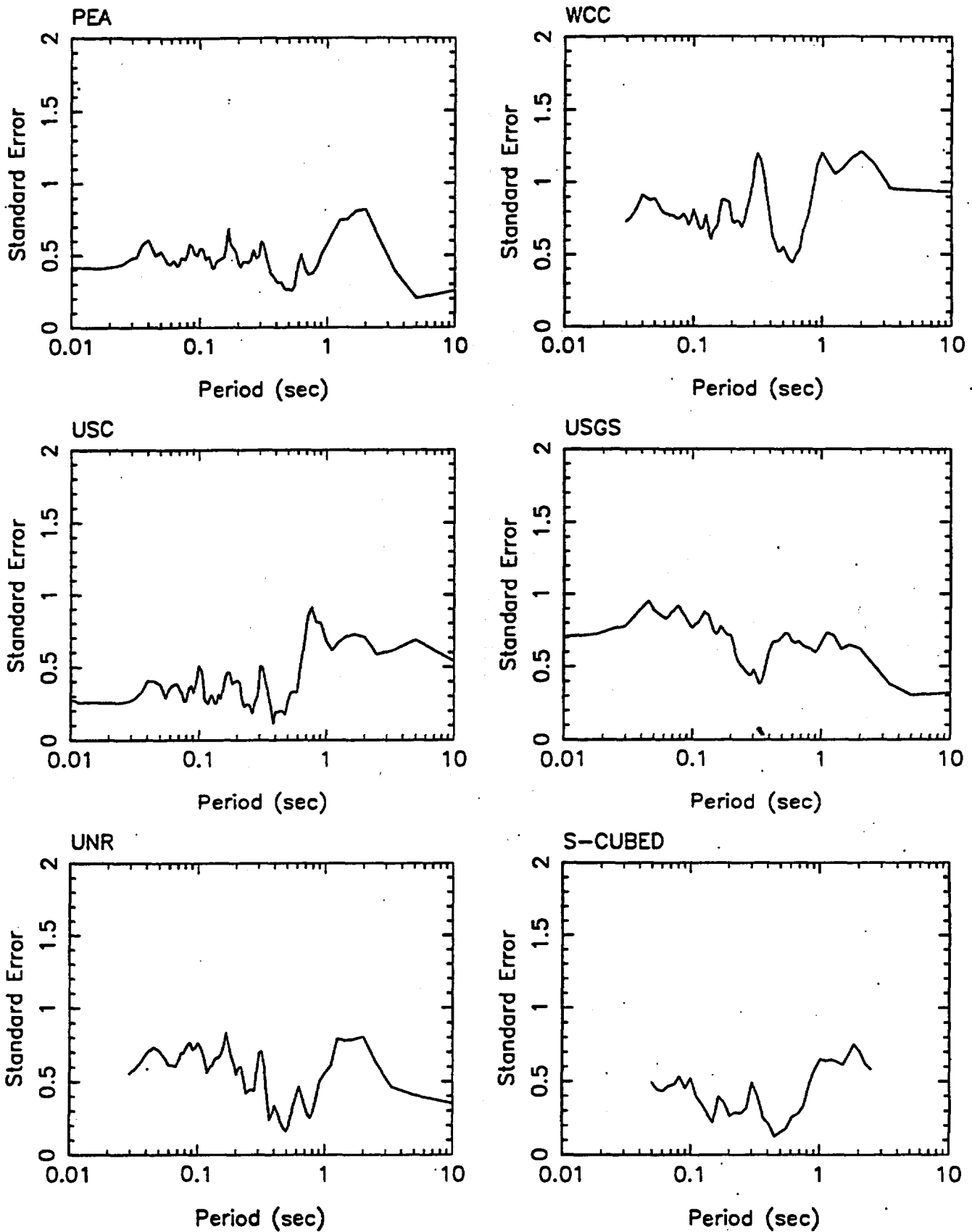


Figure 6.15. Standard error of observed versus calculated acceleration response spectra for SM1. Six sets of modeling results are shown for Station 1 to 5. (Scale is in terms of natural log, so that 1 corresponds to factor of e.)

SM1: 1-5 Sites, for Response Spectra .

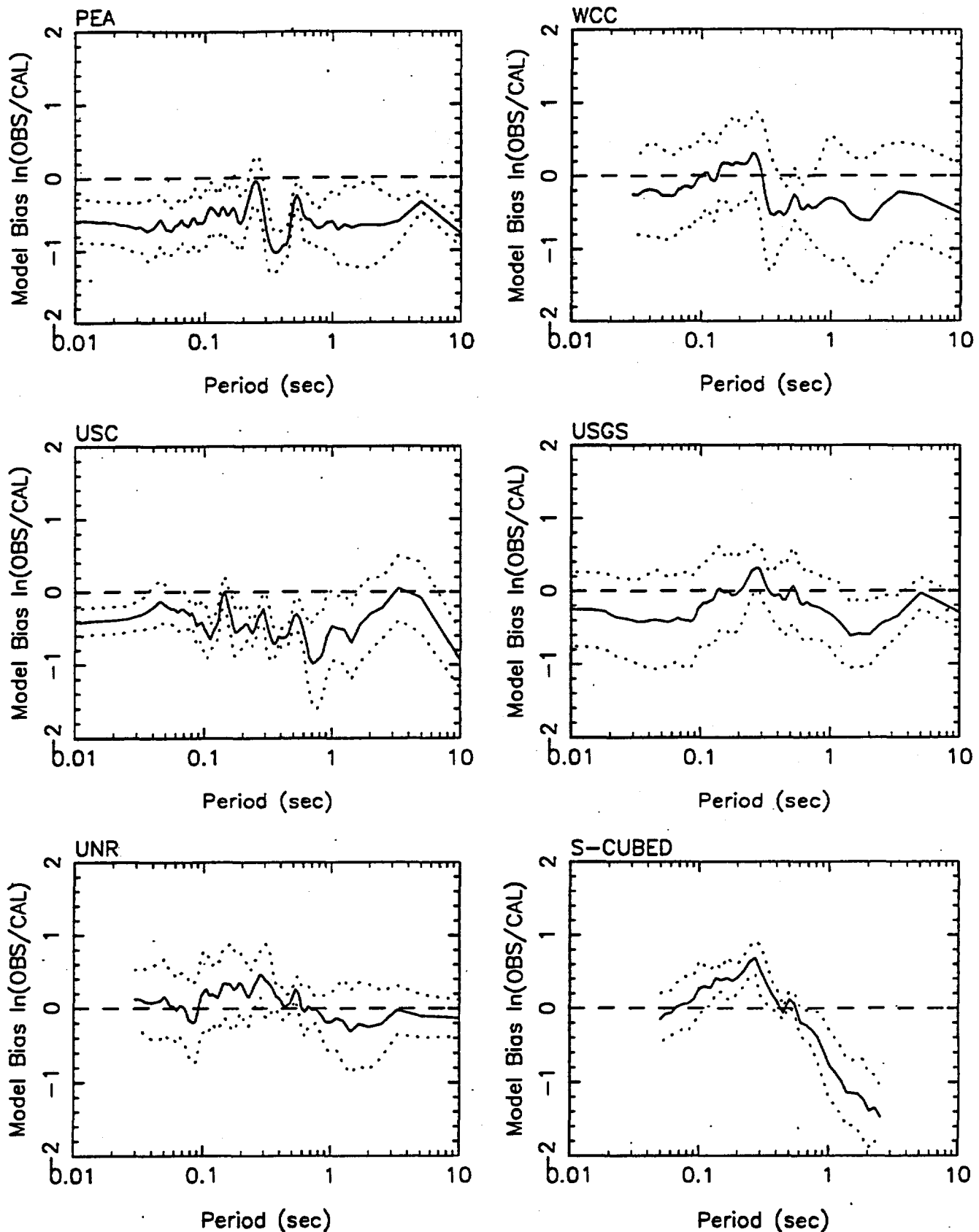


Figure 6.16. Model bias of observed relative to calculated response spectra for SM1. Negative model bias corresponds to overprediction of calculated response. Dotted lines represent  $\pm 1\sigma$  bounds.

### SM1: 1-5 Sites, for Acceleration Duration

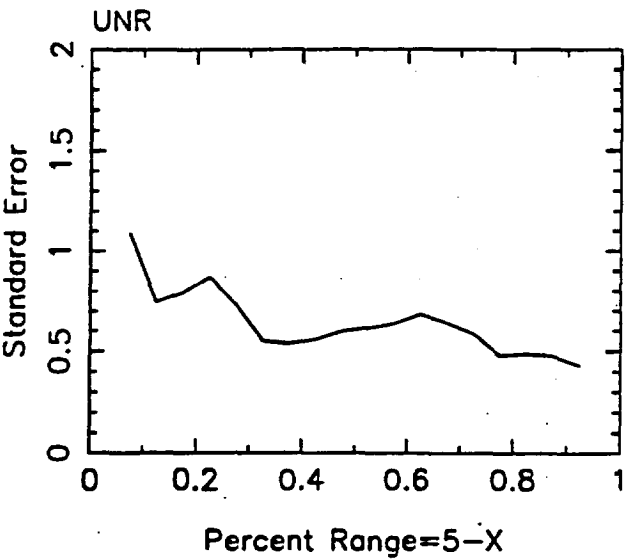
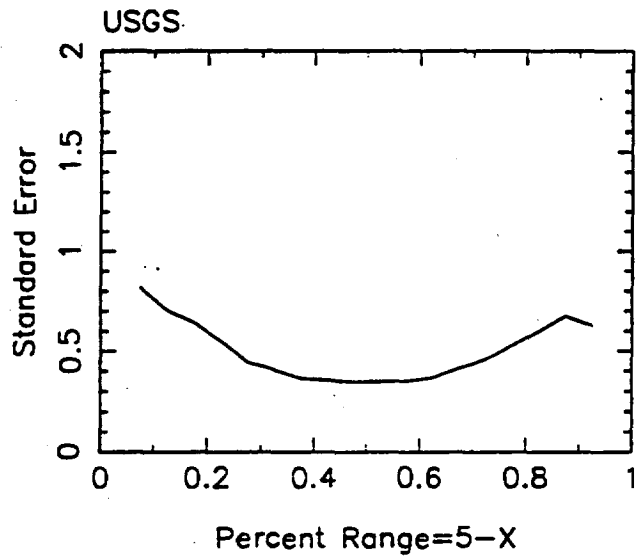
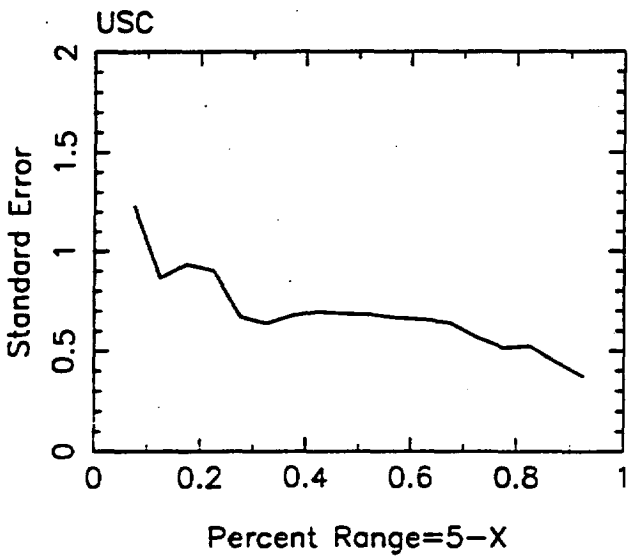
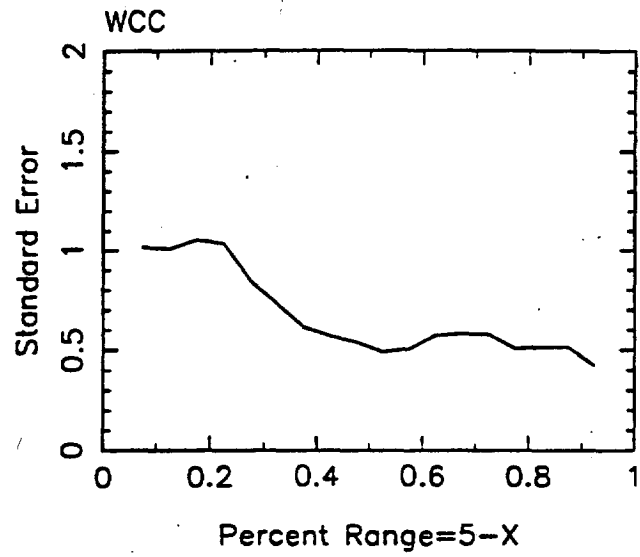
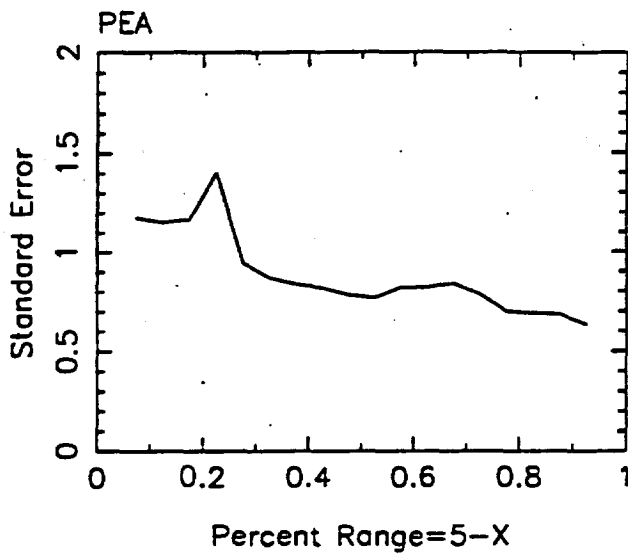


Figure 6.17. Standard error of observed versus calculated acceleration duration for SM1.

SM1: 1-5 Sites, for Acceleration Duration

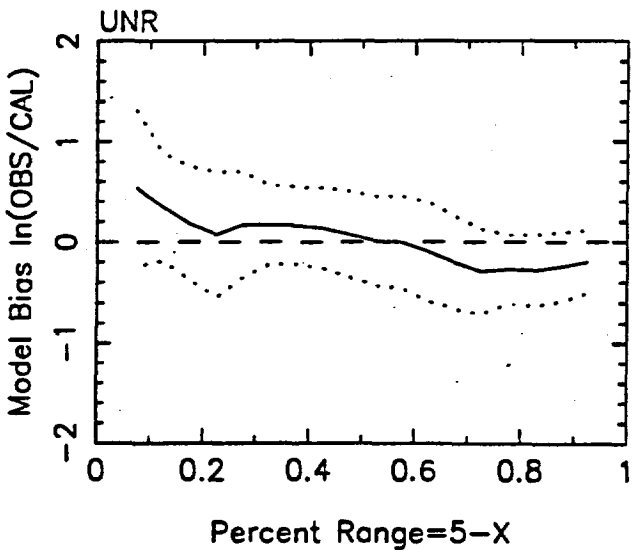
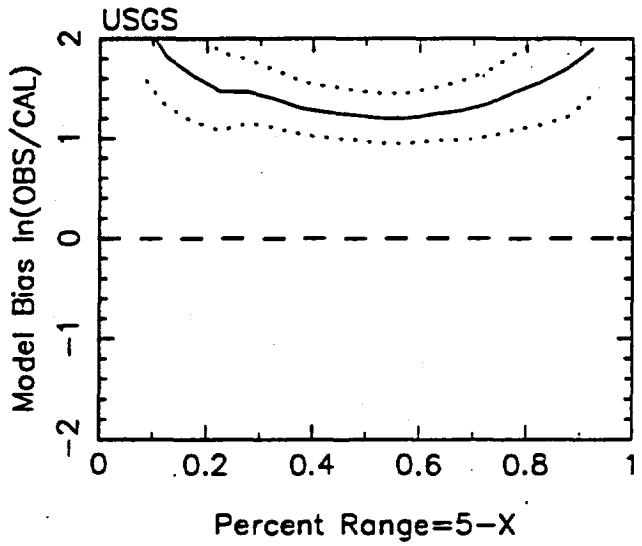
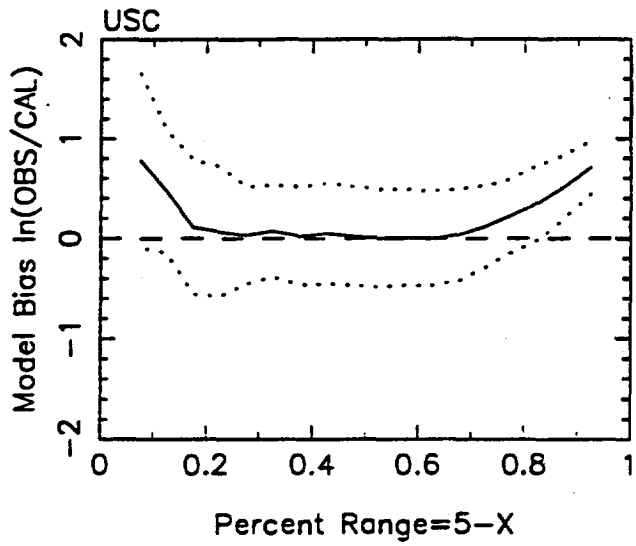
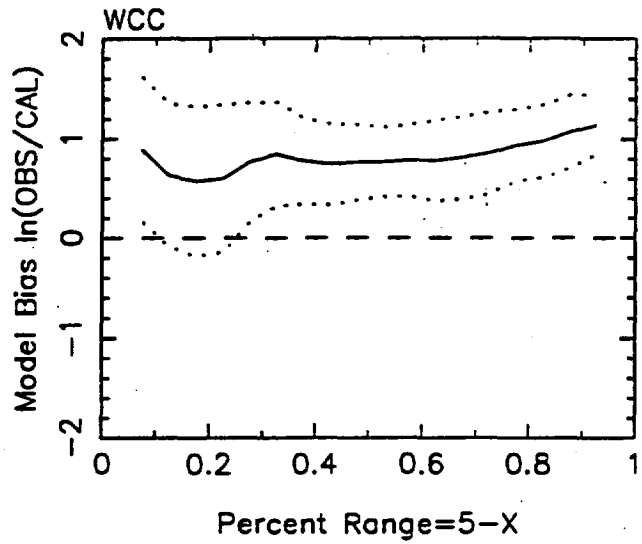
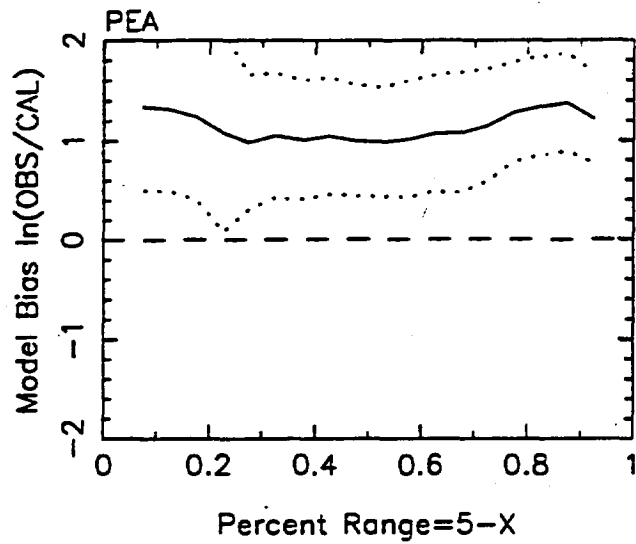


Figure 6.18. Model bias of observed relative to calculated acceleration duration for SM1.

# SM2, STATION # 1 : Lathrop Wells

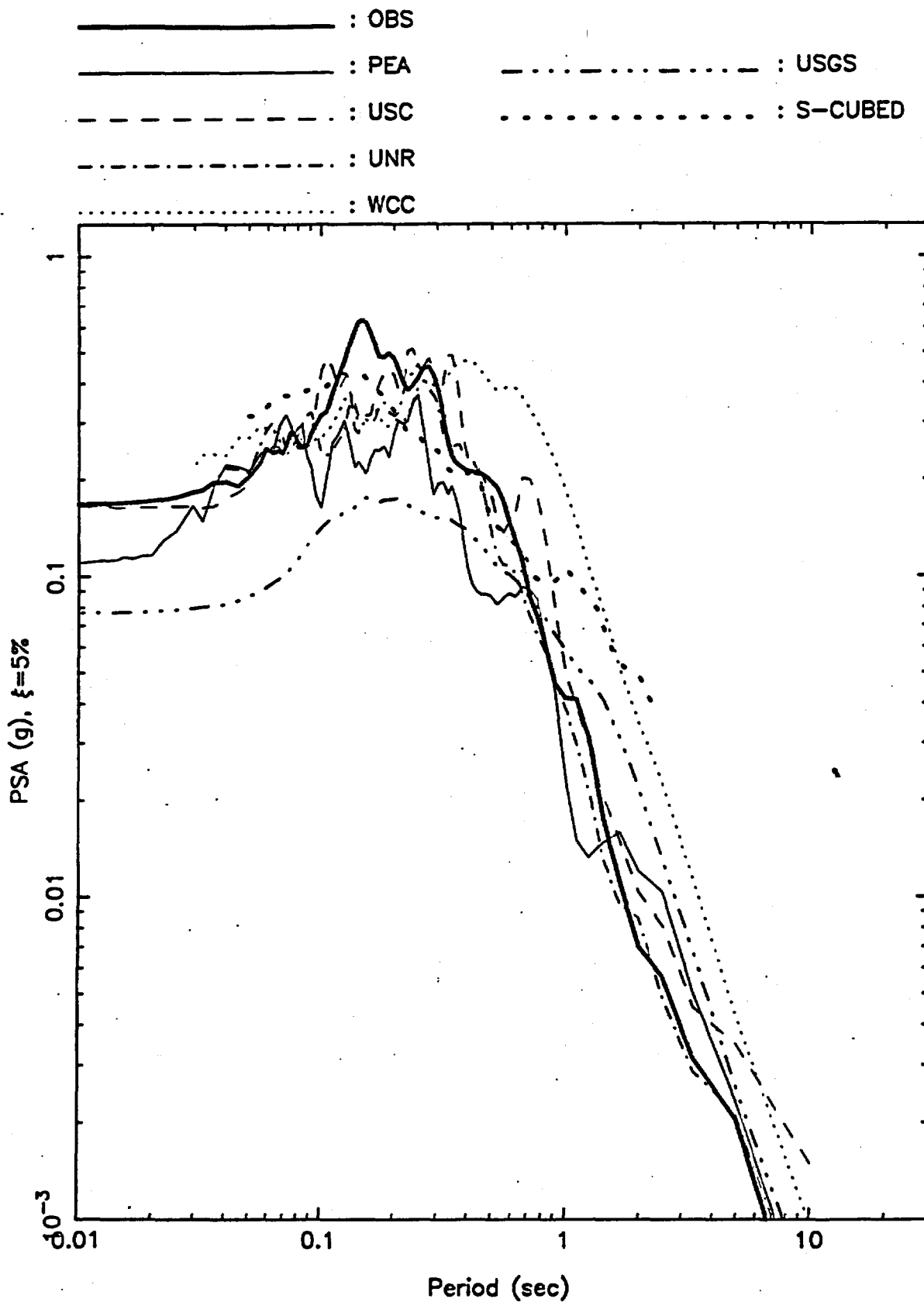


Figure 6.19 Calculated versus observed 5% damped acceleration response spectra for Station 1 (Lathrop Wells) for the Little Skull Mountain Exercise SM2 (preferred case).

# SM2, STATION # 2 : NTS Control Point 1

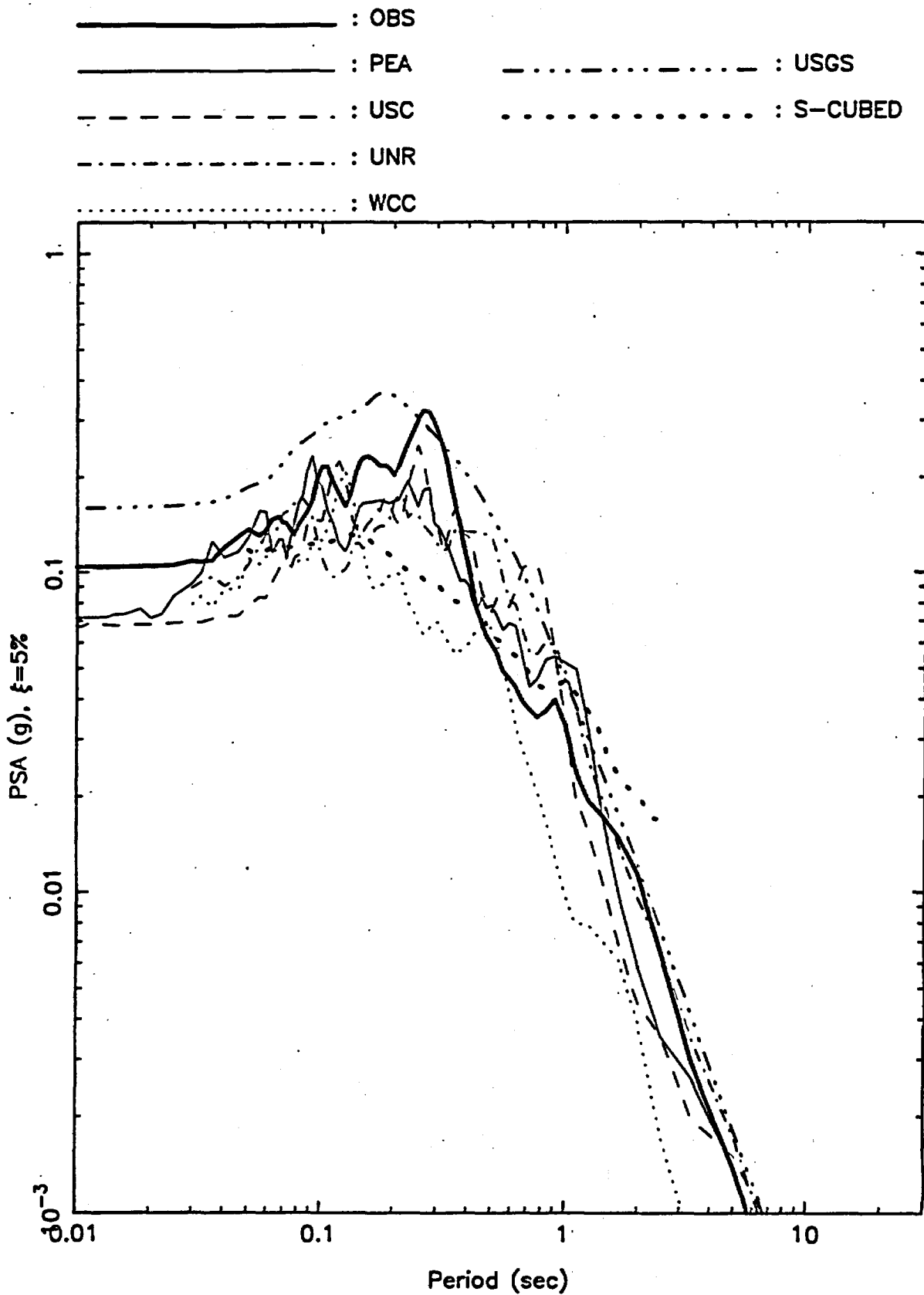


Figure 6.20 Calculated versus observed 5% damped acceleration response spectra for Station 2 (NTS Control Point 1) for the Little Skull Mountain Exercise SM2.

# SM2, STATION # 3 : Beatty

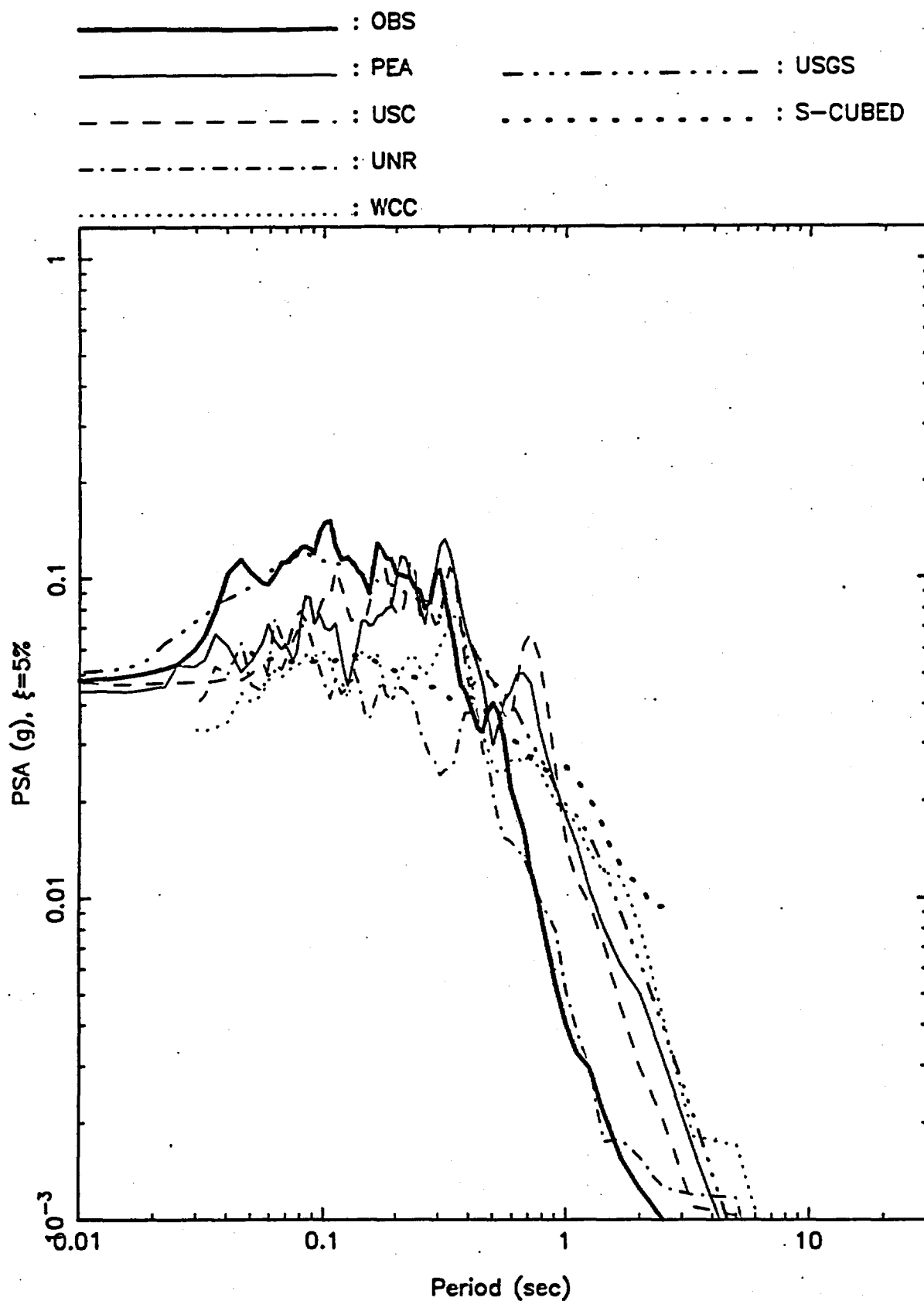


Figure 6.21 Calculated versus observed 5% damped acceleration response spectra for Station 3 (Beatty) for the Little Skull Mountain Exercise SM2.

# SM2, STATION # 4 : Pahrump 2

- : OBS
- : PEA
- - - - - : USC
- . - . - : UNR
- ..... : WCC
- . - . - : USGS
- ..... : S-CUBED

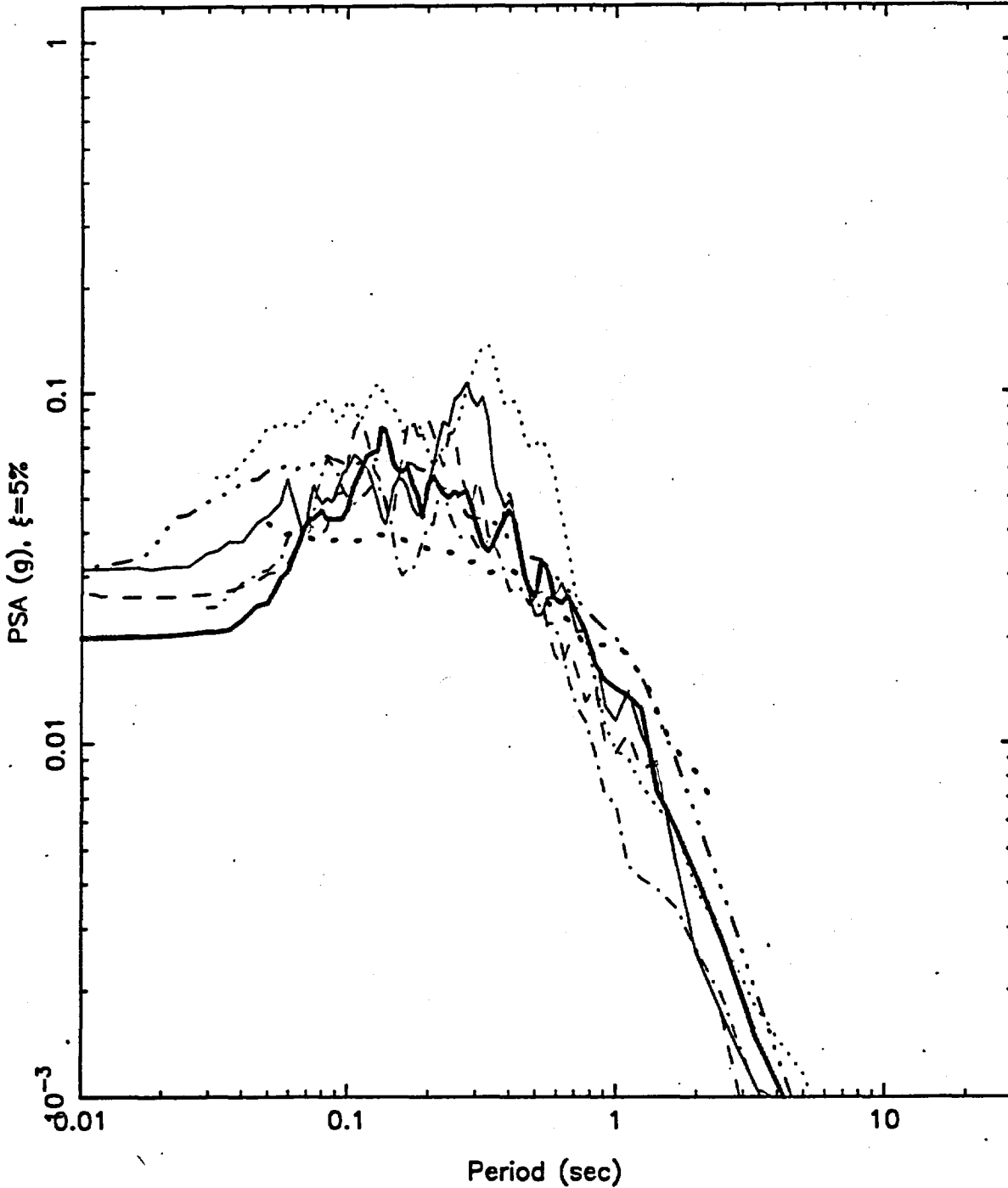


Figure 6.22 Calculated versus observed 5% damped acceleration response spectra for Station 4 (Pahrump 2) for the Little Skull Mountain Exercise SM2.

# SM2, STATION # 5 : Pahrump 1

- : OBS
- : PEA
- : USC
- ..... : UNR
- ..... : WCC
- : USGS
- ..... : S-CUBED

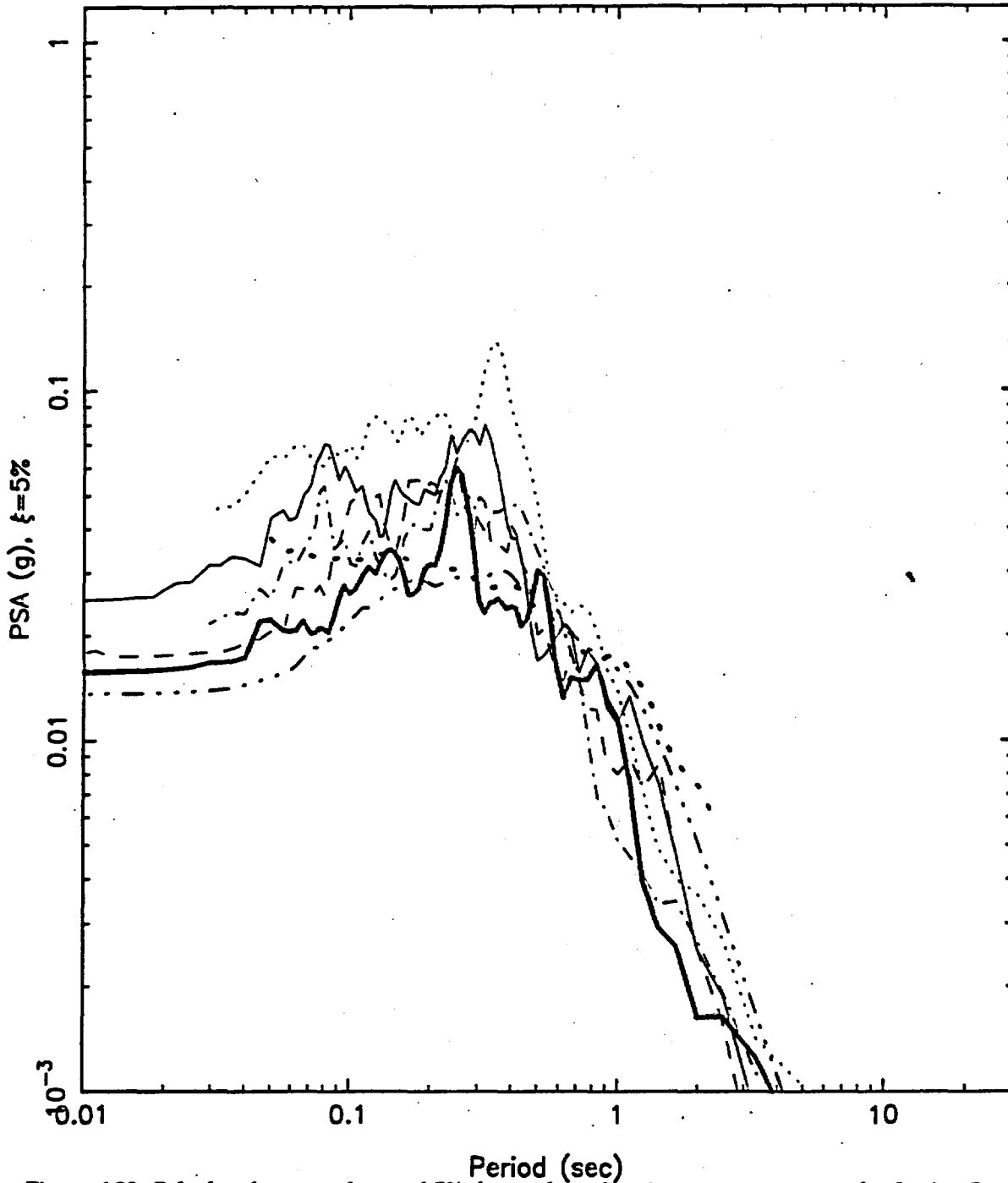


Figure 6.23 Calculated versus observed 5% damped acceleration response spectra for Station 5 (Pahrump 1) for the Little Skull Mountain Exercise SM2.

# SM2: 1-5 Sites, for Response Spectra

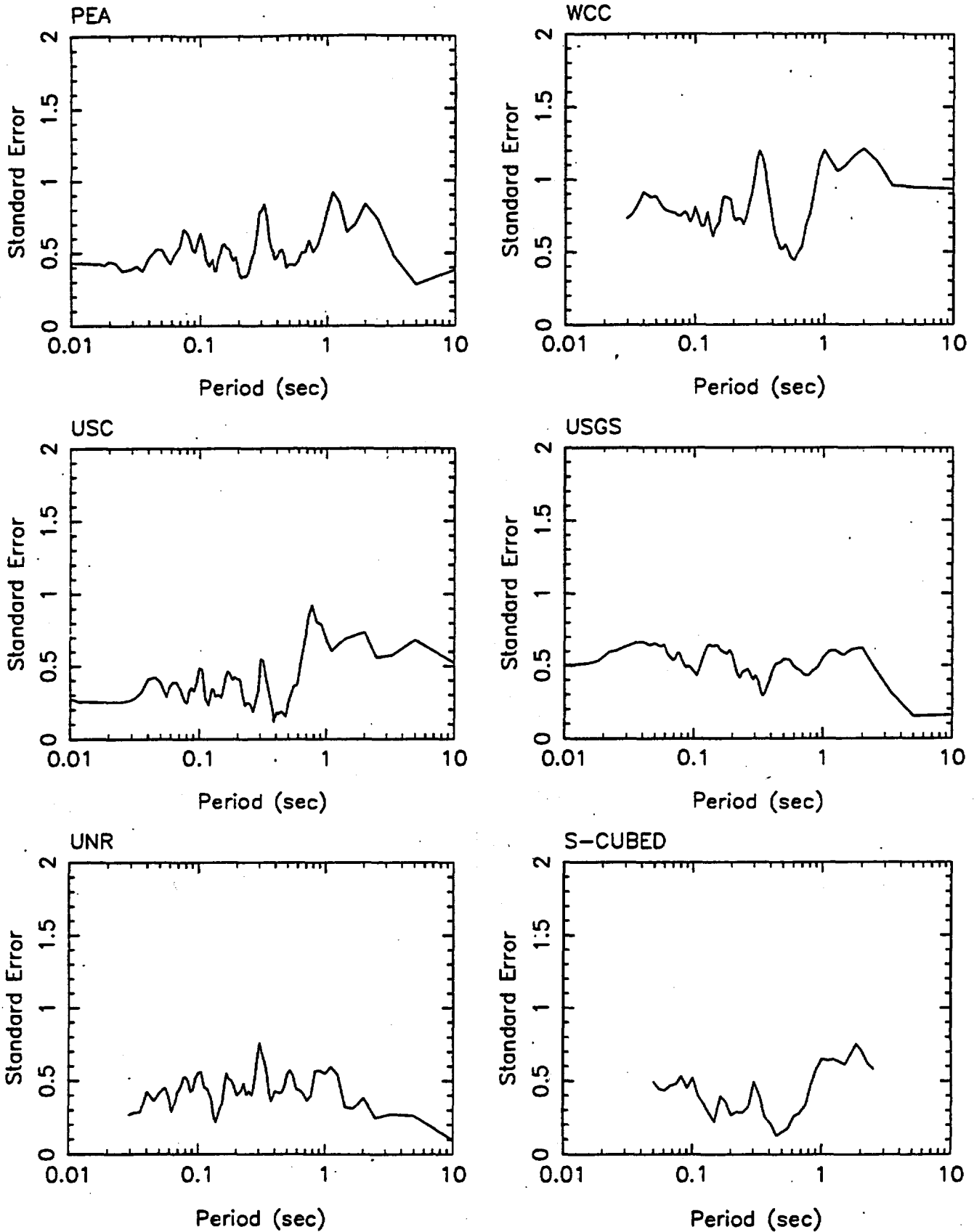


Figure 6.24 Standard error of observed versus calculated acceleration response spectra for the Little Skull Mountain Exercise SM2.

SM2: 1-5 Sites, for Response Spectra

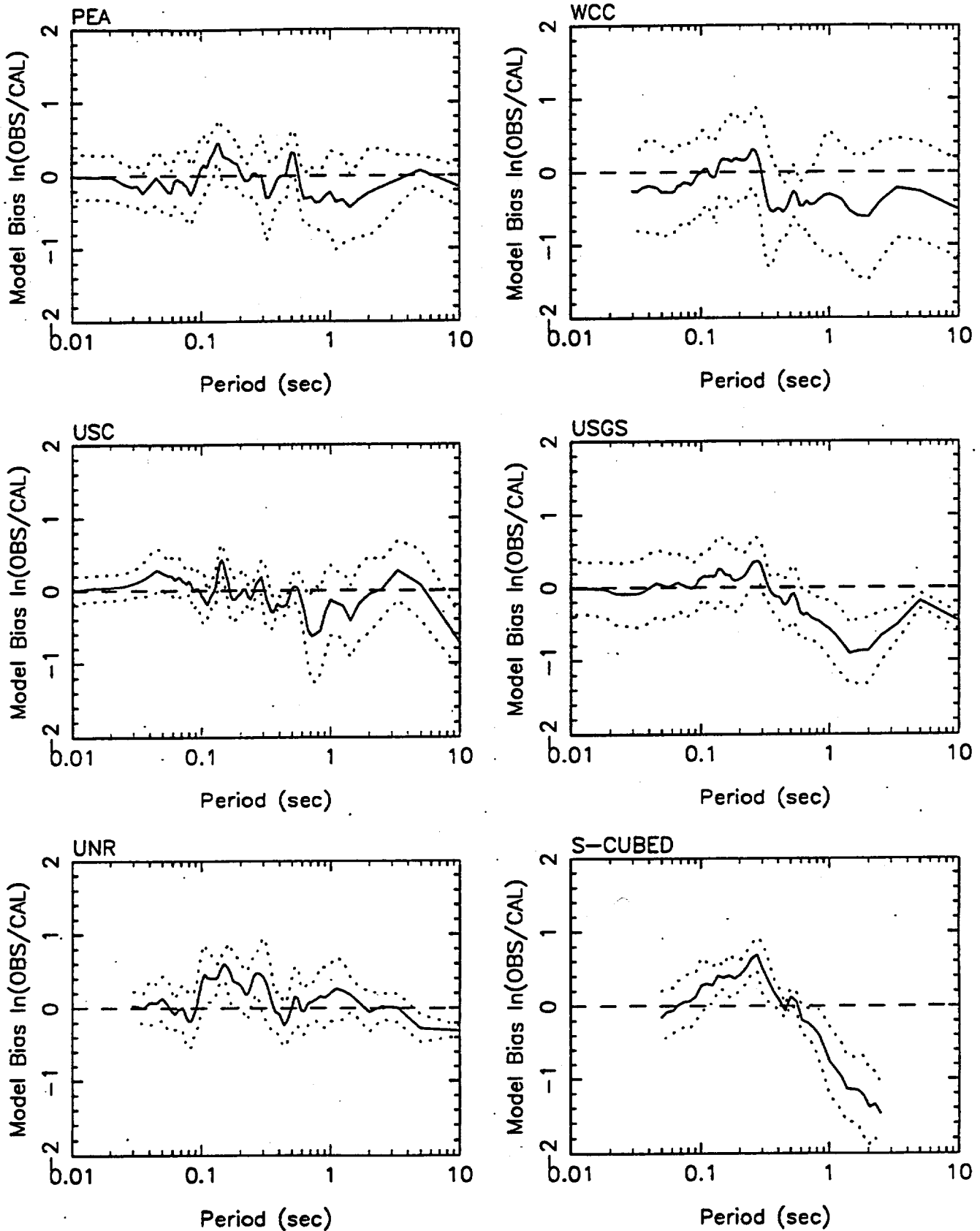


Figure 6.25 Model bias of observed relative to calculated response spectra for the Little Skull Mountain Exercise SM2.

### SM2: 1-5 Sites, for Acceleration Duration

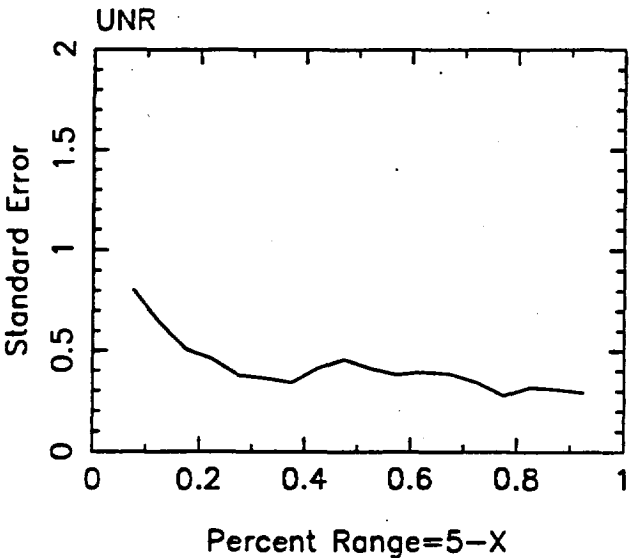
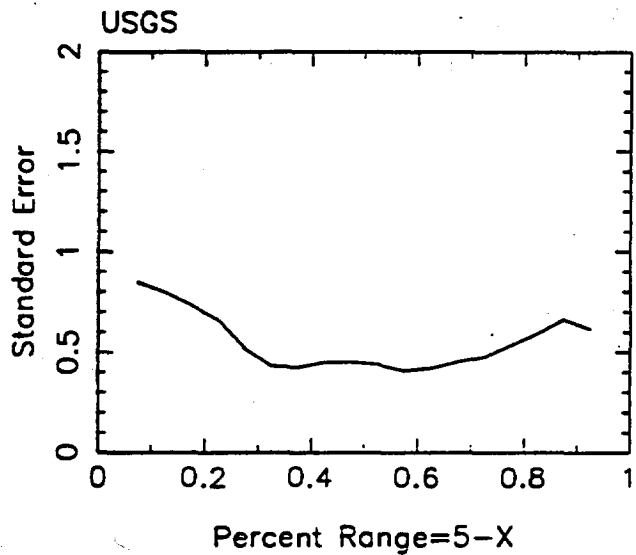
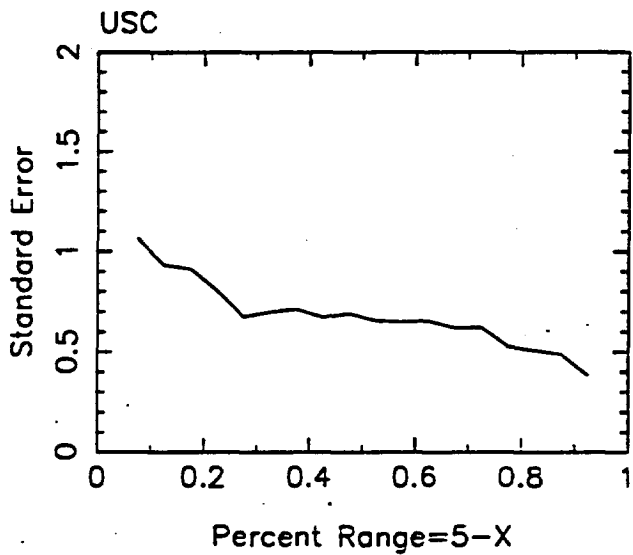
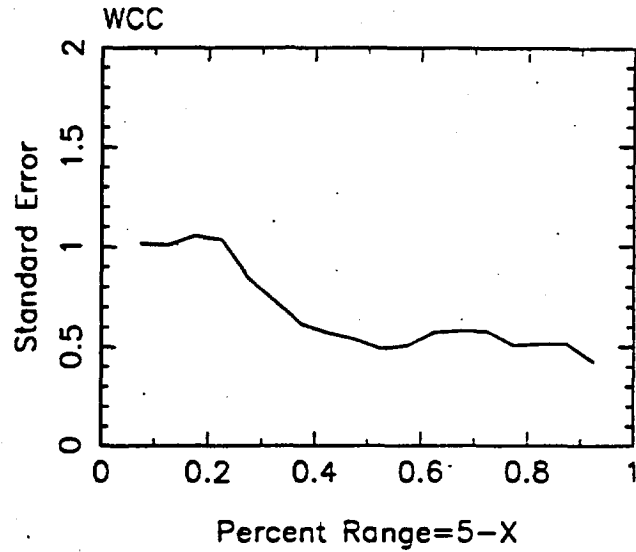
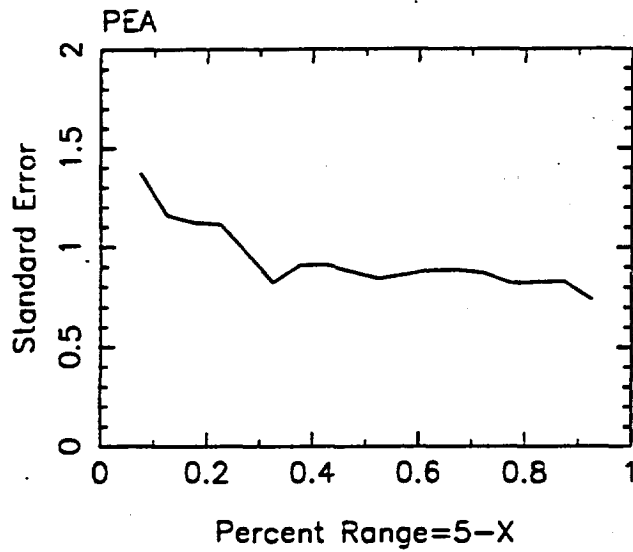


Figure 6.26. Standard error of observed versus calculated acceleration duration for SM2.

### SM2: 1-5 Sites, for Acceleration Duration

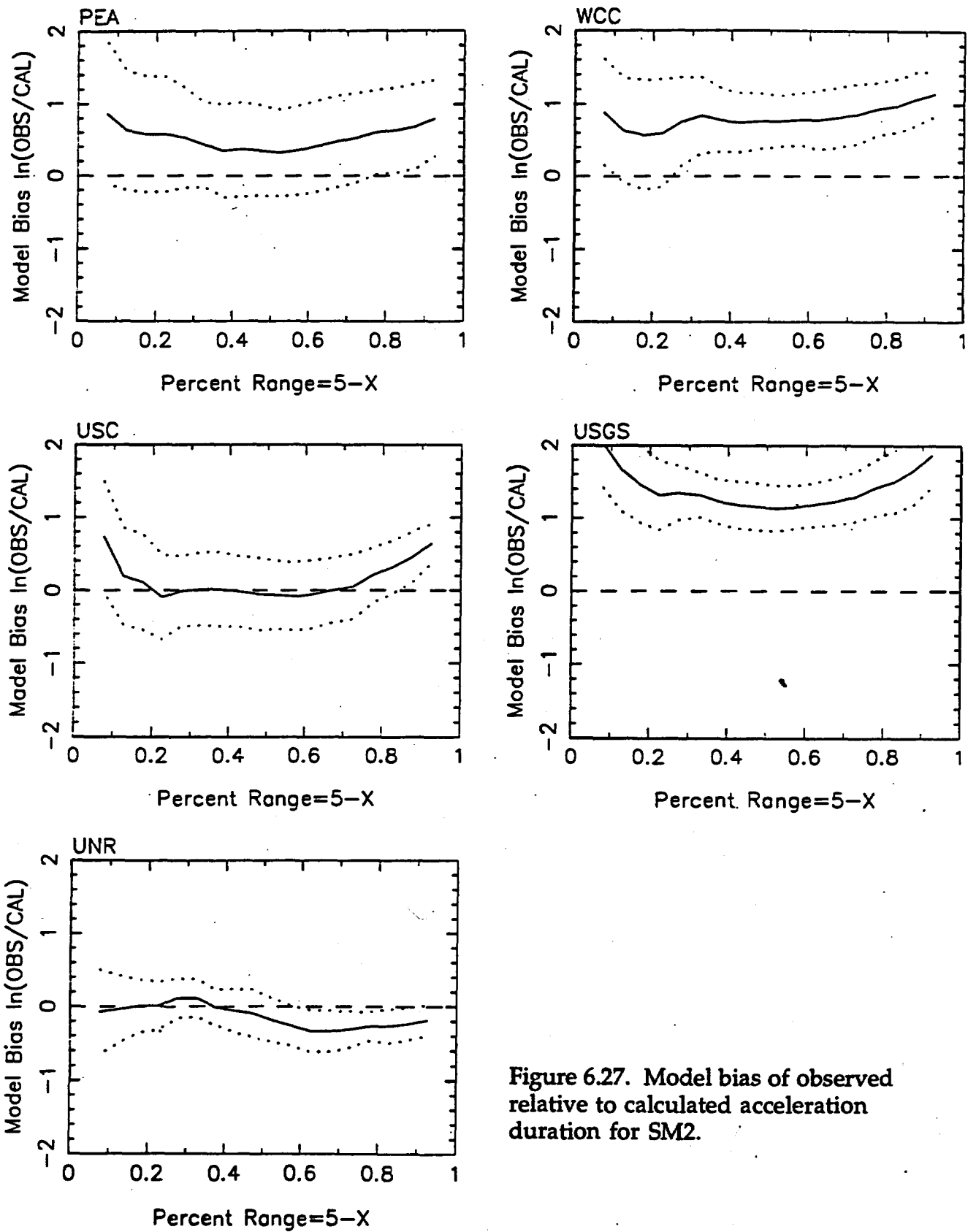


Figure 6.27. Model bias of observed relative to calculated acceleration duration for SM2.

## 7. NON-LINEAR EFFECTS

Most of the numerical simulation methods assumed linear site response (USC, UNR, WCC, and USGS). Only PEA included the effect of non-linear response of the tuffs (as allowed in the exercise instructions) directly in the computed ground motions. The primary reason that the other modelers did not include non-linear site response was not that they did not believe that it was appropriate, but rather that they did not have an efficient means to include non-linear response effects in the available time and budget. The modelers agreed that the non-linear amplification computed by PEA should be applicable to all of the ground motions computed assuming linear site responses.

PEA computed the ground motions assuming both linear and non-linear response of the tuff. The ratio of the non-linear/linear response is used as the scale factor to correct the other modeling methods to account for non-linear response. The development of these site response ratios is given below.

### Computational Scheme

The computational scheme employed to compute the site response uses the stochastic model to generate the power spectral density and spectral acceleration of the rock or control motion. This motion or power spectrum is then propagated through the one-dimensional profile using the plane-wave propagators of Silva (1976). In this formulation only SH waves are considered. Arbitrary angles of incidence may be specified but normal incidence is used throughout the present analyses.

In order to treat possible material non-linearities, the equivalent-linear formulation is employed. Random process theory is used to predict peak time domain values of shear strain based upon the shear strain power spectrum. In this sense, the procedure is analogous to the program SHAKE (Schnabel and others, 1972) except that peak shear strains in SHAKE are measured in the time domain. The purely frequency domain approach obviates a time domain control motion and, perhaps just as significant, eliminates the need for a suite of analyses based on different input motions. This arises because each time domain analysis may be viewed as one realization of a random process. In this case, several realizations of the random process must be sampled to have a statistically stable estimate of site response. The realizations are usually performed by employing different control motions with approximately the same level of peak acceleration.

In the case of the frequency domain approach the estimates of peak shear strain as well as oscillator response are, as a result of the random process theory, fundamentally probabilistic in nature. Stable estimates of site response can then be computed by forming the ratio of spectral acceleration predicted at the surface of the profile to the spectral acceleration predicted for the control motion.

The procedure of generating the stochastic power spectrum, computing the equivalent-linear layered-soil response, and estimating peak time domain values has been incorporated into a code termed RASCALS. The code has been QA verified to NRC standards.

### **Site Shear-Wave Velocity Profile and Non-linear Response Model**

The base case profile specified for the site response analyses is shown in figure 7.1. The near surface materials consist of 40 m of relatively soft volcanic tuff with a shear-wave velocity of 600 m/sec overlying more competent tuff with a shear-wave velocity of 1.2 km/sec. Because of the high levels of loading (0.50 g) at close-in sites for some of the scenario earthquakes, significant shear strains ( $> 10^{-2}$  percent) are built up in the top layer. This surficial layer, although stiff compared to typical cohesionless soils such as sands and gravels, is not considered to be hard competent bedrock material in terms of site response characteristics. Stiff soils with comparable shear-wave velocities are expected to exhibit non-linear dynamic material behavior for cyclic shear-strains exceeding about  $10^{-2}$  percent (Dobry, 1991; EPRI, 1993) and recent laboratory dynamic testing of soft rock samples show material behavior with characteristics very similar to sands and gravels (Ken Stokoe, University of Texas, and Carl Costantino, City College of New York, personal communication, 1995). Additionally, the only available information on dynamic material properties of tuff is from samples taken at the Los Alamos National Laboratory at depths of about 10 m and 100 m (Wong and others, 1993). Results of dynamic tests on these samples show modulus reduction and damping strain dependencies (fig. 7.2) similar to cohesionless materials (EPRI, 1993). While the tuffs at Yucca Mountain may have dynamic material properties unlike those of the Los Alamos tuffs and more complete shear-wave velocity information may reveal that the near-surface material are, on average, significantly stiffer than current data indicate, consideration of available information suggests that non-linearities in dynamic response of the top layer (fig. 7.1) should be considered for very high levels of loading.

FIGURE 7.1 - NEAR HERE

FIGURE 7.2 - NEAR HERE

In order to accommodate uncertainty and variation in the shear-wave velocity profile over the site area, the base-case profile velocity and profile depth (depth-to-rock, layer 2) are randomized using a profile correlation model (EPRI, 1993). The uncertainty model for velocity and layer thickness randomization is based on statistical analysis of over 350 shear-wave velocity profiles. The depth variation is taken as  $\pm 15$  m (uniform distribution) to accommodate a reasonable variation in depth to the 1.20 km/sec materials under the site.

In addition to shear-wave velocity profile variation and uncertainty, similar considerations apply to the modulus reduction and damping curves used for the surficial tuff layer. To accommodate a large uncertainty (since site specific laboratory dynamic tests were unavailable) as well as variability in the dynamic material properties, a randomization appropriate for generic applications was used (EPRI, 1993). The uncertainty model for generic modulus reduction and damping curves appropriate for applications to profile classes (that is, soil profiles comprised of sands, gravels, and low PI clays) is a lognormal distribution with a standard deviation of 0.35 natural log units at a shear strain of  $3 \times 10^{-2}$  percent (EPRI, 1995). This represents a wide range and site-specific test data would be expected to decrease this variability considerably. In the generation of random curves, the perturbation at  $10^{-2}$  percent strain is applied to the base case curve and an algorithm is used to preserve the shape of the base case curve throughout the strain range. The distribution is truncated at two-sigma to preserve physically reasonable modulus reduction and damping values (EPRI, 1993). Truncation is also applied to  $G/G_{\max} > 1$  and to very low damping values, again based on physical arguments. In the analyses, 50 random profiles and sets of modulus reduction and damping curves are used to develop the median and one-sigma response characteristics of the categories.

In typical applications of strain dependent amplification factors, ratios of 5 percent damped response spectra computed at the top of soil to outcrop bedrock motions are used to modify motions produced for the rock surface. Generally a suite of amplification factors are generated for a range in outcrop (control) motion levels. This is accomplished by selecting magnitude and distance pairs for the stochastic point source model that result in discrete PGA values of the outcrop motions which cover the expected range in the hazard predictions. Both magnitudes and distances are selected to be in accord with the regional seismic environment.

In this case, however, transfer functions are required to modify motions computed for the top of the profile assuming the near-surface layer (layer 1) exhibits linear response. To accommodate this application, transfer functions are computed as the ratio of motions computed at the top of the surface layer using equivalent-linear response to motions computed at the same point but assuming linear response. As with the more conventional approach, a range in control motions is used, but in this case the range is determined by the 5 percent damped response spectral acceleration at 34 Hz computed at the profile surface assuming linear response. This definition was chosen because all modelers shared this spectral frequency in common. It should be emphasized that for low damping rock sites, 5 percent damped response spectral acceleration does not saturate to PGA at 34 Hz. For Yucca Mountain rock ( $\kappa$  values near 0.02 sec), saturation to PGA occurs between 50 to 100 Hz while for soft California rock, with typical  $\kappa$  values near 0.04 sec (Silva and Darragh, 1995), saturation occur at around 30 Hz (Silva, 1991).

The discrete values in 34 Hz 5 percent damped response spectra computed at the surface assuming linear response are shown in table 7.1. The values range from 0.05 g to 3.00 g to accommodate a range in ground motion predictions. The motions were computed using the stochastic point source model (Silva, 1991) with the base parameters of  $\kappa = 0.02$  sec,  $Q(f) = 250 f^{0.4}$ , Yucca Mountain crustal model (table 5.2), and a stress drop of 50 bars. Hypocentral distances and magnitudes are listed in table 7.1. Figure 7.3 shows median and  $\pm 1$  sigma response spectra computed at the surface of the tuff assuming equivalent-linear response as well as the 10 percent g (at 34 Hz) motions assuming linear response of the tuff. Figure 7.4 shows the median and  $\pm 1$  sigma amplification factors for 10 percent g (34 Hz spectra) which are simply the ratios computed with respect to the linear motions shown in figure 7.3. The median amplifications factors show pronounced minima due to resonances in the linear surface motions (fig. 7.3). Randomization of the surface layer for the linear analyses would result in smooth median spectra but would require many more runs. For application to each of the modelers outcrop motions, the amplification factors should be smooth since the identical resonances will likely not be present in each of the modeler's motions. To accomplish this, a smooth functional form has been fit to the amplification factors resulting in a suite of smooth factors as a function of 34 Hz outcrop response spectral acceleration.

TABLE 7.1 - NEAR HERE

FIGURE 7.3 - NEAR HERE

FIGURE 7.4 - NEAR HERE

### Development of Smooth Site Response Ratios

For application to the response spectra from the modeling exercises, a smooth set of linear/non-linear site response ratios is needed. Smooth site response factors were developed by fitting an equation to the raw site response ratios computed by PEA. These raw ratios are shown in figure 7.5 for a range of input level motions of the linear response ground motion. It should be noted that these site response ratios are strictly valid for 5 percent damping only. Differences may exist for other damping values.

FIGURE 7.5 - NEAR HERE

The site response ratio is modeled using a piecewise continuous model that has a break at the peak (near 1 second). For long periods, the ratio is modeled by the form of a filter and at short periods ( $T < 1$  sec) the ratio is modeled by a polynomial in terms of the log period. The resulting model is,

$$\text{Ratio} = \text{Exp} \left[ \frac{c_1}{1 + \left[ \frac{0.034 - \text{Log}(T)}{c_2 + c_3 I + c_4 I^2} \right]^{c_5 + c_6 I + c_7 I^2}} \right] \quad (7.1)$$

for  $T \leq 1.081$  seconds and  $I$  is the input level motion for linear response given by the spectral acceleration at 34 Hz. For periods greater than 1.081 seconds, the resulting model is,

$$\text{Ratio} = \text{Exp} \left[ \left( c_1 + \sum_{i=2}^6 b_i f_1^i \right) + \left( c_8 + \sum_{i=1}^3 a_i I^i \right) \left( 1 + \sum_{i=2}^5 d_i f_2^i \right) \right] \quad (7.2)$$

where,

$$f_1 = (\text{Log}(T) - 0.034) \quad (7.3)$$

and

$$f_2 = (\text{Log}(T) - 2.0) \quad (7.4)$$

and the coefficients are listed in table 7.2 . A comparison with models and the raw ratio data is shown in figure 7.5. The smoothed model is shown alone in figure 7.6.

TABLE 7.2 - NEAR HERE

FIGURE 7.6 - NEAR HERE

**Table 7.1. Control motions magnitude and distances.**

| <b>34 Hz (g) 5 percent Damped</b> | <b>Moment Magnitude</b> | <b>Hypocentral Distance (km)</b> |
|-----------------------------------|-------------------------|----------------------------------|
| 0.10                              | 6.4                     | 40.23                            |
| 0.20                              | 6.4                     | 25.43                            |
| 0.30                              | 6.4                     | 18.99                            |
| 0.40                              | 6.4                     | 15.25                            |
| 0.60                              | 6.4                     | 11.03                            |
| 0.80                              | 6.4                     | 8.66                             |
| 1.00                              | 6.4                     | 7.14                             |
| 1.20                              | 6.4                     | 6.08                             |
| 1.50                              | 6.4                     | 4.98                             |
| 1.75                              | 6.4                     | 4.33                             |
| 2.00                              | 6.4                     | 3.83                             |
| 2.50                              | 6.4                     | 3.11                             |
| 3.00                              | 6.4                     | 2.62                             |

**Table 7.2. Coefficients for non-linear/linear ratio model.**

| Coefficient    | Value  |
|----------------|--------|
| c <sub>1</sub> | 0.039  |
| c <sub>2</sub> | 0.010  |
| c <sub>3</sub> | 0.103  |
| c <sub>4</sub> | -0.017 |
| c <sub>5</sub> | 0.308  |
| c <sub>6</sub> | 0.890  |
| c <sub>7</sub> | -0.197 |
| c <sub>8</sub> | 0.111  |
| b <sub>2</sub> | -1.144 |
| b <sub>3</sub> | 2.455  |
| b <sub>4</sub> | -2.216 |
| b <sub>5</sub> | 0.931  |
| b <sub>6</sub> | -0.149 |
| a <sub>1</sub> | -0.136 |
| a <sub>2</sub> | 0.029  |
| a <sub>3</sub> | 0.0032 |
| d <sub>2</sub> | 2.169  |
| d <sub>3</sub> | 3.533  |
| d <sub>4</sub> | 1.888  |
| d <sub>5</sub> | 0.347  |

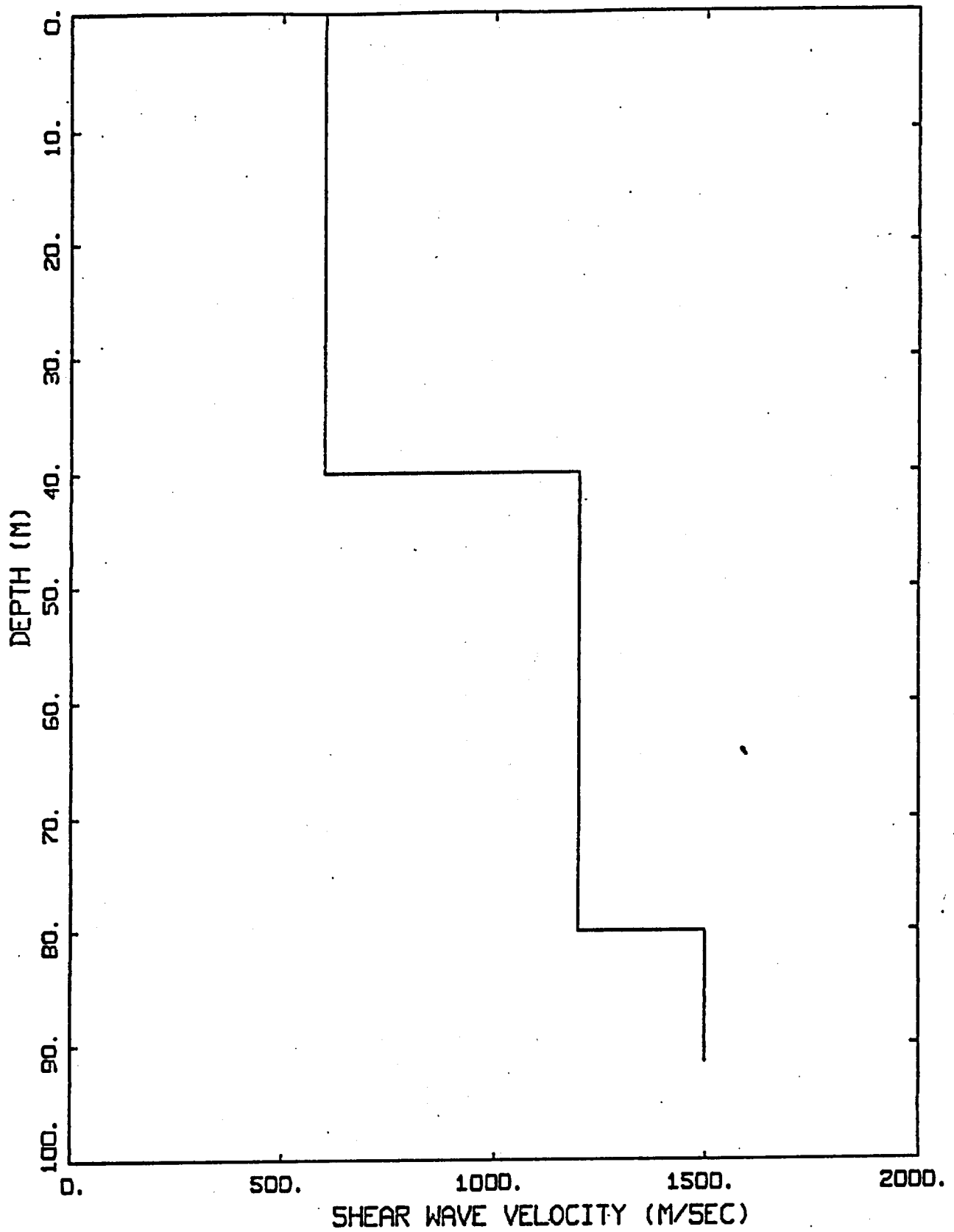


Figure 7.1. Top 100m of the Yucca Mountain shear-wave velocity profile.

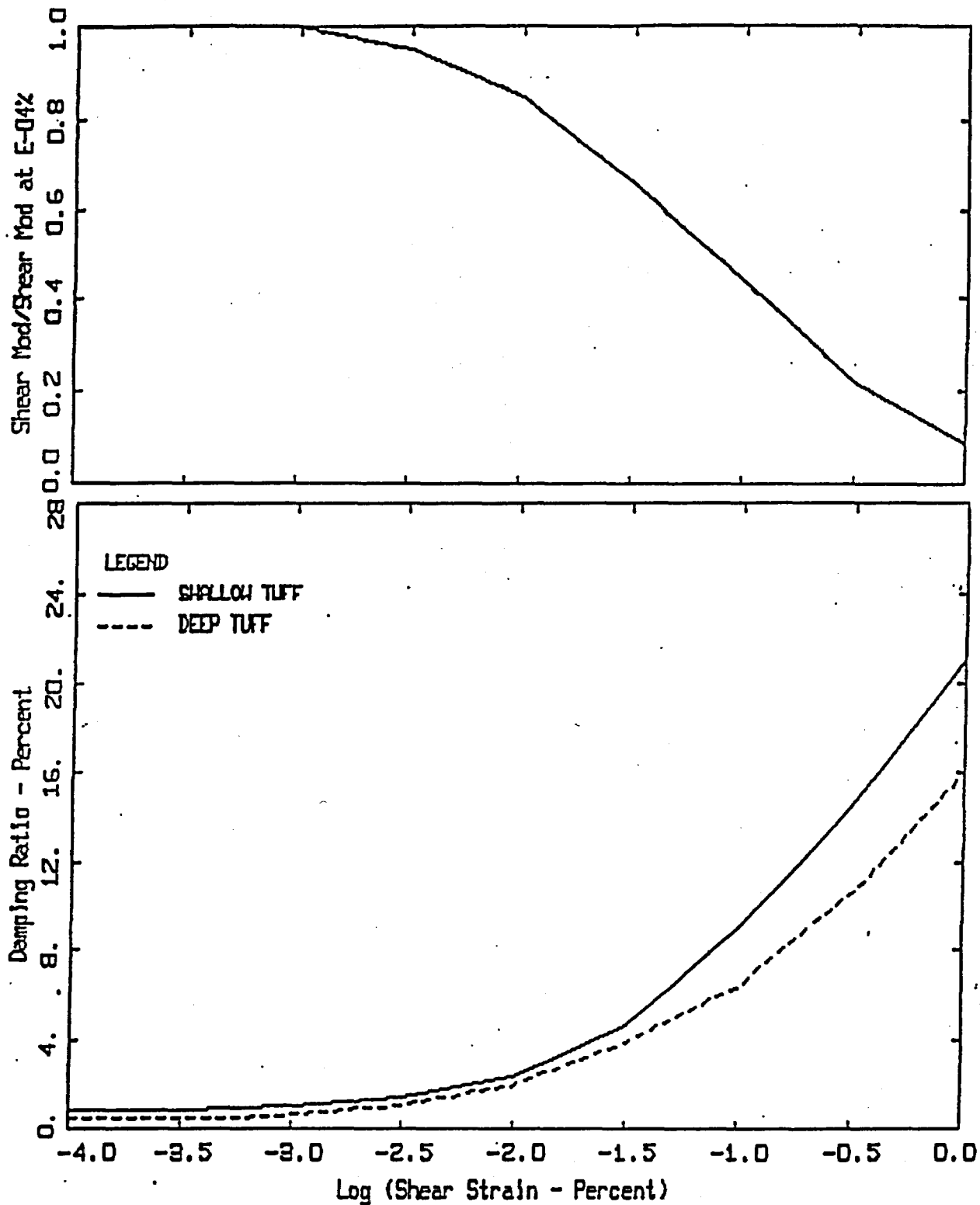
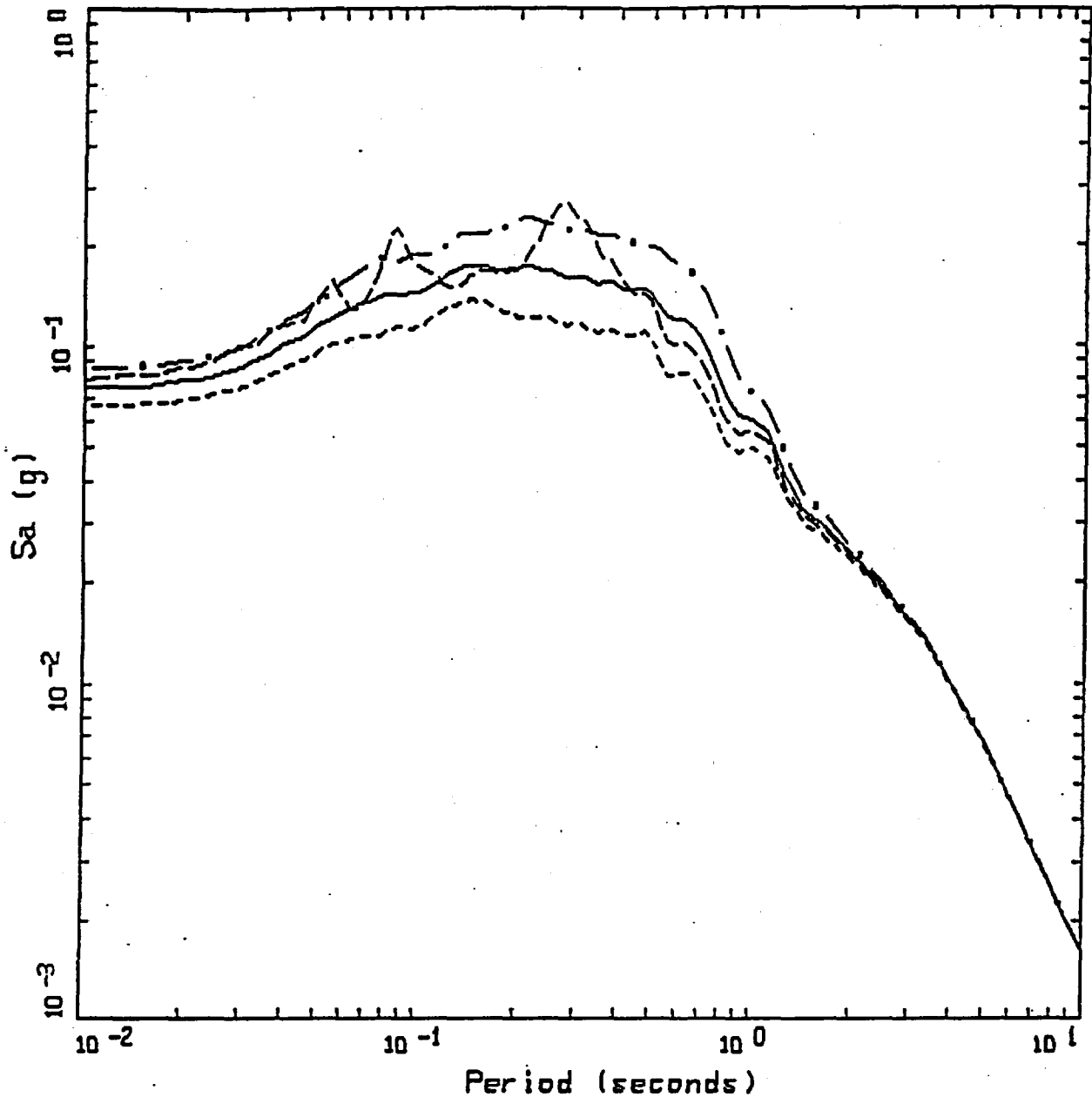


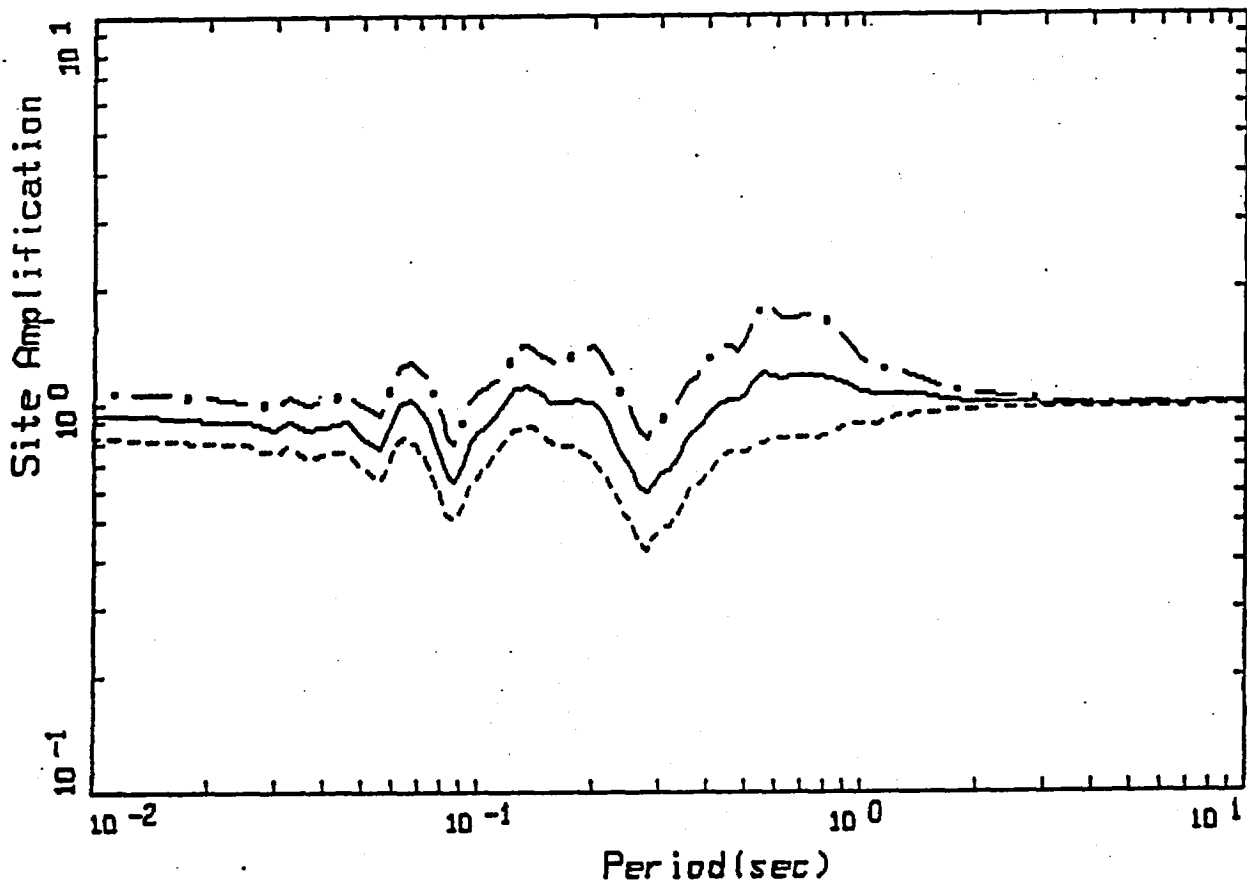
Figure 7.2. Modulus reduction and damping curves based on laboratory dynamic testing of Tuff samples taken at the Los Alamos National Laboratory (Wong et al., 1993). The shallow Tuff was sampled in the top 44m, is moderately welded, has a shear-wave velocity of about 600m/sec and is unsaturated. The deep Tuff was sampled at 157m, is nonwelded, has a shear-wave velocity of 700m/sec, and was 63% saturated.



M 6.4 POINT SOURCE, LINEAR MOTION 0.10 G AT 34 HZ  
 VARIATION OF TUFF VELOCITY, DEPTH OF TUFF, MATERIAL MODEL

- LEGEND
- LINEAR MOTION ; 0.10 G AT 34 HZ
  - . - 84TH PERCENTILE, PARAMETRIC UNCERTAINTY; PGA = 0.086 G
  - 50TH PERCENTILE, PARAMETRIC UNCERTAINTY; PGA = 0.076 G
  - 16TH PERCENTILE, PARAMETRIC UNCERTAINTY; PGA = 0.056 G

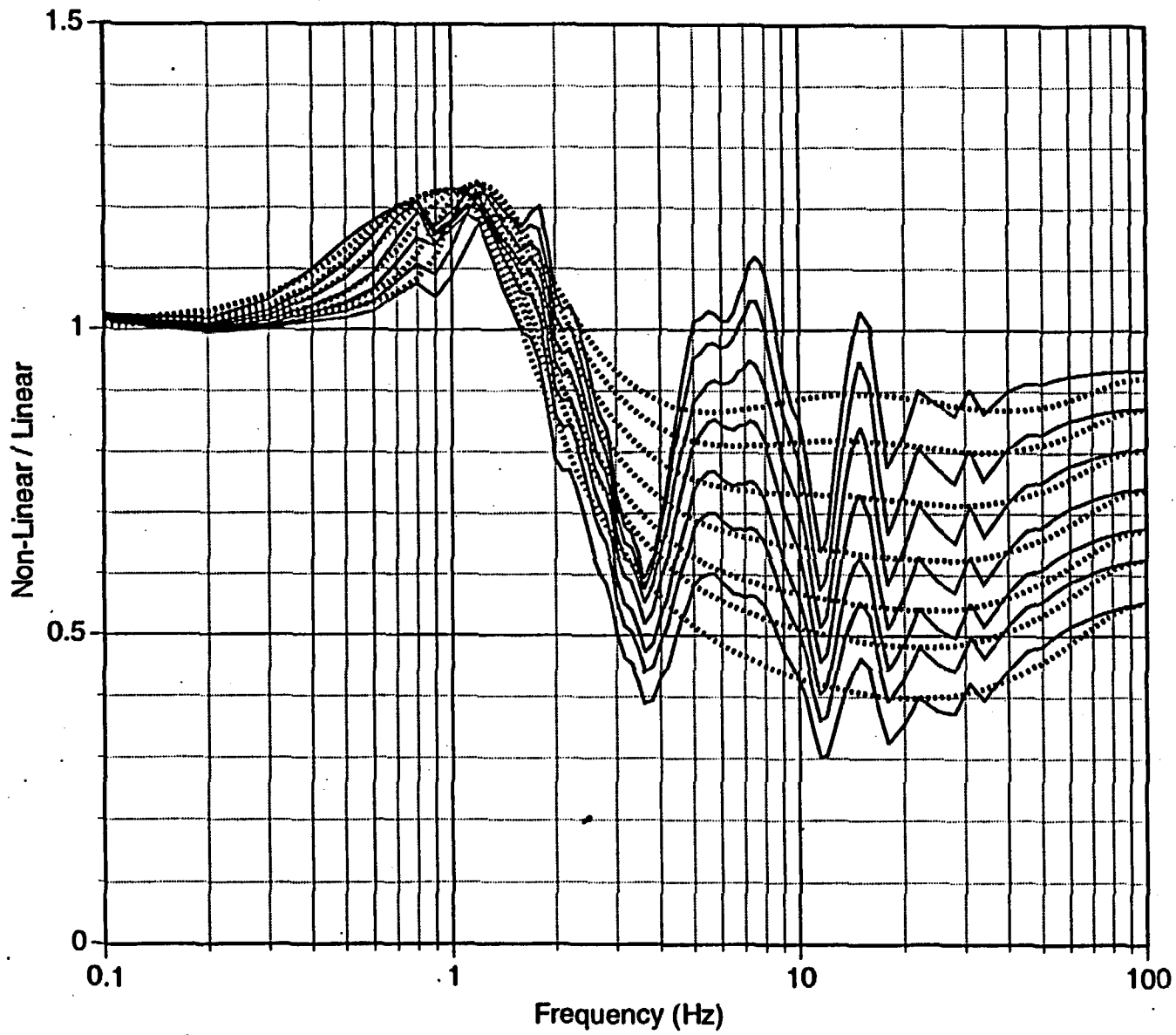
Figure 1.3. Median and  $\pm 1$  sigma 5% damped response spectra computed using equivalent-linear response for the surficial Tuff layer for input motions which produced 10%g at 34 Hz at the surface of the Tuff assuming linear response.



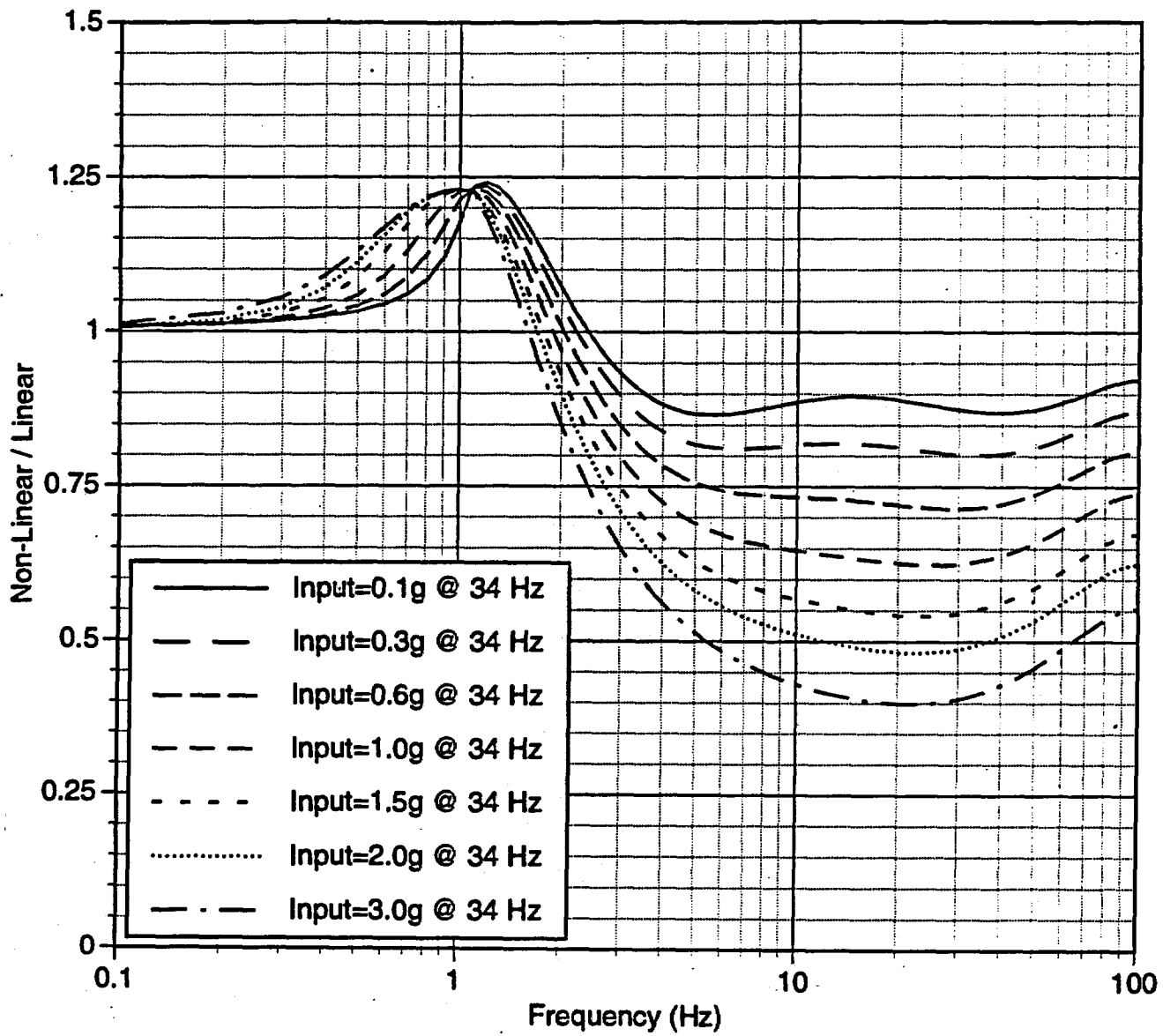
AMPLIFICATION FACTORS  
 INPUT MOTION 0.10 G AT 34 HZ

LEGEND  
 - . - 84TH PERCENTILE  
 ——— 50TH PERCENTILE  
 - - - 16TH PERCENTILE

Figure 74. Median and  $\pm 1$  sigma amplification factors computed using equivalent-linear response for the surficial Tuff layer to input motions which produced 10%g at 34 Hz at the surface of the Tuff assuming linear response.



- Sa (34Hz) = 0.1g
- Sa (34Hz) = 0.3g
- Sa (34Hz) = 0.6g
- Sa (34Hz) = 1g
- Sa (34Hz) = 1.5g
- Sa (34Hz) = 2g
- Sa (34Hz) = 3g
- ..... 0.1 model
- ..... 0.3 model
- ..... 0.6 model
- ..... 1 model
- ..... 1.5 model
- ..... 2 model
- ..... 3 model



## 8. NORMAL FAULTING EXERCISES

### Fault-Site Geometry and Reciprocity

Because of the limited range of magnitudes (and inferred fault areas) associated with the normal faulting scenarios (table 8.1), the range of behavior of these normal faults can be fairly well represented by a single fault area combined with variations in other fault parameters. In effect, the differences in fault length are relatively small relative to the rest of the source rupture properties that need to be evaluated. Each fault is also approximated by a rectangular area, which projects to the surface as a straight line. Given these geometrical simplifications, rather than considering several different fault locations relative to a single site (that is, as shown in fig. 2.2), an equivalent (or reciprocal) view is to consider a fixed fault relative to a suite of sites, each of which represents the unique geometry of a different fault relative to Yucca Mountain. Figures 8.1a-b illustrate the concept. Figure 8.1a shows the location of the Bare Mountain (BM), Solitario Canyon (SC), Bow Ridge (BR), and Paintbrush Canyon (PC) faults relative to Yucca Mountain projected in cross section approximately perpendicular to strike and at dips of 57.5 degrees. Figure 8.1b shows the site-source reciprocal relation whereby the fault is fixed and the Yucca Mountain site is projected to preserve the original source-site geometries.

TABLE 8.1 -- NEAR HERE

FIGURE 8.1 -- NEAR HERE

Since the numerical modeling computer programs are set up for computing the ground motion at multiple sites efficiently, by taking advantage of this reciprocal-relation convenience, multiple scenarios can be evaluated more efficiently. This added efficiency allows for a wider range of faulting parameters to be explored.

#### **Base Case Exercise (N01)**

As a first exercise, a base case normal faulting ground motion exercise was established to calibrate differences between the various modeling methods. This exercise (referred to as N01) represents essentially a median case for the range of three simple normal faulting scenarios (1, 2, and 4).

The estimation of ground motion for the scenario earthquakes requires that some additional seismological constraints be developed in addition to the geological/seismological constraints given in Section 2. In effect, these constraints place limits on certain static characteristics of the earthquake such as location, magnitude, and style of faulting (or focal mechanism). These constraints are listed in table 8.2. However, ground motion is a product of dynamic properties of earthquake generation (source), followed by wave propagation in the earth's crust (path) and near-surface layers below the site. Characteristics of the source, path and site properties each contribute substantially to the variability of ground motion. Thus, the modeling exercises are designed to place some reasonable limits on both the static and dynamic properties in the context of their impact on the generation of ground motion.

**TABLE 8.2 -- NEAR HERE**

Modelers are free to use empirical Green's functions in lieu of the crustal structure specified in table 5.2. The average kappa values should be corrected to 0.02 sec and high strain properties should be included as appropriate for Layer 1 (that is, upper 100 meters). Digital seismograms are available from the mainshock and two of the largest aftershocks of the Little Skull Mountain earthquake.

The model parameter values used for scenario N01 are listed in tables 8.3a-d. This table helps to identify which parameters are used in the different methods. A "±" in the table indicates that this parameter is randomized in the individual realizations. This randomization is different from the multiple realizations of the source process. It represents random variations of a parameter within a single earthquake as compared to random variations of a parameter between different earthquakes. This internal randomization is part of the model.

TABLE 8.3a,b,c,d -- NEAR HERE

The N01 exercise is described below and the fault-site geometry is shown in figure 8.2. The fault coordinates are listed in table 8.4. Note that several additional (hypothetical) sites have also been included for the purpose of testing sensitivities of the models to a broader range of conditions than is afforded by the specific scenarios themselves. The site locations are listed in table 8.5.

FIGURE 8.2 -- NEAR HERE

TABLES 8.4, 8.5 NEAR HERE

## Multiple Source Realizations

In the scenario exercises, the magnitude of the event and the geometry (dimension and location) are specified, but for future events, many of the source properties are unknown. The source parameters that are modeled using site-specific information need to be randomly sampled for future unknown events. In order to develop a stable estimate of the median and variability, a minimum of about 30 realizations is required for each event. The key source parameters are hypocentral location, slip distribution, and rake angle (table 8.2). To limit the number of runs, the slip distribution and rake angle are randomized at the same time. Most of the simulation methods are set up for a single specified hypocenter. There are three hypocentral locations (one at each end of the fault and one in the middle) that are specified; however, the hypocenters can also be randomized along with the slip and rake angles as long as the total number of realizations is at least 30. If random hypocenters are used, they should be uniformly distributed over the lower half of the fault plane excluding the 10 percent of the fault length (along strike) near each edge. This hypocentral zone reflects the observation that rupture initiation in moderate to large earthquakes tends to occur in the deeper half of the fault near the base of the seismogenic crust.

The randomizations of the parameters (slip distribution and rake) are handled differently by the different models. For example, USC changes the sub-event stress-drop as a "variation of slip" whereas other models use different slip distributions.

## Output Specifications

The output specifications for all of the modeling exercises are standardized in order to facilitate comparison of results and statistical analyses which are developed in a later section. All ground motion estimates are presented in terms of 5 percent damped PSV response spectra for the geometric mean of horizontal components. The response spectra are computed at the same 89 frequency points between 0.1 and 100 Hz as used in the Little Skull Mountain validation (table 6.11).

The time history records (velocity and acceleration) are developed for either two horizontal components (fault parallel and perpendicular) or one average horizontal component. The durations of the velocity and acceleration time histories are also computed in terms of the normalized Arias intensity of the vector sum of the two horizontal components or the single average horizontal component.

## N01 Modeling Results

Several sets of preliminary results were presented in progress reports and workshops. The initial results of the base case normal faulting exercise (N01) were presented in the June 1995 report, "Provisional Results for Activity 8.3.1.17.3.3 (3GSA512M)" (Schneider, 1995). An updated set of results were presented and discussed at Meeting 3 of the ground motion modeling phase of the project, held on 31 July 1995 at the USGS in Menlo Park, CA. The preliminary results were further refined and presented at the September 15-16 workshop held in Georgetown, CA.

In the preliminary reports, all of the modelers assumed linear site response of the tuff except for PEA which included variable modulus reduction and damping for the tuff depending on the amplitude of the motion. Usually, rock sites are assumed to behave linearly; however, based on the assumed properties of the Yucca Mountain tuff and the high levels of shaking, the tuff is expected to exhibit non-linear response effects. The modelers that had assumed linear response agreed that non-linear response is likely to occur at the very high ground motion levels. The non-linear effects are approximated using the non-linear/linear site response scale factors developed in Section 7 (fig. 7.6). All of the simulations (except for the S-cubed empirical model) were scaled by these factors to approximate the non-linear response effects.

The resulting median acceleration response spectra from each method are shown in figures 8.3a-d for the four scenario sites: 02, 04, 05, and 07, corresponding (reciprocally) to the location of Yucca Mountain with respect to the Bow Ridge, Paintbrush, Bare Mountain, and Solitario Canyon faults, respectively. A full set of plot of the spectra for all 14 sites is given in Appendix D.

FIGURE 8.3 – NEAR HERE

The median spectra are computed from the suite of fault rupture realizations for each method (that is, combinations of fault slip distribution, hypocentral location and rake angle). The peak accelerations are generally high, averaging 1 g or more adjacent to the fault (for example, Site 02). The average spectral shapes for each of the models are generally similar with the PEA model showing the largest high frequency content and the WCC model showing the largest moderate frequency content. The largest differences in the numerical simulations is for site 05 (Bare Mountain) for which the USGS model is much lower than the other models. The S-cubed empirical model tends to be lower than the simulations over the period band of 0.2 to 1.0 seconds.

The attenuation of spectral acceleration with respect to distance from the fault trace is shown in figures 8.4a-f for six different frequencies: 0.2, 1.0, 5.0, 10.0, 20.0, and 34.0 Hz. At each frequency, numerical model calculations for the five finite-fault models and the S-cubed empirical model are juxtaposed against a suite of empirical ground motion relations for rock. Note that the model results for each frequency-distance pair are median values obtained from the multiple realizations of the fault rupture process.

FIGURE 8.4 -- NEAR HERE

For comparison, a point-source model was also used to predict the ground motions for these sites. The point-source model results were generated by PEA assuming a single-corner source spectrum (Brune, 1970, 1971), with a Brune stress drop of 50 bar. In this model the crustal-structure effect was approximated using a set of frequency-dependent amplification factors consistent with the Yucca Mountain crustal structure used (fig. 6.3). Non-linear site response was included. The point source distance was computed using a focal depth of 6 km (middle of rupture) and a Joyner-Boore horizontal distance (that is, shortest distance to the vertical projection of the fault plane). The point source model is discussed in more detail later in this section.

The first four empirical relations (Sadigh and others, 1993; Idriss 1991, 1994; Boore-Joyner-Fumal (BJF), 1994; and Abrahamson and Silva, 1995) were developed for application to western North America (WNA), but are calibrated primarily using data from California. The EPRI (1993) relation was developed for application to eastern North America (ENA), east of the Rocky Mountains. These empirical models use different distance measures. In figures 8.4a-f, the empirical relations are plotted as a function of the horizontal distance from the surface trace of the fault.

The most salient difference amongst the WNA curves is the flattening of the BJF curve relative to the other models. The flattening is a result of the source-distance metric, wherein distance to the fault is measured relative to the surface projection of the fault. Therefore, for a dipping fault, any point above the fault is at zero distance. By contrast, the other models measure source distance to the fault trace (or its surface projection). The Abrahamson and Silva model distinguishes between sites on the hanging wall and footwall which also produces a flattening of the attenuation over the hanging wall. The EPRI model uses the same distance measure as the BJF model so it also shows flat attenuation for sites over the hanging wall. The EPRI model is generally higher in the 10 - 30 km range due to the generally much smaller near-surface damping ( $\kappa=0.006$  seconds) used in this model for ENA.

The ratio between the median ground motion from the six models and the median of the four WNA attenuation relations is shown in figure 8.5. This comparison gives an indication of the modifications that could be made to the standard WNA empirical attenuation relations to make them appropriate for Yucca Mountain. At short distances, the model results exceed the empirical relations by about a factor of 1.5 on average. A significant factor leading to larger high frequency motions for the numerical calculations is the relatively low site damping factor ( $\kappa$ ), which was set to 0.02 seconds. The average  $\kappa$  for WNA is 0.04 seconds (Silva and Darragh, 1995). The effect of differences in  $\kappa$  are most pronounced above about 5 Hz. Another factor is the greater crustal amplification obtained in the specified Yucca Mountain profile over the amplification inherent to the majority of the data that forms the bases for the empirical relations. (The surface:source impedance contrast is about 3.0 for this model, as opposed to 2.5 for the BJJF model as shown in fig. 6.4.)

FIGURE 8.5 - NEAR HERE

#### Parametric Variability

The median spectra discussed above are the median values from a large suite of source realizations. The variability of the ground motions for the different realizations is the parametric aleatory variability (discussed in Section 4).

Figures 8.6 to 8.9 show median values with  $\pm 1$  standard deviation of 5 percent damped acceleration response spectra, again for sites 02, 04, 05, and 07. Note that the variability tends to be model and site dependent, with the greatest variability shown in the PEA model and the least apparent in the WCC and UNR models. This parametric variability is part of the total variability discussed in Section 10.

FIGURES 8.6,8.7,8.8,8.9 - NEAR HERE

### Duration

The mean acceleration and velocity durations are shown in figure 8.10a-b, respectively for the four scenario sites. The durations for the different models are within about a factor of 2 of each other except for the USGS model which produces much shorter durations than the other four models. These much smaller durations for the USGS model are consistent with the large positive bias (underprediction) found for the acceleration duration from the Little Skull Mountain (LSM) validation exercise (fig. 6.27). Of the four similar models, the USC model tends to produce the longest durations and the UNR model tends to produce the shortest durations. The longer durations for the USC model are consistent with the comparisons of the durations from LSM validation results (the USC model was unbiased, whereas the WCC and PEA models tended to underpredict the duration). In contrast, the shorter durations for the UNR model are contrary to the LSM validation results which showed longer durations (and unbiased) for the UNR model.

As with the response spectral values, the parametric variability of the durations is considered by examining the variability of the duration from multiple realizations of the source process. Figures 8.11 to 8.14 show mean values with  $\pm 1$  standard deviation of the duration of acceleration time histories for the same four sites. The similar parametric variability of the velocity duration is shown in figures 8.15 to 8.18. The trends in the velocity duration are quite similar to those for acceleration.

FIGURE 8.10,8.11,8.12,8.13,8.14,8.15,8.16,8.17,8.18 - NEAR HERE

### **Point-Source Exercise and Results**

Figures 8.19a-f show comparisons of the response spectral attenuation for the finite fault simulations with those for the point-source model for stress drops of 25, 50, and 100 bars. The point source distance was computed using a focal depth of 6 km (middle of rupture) and a Joyner-Boore horizontal distance (that is, shortest distance to the vertical projection of the fault plane). The 25 bar values tend to fall toward the lower range of the finite-fault predictions and the 100 bar values tend to fall toward the upper range bound of these predictions. Recall that the estimated stress drop for the Little Skull Mountain earthquake ranged from 25 to 50 bars (Section 6). The finite-fault simulations correspond to higher equivalent point-source stress drops (on average) than observed for the Little Skull Mountain earthquake.

**FIGURE 8.19 - NEAR HERE**

### **Additional Exercises and Results**

In addition to the base case (N01), several additional cases were considered to estimate the impact of variations in the fixed source parameters (those fixed as part of the exercise). These additional normal faulting exercises are denoted N02 to N08 are listed in Table 8.6.

TABLE 8.6 -- NEAR HERE

#### **Preferred Base Case (N02)**

The modelers were allowed to make variations in the fixed source parameters for N01 if in their judgment it would be more applicable to their specific method. This preferred case was denoted N02. None of the modelers used this option.

#### **Sensitivity to Dip (N03 and N04)**

The N03 and N04 exercises evaluated the effect of different dip angles on the ground motion. The surface trace of the fault is held fixed and the dip angle was varied from 45 to 70 degrees (fig. 8.20). The median difference between cases N03 and N01 and between N04 and N01 are shown in figures 8.21 to 8.24 for the four scenario sites. For the two sites over the hanging wall (sites 2 and 4) and for the more distant hanging wall side site (site 5), changing the dip by 12.5 degrees changes the high frequency ground motions by about 10 to 15 percent with larger motions for the smaller dip (N03) and smaller motions for the larger dip (N04). For the site on the foot wall (Site 07), a similar but slightly smaller effect is seen but with the larger motions for the steeper dips.

FIGURE 8.20, 8.21, 8.22, 8.24 - NEAR HERE

The standard error of the ground motion due to the uncertainty in dip is part of the epistemic parametric variability. It is epistemic because it represents scientific uncertainty in the dip angle and it is parametric because it relates to an event-specific parameter of the model. This variability is used as part of the total variability in Section 10.

#### **Preliminary Sensitivity to Rupture Area (N05 and N06)**

The N05 and N06 exercises were intended to evaluate the effect of the uncertainty in specifying the magnitude for the given fault area. In these exercises, the magnitude of the event was varied by  $\pm 0.2$  magnitude units for the fixed fault area. This approach was intended to evaluate the uncertainty in the median static stress drop, but the problem with this approach is that it not only changes the stress drop but also the magnitude of the event. As a result, the comparisons are for a smaller magnitude low stress-drop event with a larger magnitude high stress-drop event. This leads to a very large variability of the ground motions that are not representative of the effect that we are interested in. Therefore, these exercises were not considered further.

#### **Revised Sensitivity to Rupture Area (N07 and N08)**

The N07 and N08 exercises were developed to address the problems with the N05 and N06 exercises discussed above. In these exercises, the fault area is varied, but the magnitude is held fixed. In this manner, these exercises address the variability in ground motion due to the variability in static stress-drop. In N07, the fault length was increased from 18 to 29 km and in N08, the length was decreased from 18 to 11 km. These changes in fault length (with fault width held fixed) correspond to plus or minus a factor of 2 in static stress drop.

The median difference between cases N07 and N01 and between N08 and N01 are shown in figures 8.25 to 8.28 for the four scenario sites. The lower static stress drop (N07) leads to an average reduction of 10 to 20% for spectral accelerations in the range of 0.1 to 1.0 seconds.

**FIGURES 8.25, 8.26, 8.27, 8.28 - NEAR HERE**

**Table 8.1 Primary normal faulting scenario earthquakes.**

| Scenario | Fault                             | Length<br>(km) | Width<br>(km) | Dip       | Rake                    | M    | Dist.<br>(km) |
|----------|-----------------------------------|----------------|---------------|-----------|-------------------------|------|---------------|
| 1        | Paintbrush<br>Canyon-Bow<br>Ridge | 14 - 15        | 14.2          | 45-70° W  | -70°<br>(Normal/LL)     | 6.31 | 4.5/2.5       |
| 2        | Solitario<br>Canyon               | 21 ± 7         | 14.2          | 58 ± 6° W | -65 ± 5°<br>(Normal/LL) | 6.48 | 1.0           |
| 4        | Bare Mountain                     | 18 ± 4         | 14.2          | 45-70° E  | -90°<br>(Normal)        | 6.42 | 15.5          |

**Table 8.2 Source parameters for N01 modeling exercise.**

| <b>Fixed Parameters</b> |  |
|-------------------------|--|
| • Fault Length          | 18 km                                      |
| • Fault Width           | 14 km                                      |
| • Fault Area            | 252 km <sup>2</sup>                        |
| • Magnitude             | 6.4  |
| • Average stress drop   | 30 bar                                     |
| • Average shear modulus | $3.37 \times 10^{11}$ dyne/cm <sup>2</sup> |
| • Average slip          | 60 cm                                      |
| • Moment                | $5.1 \times 10^{25}$ dyne-cm               |
| • Fault strike          | 0 degrees ( $x = 0$ )                      |
| • Fault dip             | 57.5 degrees to east ( $Az = 90$ )         |



**Table 8.3a. Model parameters used for N01.**

| <b>Source: Sub-event</b>      |                         |                          |                                       |   |                          |
|-------------------------------|-------------------------|--------------------------|---------------------------------------|---|--------------------------|
|                               | <b>PEA</b>              | <b>USC</b>               | <b>UNR</b>                            | <b>WCC</b>  | <b>USGS</b>              |
| <b>Dimension</b>              | 3 x 2.8 km <sup>2</sup> | r=1.5 km                 | r≤4 km                                | 3x4 km <sup>2</sup>   | integration<br>time step |
| <b>Magnitude</b>              | 5.0                     | 6.0                      | varies                                | 5.2   | -                        |
| <b>Rise-time</b>              | 0.15±                   | -                        | -                                     | 0.2   | -                        |
| <b>Stress-drop<br/>(bars)</b> | 30                      | 20-40                    | 30-70<br>(constant)                   | empirical   | -                        |
| <b>Radiation<br/>pattern</b>  | rms fault<br>average    | none                     | theoretical                           | high freq -<br>empirical<br>(f>1 Hz)<br>low freq -<br>theoretical<br>(f<1 Hz) | none                     |
| <b>Source</b>                 | $\omega^2$              | $\omega^2$               | $\omega^2$                            | empirical   | -                        |
| <b>Phase</b>                  | empirical<br>(EUS)      | enveloped<br>white noise | Brune pulse<br>& Green's<br>Functions | empirical   | -                        |

**Table 8.3b. Model parameters used for N01.**

**Source: mainshock**

|                         | PEA                       | USC                         | UNR                            | WCC                   | USGS                    |
|-------------------------|---------------------------|-----------------------------|--------------------------------|-----------------------|-------------------------|
| Rise-time (sec)         | 0.74                      | -                           | -                              | 0.65                  | scales with fault width |
| Rupture velocity (km/s) | 2.8±                      | 2.8                         | 2.8                            | 2.7±                  | 2.8                     |
| Slip model              | slip distribution         | four barriers               | fractile                       | slip distribution     | wave-number spectrum    |
| Shallow slip            | Not allowed               | source at center of barrier | tapered $\Delta\sigma$ (1/4 r) | Not allowed           | Not allowed             |
| Hypocenter              | as given                  | as given                    | as given                       | as given              | as given                |
| Rupture Plane           | shifted down dip 2 km     | as given                    | as given                       | shifted down dip 2 km | as given                |
| Dip                     | as given                  | as given                    | as given                       | as given              | as given                |
| Magnitude               | as given                  | as given                    | as given                       | as given              | as given                |
| Rake                    | as given $\pm 30$ degrees | 3 values                    | 3 values (5x4 grid smoothing)  | fixed                 | -                       |
| Slip-time function      | -                         | -                           | -                              | -                     | Kostrov                 |

**Table 8.3c Model parameters used for N01.**

| Path                                    | PEA           | USC                       | UNR  | WCC                  | USGS                |
|---|---------------|---------------------------|--|----------------------|---------------------|
| Geometrical<br>attenuation              | 1/R           | 1/R                       | Green's<br>Functions                         | Green's<br>Functions | 1/R                 |
| Scattering                              | -             | -                         | yes  | -                    | -                   |
| Q                                       | 250 $f^{0.4}$ | 250 $f^{0.4}$             | 240 $f^{0.4}$                                |                      |                     |
| Velocity<br>structure                   | -             | -                         | as given with<br>random<br>shallow<br>layers | as given             | -                   |
| Frequency<br>dependent<br>amplification | Yucca crust   | Boore (1986)<br>WUS model | -  | -                    | Yucca<br>(smoothed) |

**Table 8.3d Model parameters used for N01.**

| <b>High Frequency Attenuation</b> |          |       |         |          |          |
|-----------------------------------|----------|-------|---------|----------|----------|
|                                   | PEA      | USC   | UNR     | WCC      | USGS     |
| Kappa                             | 0.02 sec | -     | Q model | 0.02 sec | 0.02 sec |
| $f_{max}$                         | -        | 10 Hz | -       | -        | -        |
| Non-linear                        | yes      | -     | -       | -        | -        |
| site response                     |          |       |         |          |          |

**Table 8.4 Fault coordinates for N01 modeling exercise.**

- Coordinates of fault corners in (x, y, z)
  - Point 1                       $(x_1, y_1, z_1) = (0, 0, 0)$
  - Point 2                       $(x_2, y_2, z_2) = (0, 18, 0)$
  - Point 3                       $(x_3, y_3, z_3) = (7.52, 0, 11.81)$
  - Point 4                       $(x_4, y_4, z_4) = (7.52, 18, 11.81)$
  
- Coordinates of fault corners in fault plane (L, W)
  - Point 1                       $(l_1, w_1) = (0, 0)$
  - Point 2                       $(l_2, w_2) = (18, 0)$
  - Point 3                       $(l_3, w_3) = (0, 14)$
  - Point 4                       $(l_4, w_4) = (18, 14)$

**Table 8.5 Station locations for N01 modeling exercise.**

| <b>Site #</b> | <b>Name</b>               | <b>x</b> | <b>y</b> |
|---------------|---------------------------|----------|----------|
| 01            | Solitario Canyon Inverse  | 1.0      | 13.0     |
| 02            | Bow Ridge                 | 2.5      | 12.0     |
| 03            | Fault Edge                | 3.0      | 0.0      |
| 04            | Paintbrush Canyon         | 4.5      | 12.0     |
| 05            | Bare Mountain             | 15.5     | 5.0      |
| 06            | Distant                   | 30.0     | 9.0      |
| 07            | Solitario Canyon          | -1.0     | 13.0     |
| 08            | Bow Ridge Inverse         | -2.5     | 12.0     |
| 09            | Fault Edge Inverse        | -3.0     | 0.0      |
| 10            | Paintbrush Canyon Inverse | -4.5     | 12.0     |
| 11            | Bare Mountain Inverse     | -15.5    | 5.0      |
| 12            | Distant Inverse           | -30.0    | 9.0      |
| 13            | Intermediate              | 10.0     | 9.0      |
| 14            | Intermediate Inverse      | -10.0    | 9.0      |

**Table 8.6 Source parameters for additional normal faulting exercise.**

| Run Set | Finite Source |           |        |        |                       |
|---------|---------------|-----------|--------|--------|-----------------------|
|         | M             | Dip (deg) | L (km) | W (km) | $\Delta\sigma$ (bars) |
| N01     | 6.4           | 57.5      | 18     | 14     | 30                    |
| N02     |               | Not Used  |        |        |                       |
| N03     | 6.4           | 45.0      | 18     | 14     | 30                    |
| N04     | 6.4           | 70.0      | 18     | 14     | 30                    |
| N05     | 6.2           | 57.5      | 18     | 14     | 15                    |
| N06     | 6.6           | 57.5      | 18     | 14     | 60                    |
| N07     | 6.4           | 57.5      | 29     | 14     | 15                    |
| N08     | 6.4           | 57.5      | 11     | 14     | 60                    |

## Figure Captions

Figure 8.1. Reciprocal fault-site geometry.

Figure 8.2. Station locations for the normal faulting exercises

Figure 8.3 (a) Median ground motions for N01 site 2 (Bow Ridge)

Figure 8.3 (b) Median ground motions for N01 site 4 (Paintbrush Canyon)

Figure 8.3 (c) Median ground motions for N01 site 5 (Bare Mountain)

Figure 8.3 (d) Median ground motions for N01 site 7 (Solitario Canyon)

Figure 8.4 (a) Comparison of ground motions with attenuation relations for N01 (34 Hz)

Figure 8.4 (b) Comparison of ground motions with attenuation relations for N01 (20 Hz)

Figure 8.4 (c) Comparison of ground motions with attenuation relations for N01 (10 Hz)

Figure 8.4 (d) Comparison of ground motions with attenuation relations for N01 (5 Hz)

**Figure 8.4 (e) Comparison of ground motions with attenuation relations for N01 (1 Hz)**

**Figure 8.4 (f) Comparison of ground motions with attenuation relations for N01 (0.2 Hz)**

**Figure 8.5 Ratio of average simulated motion to average WUS attenuation relations.**

**Figure 8.6 Parametric variability of spectral acceleration for N01 site 2 (Bow Ridge)**

**Figure 8.7 Parametric variability of spectral acceleration for N01 site 4 (Paintbrush Canyon)**

**Figure 8.8 Parametric variability of spectral acceleration for N01 site 5 (Bare Mountain)**

**Figure 8.9 Parametric variability of spectral acceleration for N01 site 7 (Solitario Canyon)**

**Figure 8.10 Comparison of median acceleration durations for N01.**

**Figure 8.11 Parametric variability of acceleration duration for N01 site 2 (Bow Ridge)**

**Figure 8.12 Parametric variability of acceleration duration for N01 site 4 (Paintbrush Canyon)**

**Figure 8.13 Parametric variability of acceleration duration for N01 site 5 (Bare Mountain)**

**Figure 8.14 Parametric variability of acceleration duration for N01 site 7 (Solitario Canyon)**

**Figure 8.15 Parametric variability of velocity duration for N01 site 2 (Bow Ridge)**

**Figure 8.16 Parametric variability of velocity duration for N01 site 4 (Paintbrush Canyon)**

**Figure 8.17 Parametric variability of velocity duration for N01 site 5 (Bare Mountain)**

**Figure 8.18 Parametric variability of velocity duration for N01 site 7 (Solitario Canyon)**

**Figure 8.19 Comparison of simulated ground motions with point source estimates.**

**Figure 8.20 Variation in dip for exercises N03 and N04.**

**Figure 8.21 Effect of dip on computed response spectra for site 2 (Bow Ridge).**

**Figure 8.22** Effect of dip on computed response spectra for site 4 (Paintbrush Canyon).

**Figure 8.23** Effect of dip on computed response spectra for site 5 (Bare Mountain)

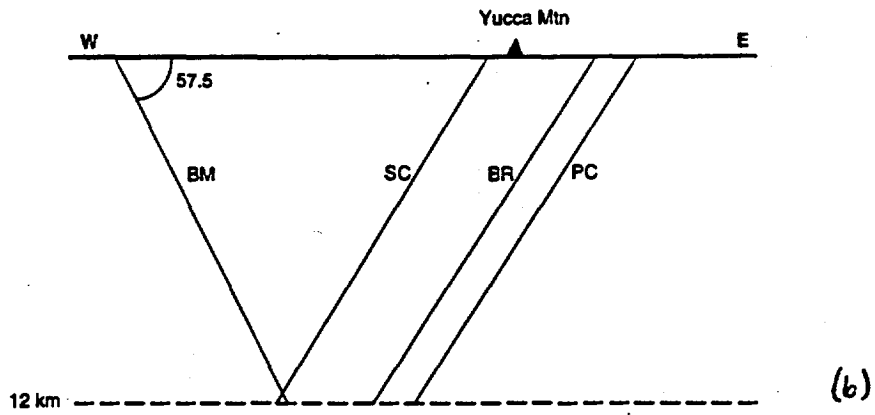
**Figure 8.24** Effect of dip on computed response spectra for site 7 (Solitario Canyon)

## **Figure Captions**

**Figure 5.1. Shear velocity as a function of depth in the vicinity of Yucca Mountain.**

**Figure 5.2. Compressional velocity as a function of depth in the vicinity of Yucca Mountain.**

**Normal Faults  
X - Section through YM**



**Normal Faults  
Reciprocal Fault-Station Section**

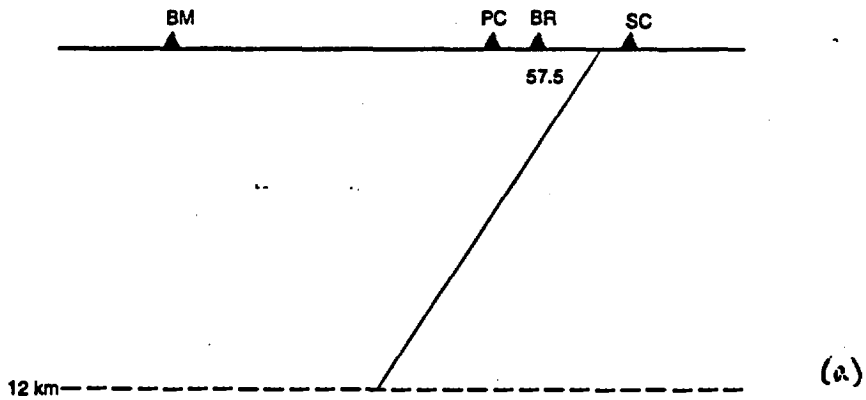
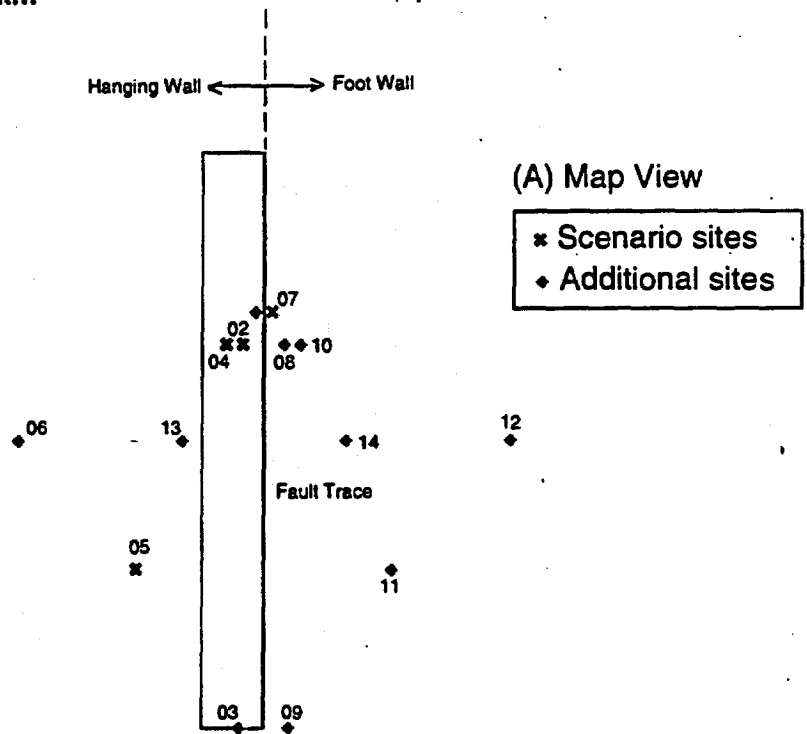


Figure 8.1

Normal Faults  
L = 18 km



(B) Cross-section

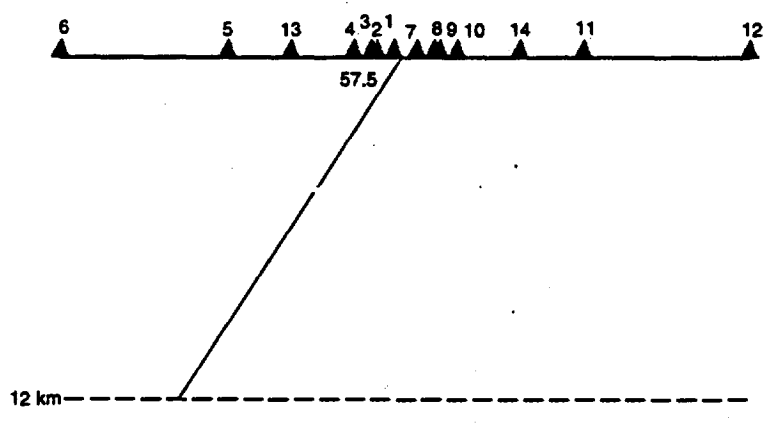


Figure 8.2

n01, STATION # 2

- \_\_\_\_\_ : mean of N01PEA02.PSV, [N=30]
- : mean of n01usc02.hpsv, [N=27]
- - - - - : mean of N01unr02.hpsv, [N=30]
- ..... : mean of N01wcc02.hpsv, [N=30]
- . - . - : mean of n01usg02.hpsv, [N=30]
- ..... : mean of n01scu02.hpsv, [N= 1]

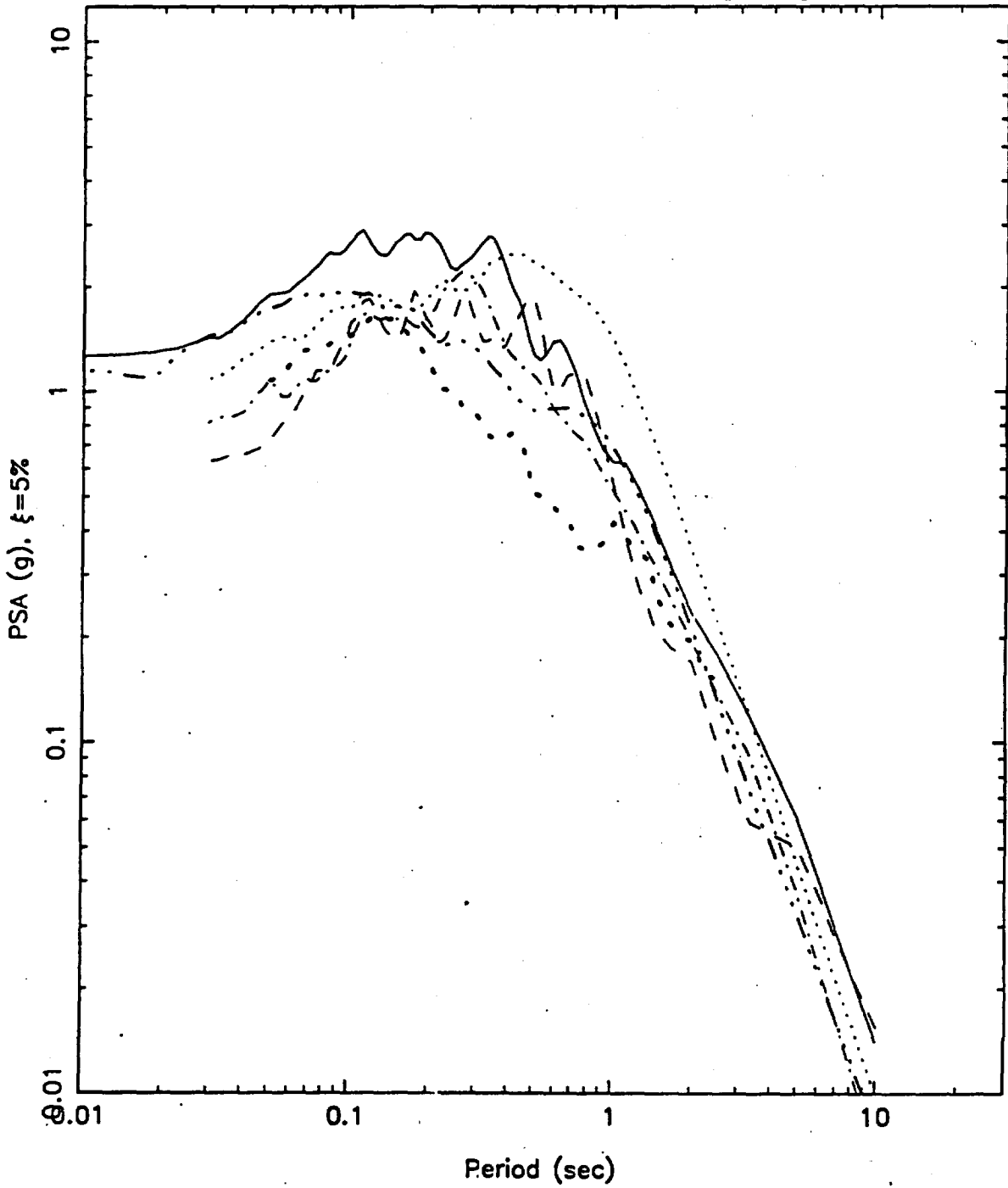


Figure 8.3 (a)

n01, STATION # 7

- \_\_\_\_\_ : mean of N01PEA07.PSV, [N=30]
- : mean of n01usc07.hpsv, [N=27]
- .-.-.-.- : mean of N01unr07.hpsv, [N=30]
- ..... : mean of N01wcc07.hpsv, [N=30]
- .-.-.-.- : mean of n01usg07.hpsv, [N=30]
- ..... : mean of n01scu07.hpsv, [N= 1]

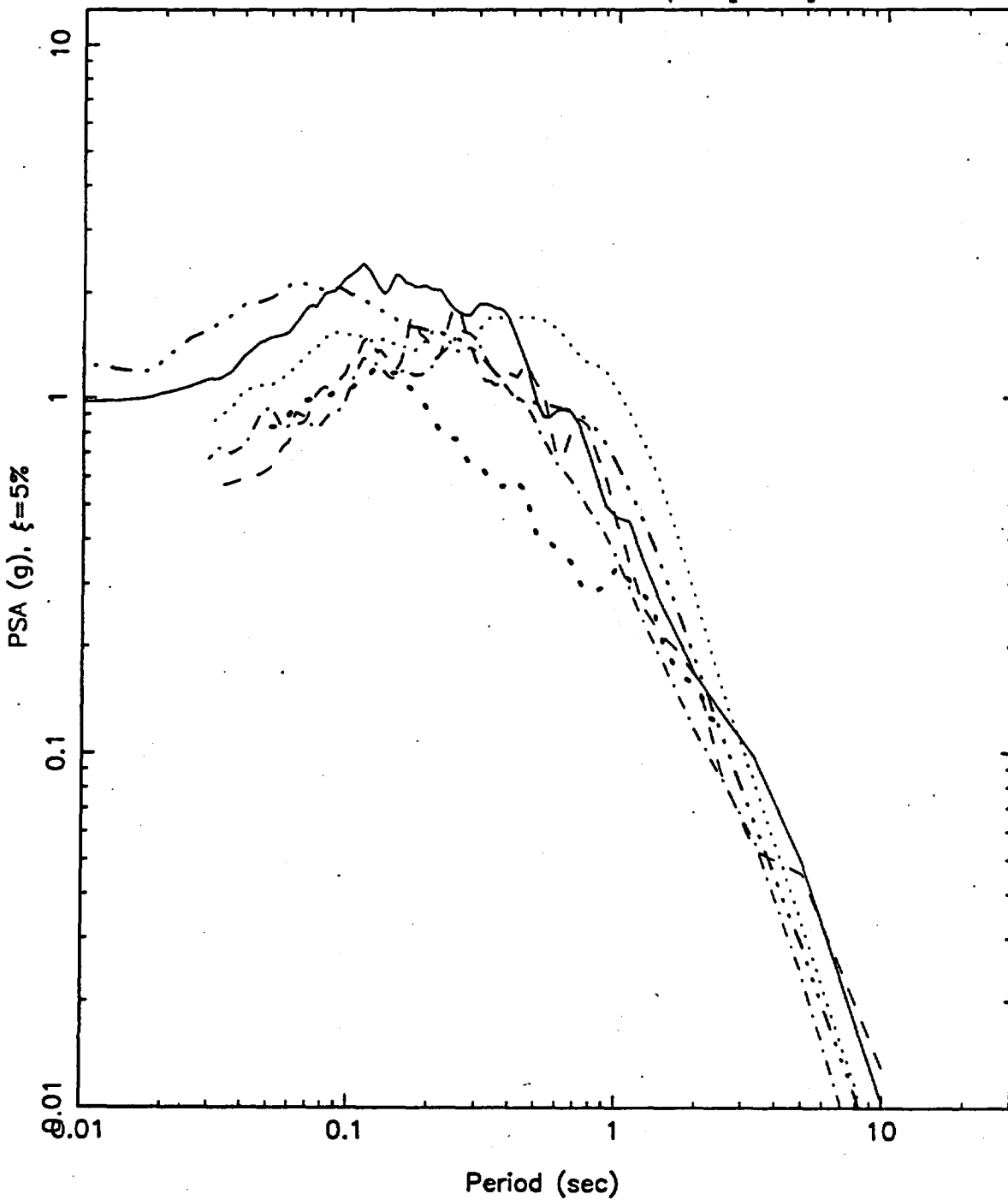


Figure 8.3 (d)

n01, STATION # 4

- \_\_\_\_\_ : mean of N01PEA04.PSV, [N=30]
- : mean of n01usc04.hpsv, [N=27]
- ..... : mean of N01unr04.hpsv, [N=30]
- ..... : mean of N01wcc04.hpsv, [N=30]
- . . . . : mean of n01usg04.hpsv, [N=30]
- ..... : mean of n01scu04.hpsv, [N= 1]

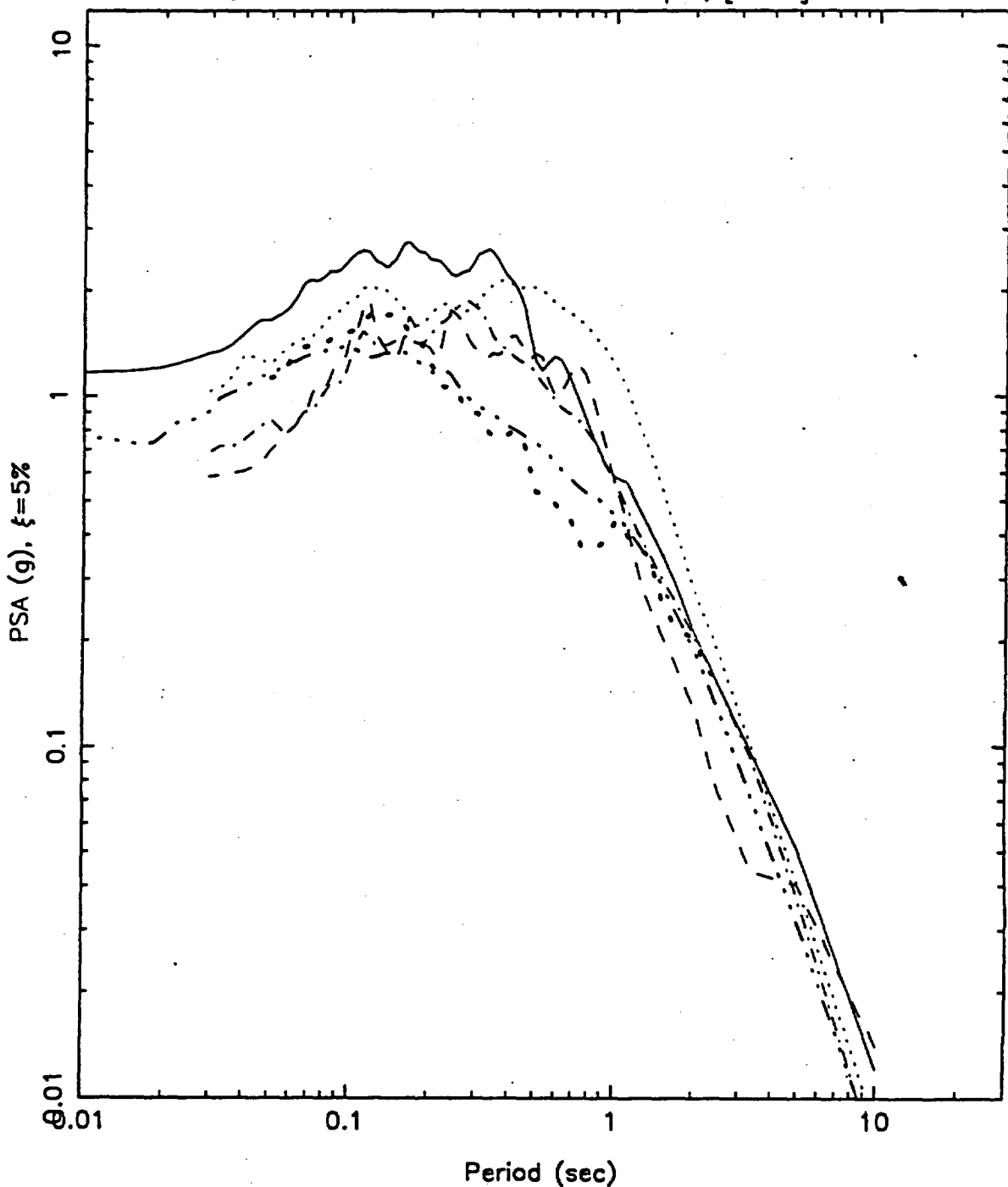


Figure 8 3 (b)

n01, STATION # 5

- \_\_\_\_\_ : mean of N01PEA05.PSV, [N=30]
- : mean of n01usc05.hpsv, [N=27]
- - - - - : mean of N01unr05.hpsv, [N=30]
- ..... : mean of N01wcc05.hpsv, [N=30]
- . - . - : mean of n01usg05.hpsv, [N=30]
- ..... : mean of n01scu05.hpsv, [N= 1]

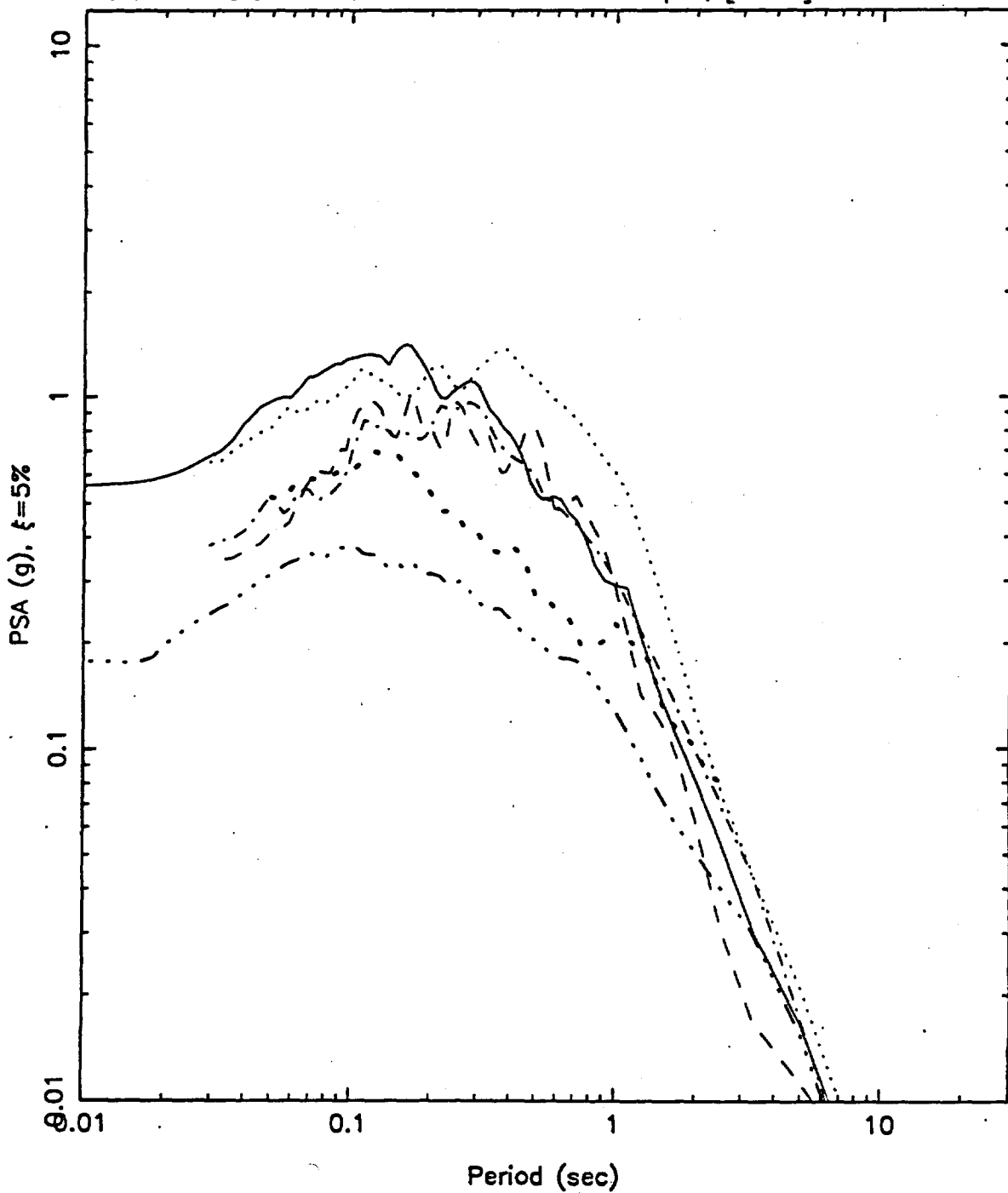
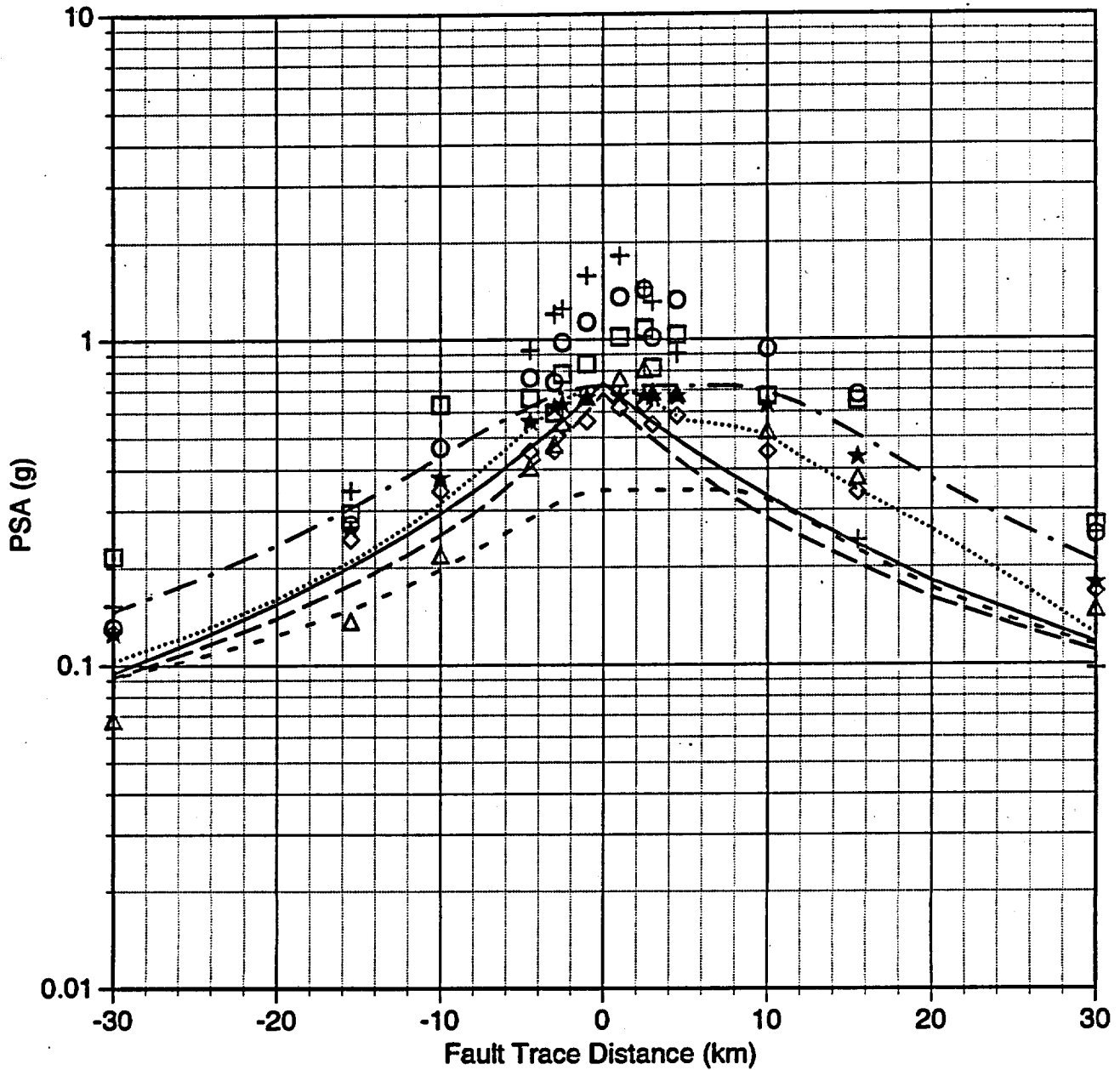


Figure 83 (c)

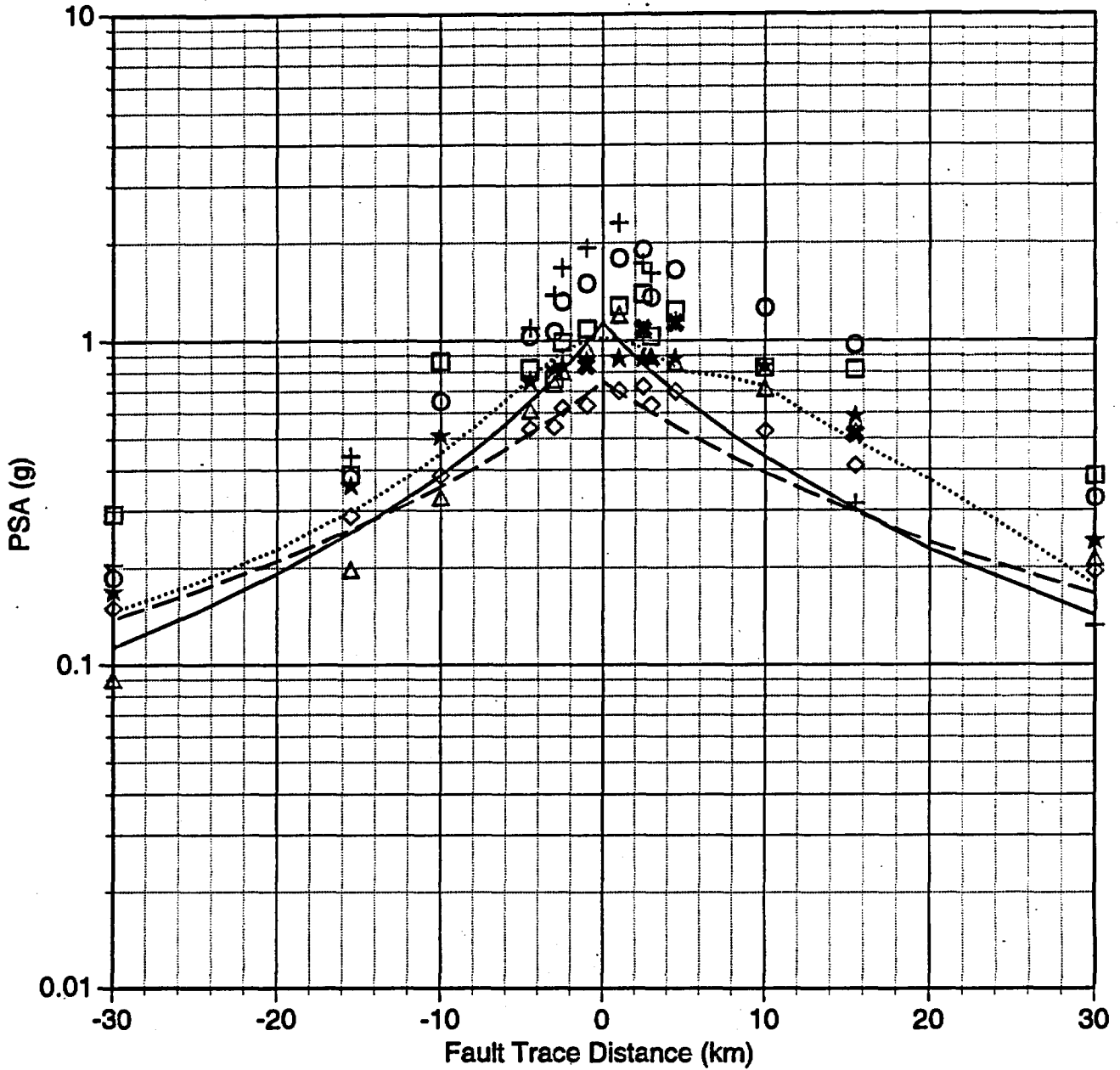
**M 6.4 Normal Fault (N01)**  
**Spectral Acceleration vs Distance (34.0 Hz)**



|         |                     |   |                      |
|---------|---------------------|---|----------------------|
| —       | Sadigh 93           | △ | 34 Hz UNR            |
| - - -   | Idriss 91;94        | ◇ | 34 Hz USC            |
| - - - - | BJT (B) 94          | □ | 34 Hz WCC            |
| .....   | Abrahamson&Silva 95 | + | 34 Hz USGS           |
| - . -   | EPRI (EUS) 93       | ★ | 34 Hz, Pt 50 bar h=6 |
| ○       | 34 Hz PEA           | ✖ | 34 Hz, S-cubed       |

Figure 8.4 (a)

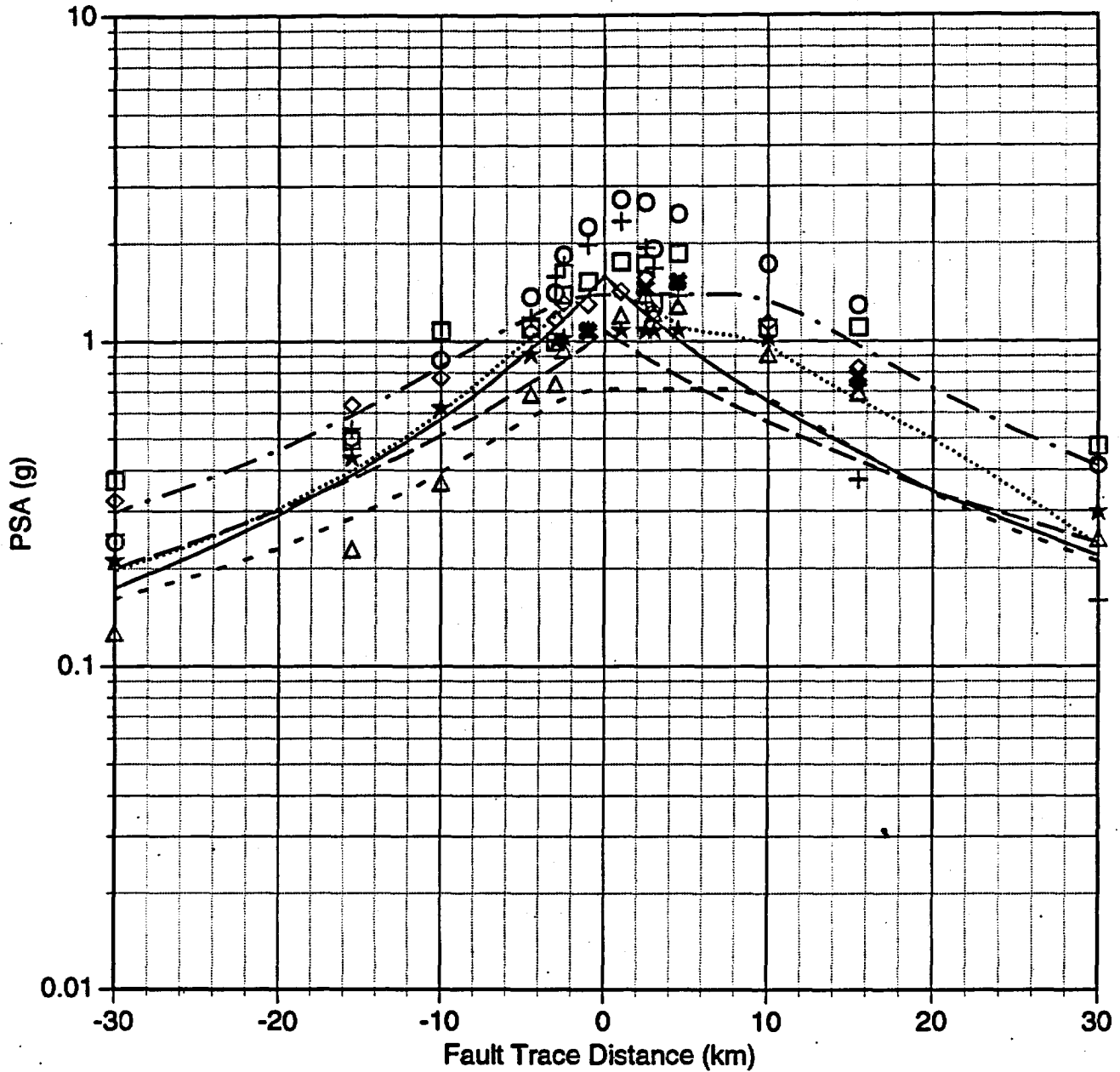
### M 6.4 Normal Fault (NO1) Spectral Acceleration vs Distance (20.0 Hz)



|           |                     |   |                      |
|-----------|---------------------|---|----------------------|
| —————     | Sadigh 93           | △ | 20 Hz UNR            |
| - - - - - | Idriss 91;94        | ◇ | 20 Hz USC            |
| - . - . - | BJJF (B) 94         | □ | 20 Hz WCC            |
| .....     | Abrahamson&Silva 95 | + | 20 Hz USGS           |
| - . - . - | EPRI (EUS) 93       | ★ | 20 Hz, Pt 50 bar h=6 |
| ○         | 20 Hz PEA           | ✱ | 20 Hz, S-cubed       |

Figure 7.4(b)

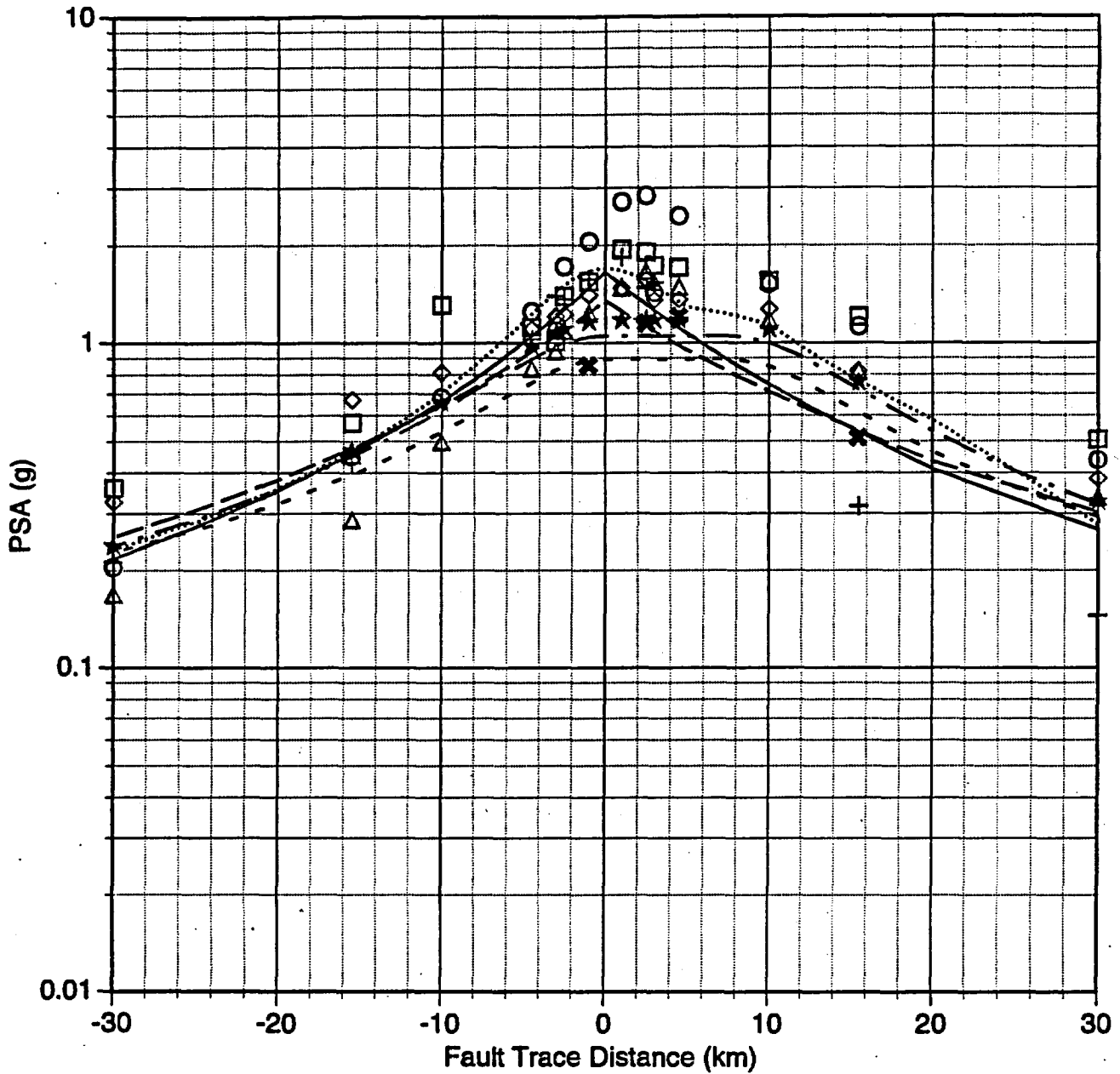
M 6.4 Normal Fault (NO1)  
Spectral Acceleration vs Distance (10.0 Hz)



|         |                     |   |                      |
|---------|---------------------|---|----------------------|
| —       | Sadigh 93           | △ | 10 Hz UNR            |
| - - -   | Idriss 91;94        | ◇ | 10 Hz USC            |
| - - - - | BJF (B) 94          | □ | 10 Hz WCC            |
| .....   | Abrahamson&Silva 95 | + | 10 Hz USGS           |
| - . -   | EPRI (EUS) 93       | ★ | 10 Hz, Pt 50 bar h=6 |
| ○       | 10 Hz PEA           | ✱ | 10 Hz, S-cubed       |

Figure 8.4 (c)

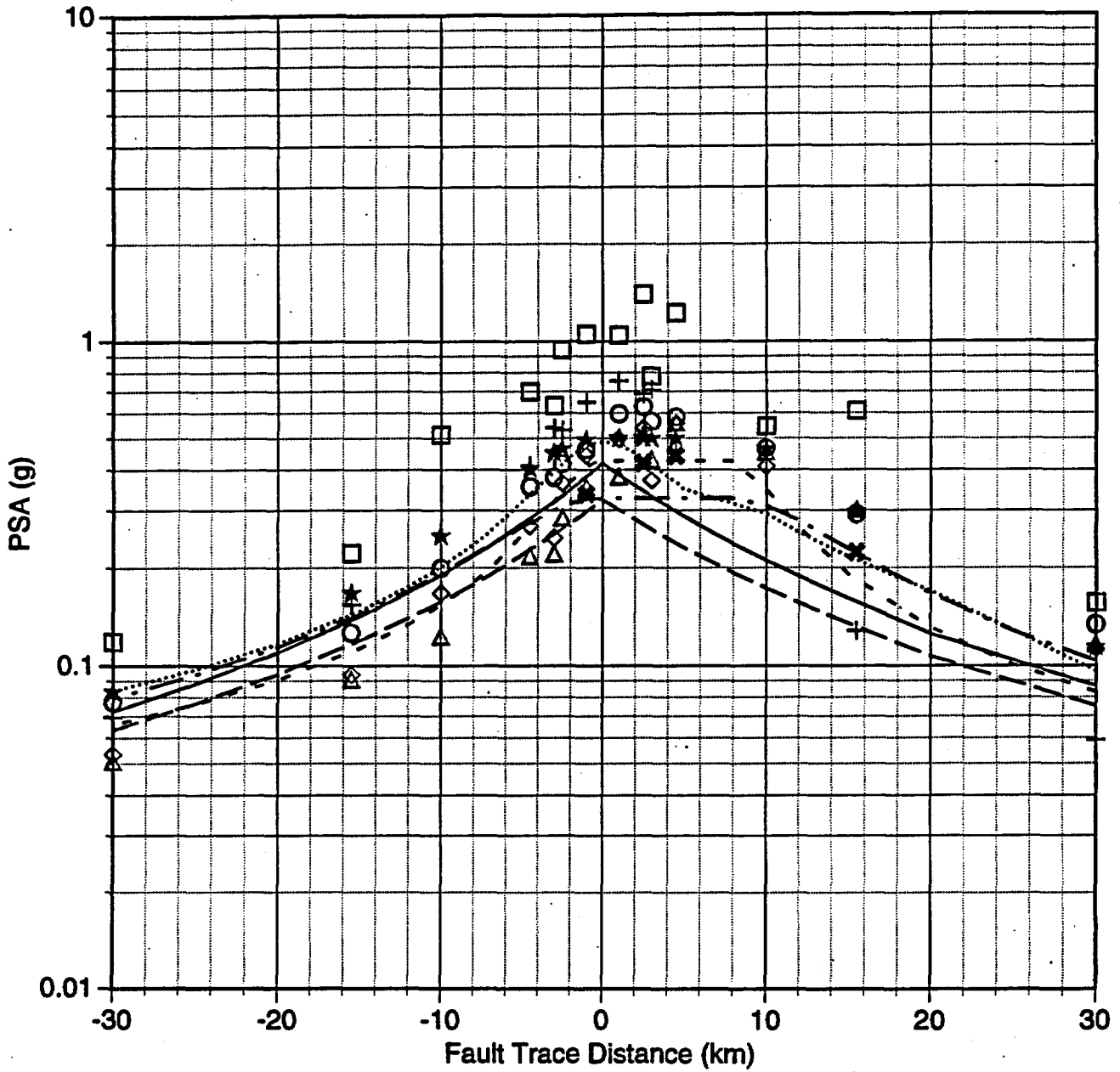
**M 6.4 Normal Fault (NO1)  
Spectral Acceleration vs Distance (5.0 Hz)**



|           |                     |   |                     |
|-----------|---------------------|---|---------------------|
| —         | Sadigh 93           | △ | 5 Hz UNR            |
| - - -     | Idriss 91;94        | ◇ | 5 Hz USC            |
| . . . . . | BJF (B) 94          | □ | 5 Hz WCC            |
| .....     | Abrahamson&Silva 95 | + | 5 Hz USGS           |
| - . - .   | EPRI (EUS) 93       | ★ | 5 Hz, Pt 50 bar h=6 |
| ○         | 5 Hz PEA            | ✱ | 5 Hz, S-cubed       |

Figure 8.4 (d)

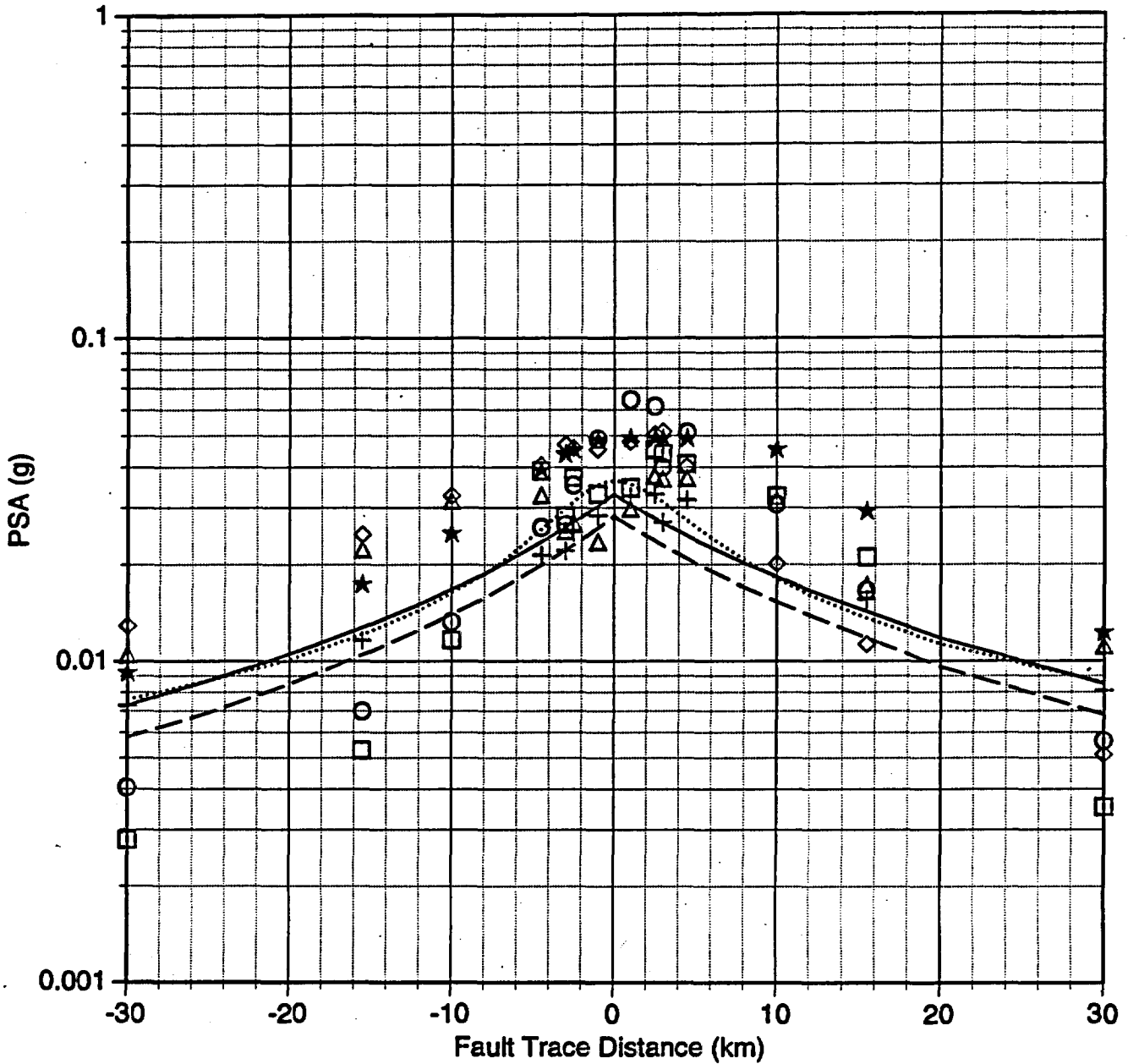
**M 6.4 Normal Fault (NO1)  
Spectral Acceleration vs Distance (1.0 Hz)**



|         |                     |   |                     |
|---------|---------------------|---|---------------------|
| —       | Sadigh 93           | △ | 1 Hz UNR            |
| - - -   | Idriss 91;94        | ◇ | 1 Hz USC            |
| - . - . | BJF (B) 94          | □ | 1 Hz WCC            |
| .....   | Abrahamson&Silva 95 | + | 1 Hz USGS           |
| - - - - | EPRI (EUS) 93       | ★ | 1 Hz, Pt 50 bar h=6 |
| ○       | 1 Hz PEA            | ✱ | 1.0 Hz, S-cubed     |

Figure 8.4 (e)

**M 6.4 Normal Fault (NO1)  
Spectral Acceleration vs Distance (0.2 Hz)**



|           |                     |   |                       |
|-----------|---------------------|---|-----------------------|
| ————      | Sadigh 93           | △ | 0.2 Hz UNR            |
| -----     | Idriss 91;94        | ◇ | 0.2 Hz USC            |
| .....     | BJT (B) 94          | □ | 0.2 Hz WCC            |
| - · - · - | Abrahamson&Silva 95 | + | 0.2 Hz USGS           |
| -----     | EPRI (EUS) 93       | ★ | 0.2 Hz, Pt 50 bar h=6 |
| ○         | 0.2 Hz PEA          | ✱ | 0.2 Hz, S-cubed       |

Figure 8.4 (A)

Yucca Mountain: NO1

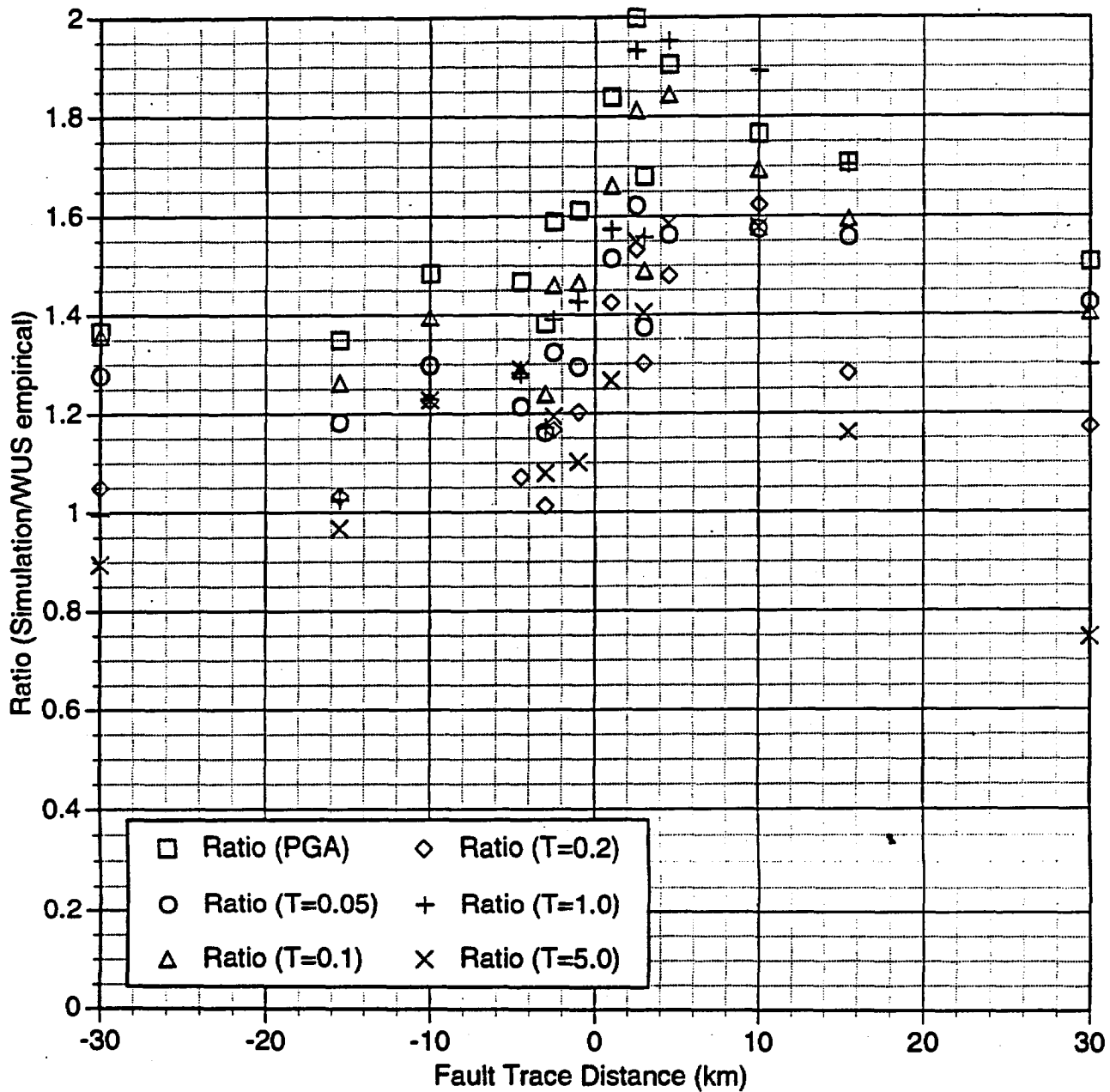


Figure 8.5

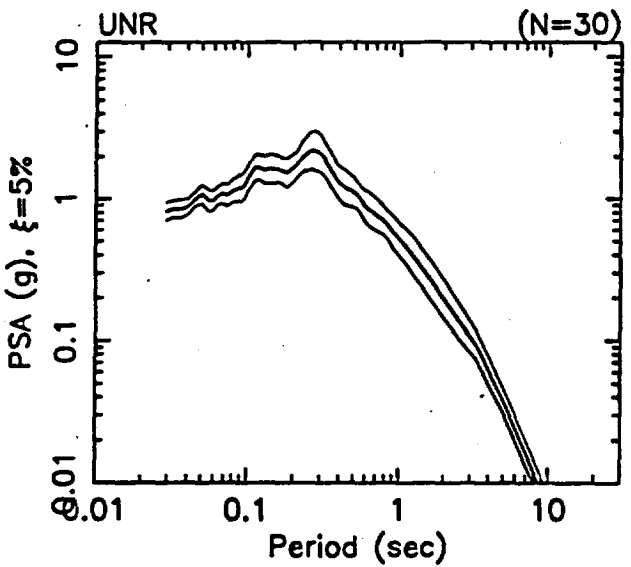
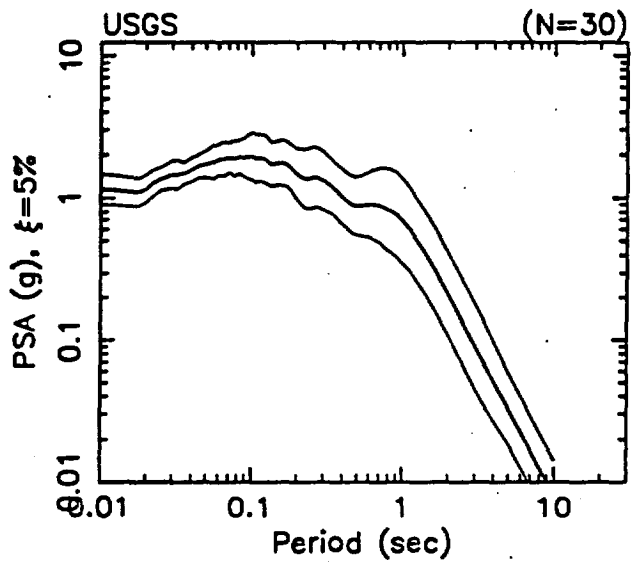
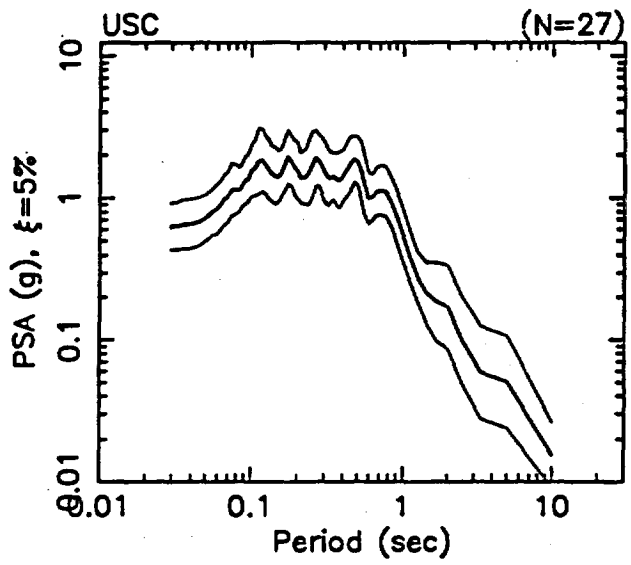
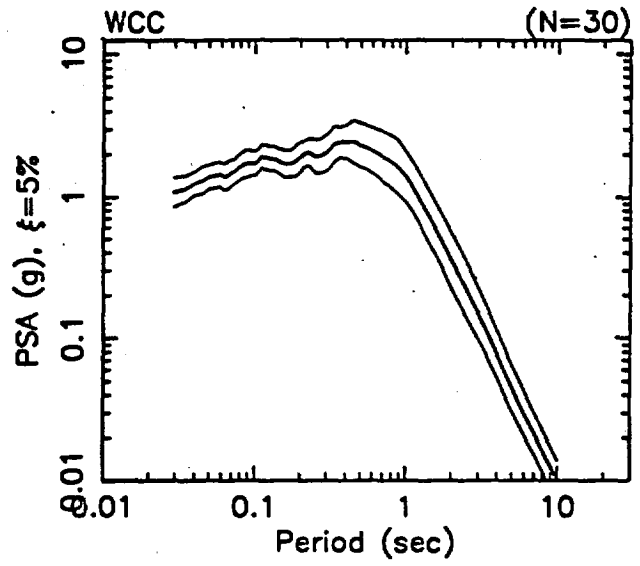
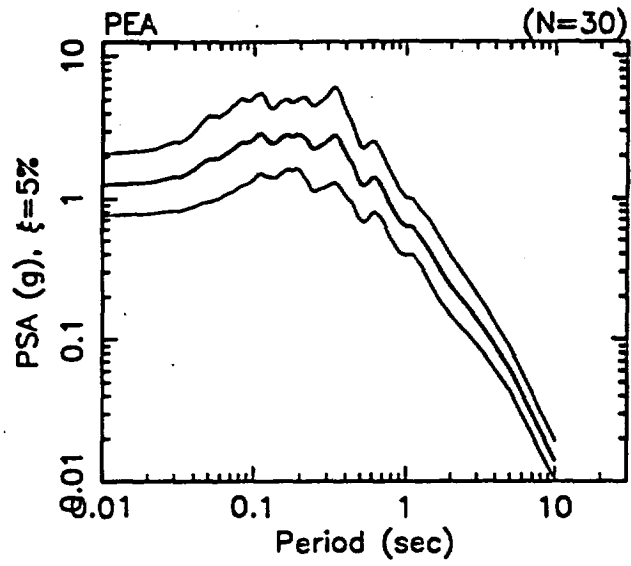


Figure 8.6

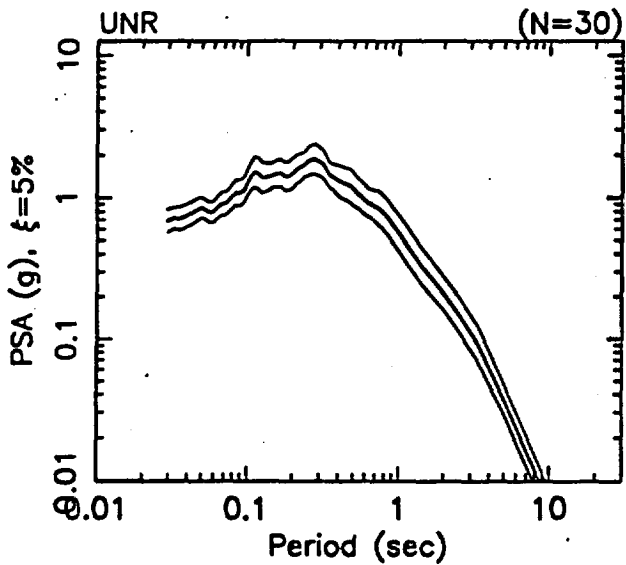
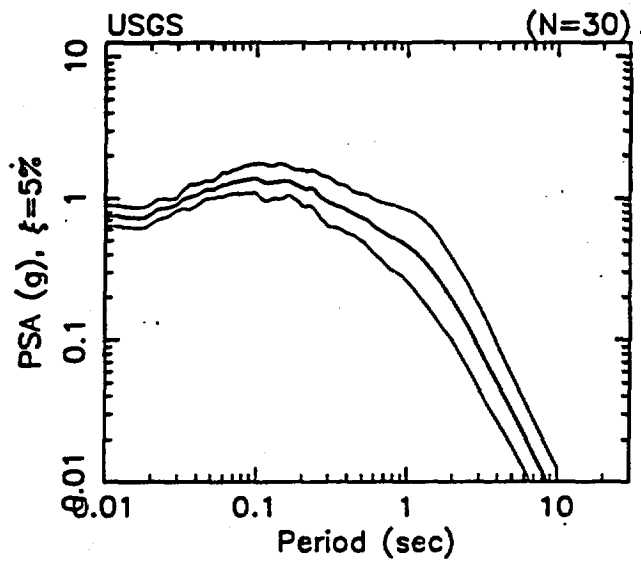
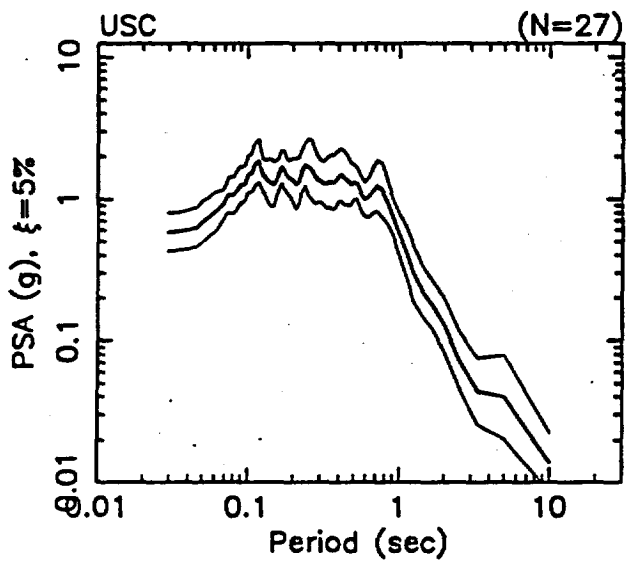
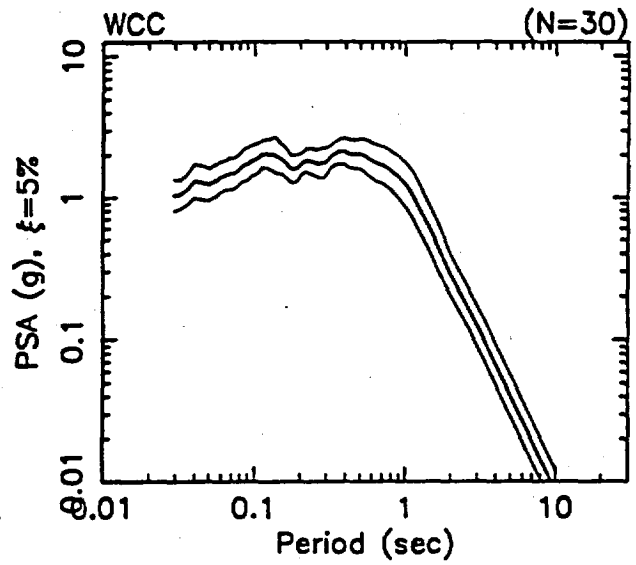
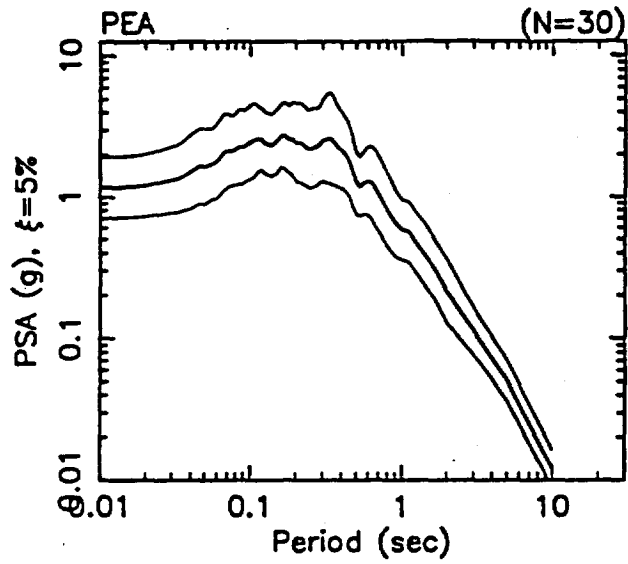


Figure 8.7

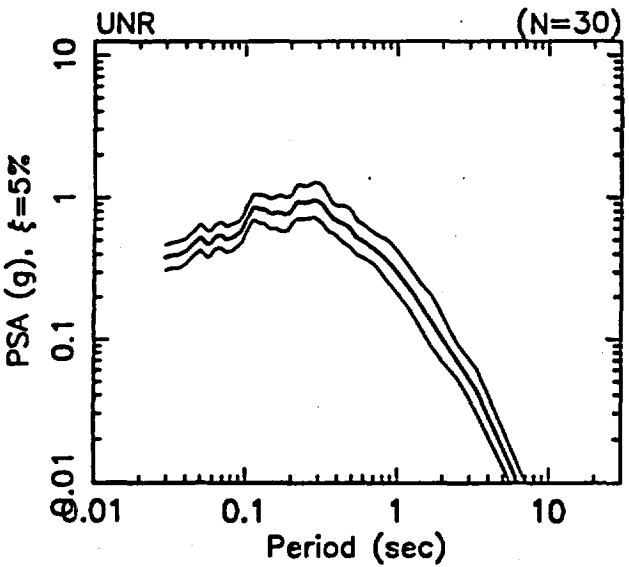
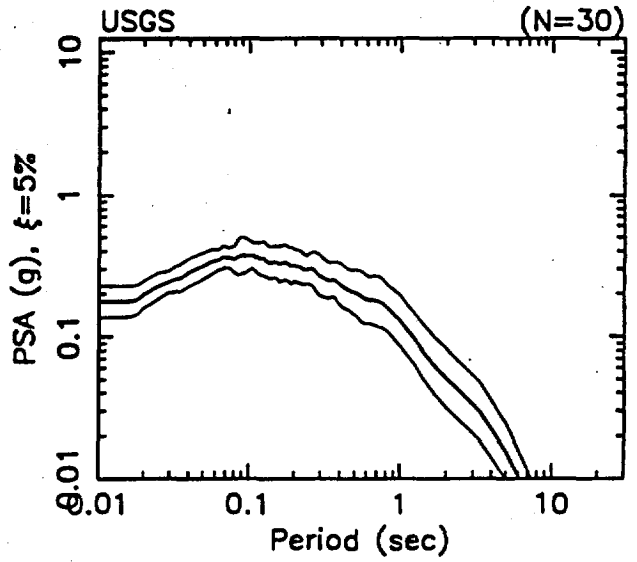
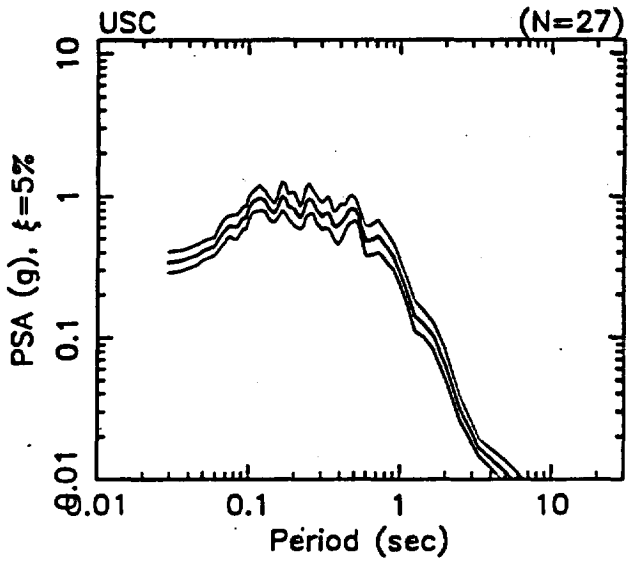
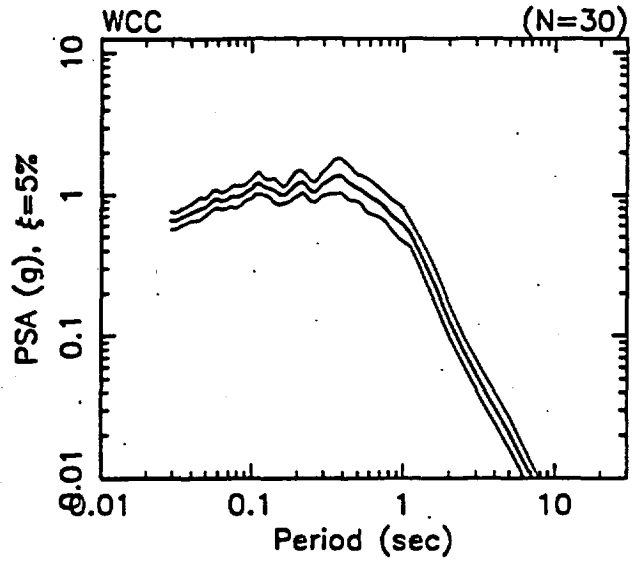
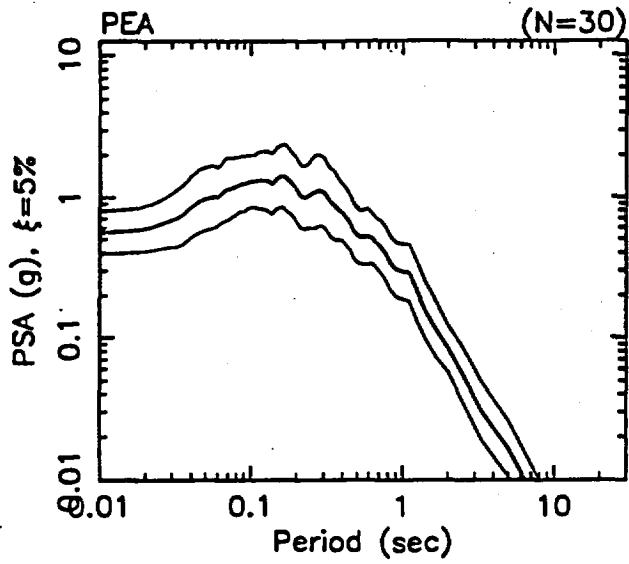


Figure 8.8

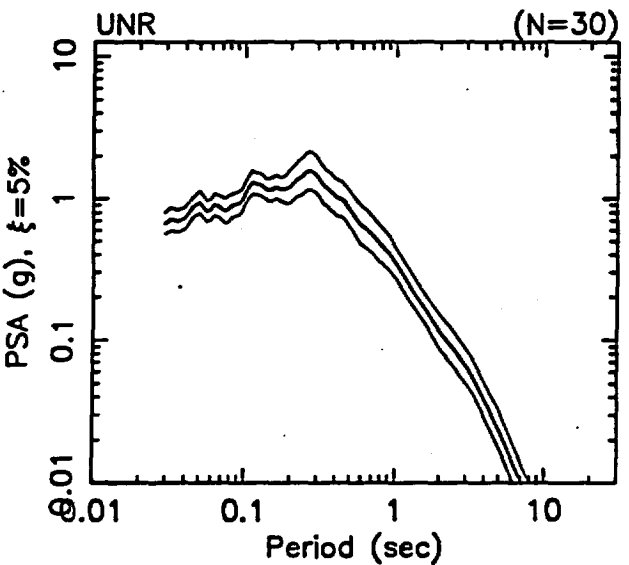
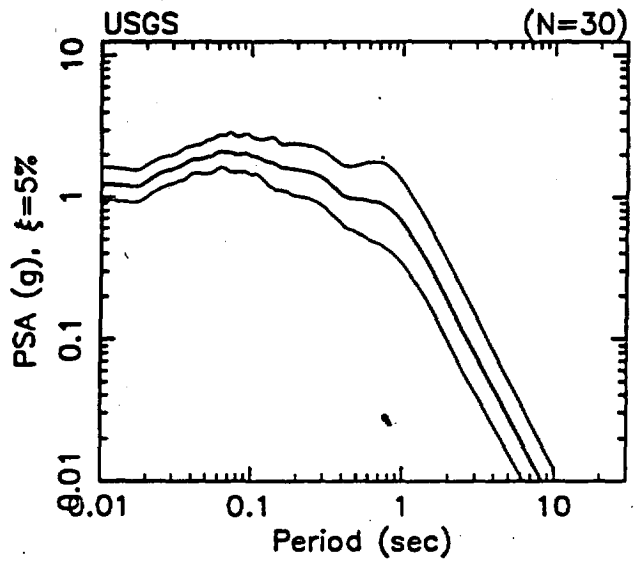
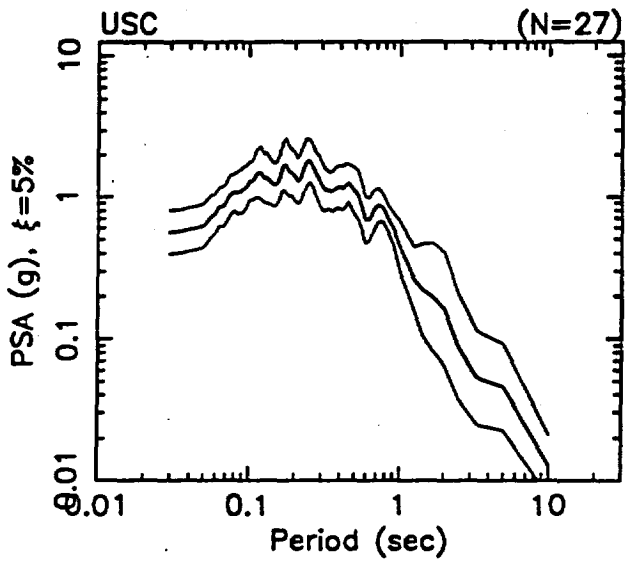
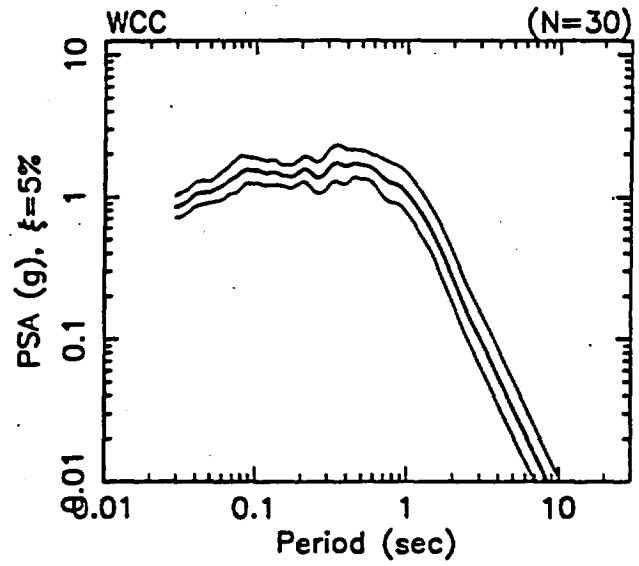
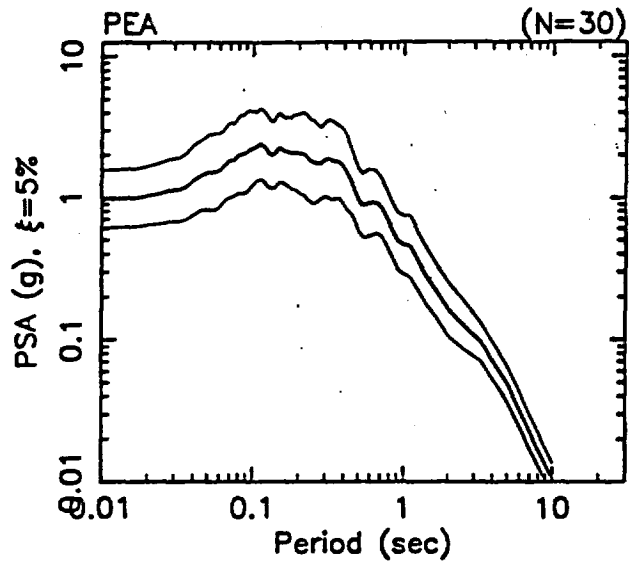
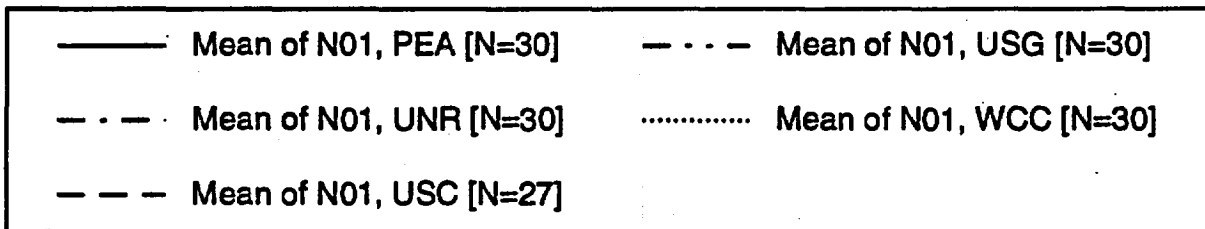
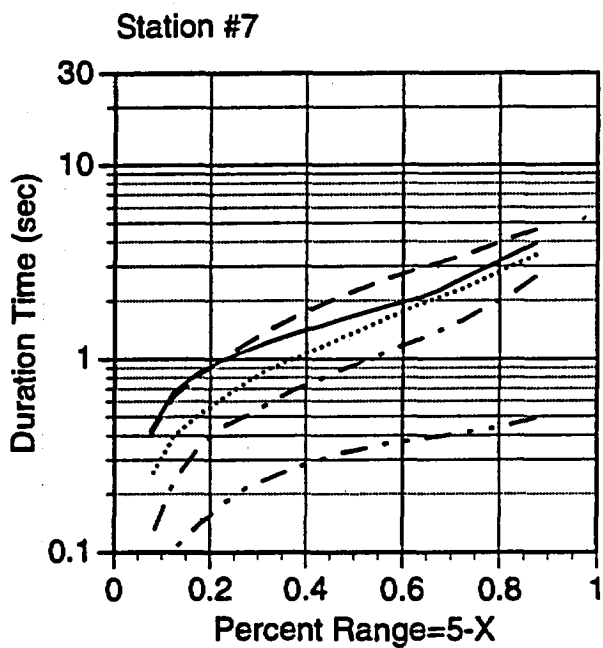
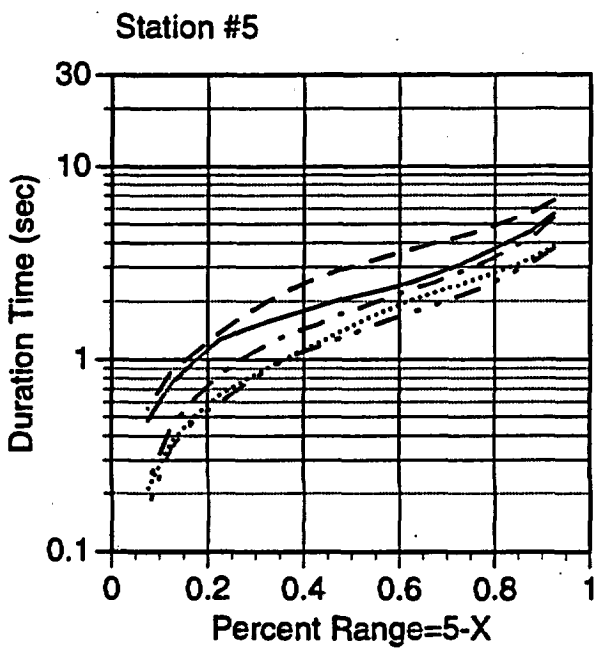
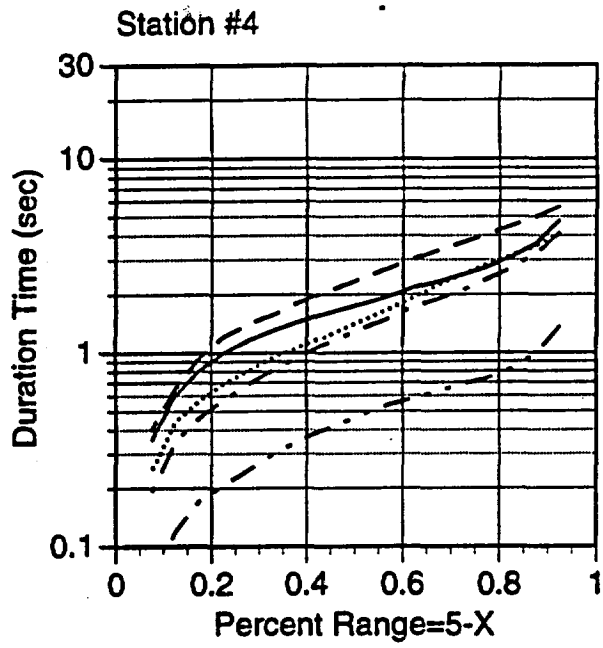
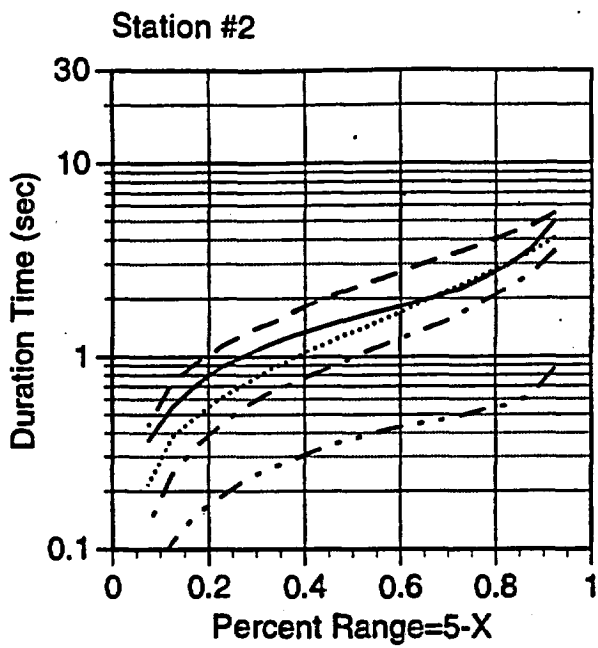


Figure 8.9



ACCELERATION DURATION

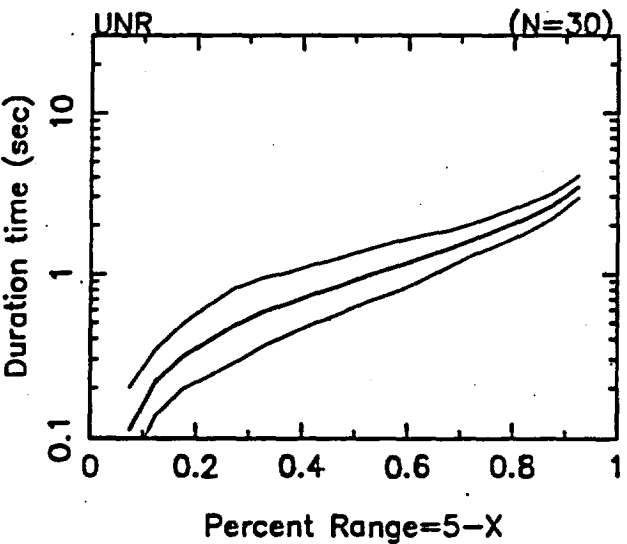
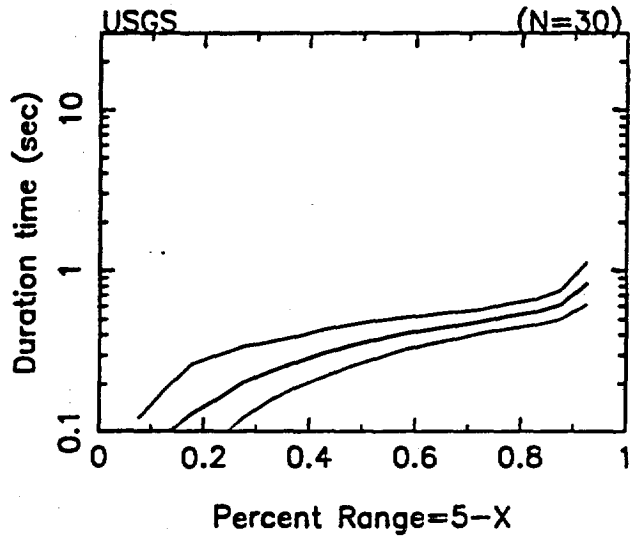
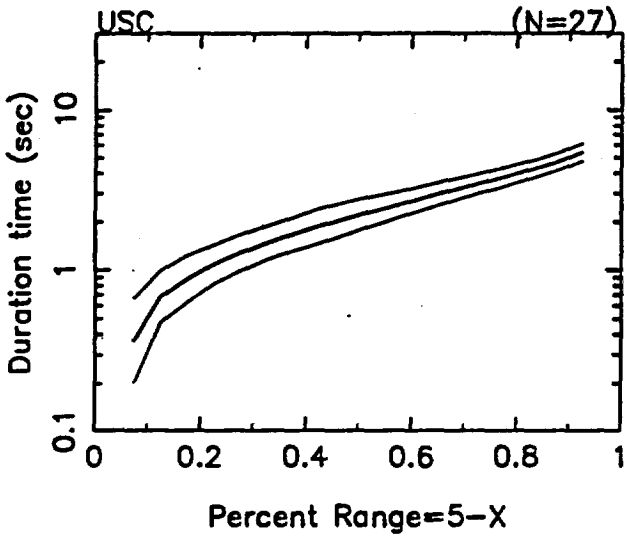
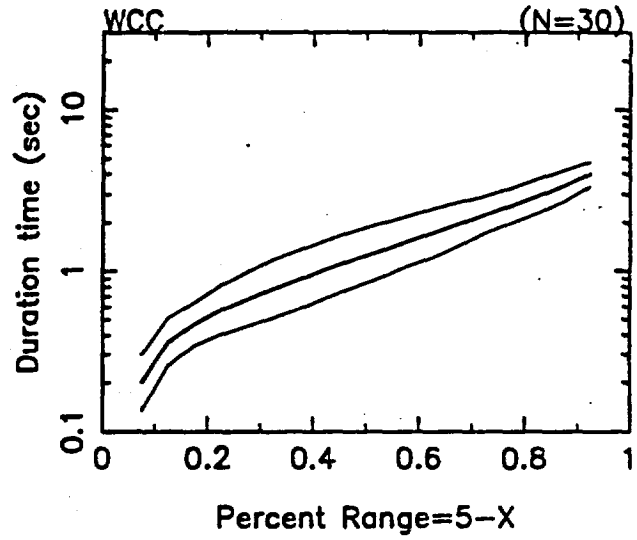
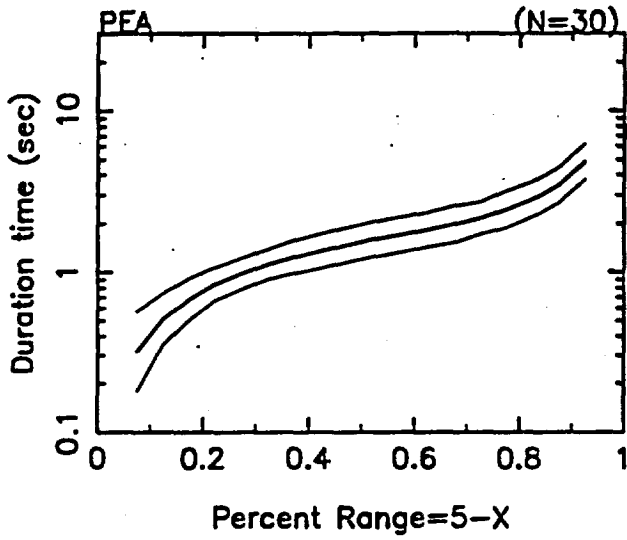


Figure 8.11

ACCELERATION DURATION

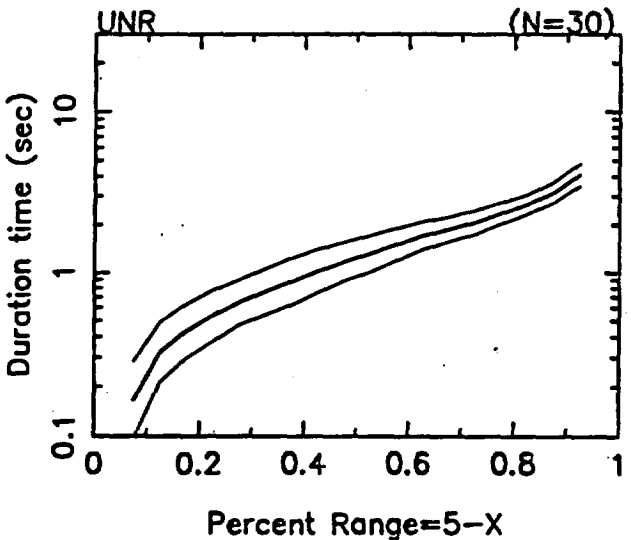
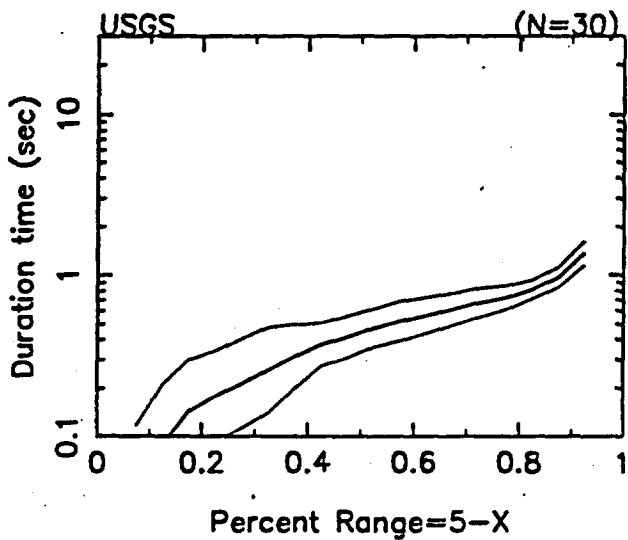
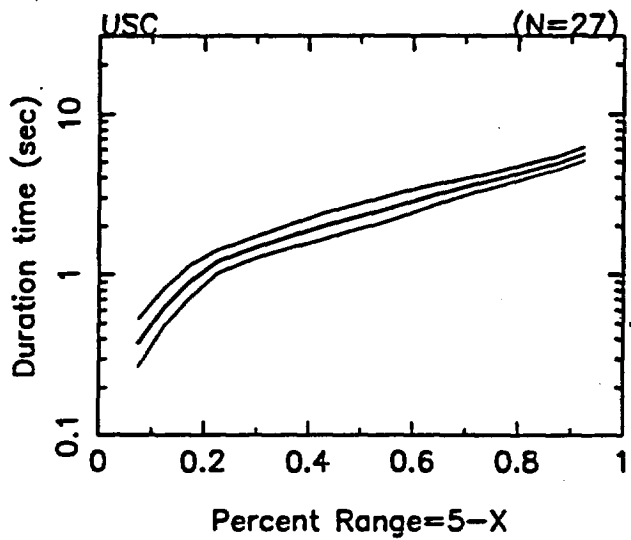
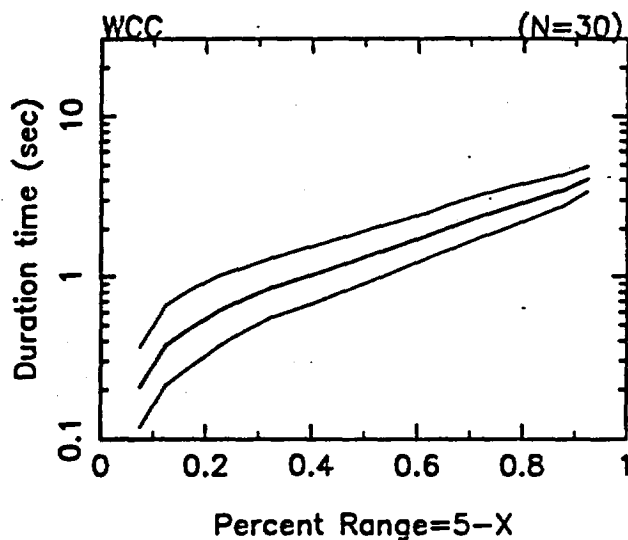
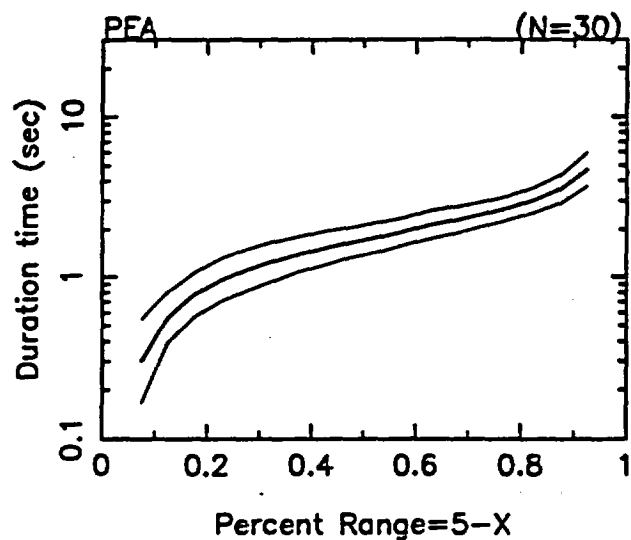


Figure 8.12

ACCELERATION DURATION

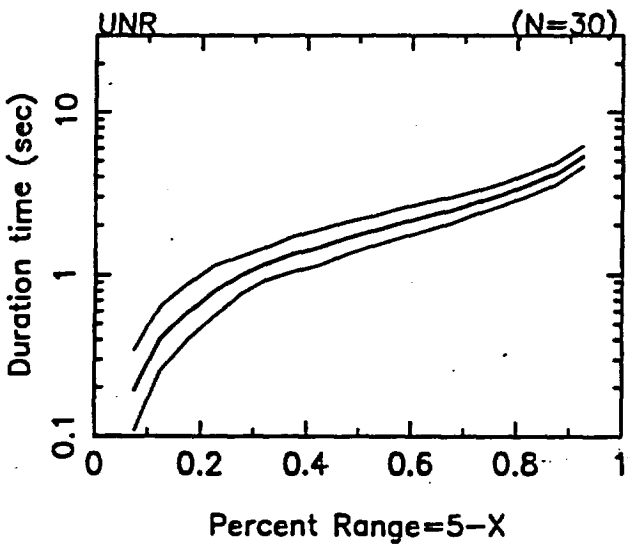
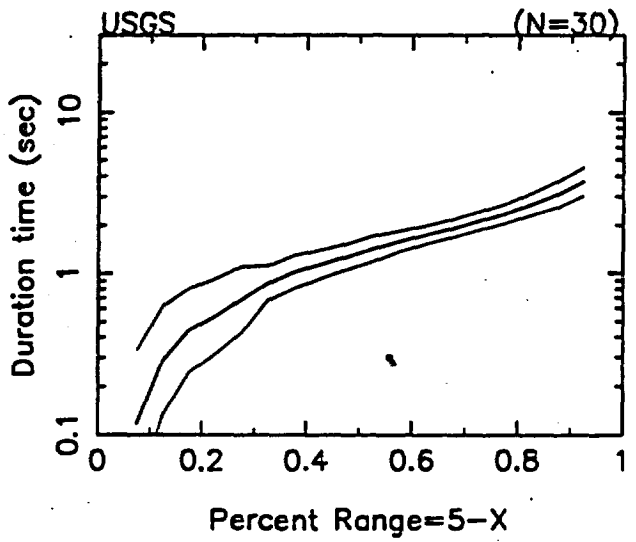
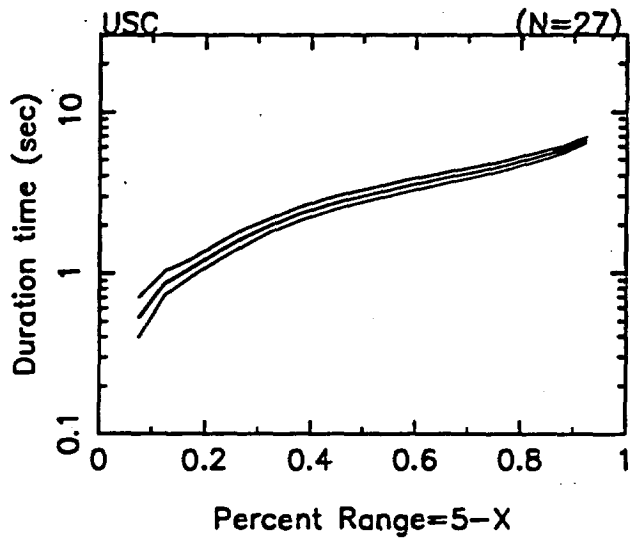
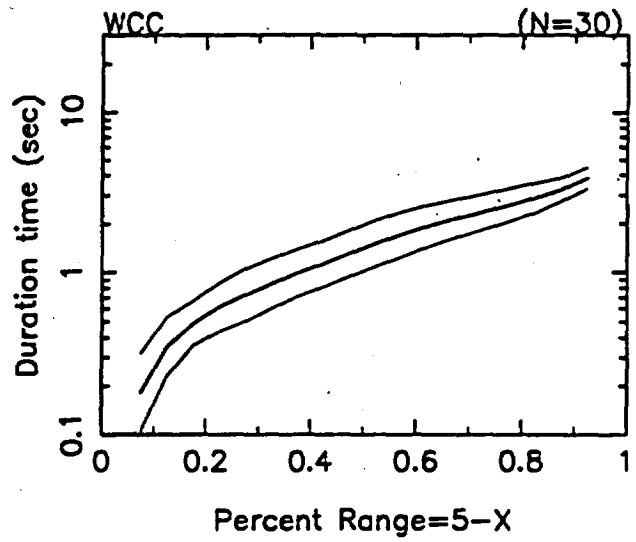
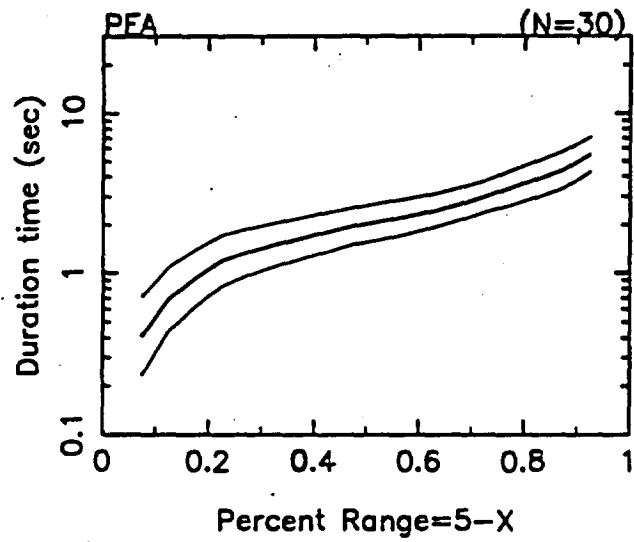


Figure 8.13

ACCELERATION DURATION

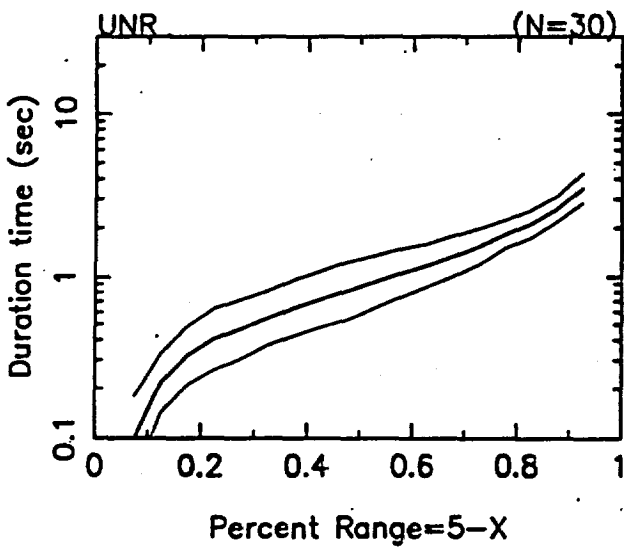
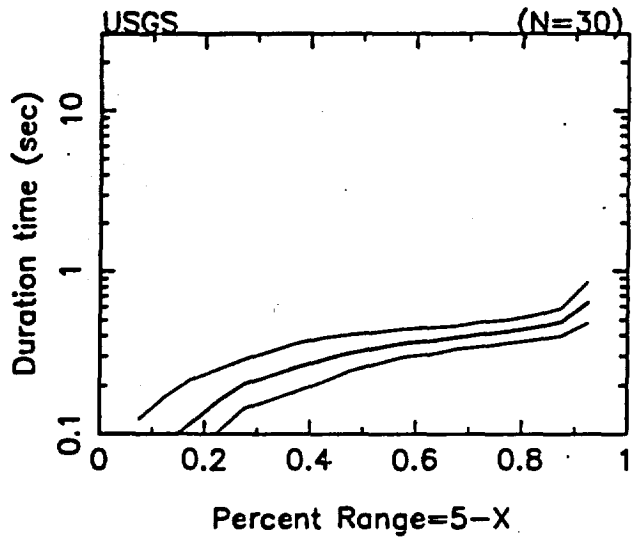
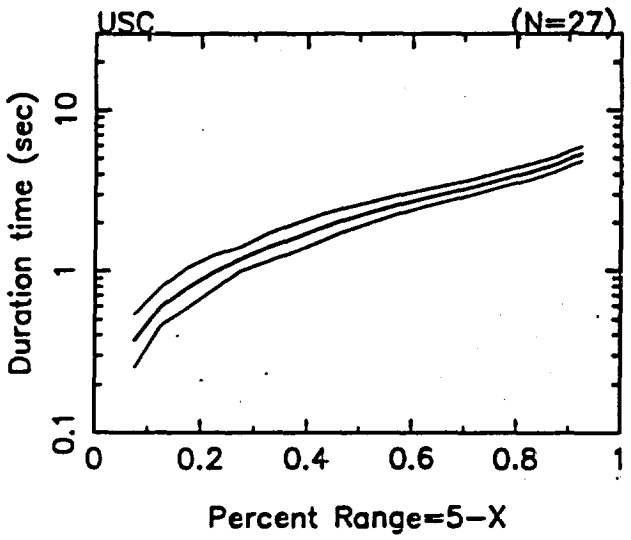
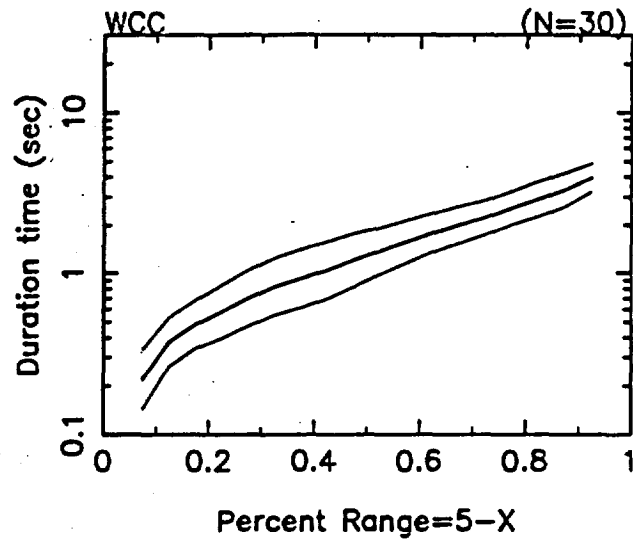
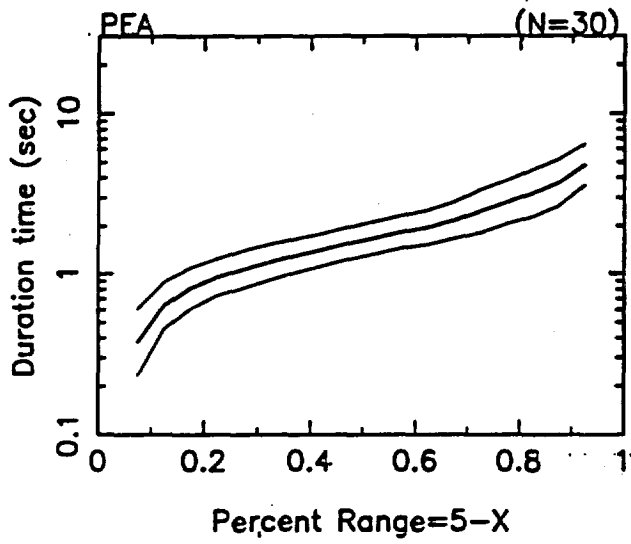


Figure 8.14

VELOCITY DURATION

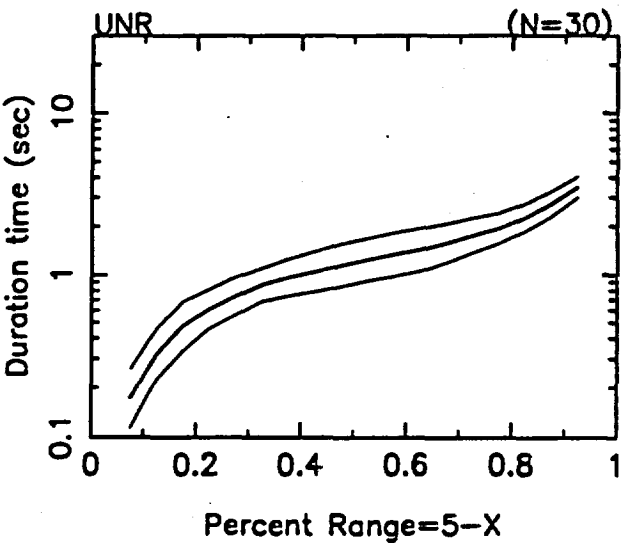
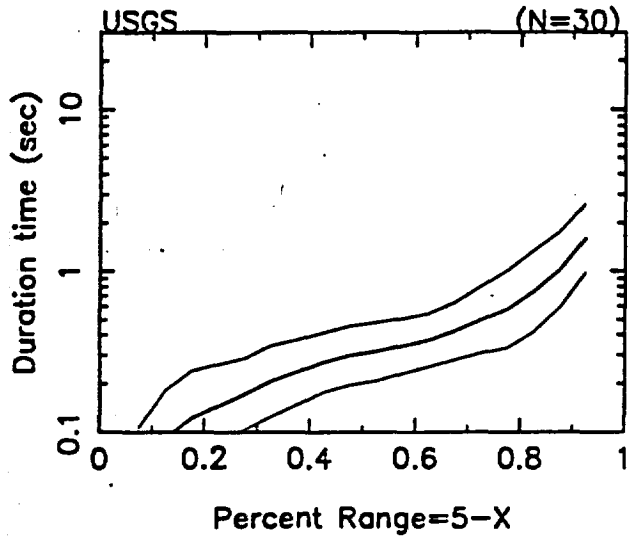
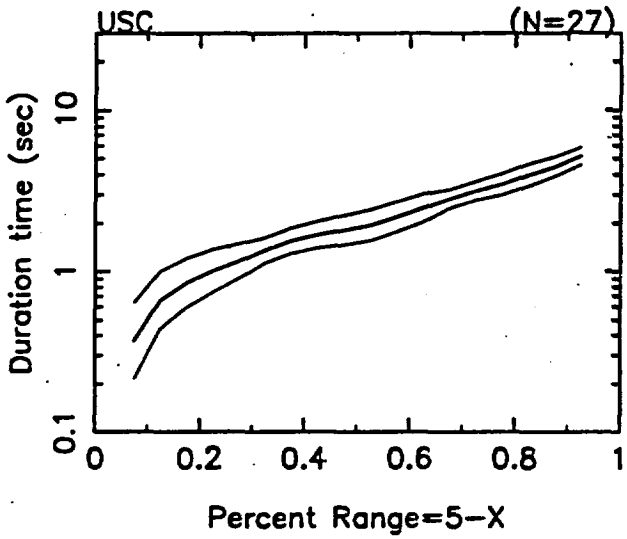
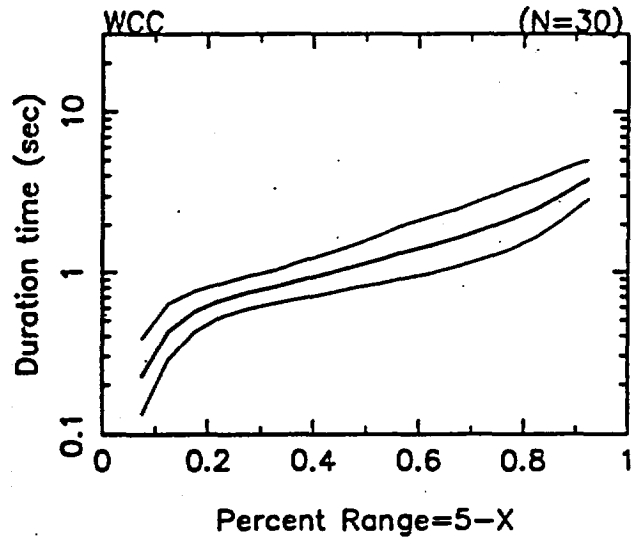
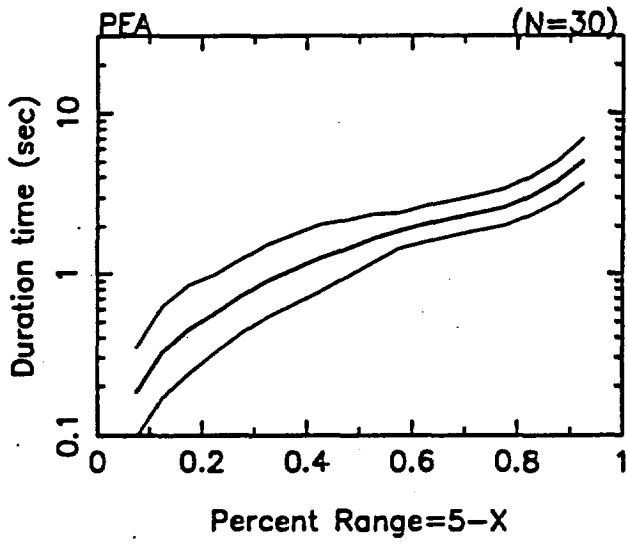


Figure 8.15

VELOCITY DURATION

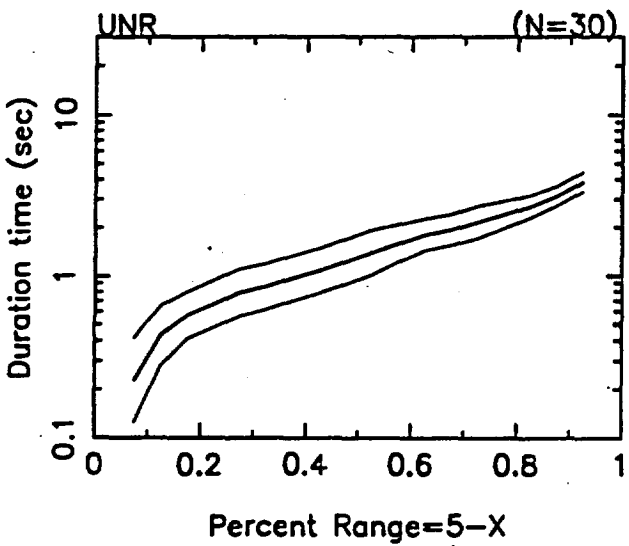
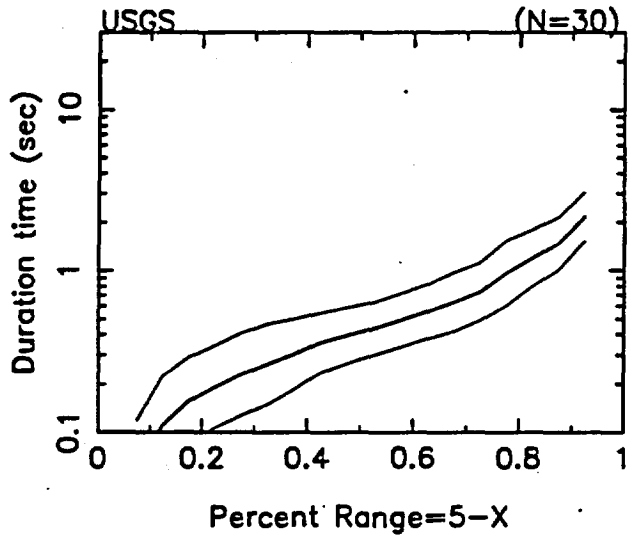
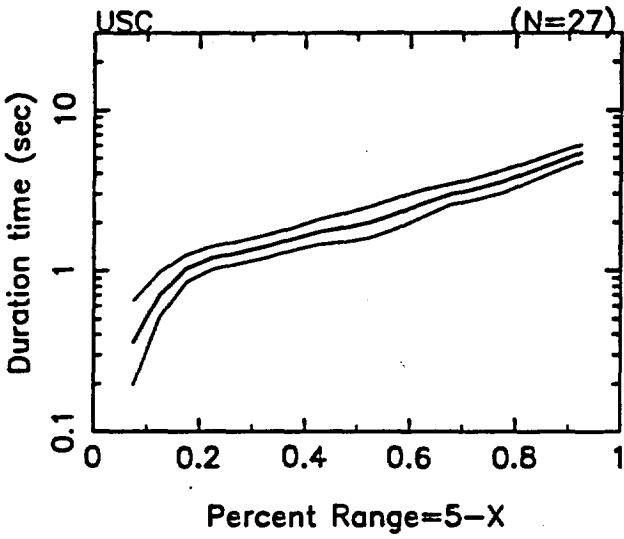
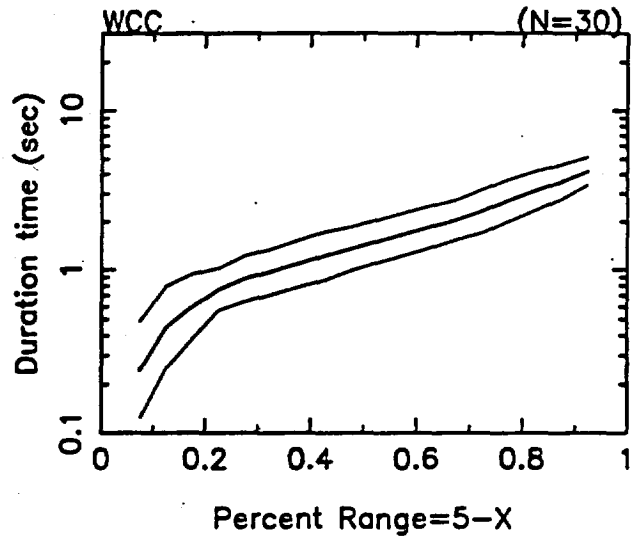
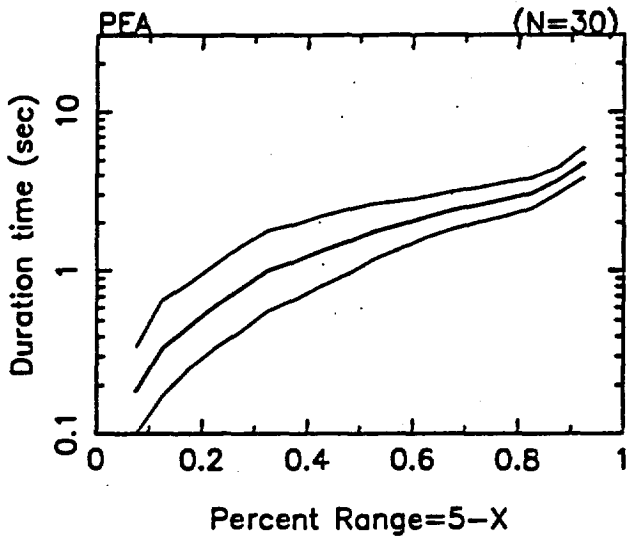


Figure 8.16

VELOCITY DURATION

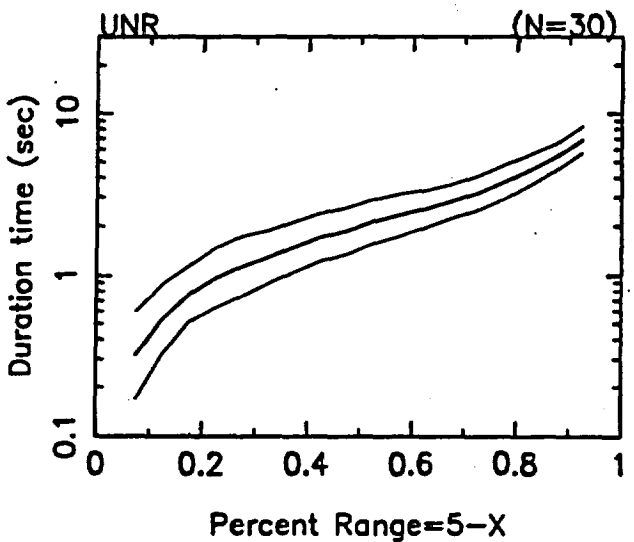
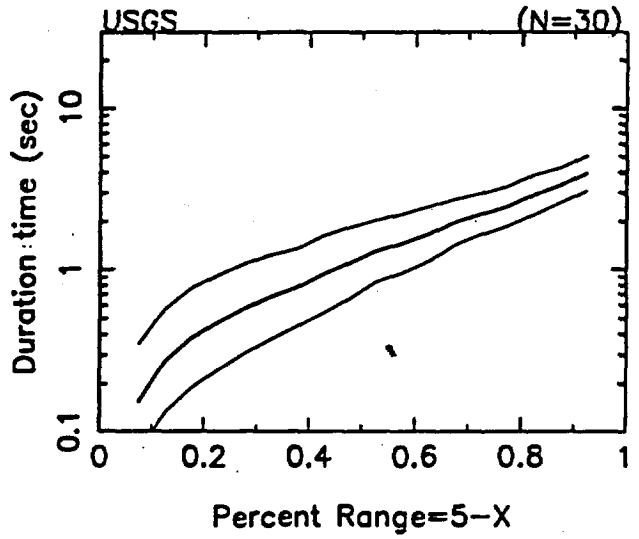
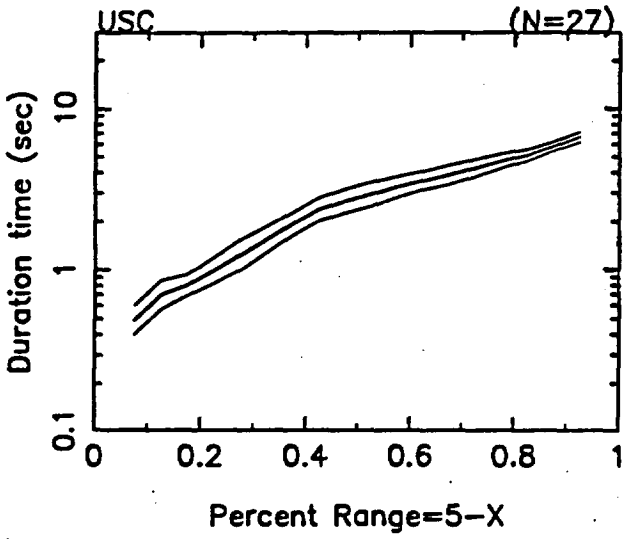
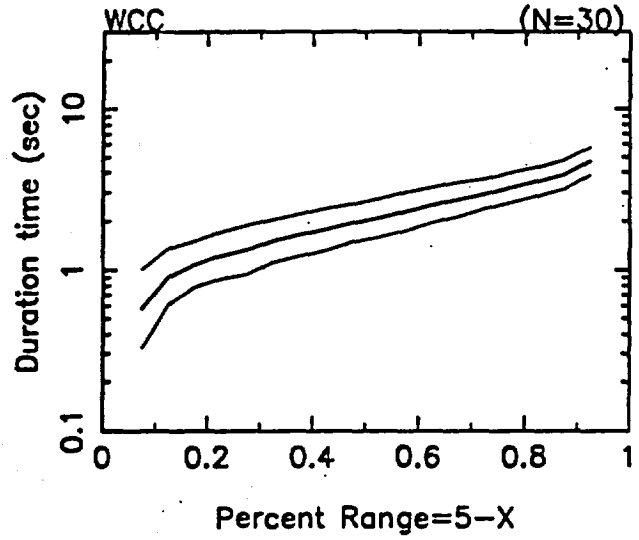
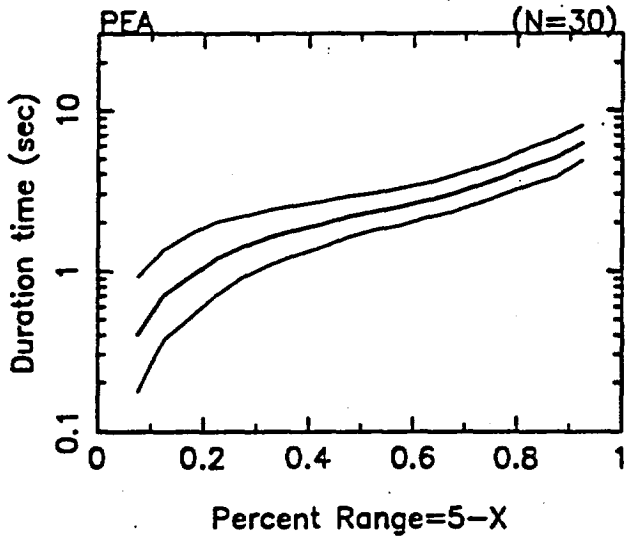


Figure 8.17

n01, STATION # 7

VELOCITY DURATION

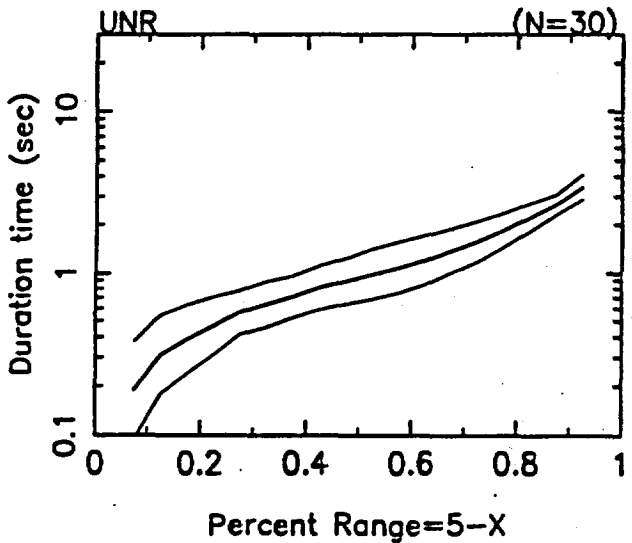
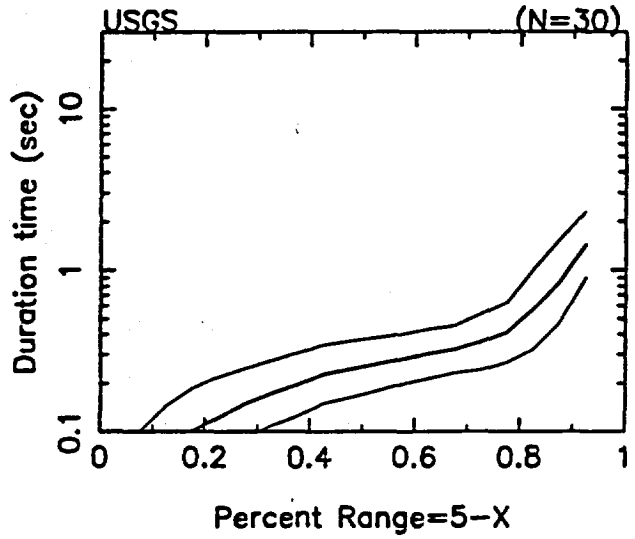
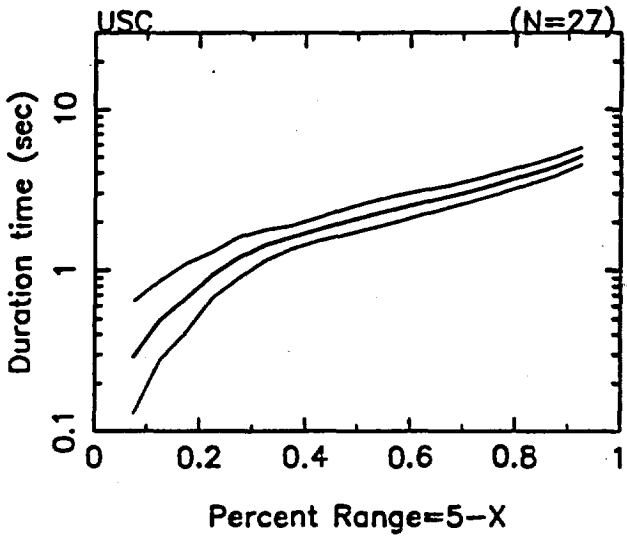
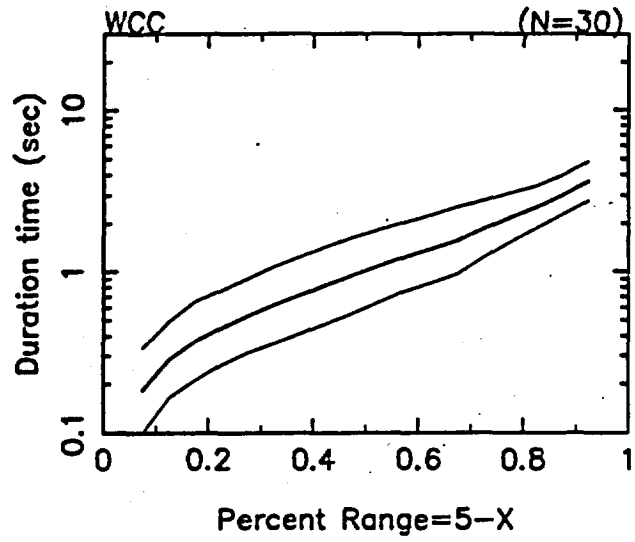
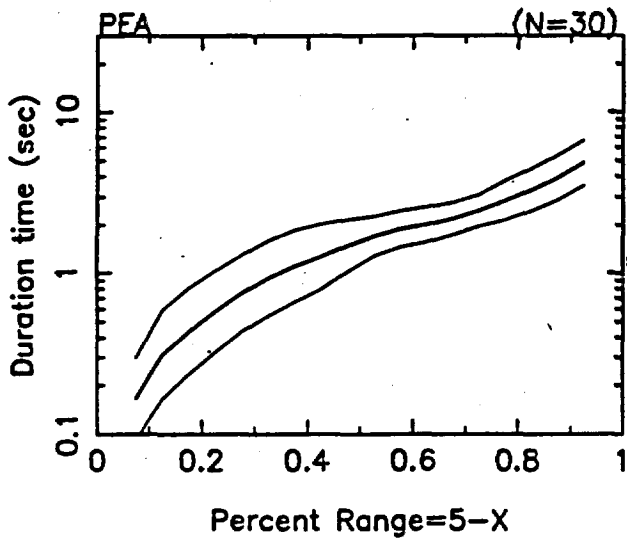
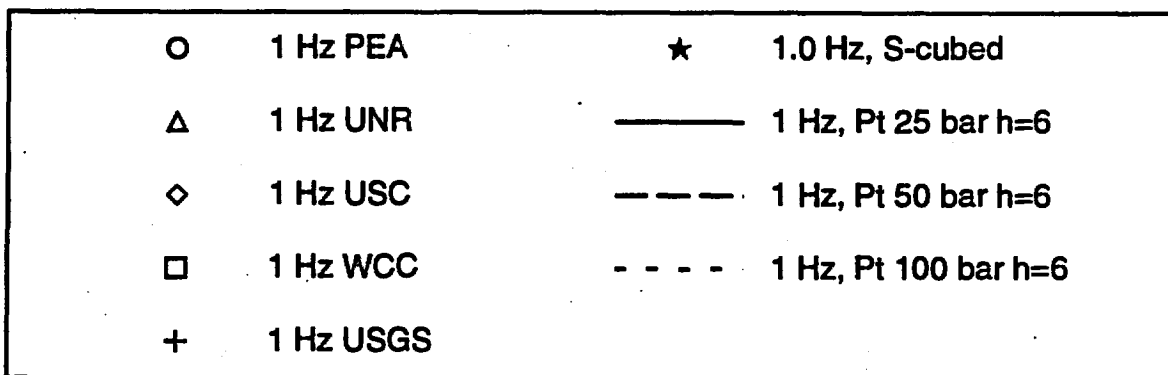
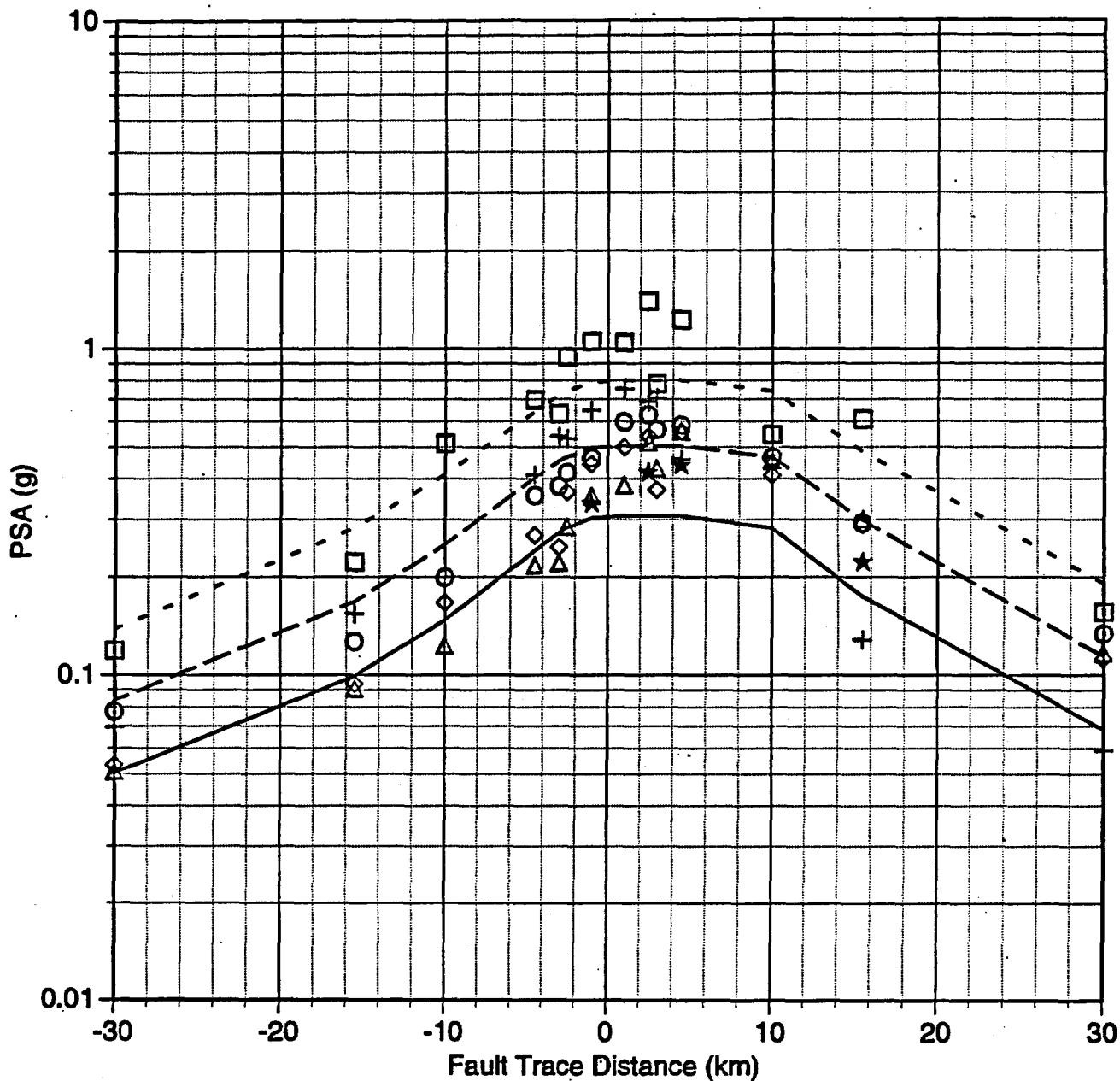
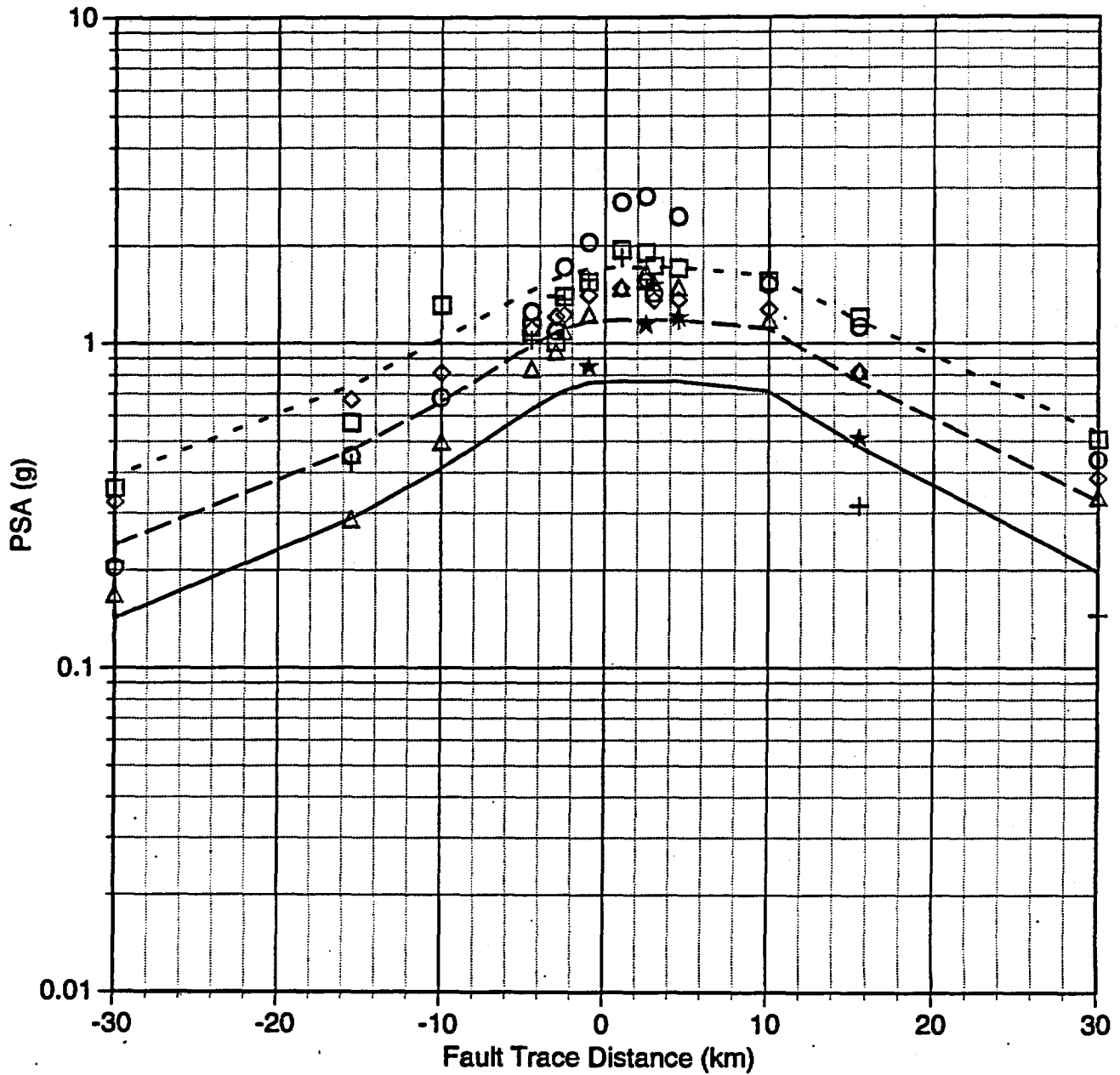


Figure 8.18

**M 6.4 Normal Fault (NO1)  
Spectral Acceleration vs Distance (1.0 Hz)**

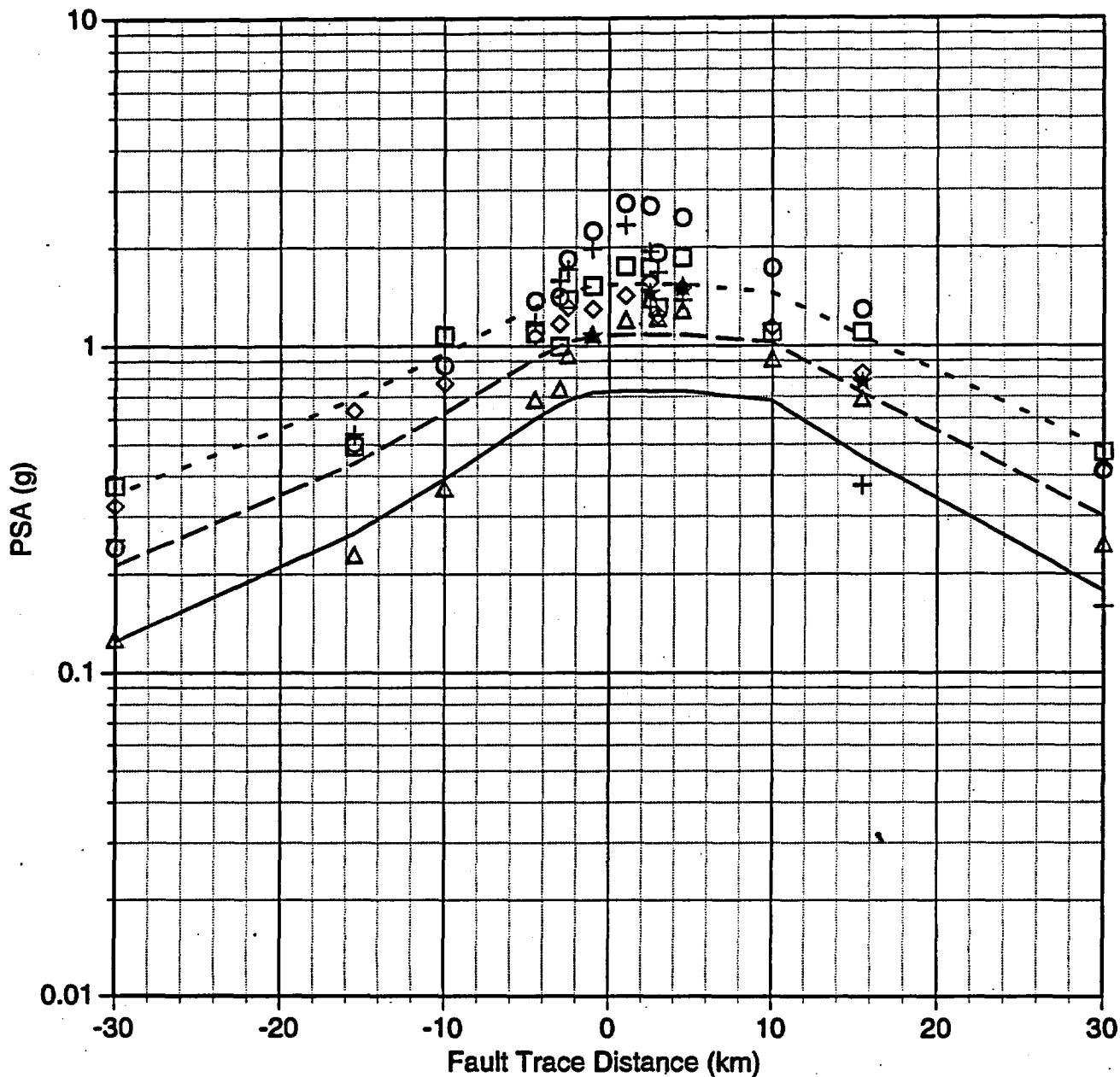


**M 6.4 Normal Fault (NO1)  
Spectral Acceleration vs Distance (5.0 Hz)**



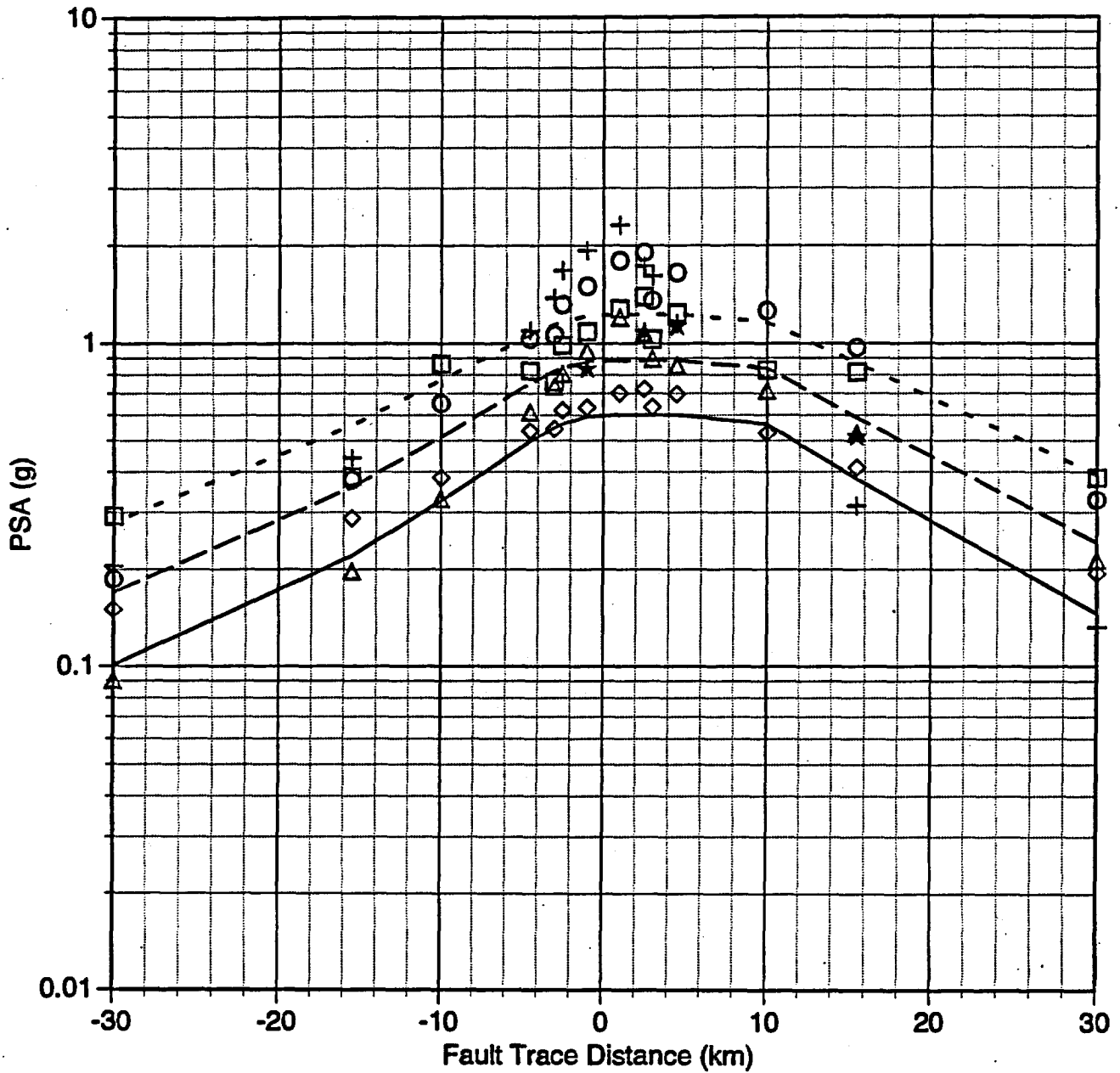
|   |           |         |                      |
|---|-----------|---------|----------------------|
| ○ | 5 Hz PEA  | ★       | 5 Hz, S-cubed        |
| △ | 5 Hz UNR  | —       | 5 Hz, Pt 25 bar h=6  |
| ◇ | 5 Hz USC  | - - -   | 5 Hz, Pt 50 bar h=6  |
| □ | 5 Hz WCC  | - · - · | 5 Hz, Pt 100 bar h=6 |
| + | 5 Hz USGS |         |                      |

**M 6.4 Normal Fault (NO1)  
Spectral Acceleration vs Distance (10.0 Hz)**



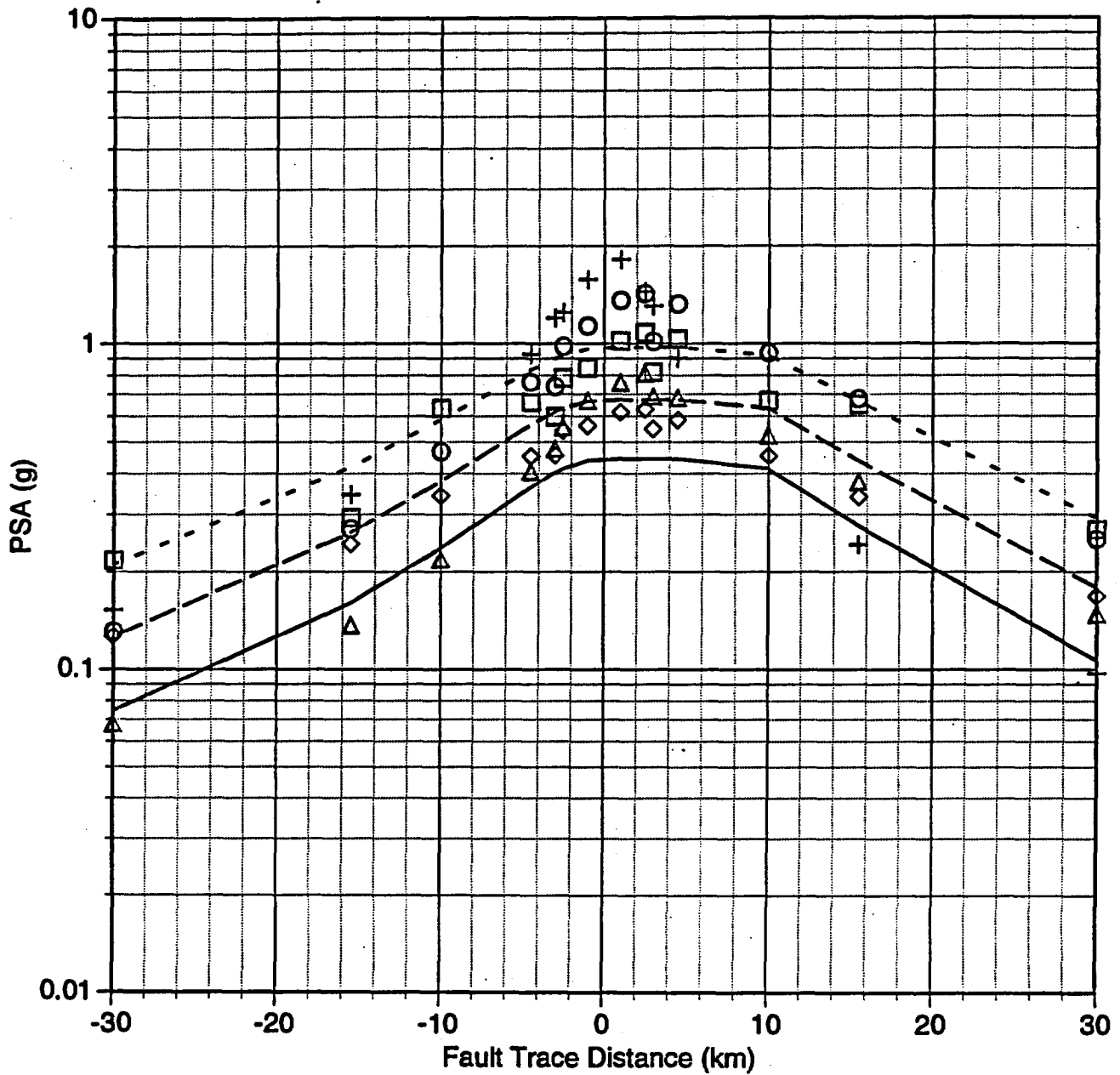
|   |            |         |                       |
|---|------------|---------|-----------------------|
| ○ | 10 Hz PEA  | ★       | 10 Hz, S-cubed        |
| △ | 10 Hz UNR  | —       | 10 Hz, Pt 25 bar h=6  |
| ◇ | 10 Hz USC  | - - -   | 10 Hz, Pt 50 bar h=6  |
| □ | 10 Hz WCC  | - . - . | 10 Hz, Pt 100 bar h=6 |
| + | 10 Hz USGS |         |                       |

**M 6.4 Normal Fault (NO1)  
Spectral Acceleration vs Distance (20.0 Hz)**



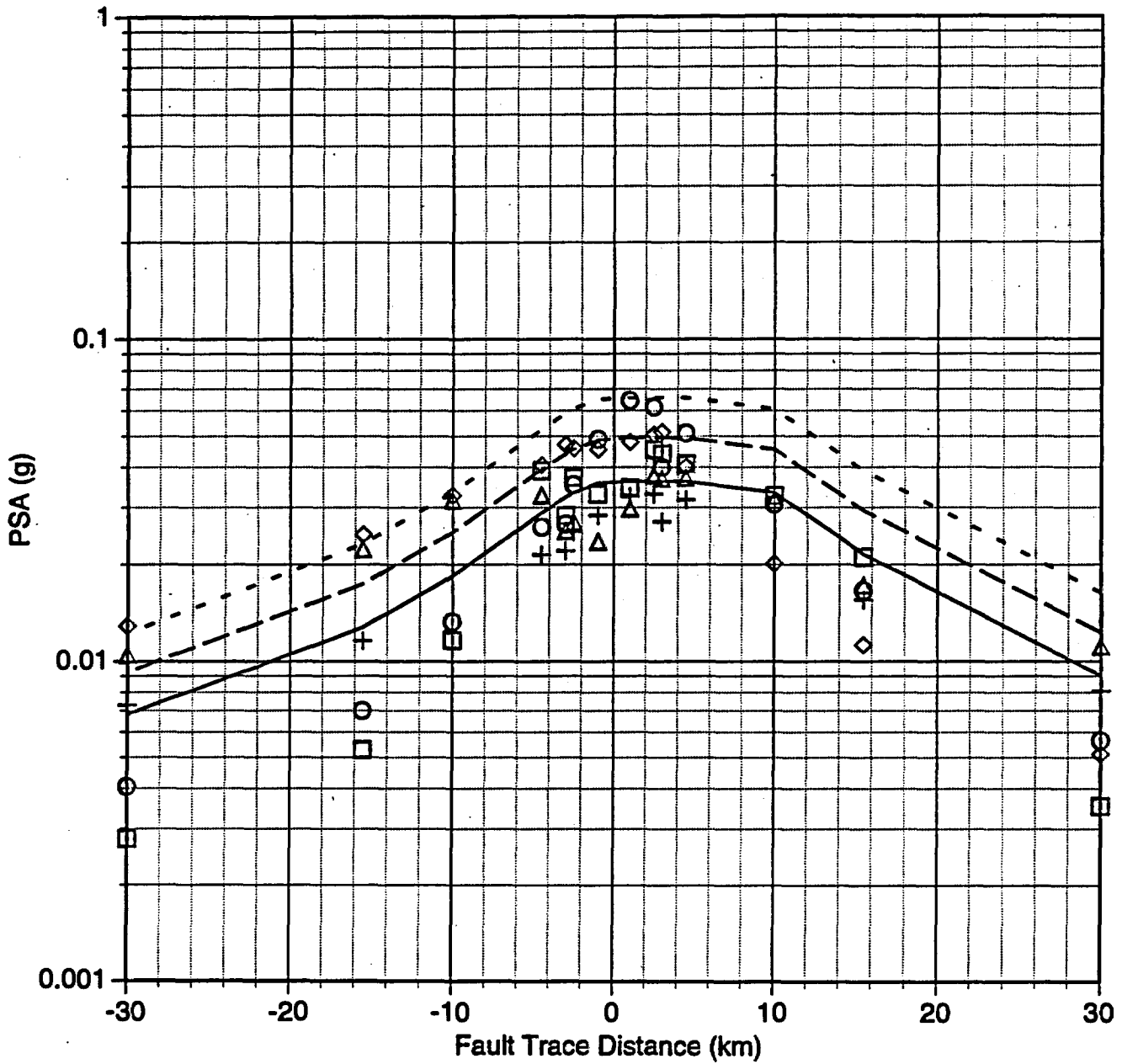
|   |            |         |                       |
|---|------------|---------|-----------------------|
| ○ | 20 Hz PEA  | ★       | 20 Hz, S-cubed        |
| △ | 20 Hz UNR  | —       | 20 Hz, Pt 25 bar h=6  |
| ◇ | 20 Hz USC  | - - -   | 20 Hz, Pt 50 bar h=6  |
| □ | 20 Hz WCC  | . . . . | 20 Hz, Pt 100 bar h=6 |
| + | 20 Hz USGS |         |                       |

### M 6.4 Normal Fault (NO1) Spectral Acceleration vs Distance (34.0 Hz)



|   |            |         |                       |
|---|------------|---------|-----------------------|
| ○ | 34 Hz PEA  | ★       | 34 Hz, S-cubed        |
| △ | 34 Hz UNR  | —       | 34 Hz, Pt 25 bar h=6  |
| ◇ | 34 Hz USC  | - - -   | 34 Hz, Pt 50 bar h=6  |
| □ | 34 Hz WCC  | - - - - | 34 Hz, Pt 100 bar h=6 |
| + | 34 Hz USGS |         |                       |

### M 6.4 Normal Fault (NO1) Spectral Acceleration vs Distance (0.2 Hz)



|   |             |         |                        |
|---|-------------|---------|------------------------|
| ○ | 0.2 Hz PEA  | ★       | 0.2 Hz, S-cubed        |
| △ | 0.2 Hz UNR  | —       | 0.2 Hz, Pt 25 bar h=6  |
| ◇ | 0.2 Hz USC  | - - -   | 0.2 Hz, Pt 50 bar h=6  |
| □ | 0.2 Hz WCC  | - . - . | 0.2 Hz, Pt 100 bar h=6 |
| + | 0.2 Hz USGS |         |                        |

### Normal Faults Variation in Dip

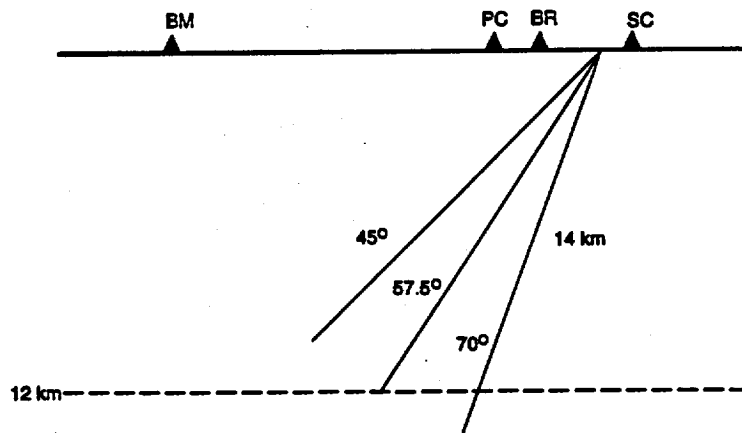
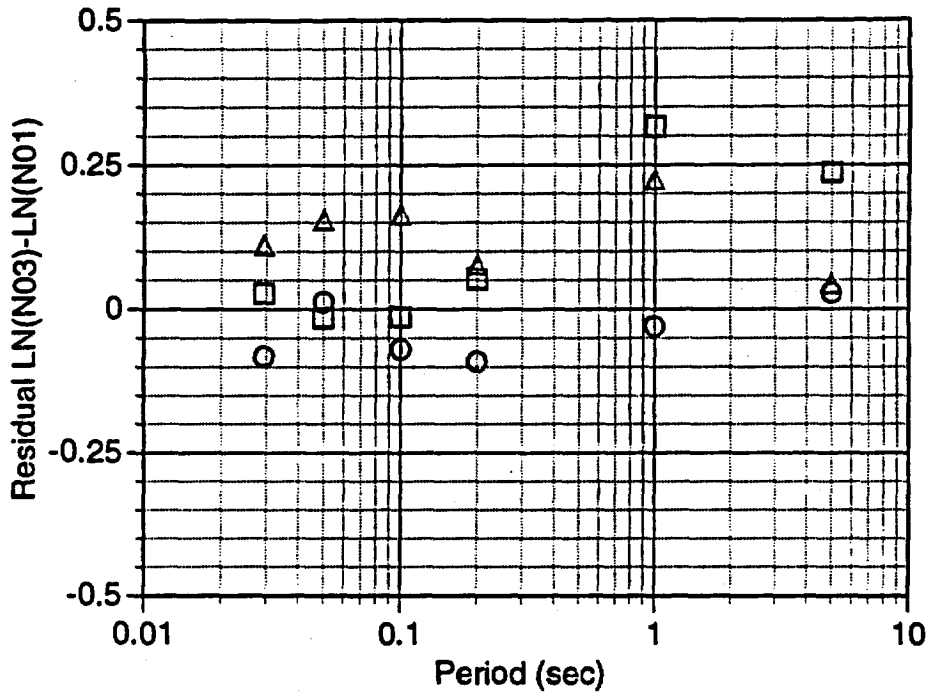
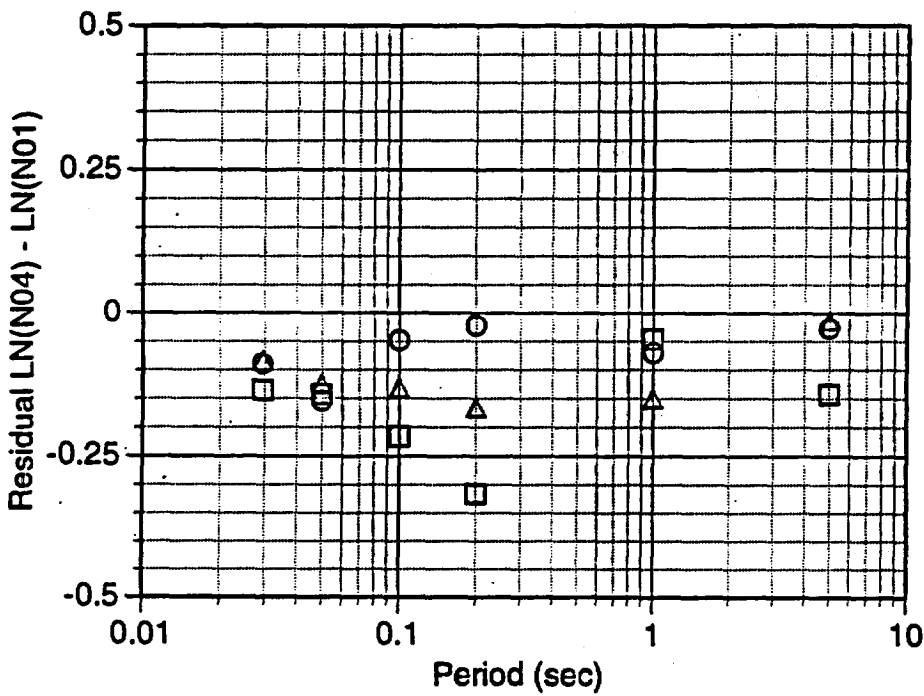


Figure 8.20

Residuals: Station #2

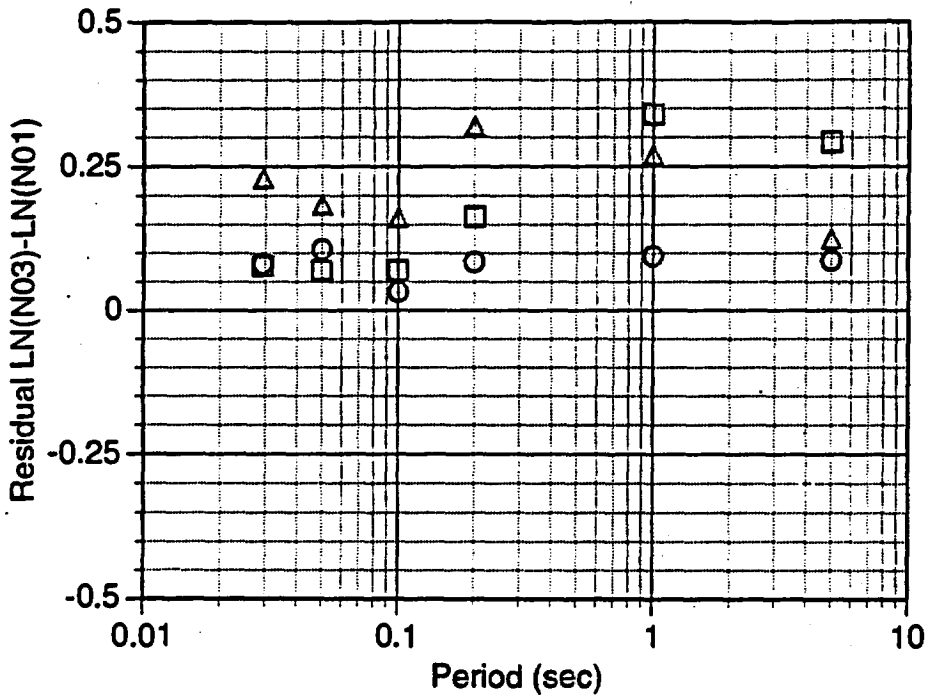


- N03-N01 (PEA#2)
- N03-N01 (UNR#2)
- △ N03-N01 (WCC#2)

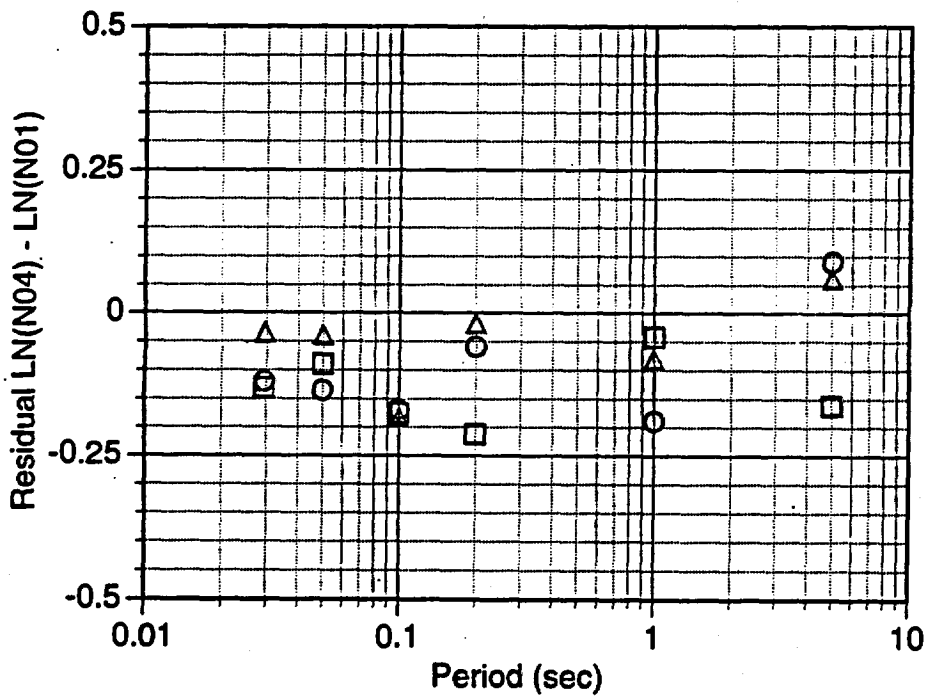


- N04-N01 (PEA#2)
- N04-N01 (UNR#2)
- △ N04-N01 (WCC#2)

Residuals: Station #4

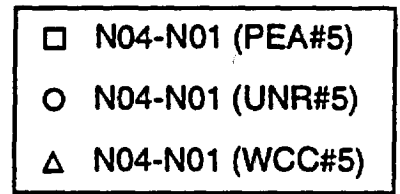
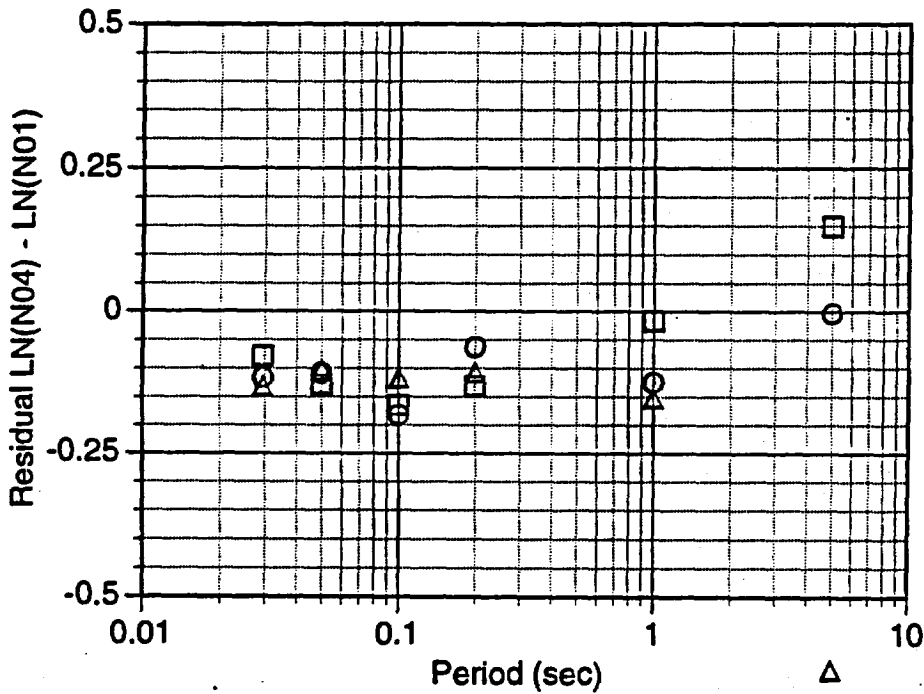
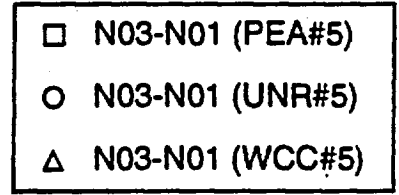
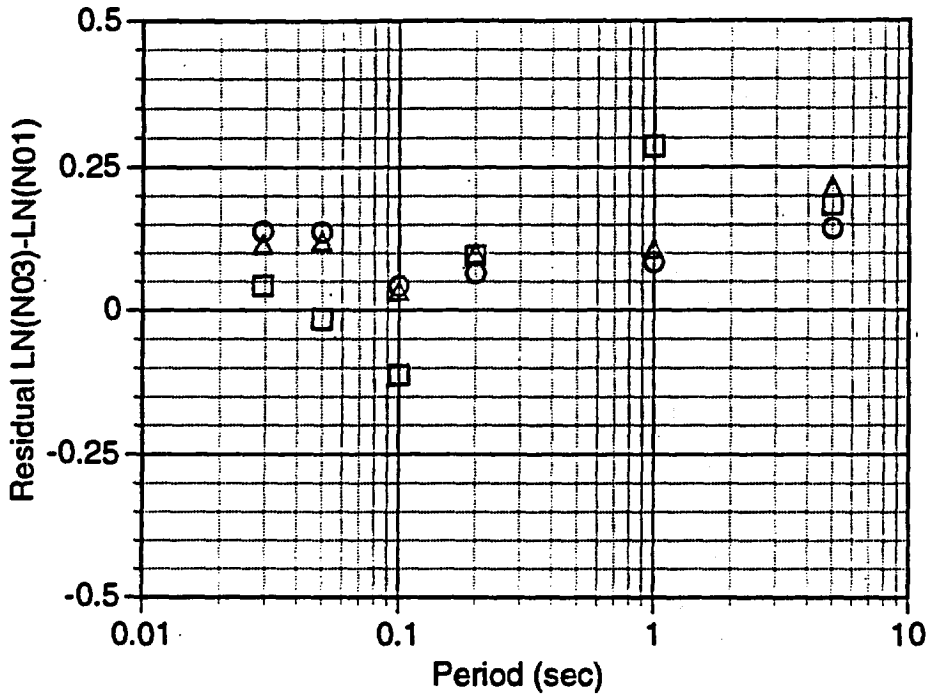


- N03-N01 (PEA#4)
- N03-N01 (UNR#4)
- △ N03-N01 (WCC#4)

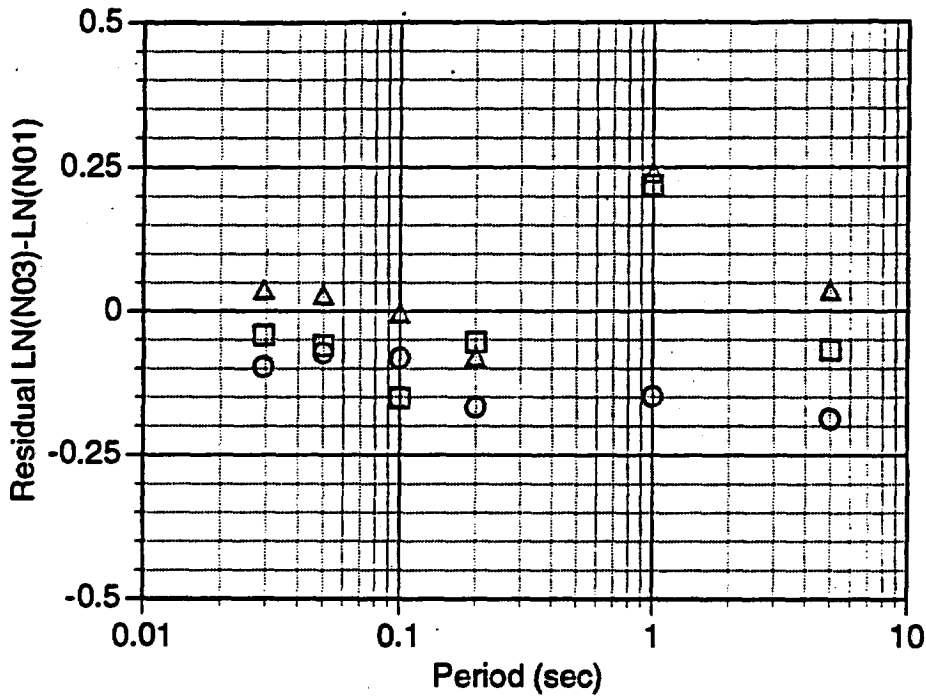


- N04-N01 (PEA#4)
- N04-N01 (UNR#4)
- △ N04-N01 (WCC#4)

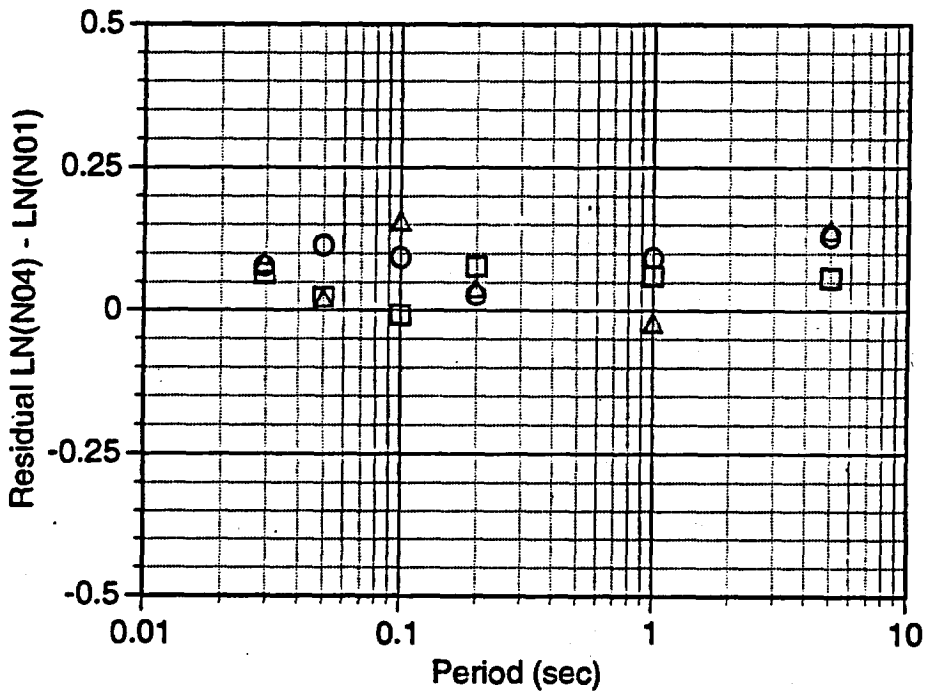
Residuals: Station #5



Residuals: Station #7

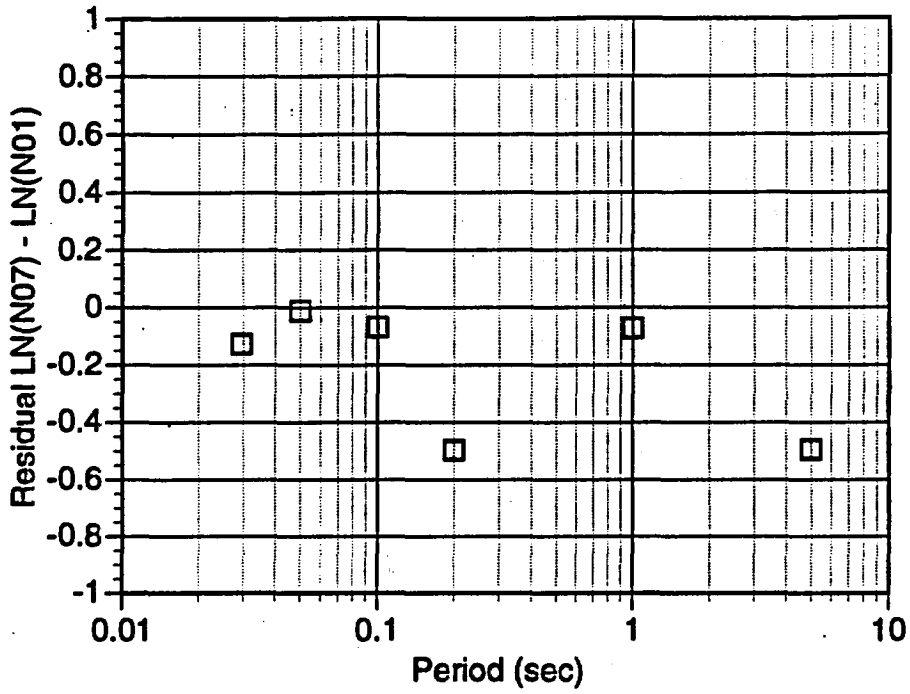


- N03-N01 (PEA#7)
- N03-N01 (UNR#7)
- △ N03-N01 (WCC#7)

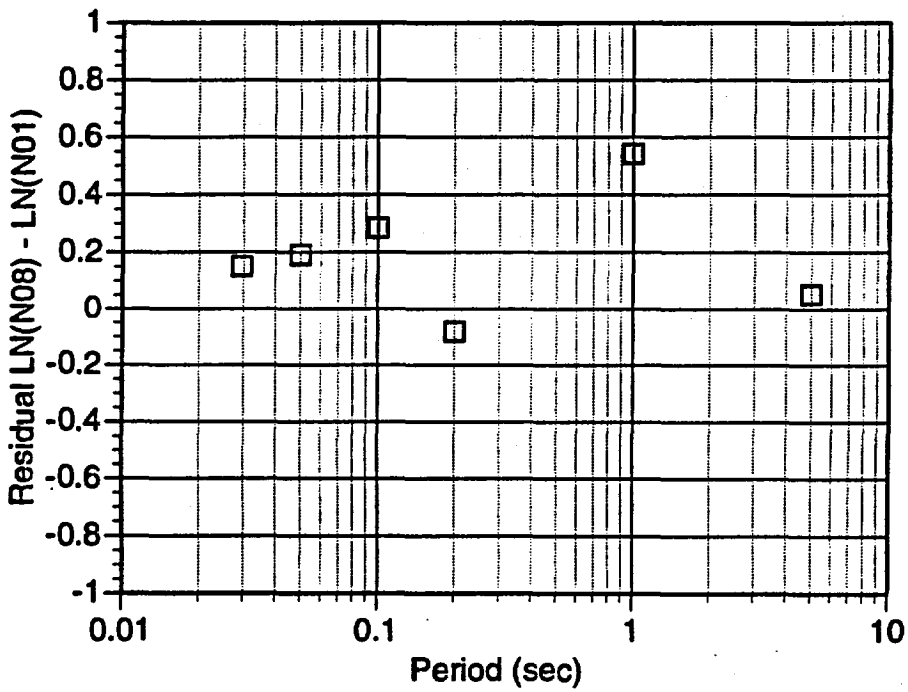


- N04-N01 (PEA#7)
- N04-N01 (UNR#7)
- △ N04-N01 (WCC#7)

Residuals: Station #2

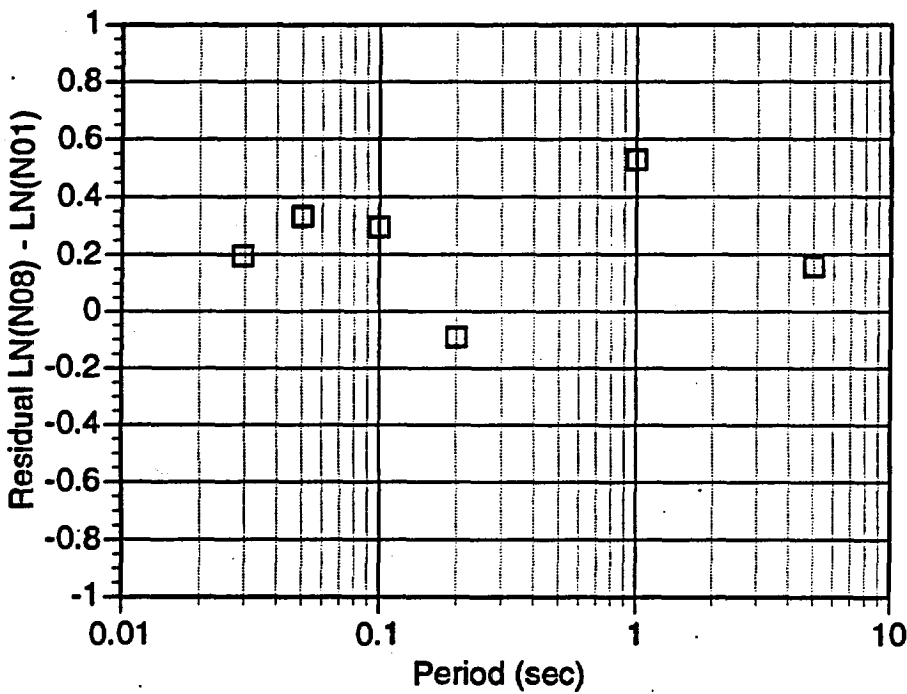
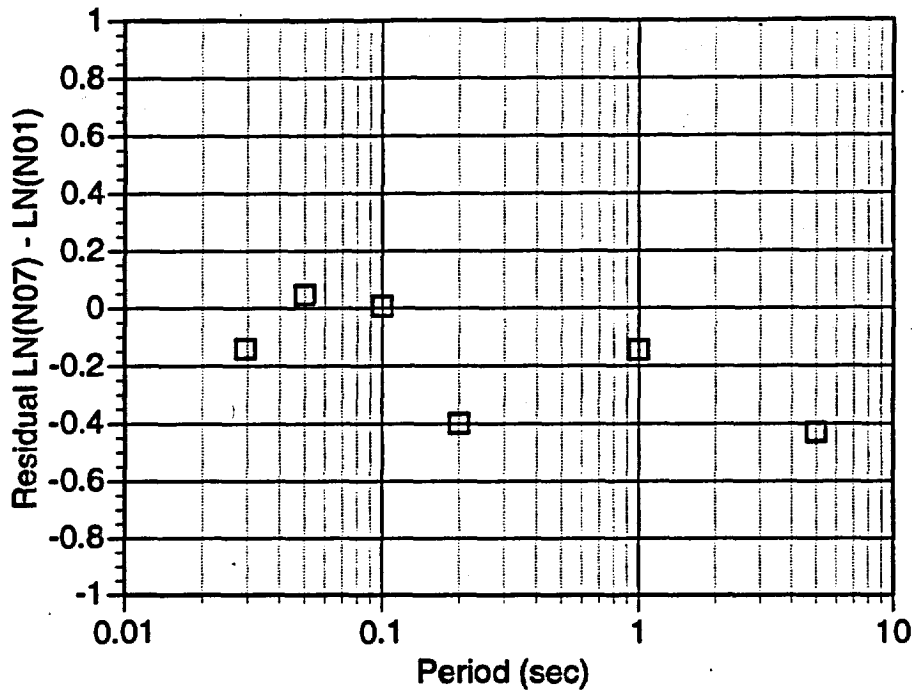


□ N07-N01 (PEA#2)

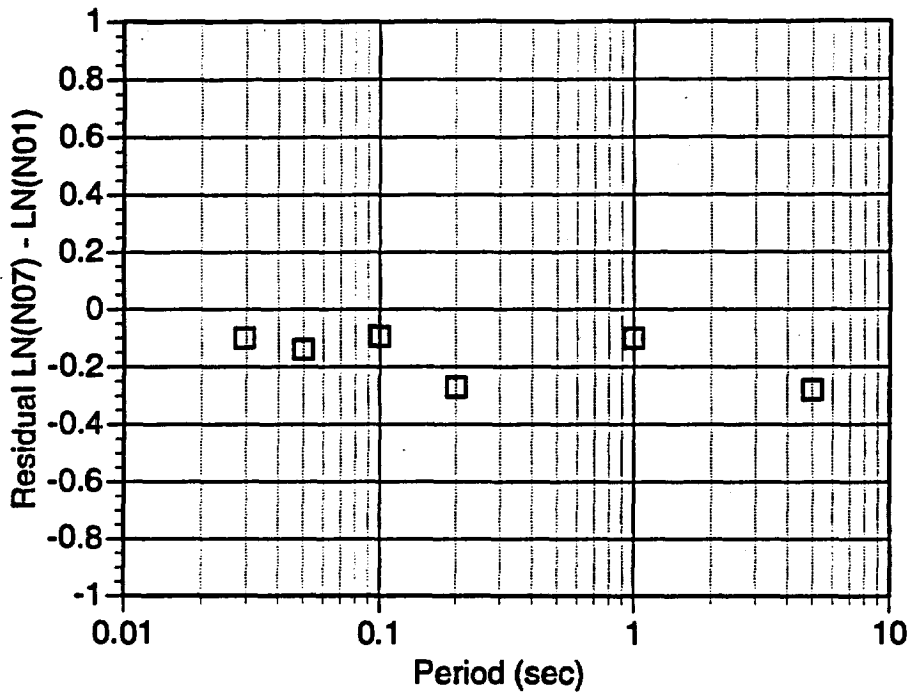


□ N08-N01 (PEA #2)

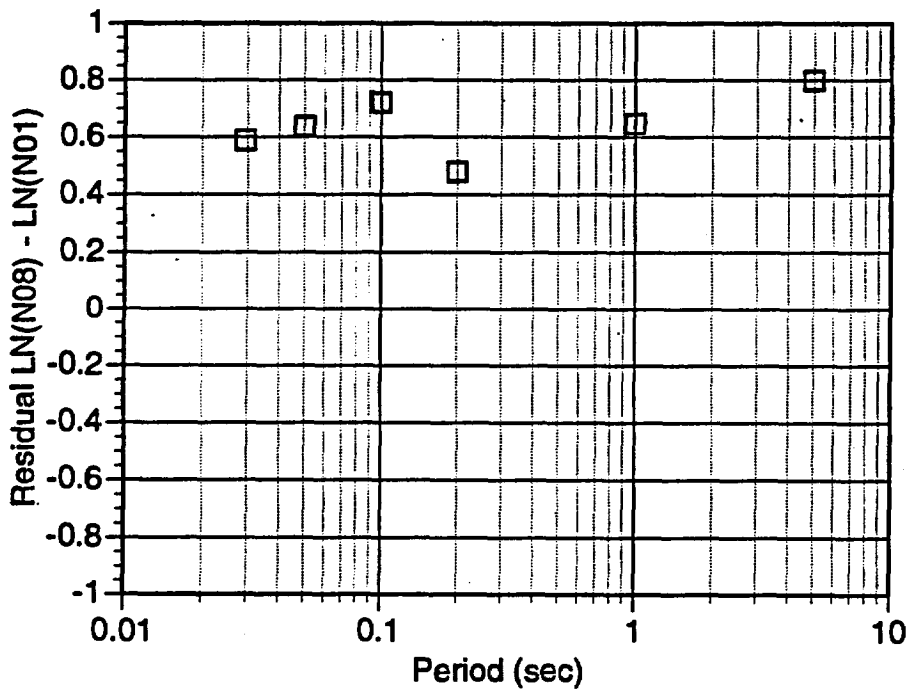
Residuals: Station #4



Residuals: Station #5

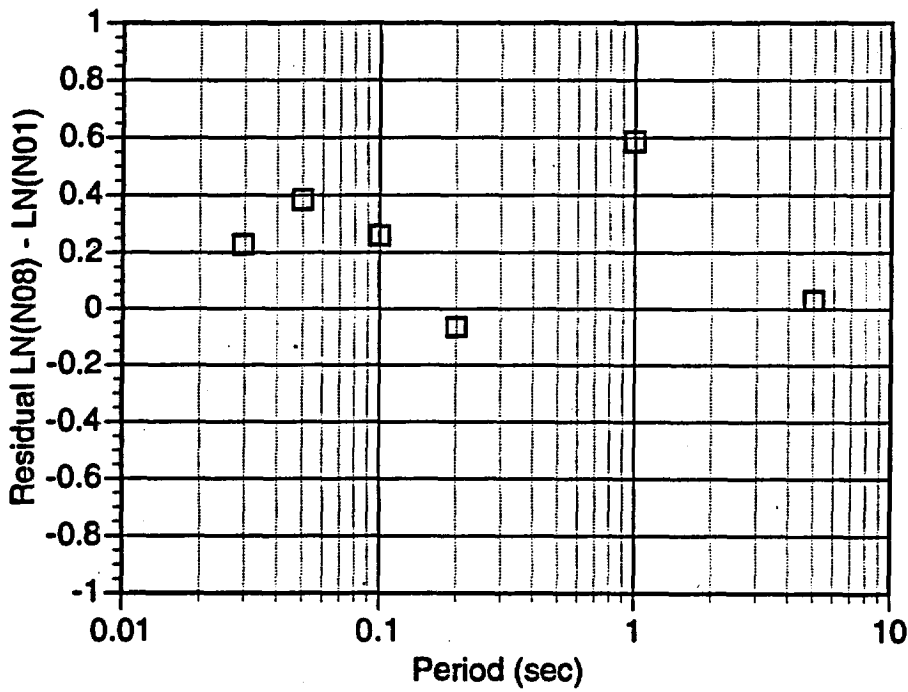
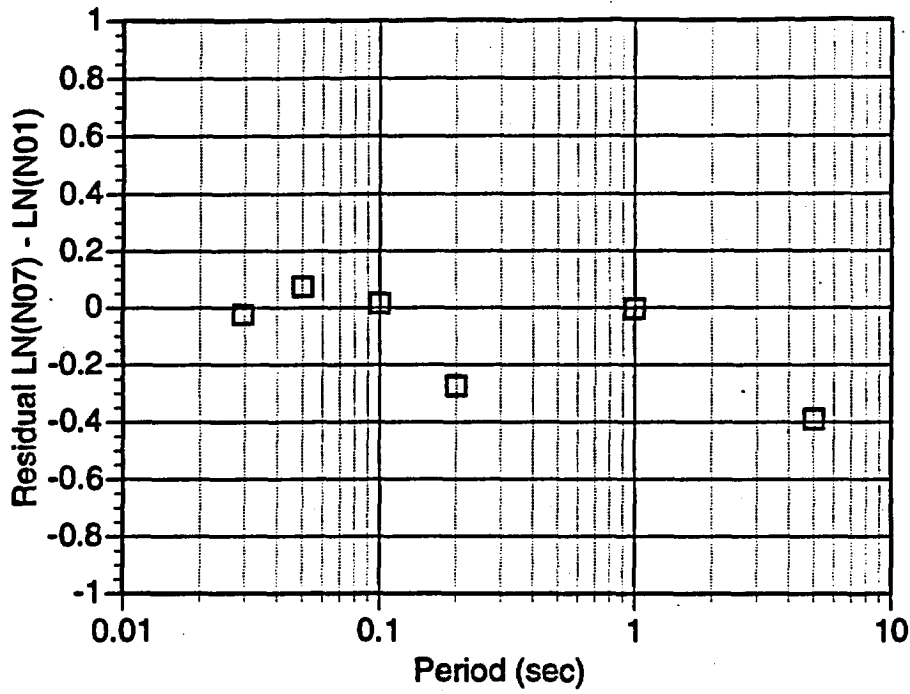


□ N07-N01 (PEA#5)



□ N08-N01 (PEA #5)

Residuals: Station #7



## 9 STRIKE-SLIP FAULTING EXERCISES

Two strike-slip scenario events were considered (scenarios 3 and 5 in table 2.4). The first scenario is a M 6.7 event on the Rock Valley fault located approximately 25 km from the site. The second event is a M 7.0 event on the Furnace Creek fault located approximately 50 km from the site. The source parameters for these two events are given in table 9.1.

TABLE 9.1 -- NEAR HERE

Not all of the modeling methods were used for these events. The Rock Valley event was modeled by PEA, USC, WCC, and USGS. The Furnace Creek event was modeled by USC, PEA, UNR, and USGS.

### Rock Valley Fault

For the Rock Valley fault scenario, the site is located at the center of the 42 km long fault at a shortest distance of 25 km (fig. 9.1). Six additional test sites were also considered (fig. 9.1). Two sites were located 10 km up and down strike of the site at the same closest distance and four sites were located at the center of the fault but at different distances. The coordinates of the sites are given in table 9.2.

FIGURE 9.1 -- NEAR HERE

TABLE 9.2 -- NEAR HERE

### **Furnace Creek Fault**

For the Furnace Creek fault scenario, the site is located off the end of a 90 km fault at a shortest distance of 50 km (fig. 9.2). Four additional test sites were also considered (fig. 9.2). Two sites were located 10 km up and down strike of the site at the same closest distance and two sites were located  $\pm 5$  km perpendicular to strike. The coordinates of the sites are given in table 9.3.

**FIGURE 9.2 -- NEAR HERE**

**TABLE 9.3 -- NEAR HERE**

### **Results**

The resulting median acceleration response spectra from each method are shown in figures 9.3a and 9.3b for the Rock Valley and Furnace Creek fault scenario sites (station 3 in both cases), respectively. As for the normal faulting exercises, the median spectra are computed from the suite of fault rupture realizations for each method (that is, combinations of fault slip distribution, hypocentral location, and rake angle). The numbers of realizations range from 27 to 90, depending upon the manner in which these values were randomized or selected by each modeler.

**FIGURE 9.3a-b -- NEAR HERE**

For both events, the PEA model produces the largest high frequency motions. The USGS model produces significantly lower motions for the Rock Valley fault, and moderately lower ground motions for Furnace Creek fault.

### Parametric Variability

The median spectra discussed above are the median values from a large suite of source realizations. The variability of the ground motions for the different realizations is the parametric variability (discussed in Section 4). Figures 9.4a and 9.4b show median values with  $\pm 1$  standard deviation of 5 percent damped acceleration response spectra for site 3 for each event. As with the normal faulting events, the variability tends to be model dependent, with the greatest variability shown in the PEA model. This parametric variability is part of the total variability discussed in Section 10.

FIGURE 9.4a-b -- NEAR HERE

### Duration

The median acceleration durations are shown in figure 9.5a-b, for the Rock Valley and Furnace Creek faults, respectively. For the Rock Valley fault, the USGS and PEA models show much shorter durations than the WCC and USC models. For the Furnace Creek fault, the USGS duration remains the smallest, but the PEA duration is similar to the UNR. As with the response spectral values, the parametric variability of the durations is considered by examining the variability of the duration from multiple realizations of the source process. Figures 9.6a and 9.6b show mean values with  $\pm 1$  standard deviation of the duration of acceleration time histories for the same sites. The similar parametric variability of the velocity duration is shown in figures 9.7a and 9.7b. The trends in the velocity duration are quite similar to those for acceleration.

FIGURE 9.5a-b -- NEAR HERE

FIGURE 9.6a-b -- NEAR HERE

FIGURE 9.7a-b -- NEAR HERE

### **Comparisons of Results to Empirical Attenuation Relations**

For the Rock Valley fault, the attenuation of spectral acceleration with respect to distance from the fault trace is shown in figures 9.8a-f for six different frequencies: 0.2, 1.0, 5.0, 10.0, 20.0, and 34.0 Hz. At each frequency, numerical model calculations for the finite-fault models are juxtaposed against a suite of five empirical ground motion relations for rock. Note that the model results for each frequency-distance pair are median values obtained from at least 30 realizations of the fault rupture process.

**FIGURE 9.8a-f -- NEAR HERE**

For the Rock Valley fault, the ground motions from the modeling procedures are larger than predicted using WNA attenuation relations at high frequencies which is consistent with the lower kappa values at Yucca Mountain. At 5 Hz, the modeling results are consistent with the WNA empirical models. At 1 Hz, the modeling results again are higher than the WNA empirical and then at 0.2 Hz, the modeling results are much lower than the WNA empirical. The ratio of the average modeling prediction to WNA empirical attenuation prediction is shown in figure 9.9.

**FIGURE 9.9 -- NEAR HERE**

For the Furnace Creek fault, the attenuation of spectral acceleration with respect to distance from the fault trace is shown in figures 9.10a-f for six different frequencies: 0.2, 1.0, 5.0, 10.0, 20.0, and 34.0 Hz. The modeling results are consistent with the WNA empirical prediction for all frequencies except for the most distant site (80 km distance). At 80 km, the modeling predictions are significantly larger than the empirical models. This difference is likely due to post-critical reflected waves as seen in the 1989 Loma Prieta earthquake at Bay Area sites. The ratio of the average modeling prediction to WNA empirical attenuation prediction is shown in figure 9.11.

FIGURE 9.10a-b -- NEAR HERE

FIGURE 9.11 -- NEAR HERE

**Table 9.1 Strike-slip faulting scenarios exercises.**

| Parameter   | Rock Valley Fault     | Furnace Creek Fault   |
|---|-----------------------|-----------------------|
| • Length (L) (km)   | 42                    | 90                    |
| • Width (W) (km)  | 12                    | 12                    |
| • Area (A) (L x W) (km <sup>2</sup> )                     | 504                   | 1080                  |
| • Average stress drop ( $\Delta\sigma$ ) (bar)            | 30                    | 30                    |
| • Average shear modulus ( $\mu$ ) (dyne/cm <sup>2</sup> ) | $3.37 \times 10^{11}$ | $3.37 \times 10^{11}$ |
| • Average slip (D) (cm)                                   | 77.4                  | 113.3                 |
| • Moment ( $M_0$ ) ( $\mu DA$ ) (dyne-cm)                 | $1.31 \times 10^{26}$ | $4.12 \times 10^{26}$ |
| • Moment Magnitude  | 6.71                  | 7.04                  |
| • Fault strike, (x, y) coordinates                        | 0 degrees (x = 0)     | 0 degrees (x = 0)     |
| • Fault dip (degrees)                                     | 90                    | 90                    |
| • Rake (degrees)  | 0 (left-lateral)      | 180 (right-lateral)   |
| • Fault Corners:  |                       |                       |
| Point 1 ( $x_1, y_1, z_1$ )                               | (0, 0, 0)             | (0, 0, 0)             |
| Point 2 ( $x_2, y_2, z_2$ )                               | (0, 42, 0)            | (0, 90, 0)            |
| Point 3 ( $x_3, y_3, z_3$ )                               | (0, 0, 12)            | (0, 0, 12)            |
| Point 4 ( $x_4, y_4, z_4$ )                               | (0, 42, 12)           | (0, 90, 12)           |
| • Hypocenters:  |                       |                       |
| Hypo 1  | (0, 4.2, 10.2)        | (0, 9, 10.2)          |
| Hypo 2  | (0, 21, 10.2)         | (0, 45, 10.2)         |
| Hypo 3  | (0, 37.8, 10.2)       | (0, 81, 10.2)         |

**Table 9.1 (continued) Strike-slip faulting scenarios exercises.**

---

| <b>Parameter</b>                    |  |
|-------------------------------------|--|
| • Slip distributions:               | 10 variations with slip weighted toward lower half of fault.   |
| • Realizations:                     | $1 M_0 \times 1 \text{ dip} \times (10 \text{ slip dist.} \times 3 \text{ hypocenters}) = 30$<br>realizations for each site per event. |
| • Yucca Mountain Crustal Structure: | Same as N01  |
| • Modulus Reduction and Damping:    | Same as N01  |
| • Empirical Green's functions:      | Same as N01 (as applicable)  |

**Table 9.2 Rock Valley sites.**

Locations in (x, y) for  $z = 0$ :

| Site # | Name           | x    | y    |
|--------|----------------|------|------|
| 01     | 20x            | 20.0 | 21.0 |
| 02     | 25xa           | 25.0 | 11.0 |
| 03     | Yucca Mountain | 25.0 | 21.0 |
| 04     | 25xb           | 25.0 | 31.0 |
| 05     | 30x            | 30.0 | 21.0 |
| 06     | 40x            | 40.0 | 21.0 |
| 07     | 50x            | 50.0 | 21.0 |

**Table 9.3 Furnace Creek sites.**

Locations in (x, y) for z = 0:

| Site # | Name           | x     | y     |
|--------|----------------|-------|-------|
| 01     | 40x            | -40.0 | 100.0 |
| 02     | 50xa           | -50.0 | 80.0  |
| 03     | Yucca Mountain | -50.0 | 100.0 |
| 04     | 50xb           | -50.0 | 120.0 |
| 05     | 60x            | -60.0 | 100.0 |

## Figure Captions

Figure 9.1 Station locations for RV1

Figure 9.2 Station locations for FC1

Figure 9.3 (a) Median ground motions for RV1 (site 3)

Figure 9.3 (b) Median ground motions for FC1 (site 3)

Figure 9.4 (a) Parametric variability of spectral acceleration for RV1

Figure 9.4 (b) Parametric variability of spectral acceleration for FC1

Figure 9.5 (a) median acceleration duration for RV1

Figure 9.5 (b) median acceleration duration for FC1

Figure 9.6 (a) Parametric variability of acceleration duration for RV1

Figure 9.6 (b) Parametric variability of acceleration duration for FC1

Figure 9.7 (a) Parametric variability of velocity duration for RV1

Figure 9.7 (b) Parametric variability of velocity duration for FC1

**Figure 9.8 (a) Comparison of ground motions with attenuation relations for RV1 (34 Hz)**

**Figure 9.8 (b) Comparison of ground motions with attenuation relations for RV1 (20 Hz)**

**Figure 9.8 (c) Comparison of ground motions with attenuation relations for RV1 (10 Hz)**

**Figure 9.8 (d) Comparison of ground motions with attenuation relations for RV1 (5 Hz)**

**Figure 9.8 (e) Comparison of ground motions with attenuation relations for RV1 (1 Hz)**

**Figure 9.8 (f) Comparison of ground motions with attenuation relations for RV1 (0.2 Hz)**

**Figure 9.9 Ratio of average simulated motion to average WUS attenuation relations for RV1.**

**Figure 9.10 (a) Comparison of ground motions with attenuation relations for FC1 (34 Hz)**

**Figure 9.10 (b) Comparison of ground motions with attenuation relations for FC1 (20 Hz)**

Figure 9.10 (c) Comparison of ground motions with attenuation relations for FC1 (10 Hz)

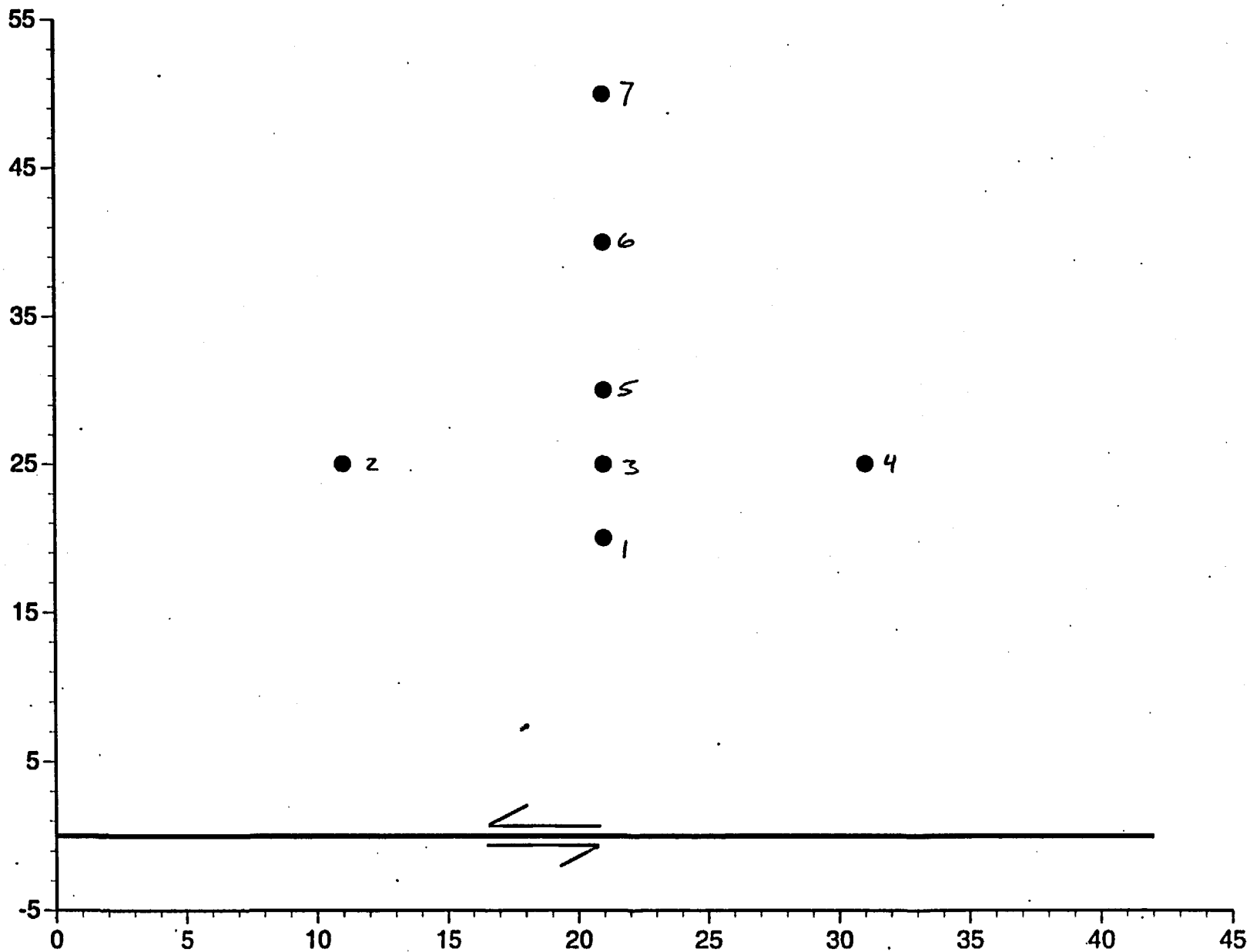
Figure 9.10 (d) Comparison of ground motions with attenuation relations for FC1 (5 Hz)

Figure 9.10 (e) Comparison of ground motions with attenuation relations for FC1 (1 Hz)

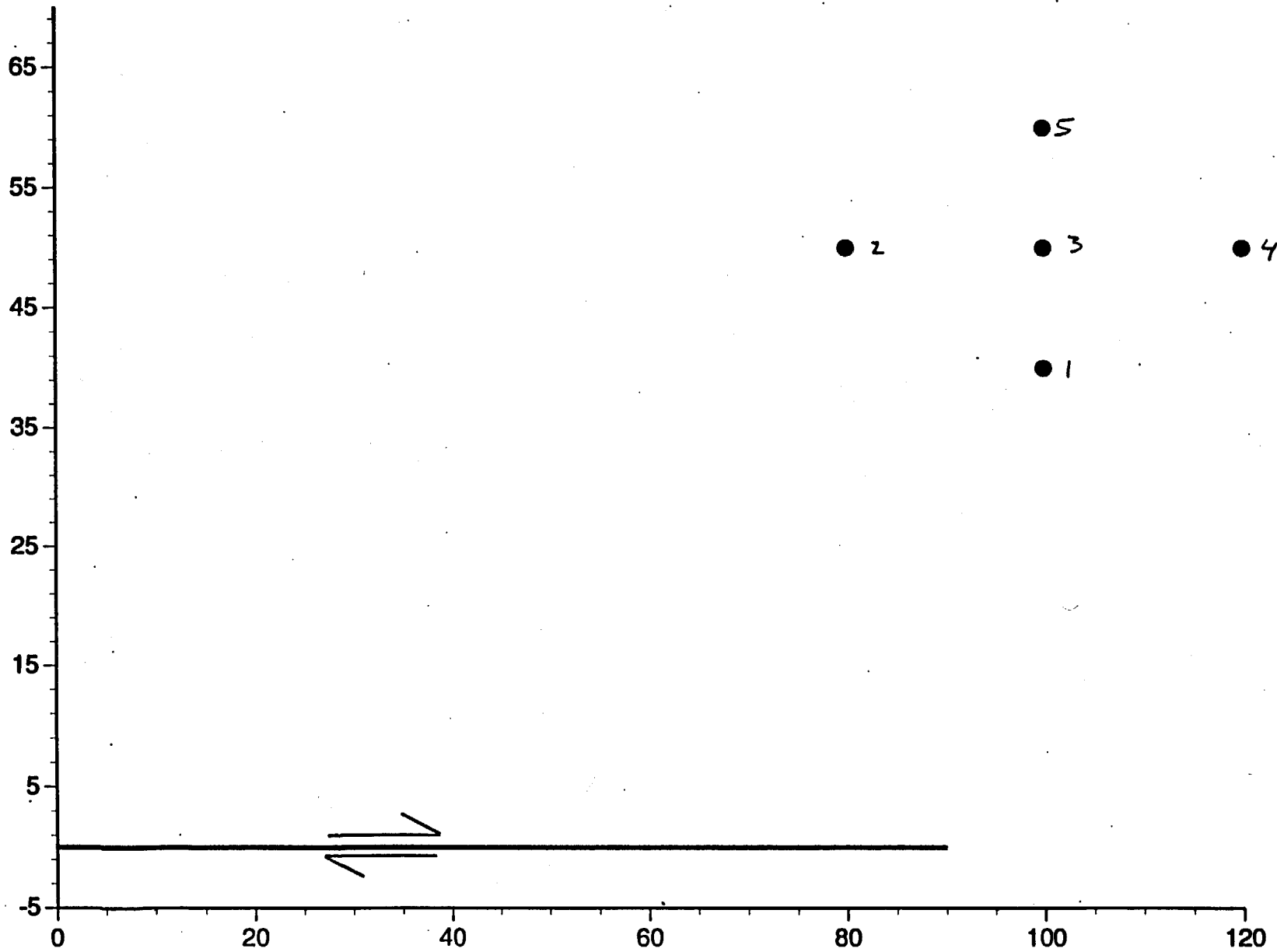
Figure 9.10 (f) Comparison of ground motions with attenuation relations for FC1 (0.2 Hz)

Figure 9.9 Ratio of average simulated motion to average WUS attenuation relations for FC1.

# Rock Valley Fault

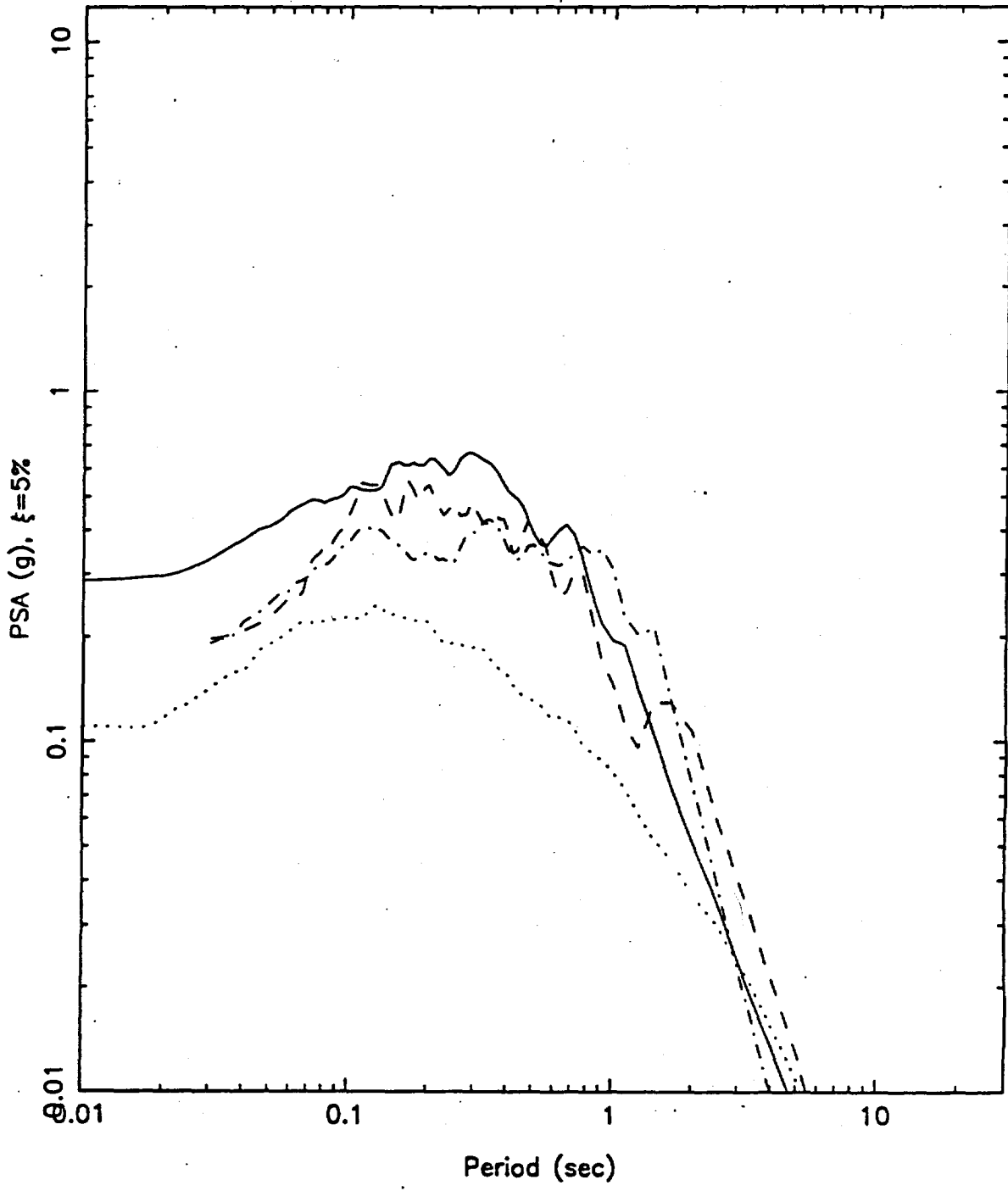


# Furnace Creek



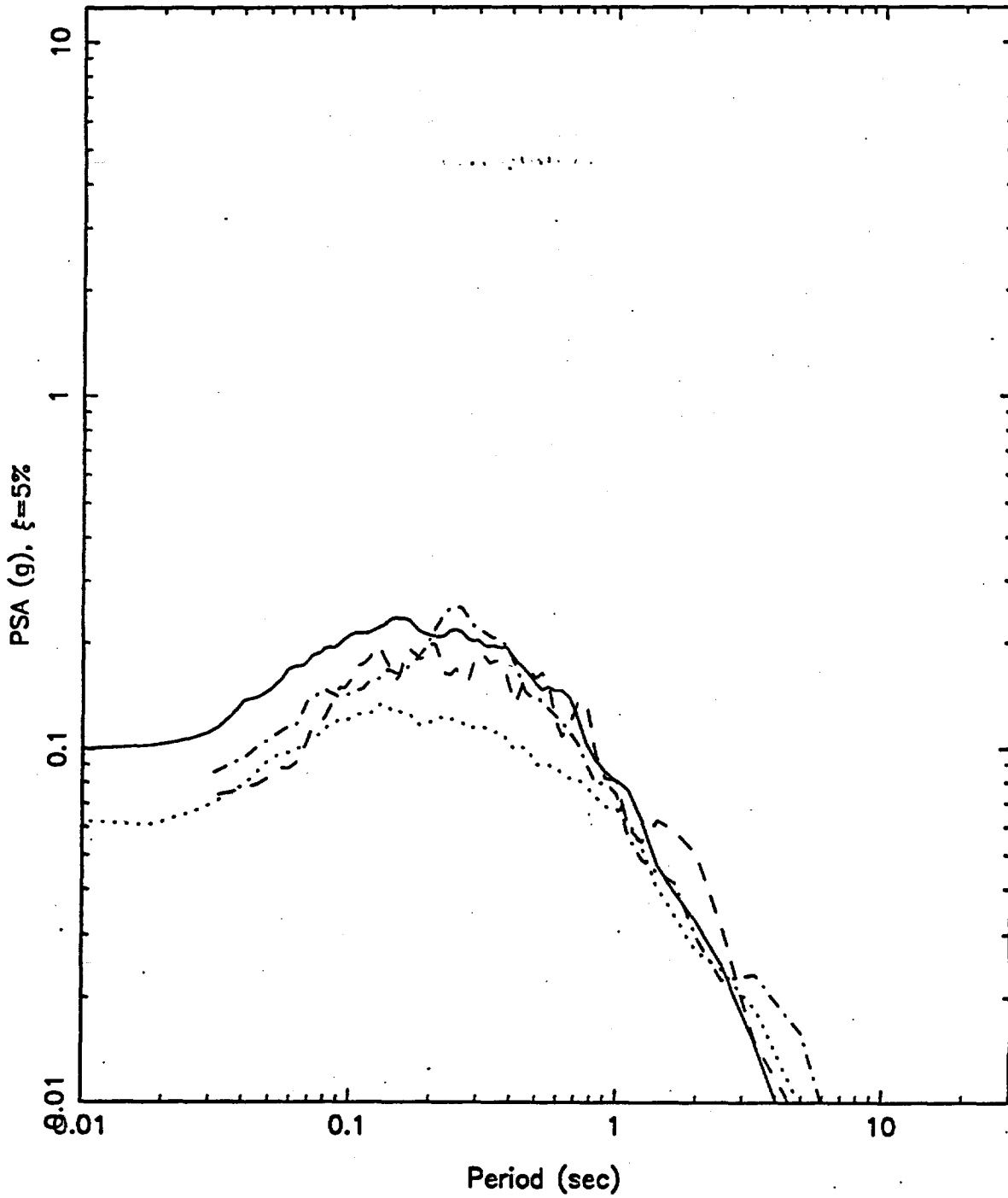
rv1, STATION # 3

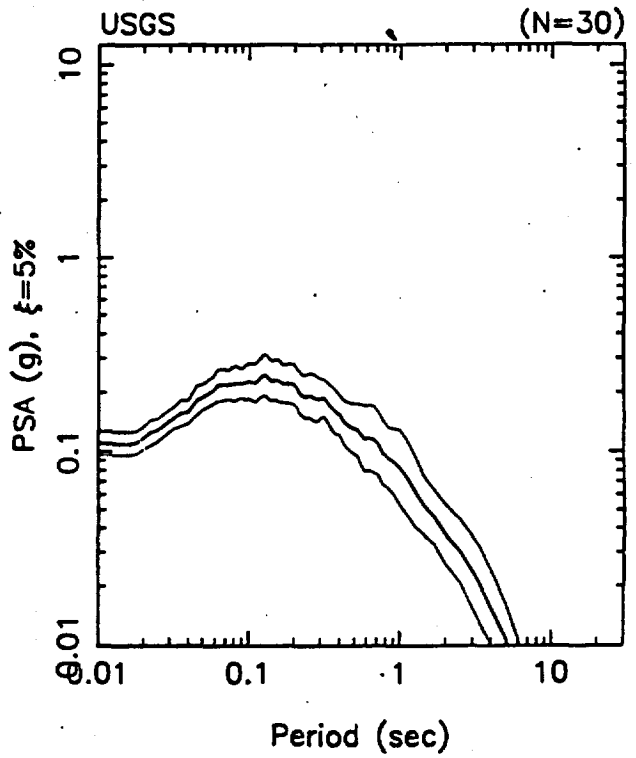
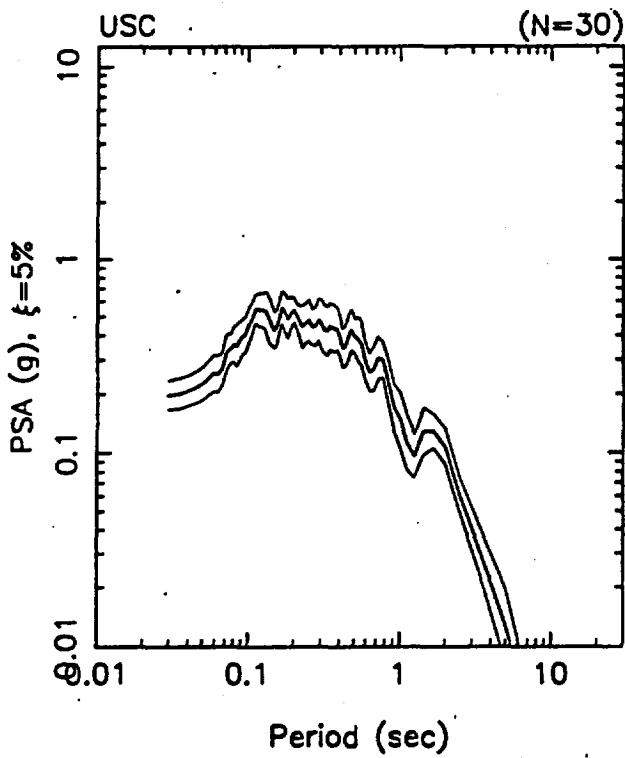
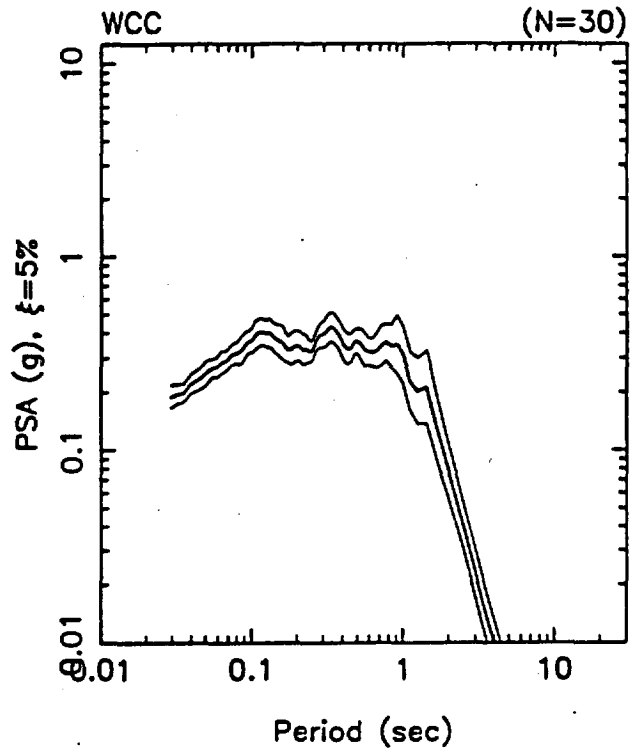
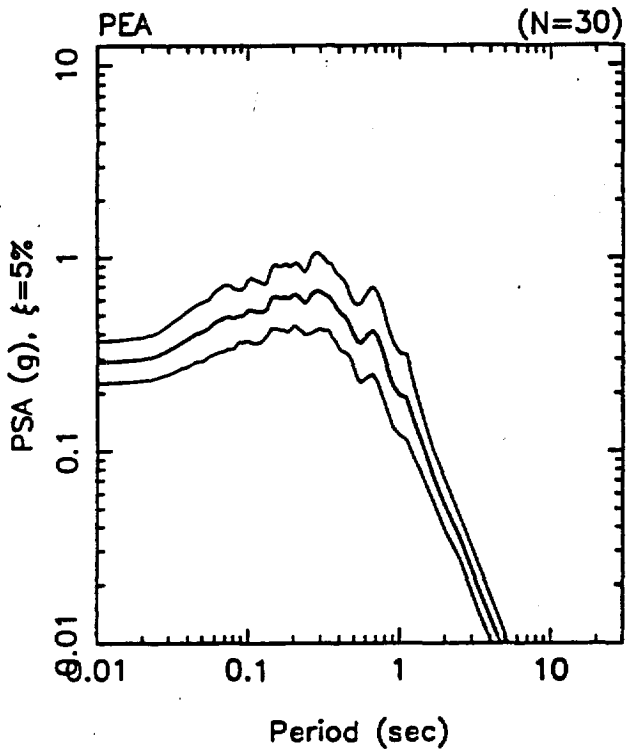
- : mean of RV1PEA03.PSV, [N=30]
- - - - - : mean of rv1usc03.hpsv, [N=30]
- · - · - : mean of RV1wcc03.hpsv, [N=30]
- ..... : mean of rv1usg03.hpsv, [N=30]



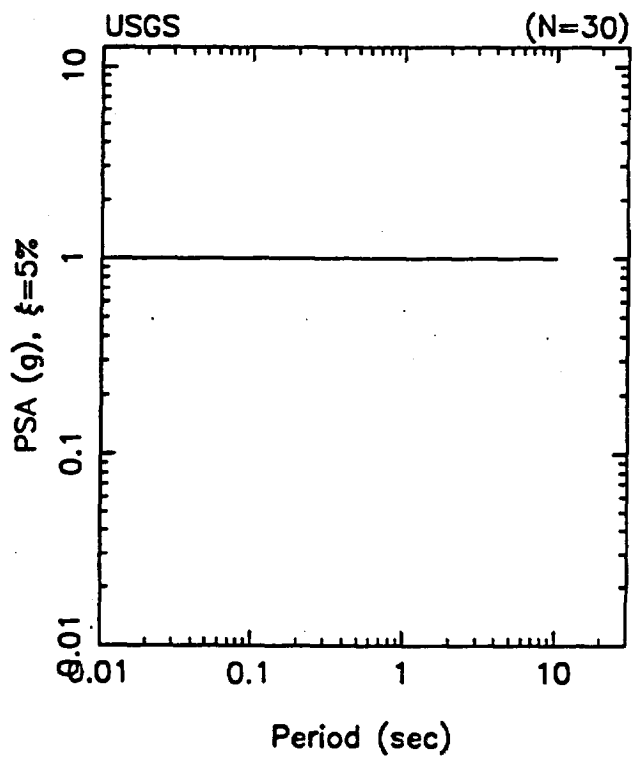
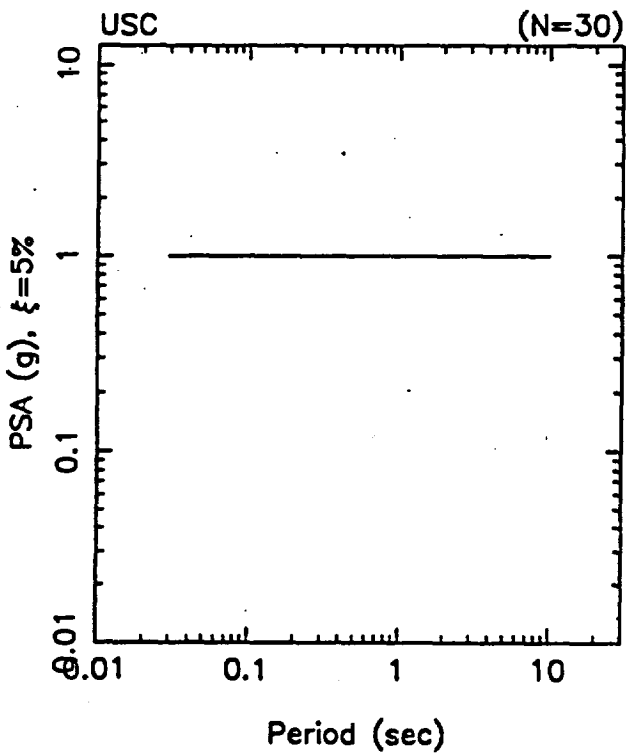
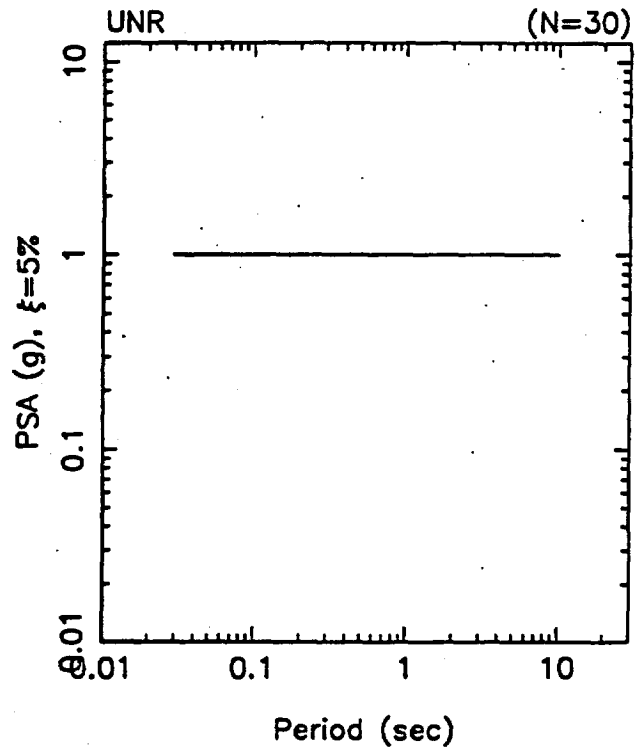
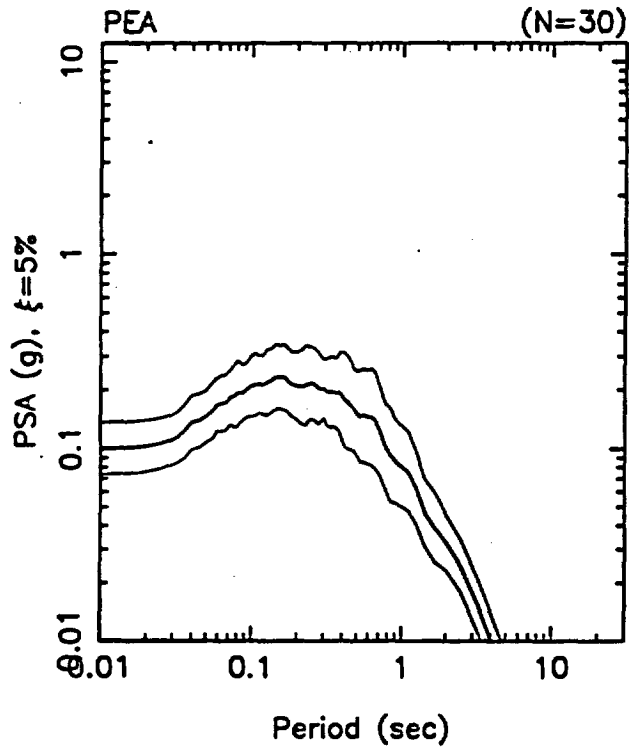
fc1, STATION # 3

- \_\_\_\_\_ : mean of FC1PEA03.PSV, [N=30]
- : mean of fc1usc03.hpsv, [N=30]
- ..... : mean of FC1unr03.hpsv, [N=30]
- ..... : mean of fc1usg03.hpsv, [N=30]

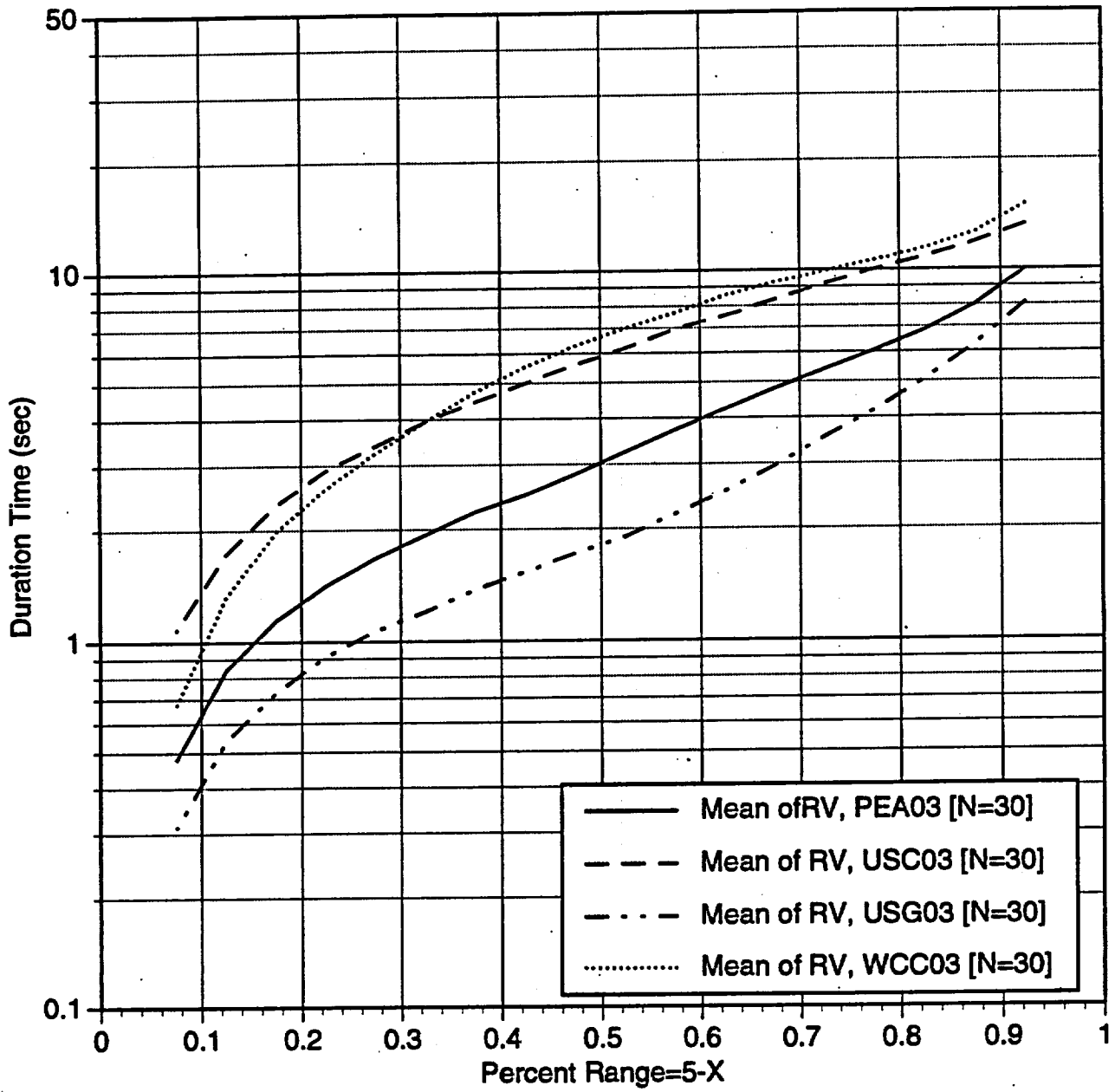




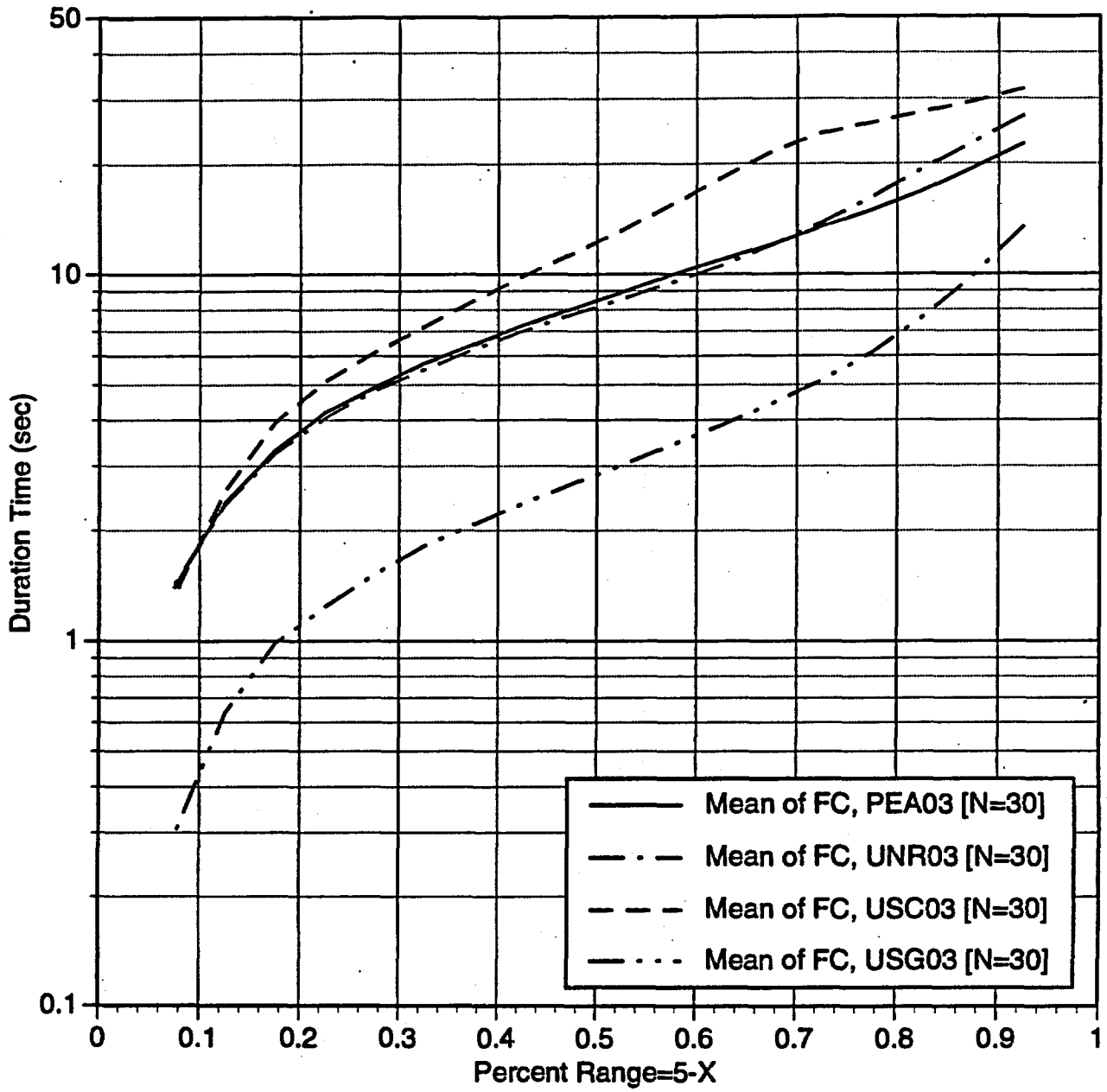
fc1, STATION # 3



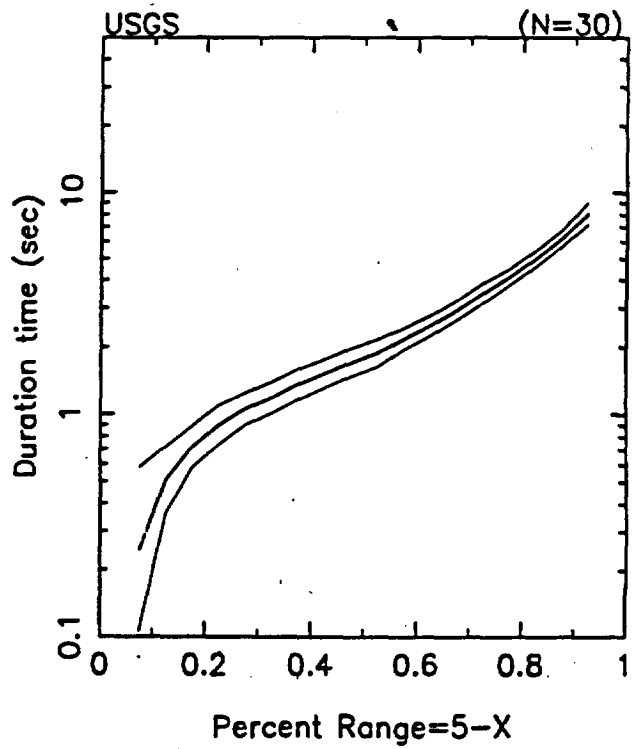
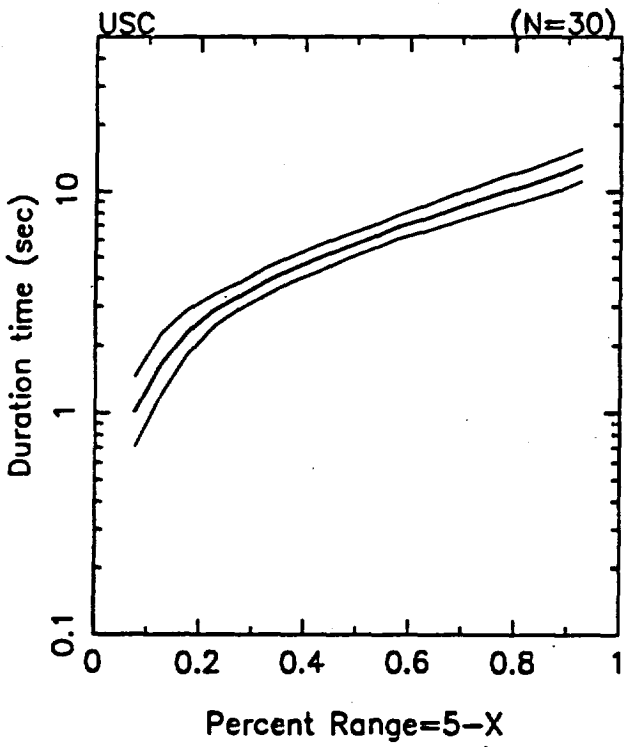
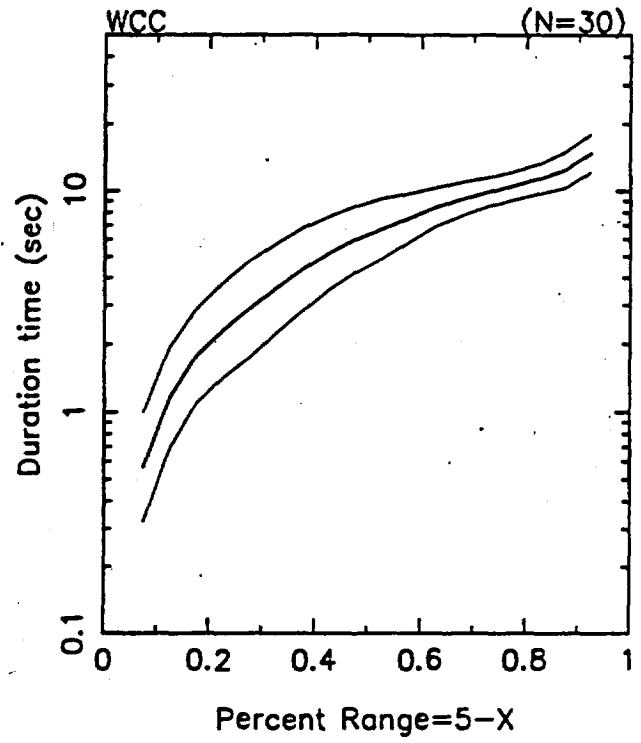
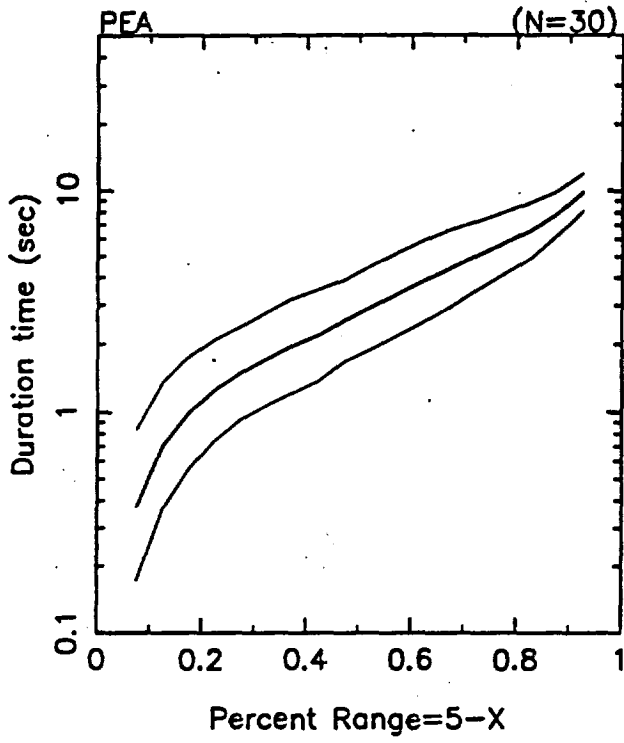
RV, Station #3: Acceleration Duration



FC, Station #3: Acceleration Duration

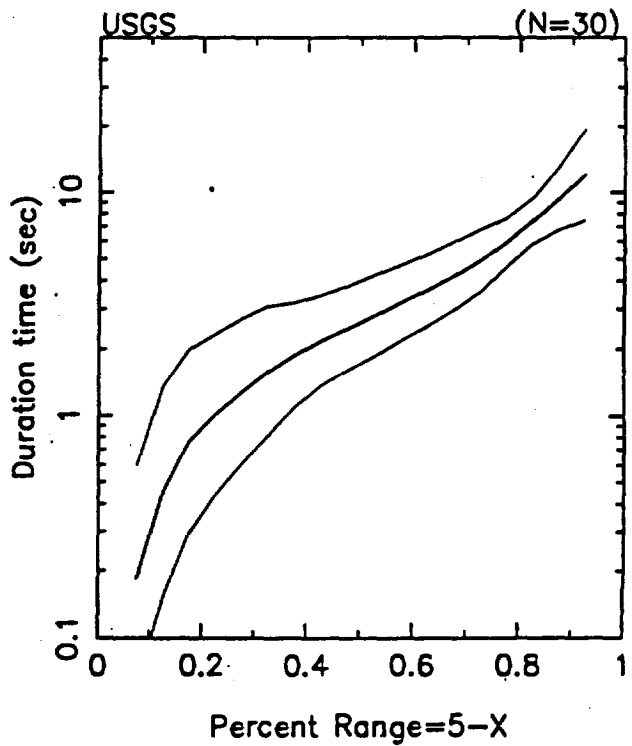
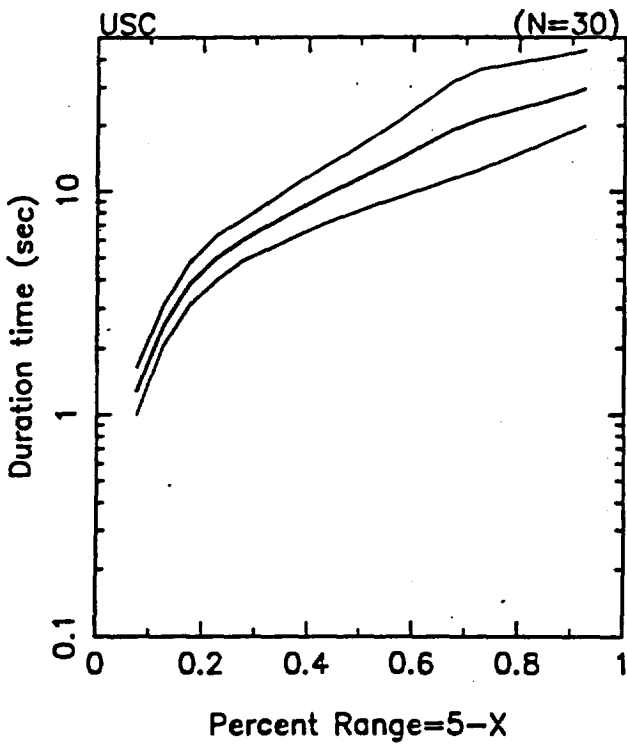
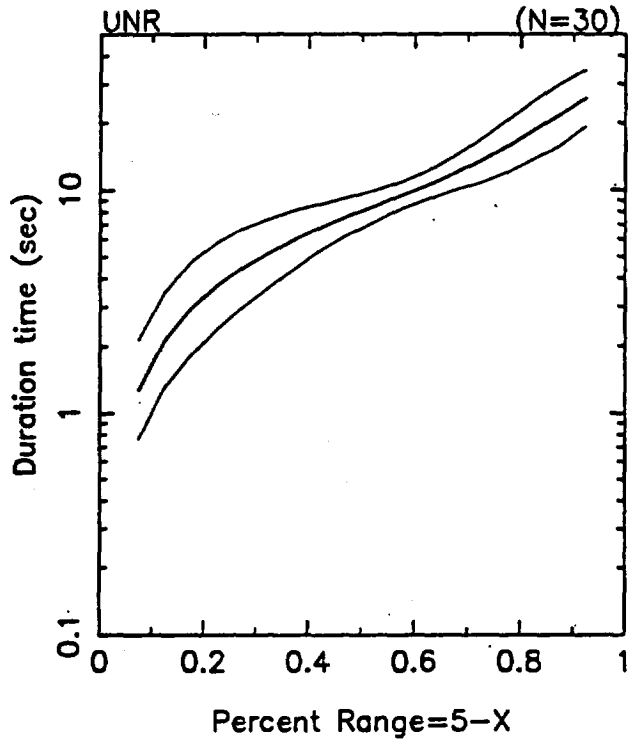
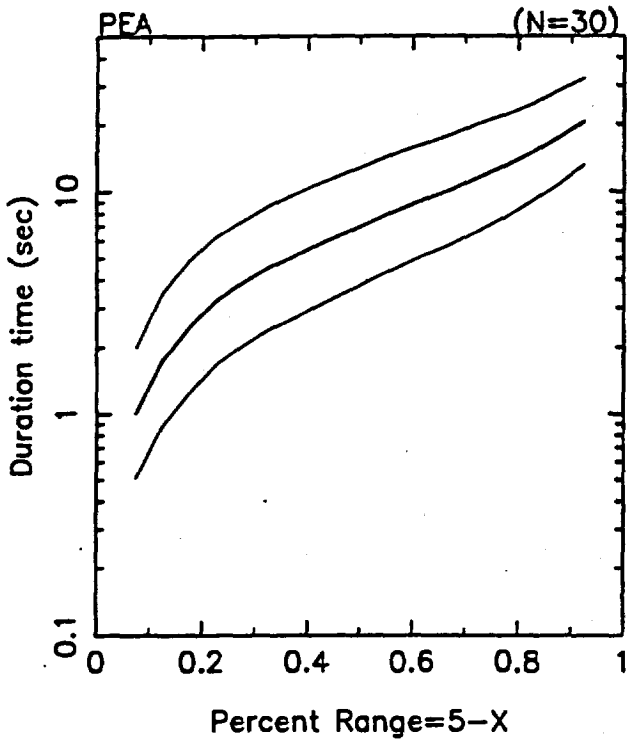


ACCELERATION DURATION



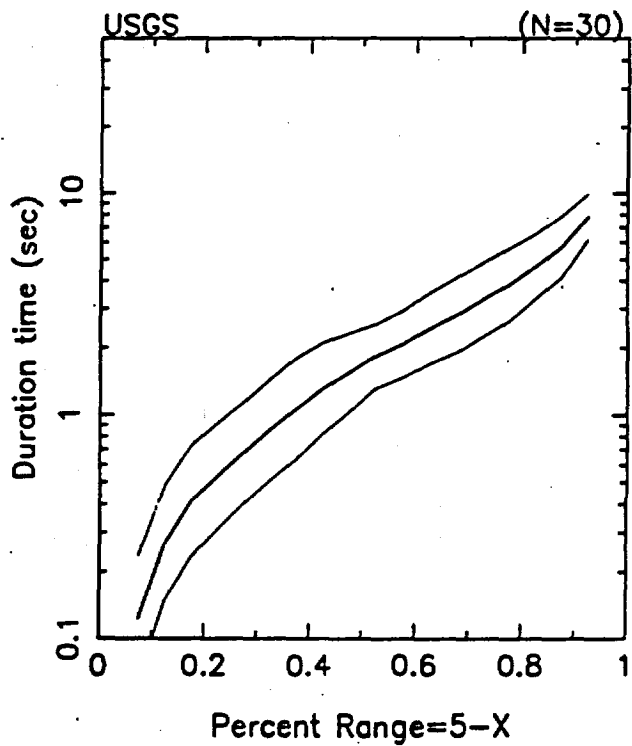
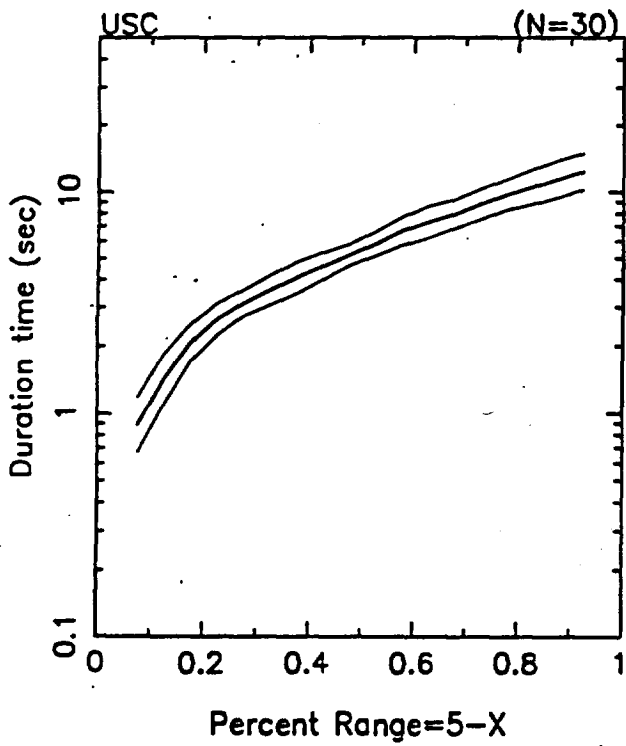
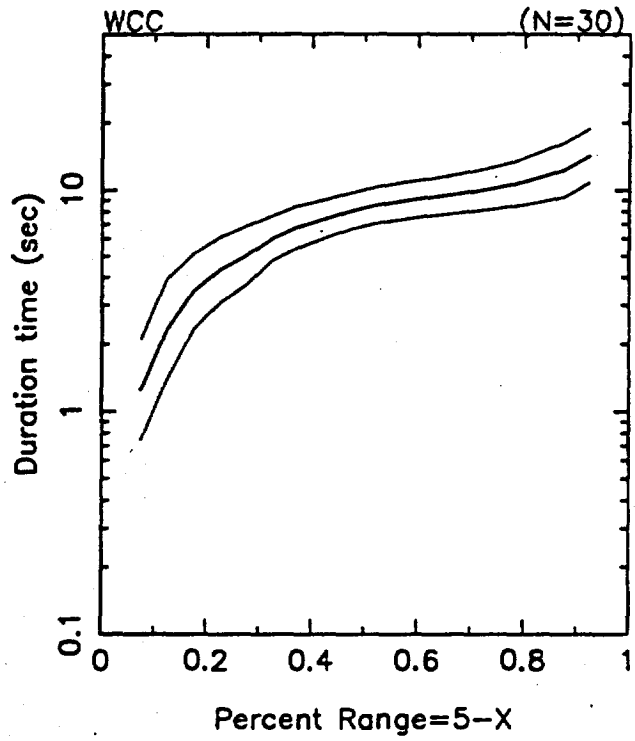
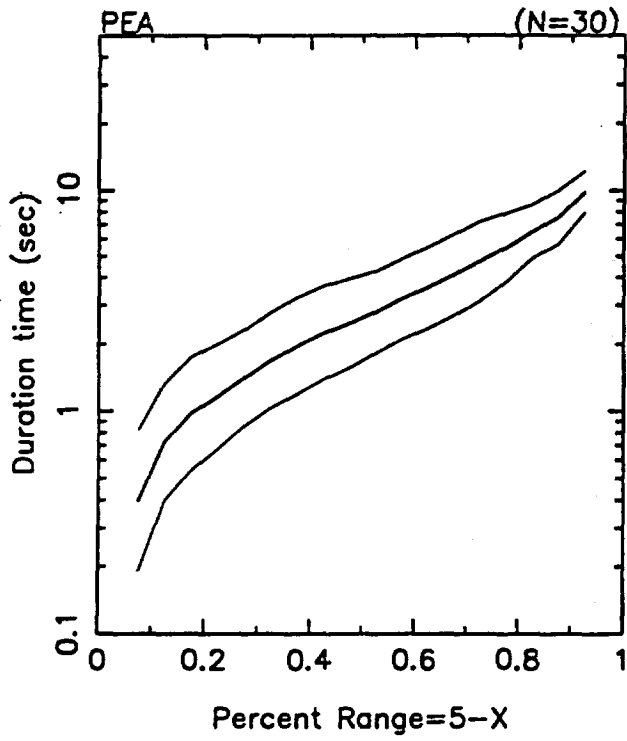
fc1, STATION # 3

ACCELERATION DURATION



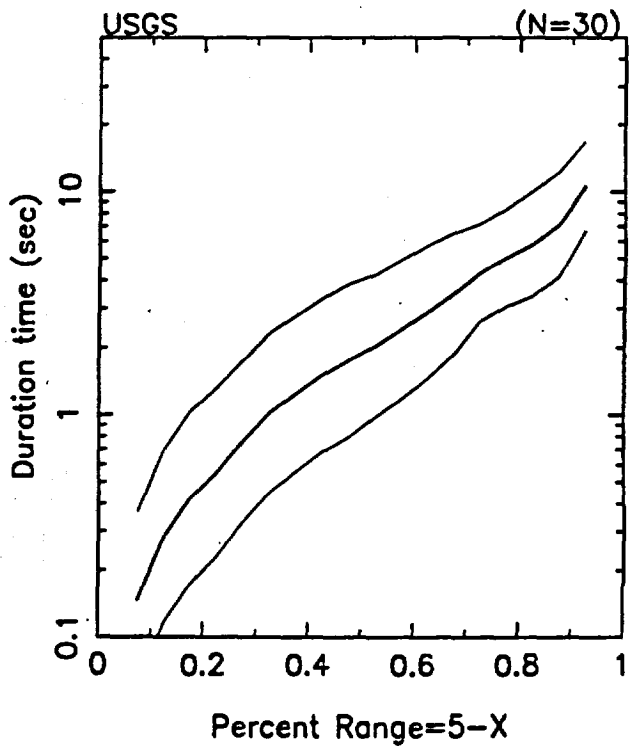
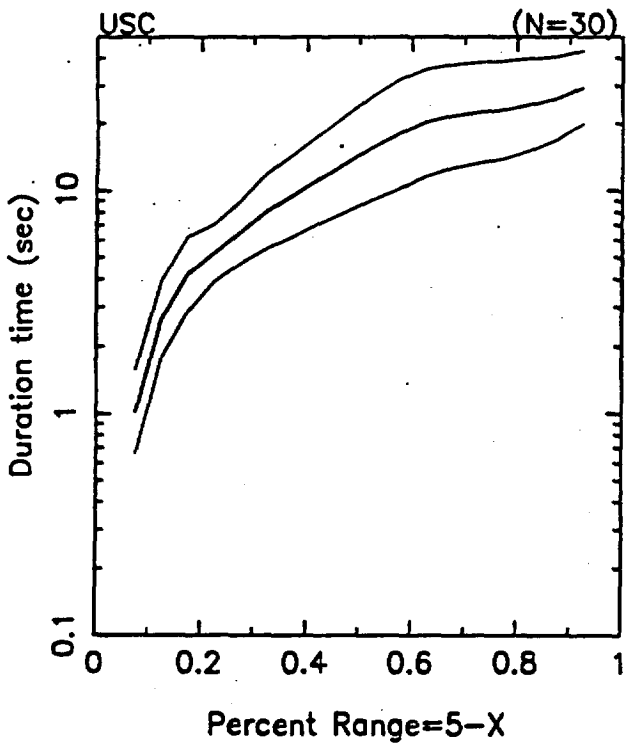
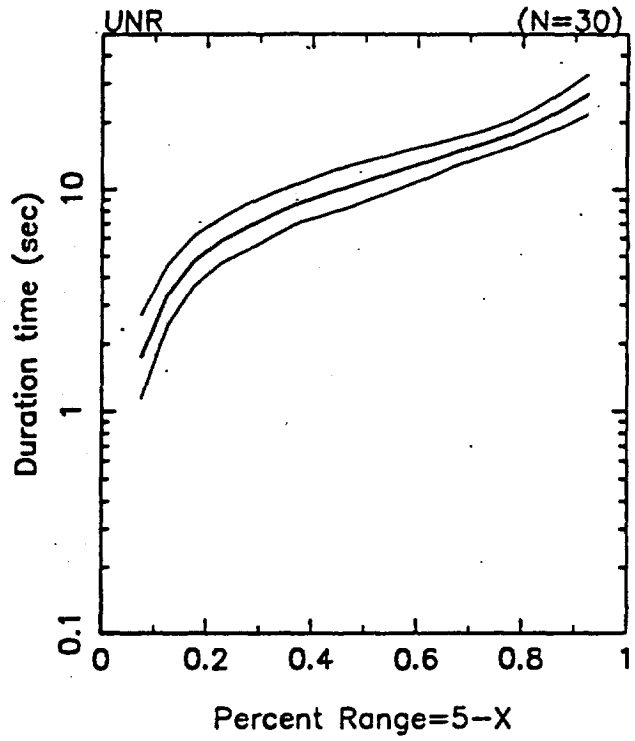
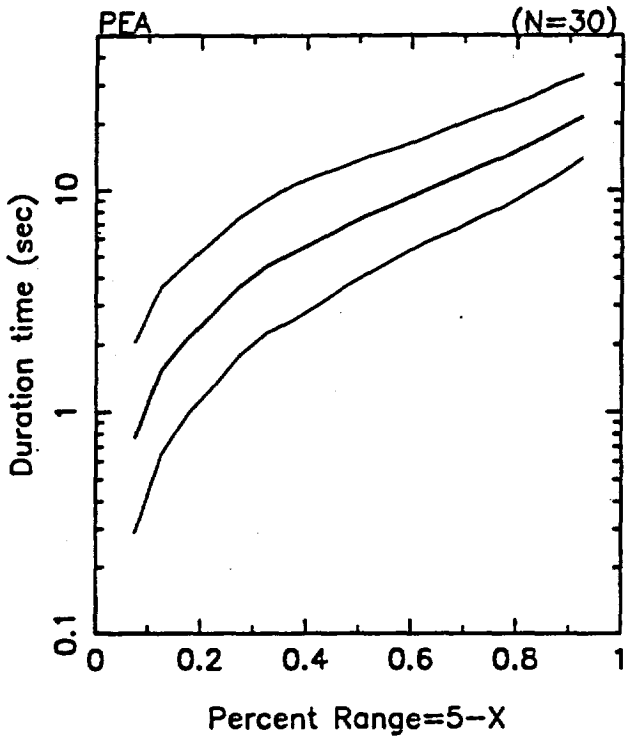
r1, STATION # 3

VELOCITY DURATION

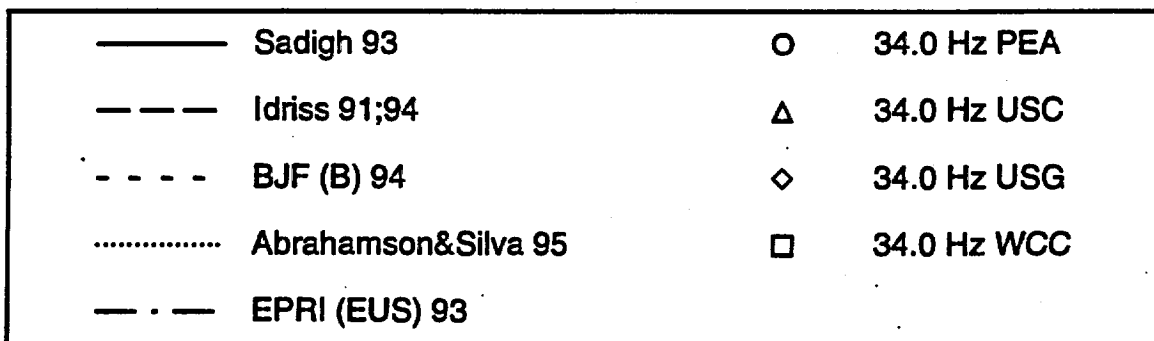
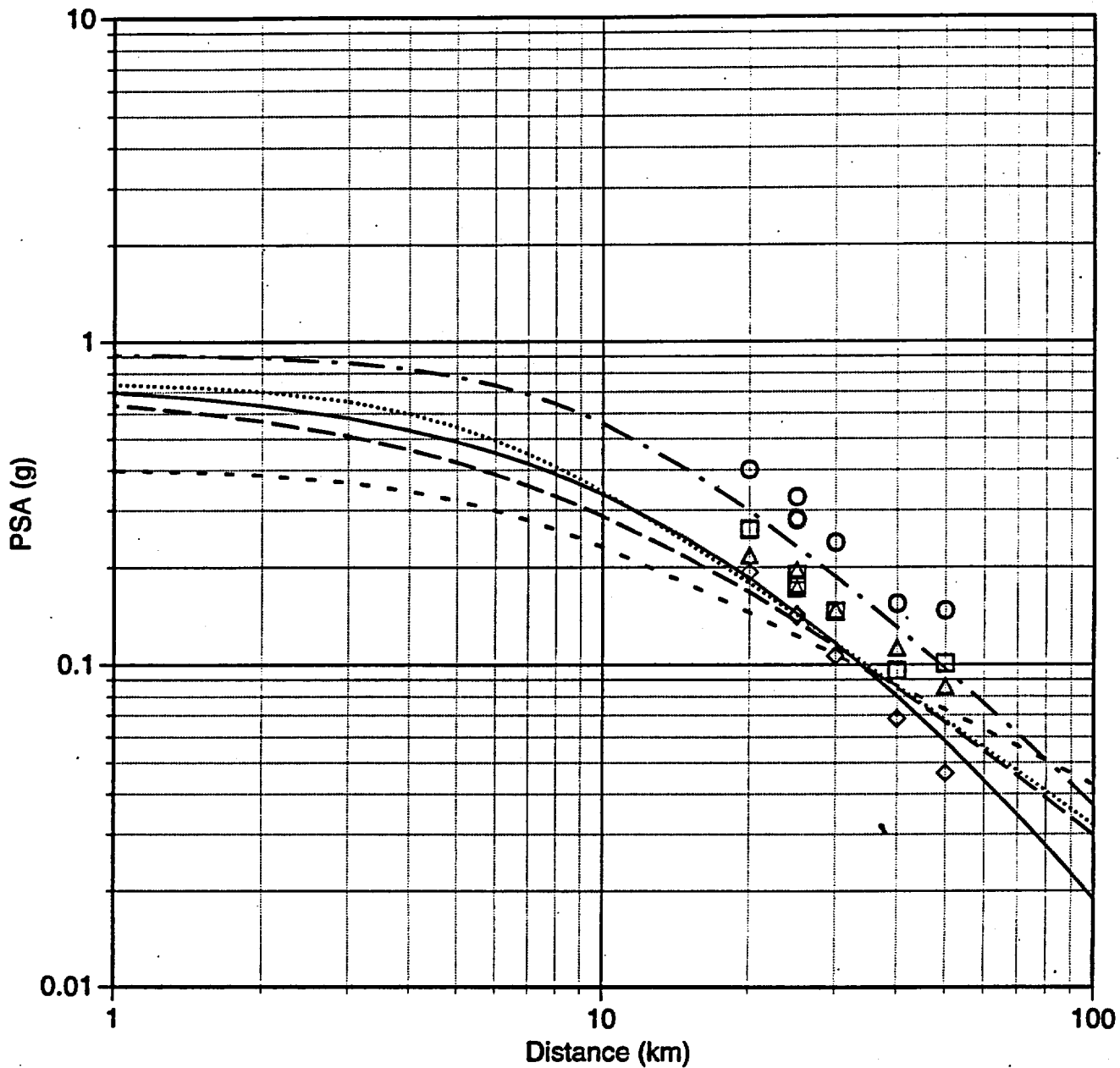


fc1, STATION # 3

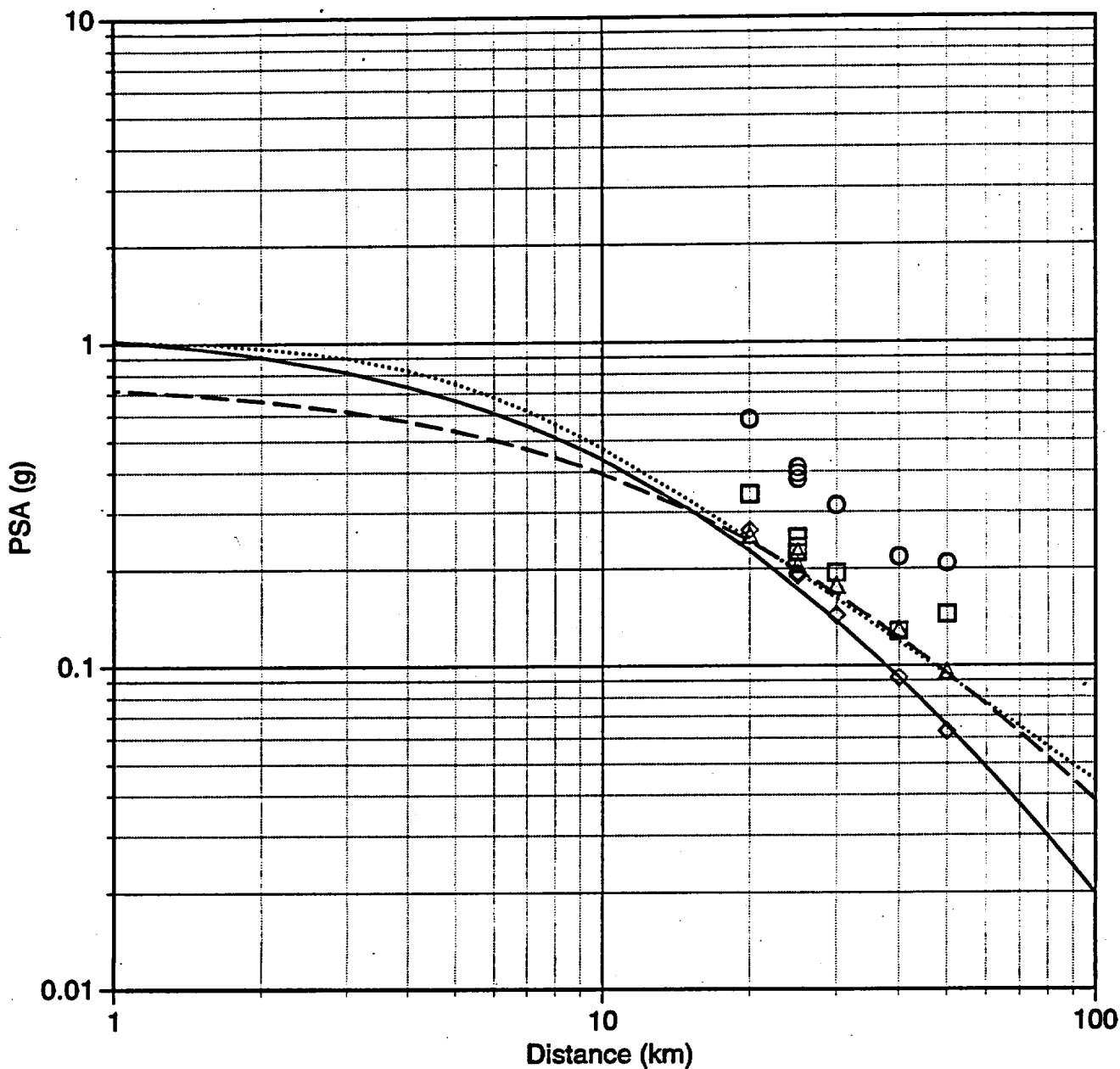
VELOCITY DURATION



## Rock Valley M 6.7 Spectral Acceleration vs Distance (PGA)

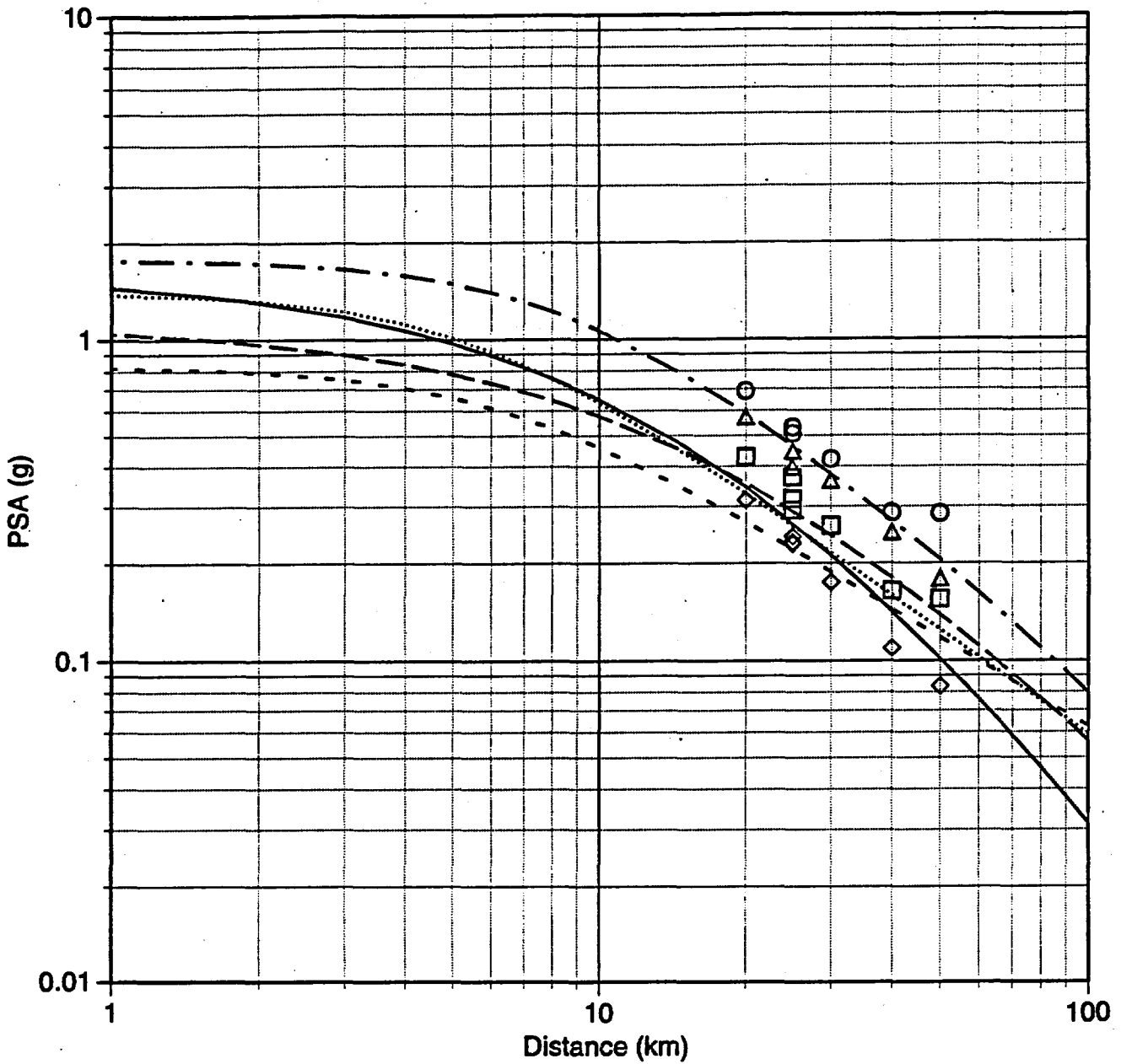


# Rock Valley M 6.7 Spectral Acceleration vs Distance (20.0 Hz)



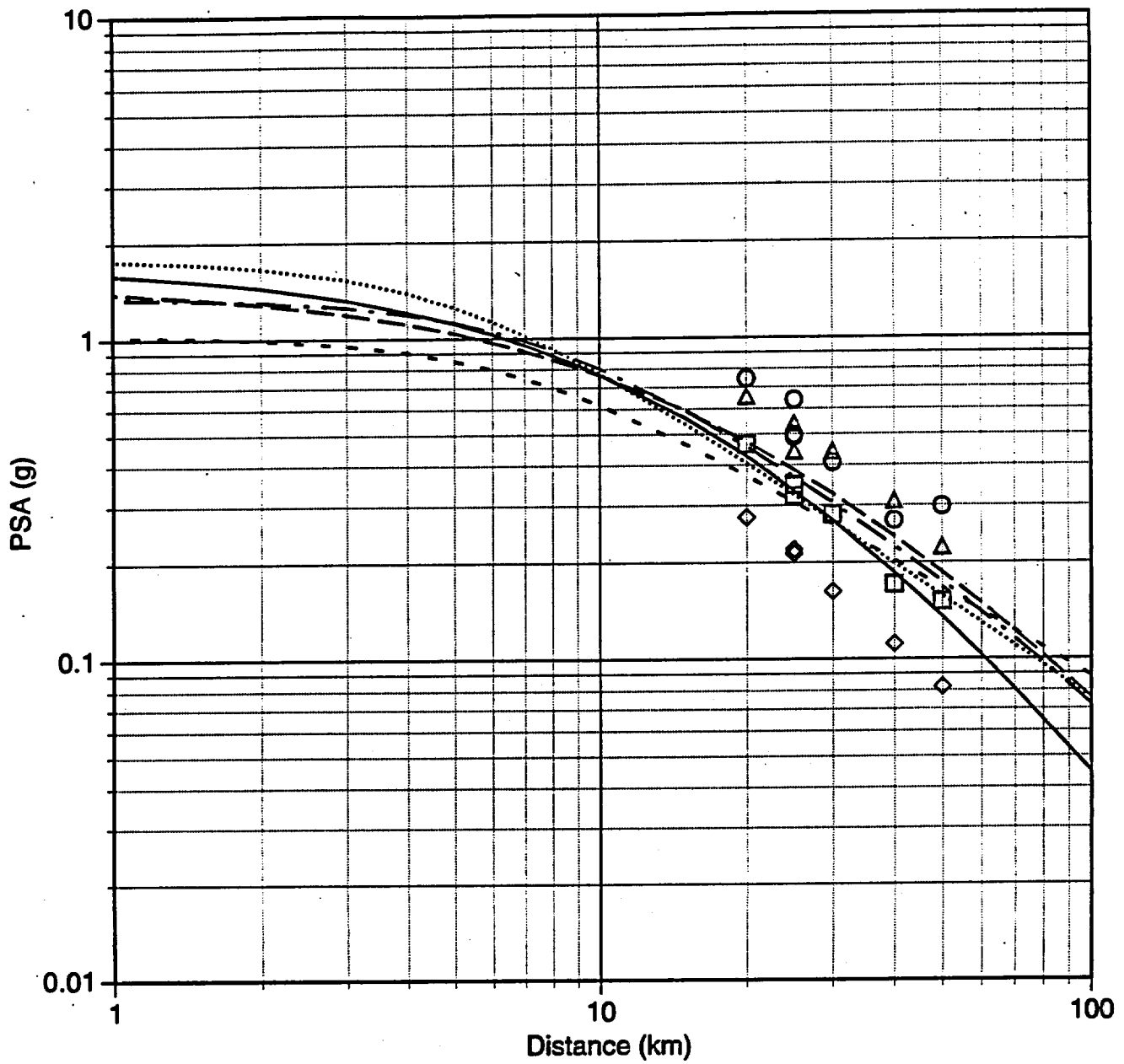
|           |                     |   |             |
|-----------|---------------------|---|-------------|
| —————     | Sadigh 93           | ○ | 20.0 Hz PEA |
| -----     | Idriss 91;94        | △ | 20.0 Hz USC |
| - . - . - | BJT (B) 94          | ◇ | 20.0 Hz USG |
| .....     | Abrahamson&Silva 95 | □ | 20.0 Hz WCC |
| -----     | EPRI (EUS) 93       |   |             |

## Rock Valley M 6.7 Spectral Acceleration vs Distance (10.0 Hz)



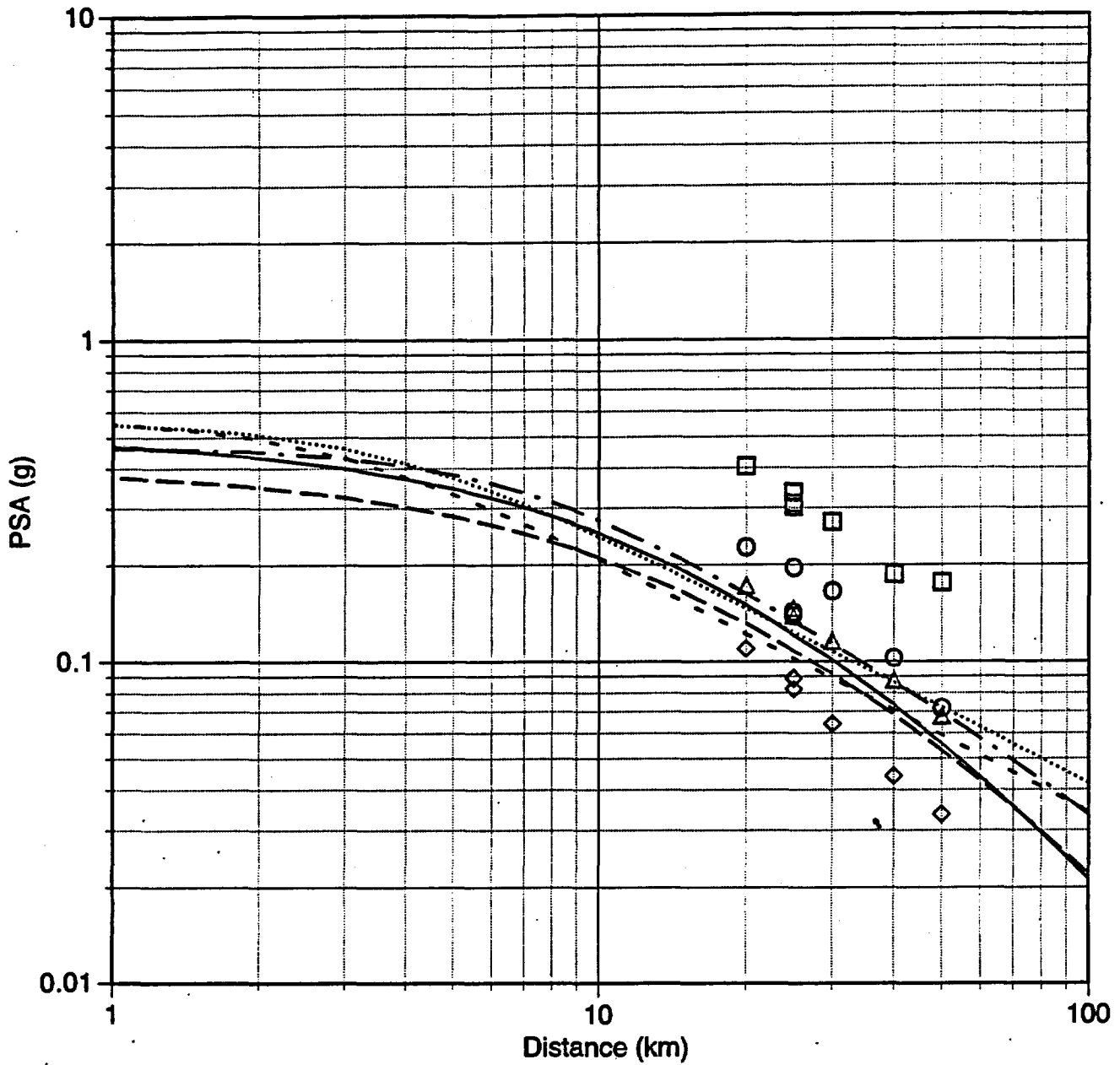
|       |                     |   |             |
|-------|---------------------|---|-------------|
| —     | Sadigh 93           | ○ | 10.0 Hz PEA |
| - - - | Idriss 91;94        | △ | 10.0 Hz USC |
| - - - | BJT (B) 94          | ◇ | 10.0 Hz USG |
| ..... | Abrahamson&Silva 95 | □ | 10.0 Hz WCC |
| - . - | EPRI (EUS) 93       |   |             |

# Rock Valley M 6.7 Spectral Acceleration vs Distance (5.0 Hz)



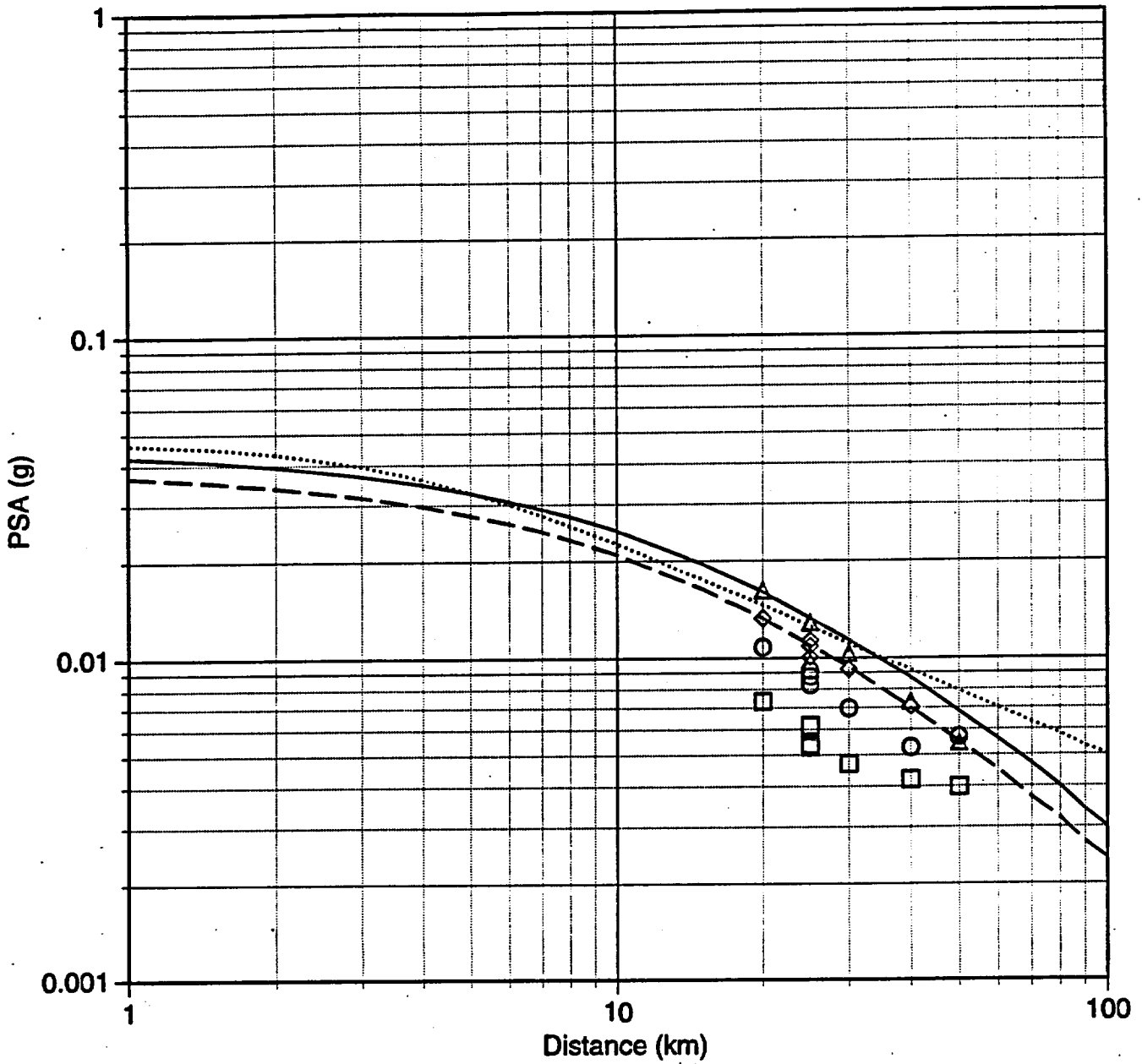
|         |                     |   |            |
|---------|---------------------|---|------------|
| —       | Sadigh 93           | ○ | 5.0 Hz PEA |
| - - -   | Idriss 91;94        | △ | 5.0 Hz USC |
| · · ·   | BJT (B) 94          | ◇ | 5.0 Hz USG |
| - · - · | Abrahamson&Silva 95 | □ | 5.0 Hz WCC |
| - - - - | EPRI (EUS) 93       |   |            |

# Rock Valley M 6.7 Spectral Acceleration vs Distance (1.0 Hz)



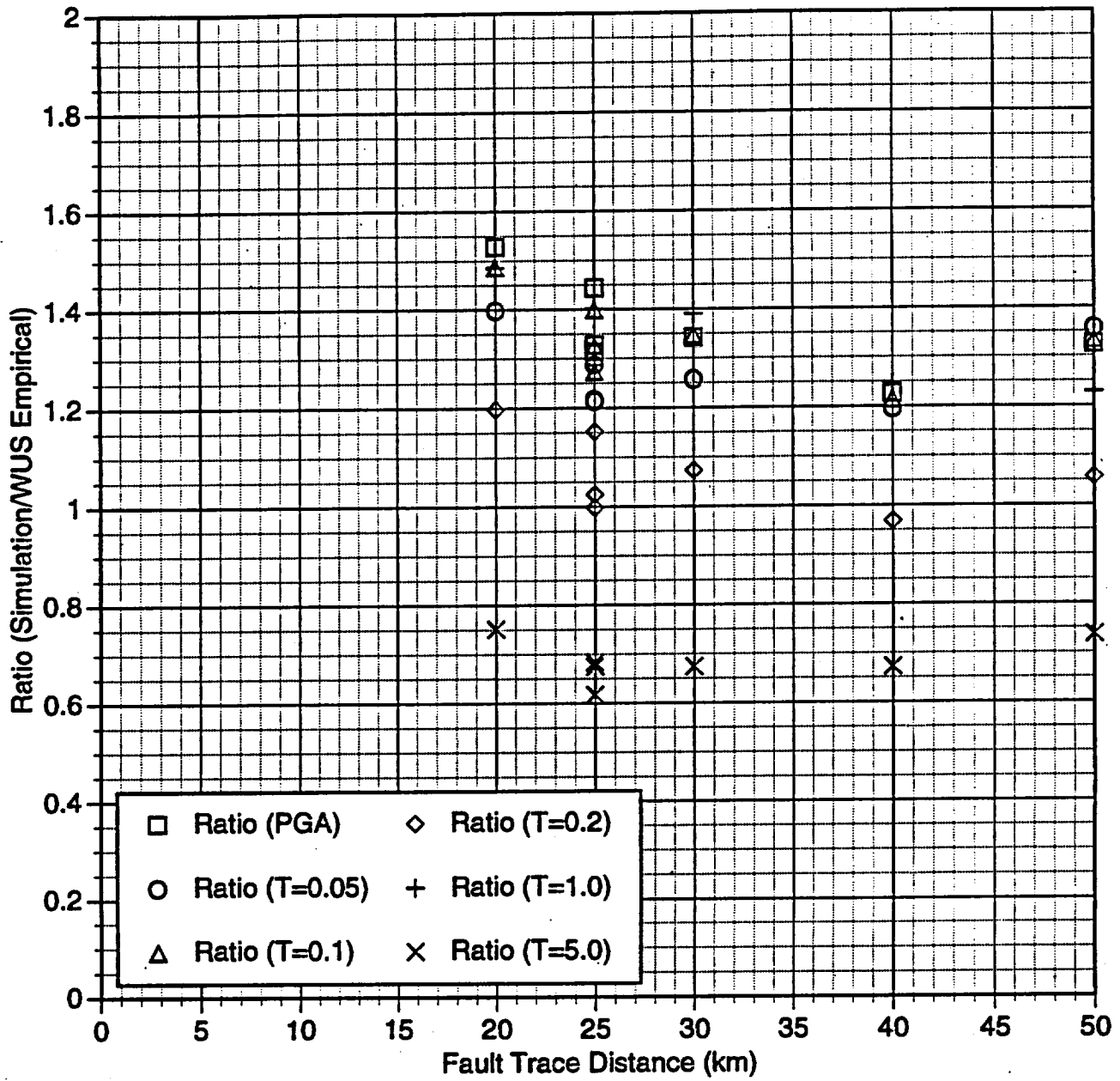
|         |                     |   |            |
|---------|---------------------|---|------------|
| —       | Sadigh 93           | ○ | 1.0 Hz PEA |
| - - -   | Idriss 91;94        | △ | 1.0 Hz USC |
| .....   | BJT (B) 94          | ◇ | 1.0 Hz USG |
| - . - . | Abrahamson&Silva 95 | □ | 1.0 Hz WCC |
| - - - - | EPRI (EUS) 93       |   |            |

# Rock Valley M 6.7 Spectral Acceleration vs Distance (0.2 Hz)

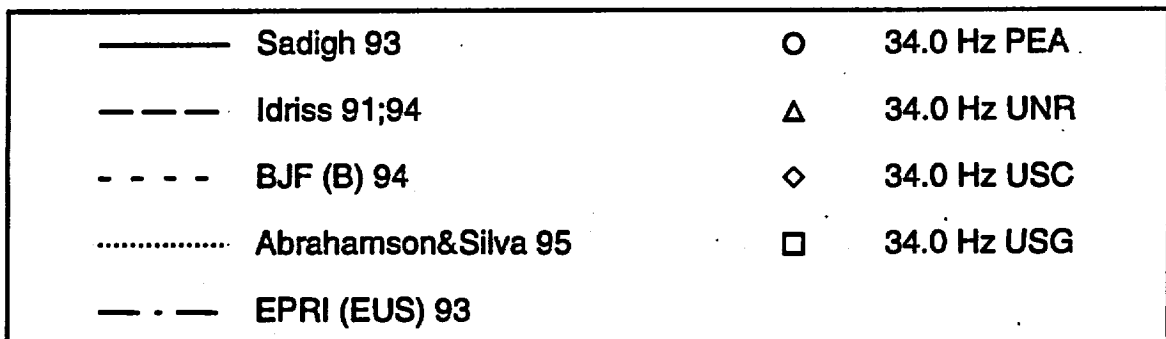
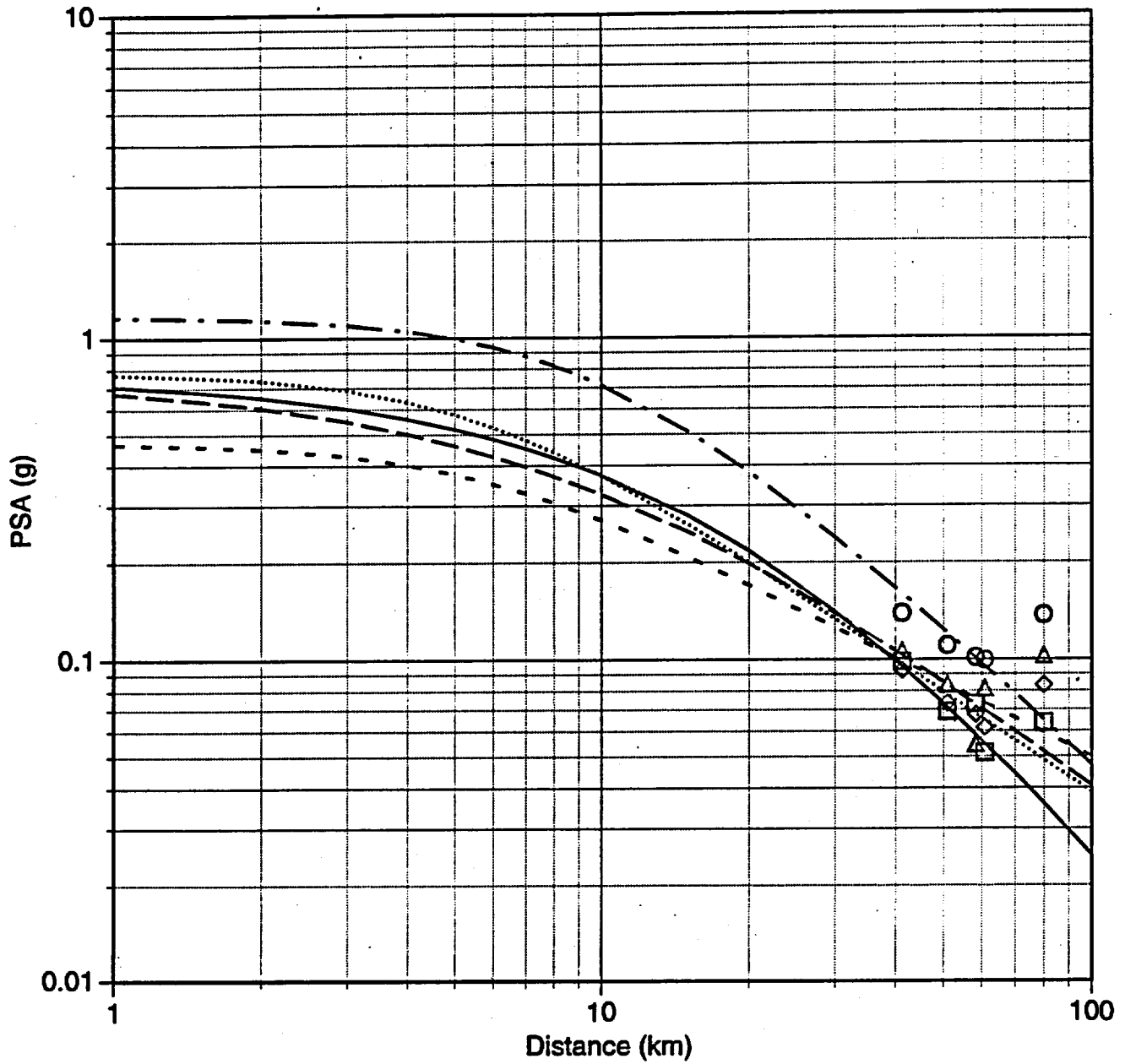


|           |                     |   |            |
|-----------|---------------------|---|------------|
| —         | Sadigh 93           | ○ | 0.2 Hz PEA |
| - - -     | Idriss 91;94        | △ | 0.2 Hz USC |
| · · · · · | BJF (B) 94          | ◇ | 0.2 Hz USG |
| - · - · - | Abrahamson&Silva 95 | □ | 0.2 Hz WCC |
| - · -     | EPRI (EUS) 93       |   |            |

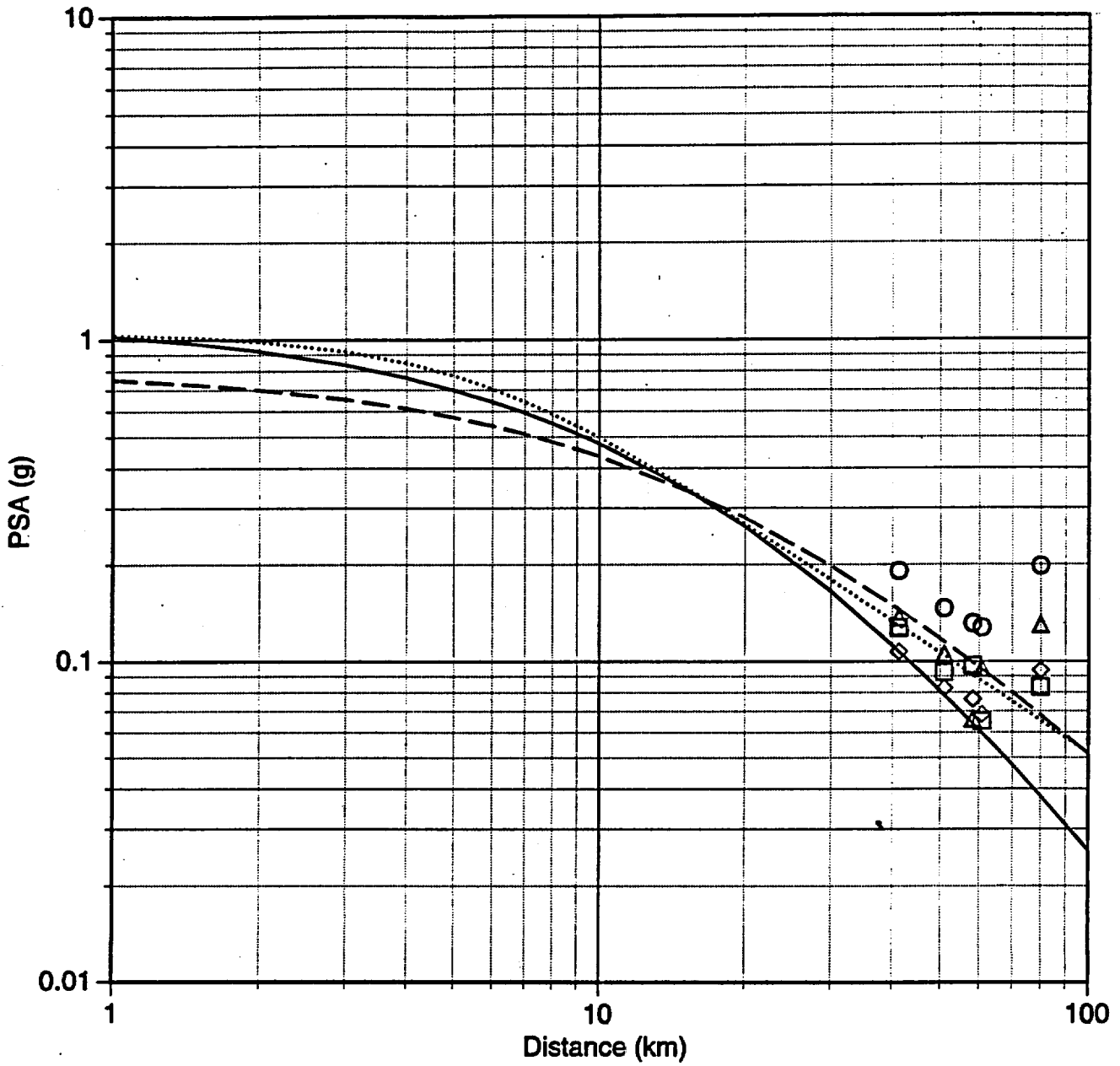
# Rock Valley



## Furnace Creek M 7.0 Spectral Acceleration vs Distance (PGA)

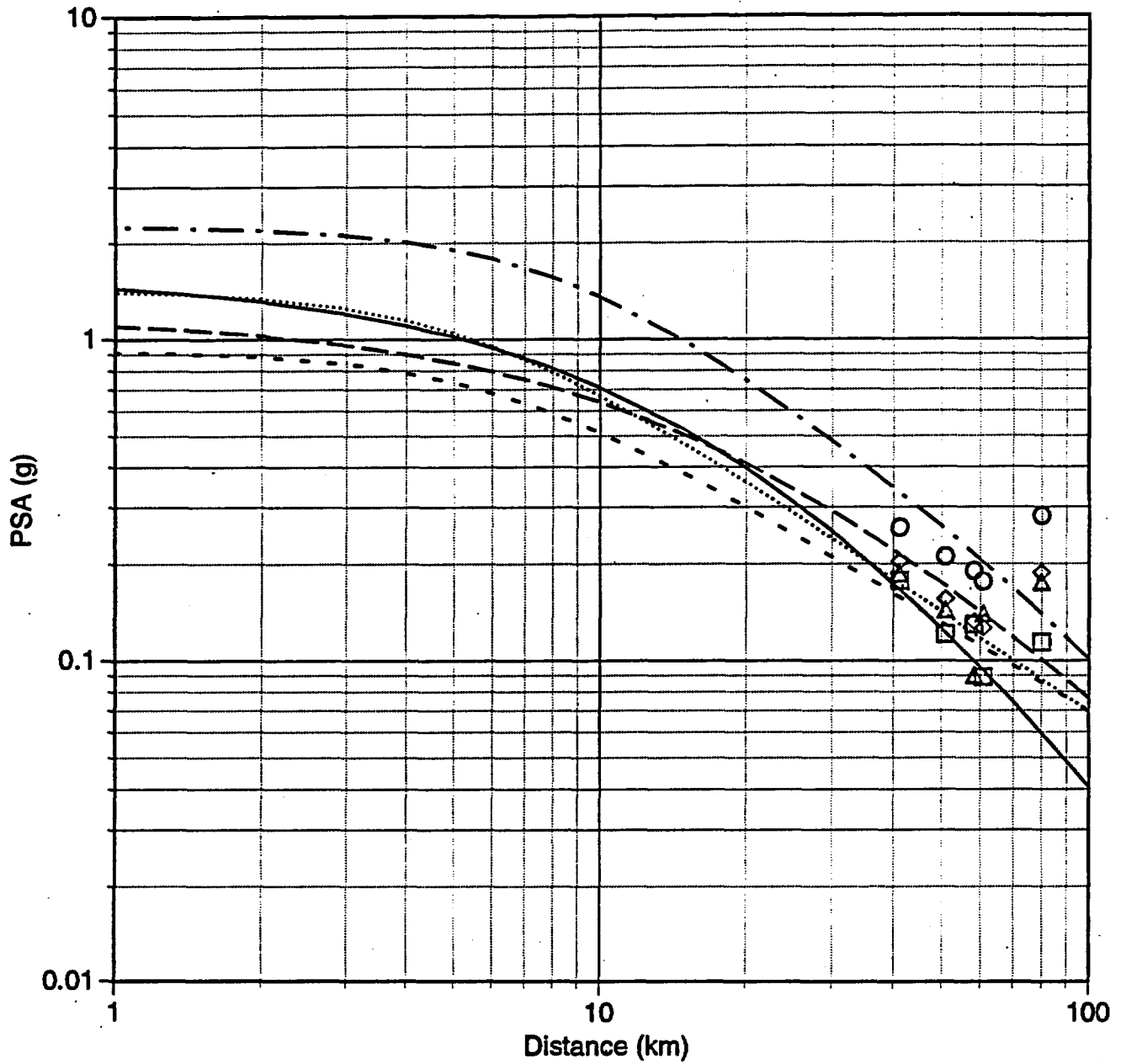


## Furnace Creek M 7.0 Spectral Acceleration vs Distance (20.0 Hz)



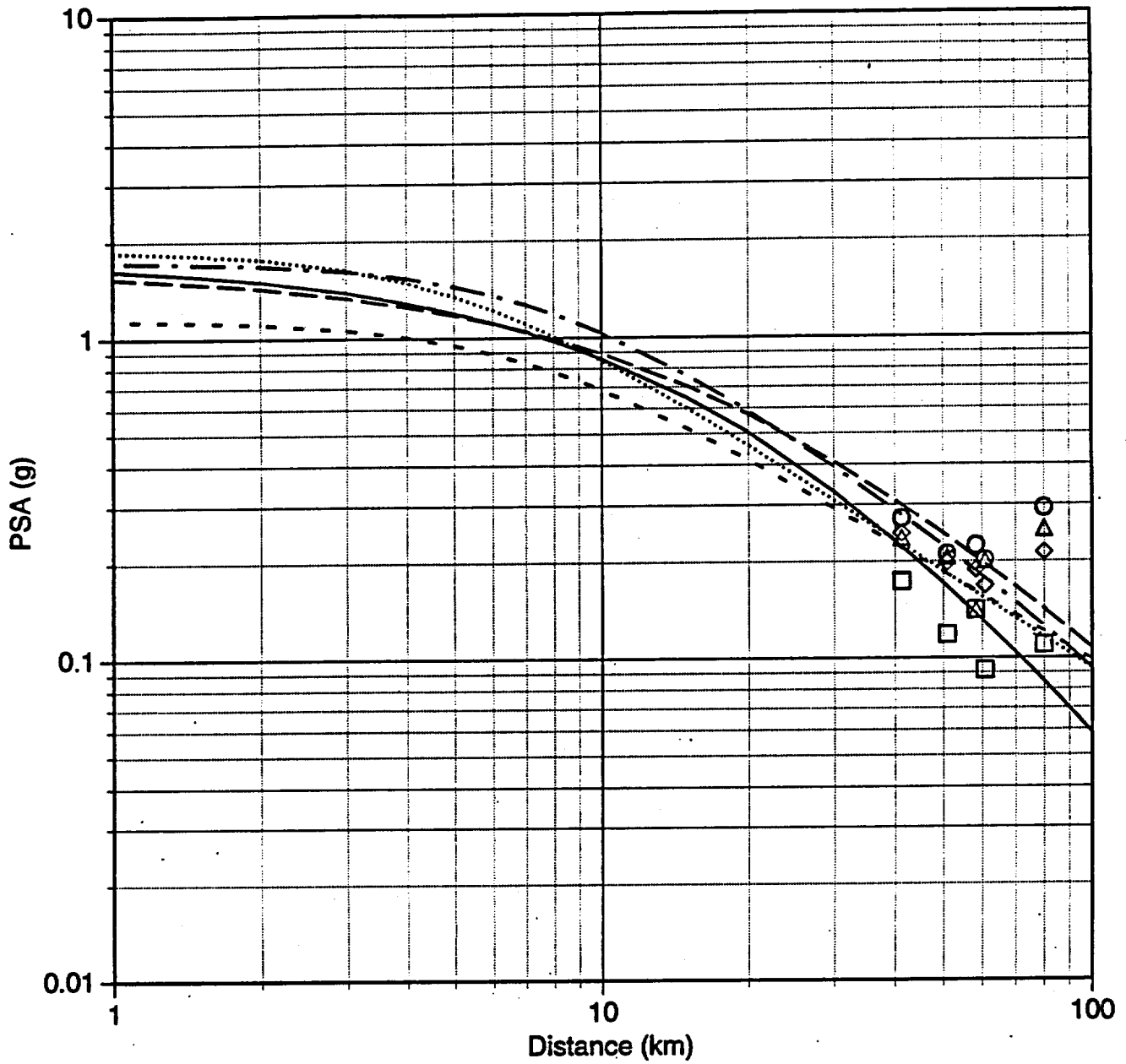
|           |                     |   |             |
|-----------|---------------------|---|-------------|
| —————     | Sadigh 93           | ○ | 20.0 Hz PEA |
| -----     | Idriss 91;94        | △ | 20.0 Hz UNR |
| - - - - - | BJF (B) 94          | ◇ | 20.0 Hz USC |
| .....     | Abrahamson&Silva 95 | □ | 20.0 Hz USG |
| - . - . - | EPRI (EUS) 93       |   |             |

## Furnace Creek M 7.0 Spectral Acceleration vs Distance (10.0 Hz)



|       |                     |   |             |
|-------|---------------------|---|-------------|
| —     | Sadigh 93           | ○ | 10.0 Hz PEA |
| - - - | Idriss 91;94        | △ | 10.0 Hz UNR |
| · · · | BJF (B) 94          | ◇ | 10.0 Hz USC |
| ..... | Abrahamson&Silva 95 | □ | 10.0 Hz USG |
| - · - | EPRI (EUS) 93       |   |             |

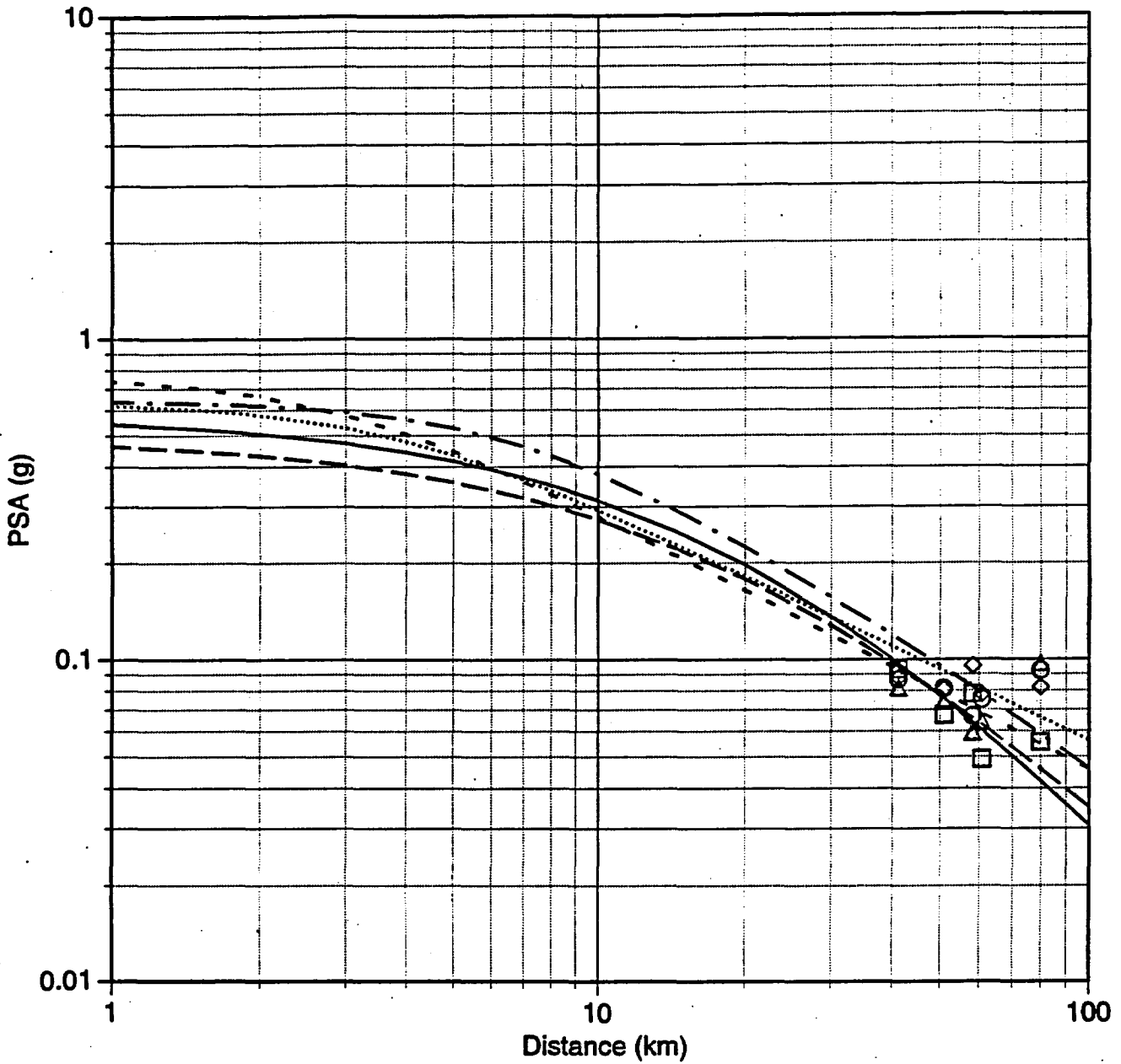
### Furnace Creek M 7.0 Spectral Acceleration vs Distance (5.0 Hz)



|  |   |
|--|---|
| <p>— Sadigh 93</p> <p>- - - Idriss 91;94</p> <p>- . - BJT (B) 94</p> <p>..... Abrahamson&amp;Silva 95</p> <p>- . - EPRI (EUS) 93</p> | <p>○ 5.0 Hz PEA</p> <p>△ 5.0 Hz UNR</p> <p>◇ 5.0 Hz USC</p> <p>□ 5.0 Hz USG</p> |
|--|---|

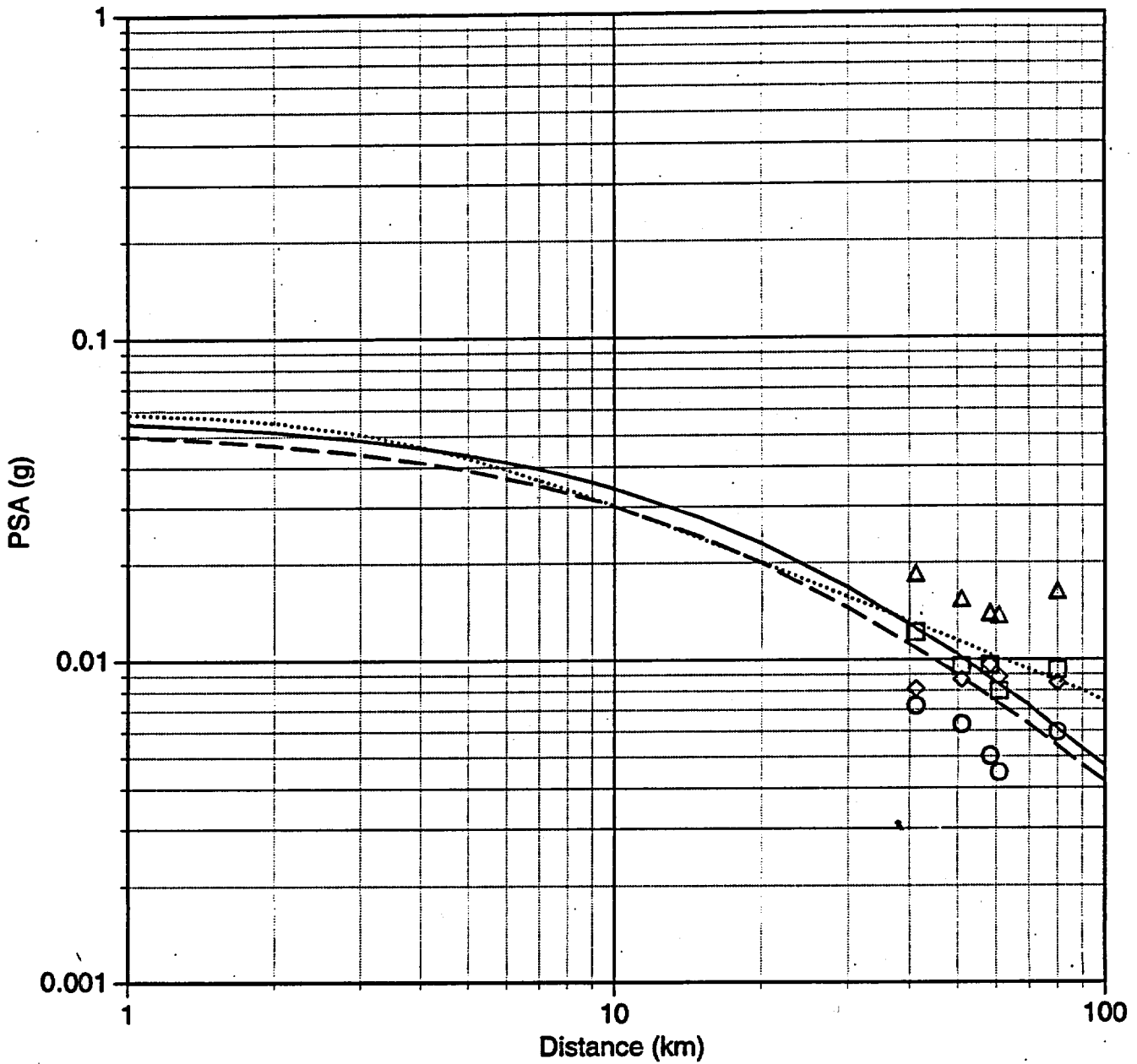
9.108

## Furnace Creek M 7.0 Spectral Acceleration vs Distance (1.0 Hz)



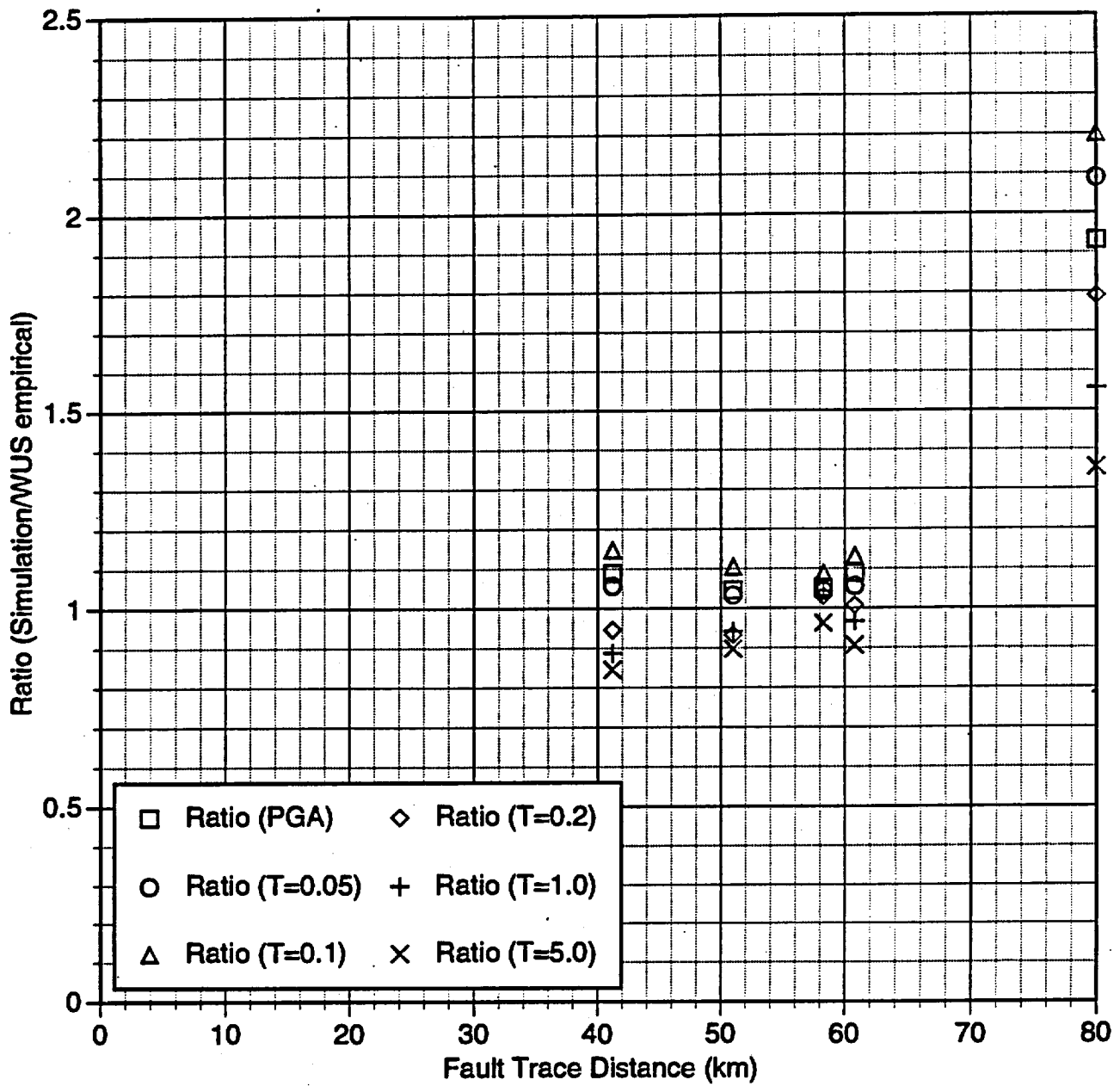
|         |                     |   |            |
|---------|---------------------|---|------------|
| —       | Sadigh 93           | ○ | 1.0 Hz PEA |
| - - -   | Idriss 91;94        | △ | 1.0 Hz UNR |
| - - - - | BJF (B) 94          | ◇ | 1.0 Hz USC |
| .....   | Abrahamson&Silva 95 | □ | 1.0 Hz USG |
| - . -   | EPRI (EUS) 93       |   |            |

## Furnace Creek M 7.0 Spectral Acceleration vs Distance (0.2 Hz)



|         |                     |   |            |
|---------|---------------------|---|------------|
| —       | Sadigh 93           | ○ | 0.2 Hz PEA |
| - - -   | Idriss 91;94        | △ | 0.2 Hz UNR |
| - . - . | BJT (B) 94          | ◇ | 0.2 Hz USC |
| .....   | Abrahamson&Silva 95 | □ | 0.2 Hz USG |
| - - - - | EPRI (EUS) 93       |   |            |

# Furnace Creek



# 10 SCENARIO EVENT GROUND MOTIONS

## **Scaling to Scenario Earthquake Magnitudes**

For the normal faulting events, the ground motions models were used to generate a M 6.4 reference event. The estimated magnitudes for the three scenario events were slightly different (table 2.4): Solitario Canyon is M 6.5 and Bow Ridge and Paintbrush Canyon are M 6.3. The simulated ground motions are adjusted for the magnitude difference using the empirical scaling relation of Sadigh and others (1993). The resulting scale factors are shown in figure 10.1. They range from about a 5 percent difference at high-frequencies to a 15 percent difference at long periods.

FIGURE 10.1 - NEAR HERE

## **Estimation of Median values and Variability**

The median ground motions for each scenario were computed giving equal weight to the response spectra predicted by each modeling method (shown in Sections 8 and 9) with the magnitude scaling described above to adjust for the specific scenario magnitudes.

The variability of the predicted motions are presented in terms of the sources of variability discussed in Section 4. Rather than develop uncertainty estimates for each model separately, composite uncertainties are developed for each scenario that are then applied to the composite median for the corresponding scenario. This approach is reasonable for models that have about the same level of complexity.

The first part of the total variability is the modeling aleatory uncertainty ( $\sigma_{\text{model}}$ ) which is estimated from the validations with previous earthquakes. The estimates of  $\sigma_{\text{model}}$  for the LSM event for the six models are shown in figure 10.2. Since the LSM validation is based on only five stations, the results have a large uncertainty (the uncertainty of the estimated uncertainty is large). In particular, the WCC estimate of  $\sigma_{\text{model}}$  is much larger than for the other models (or for previous validations of the WCC model) and is not considered representative of  $\sigma_{\text{model}}$  for this model. As a result, it is excluded from the average shown in figure 10.2. The S-cubed estimate of  $\sigma_{\text{model}}$  is also excluded from the average because this model is not a numerical simulation.

FIGURE 10.2 - NEAR HERE

The PEA, WCC, and USGS models provided estimates of  $\sigma_{\text{model}}$  for other events than the LSM event (Appendix B). These other estimates of  $\sigma_{\text{model}}$  are shown in figure 10.3 along with the average  $\sigma_{\text{model}}$  from the LSM event. In general, these other estimates of the modeling uncertainty are consistent with the average LSM modeling uncertainty. Since LSM is only based on 5 stations, an average of the four estimates is computed and this average is applied to all of the models. The reason for doing this rather than using the model specific estimates is that estimates of  $\sigma_{\text{model}}$  for other events have not been developed for all of the models; the poorly resolved LSM estimate of  $\sigma_{\text{model}}$  would have to be used for these models.

FIGURE 10.3 - NEAR HERE

The second part of the variability is the modeling epistemic term. This term represents the variability in the median predictions from the different methods. It is computed from the standard error of the differences in the medians from the different methods. The computed  $\sigma_{\text{method}}$  for each scenario is shown in figure 10.4.

FIGURE 10.4 - NEAR HERE

The third part of the variability is the parametric aleatory uncertainty. This is the variation in the ground motions from the multiple realizations of the source process including random variations in the hypocentral location, slip model, and other source parameters. It is given by the standard error of the realizations for each method independently. The estimates of the parametric aleatory uncertainty are shown in figures 10.5a-f for each scenario event. The average of the standard errors for the different methods is used for each scenario.

FIGURES 10.5A, 10.5B, 10.5C, 10.5D, 10.5E, 10.5F - NEAR HERE

The fourth and final part of the variability is the parametric epistemic uncertainty. This is the variation due to unknown distributions of source parameters and source geometry. In this study, the variability due to uncertainty in the source parameters distributions (for example, what is the uncertainty in the specified range of hypocenters?) was not considered because uncertainties are much smaller than the parameteric aleatory uncertainty. The only parametric epistemic uncertainty considered is that due to uncertainty in the dip of the fault. The resulting parametric epistemic uncertainty is shown in figure 10.6.

FIGURE 10.6 - NEAR HERE

The total uncertainty for each scenario is computed by combining these four sources of uncertainty assuming that they are uncorrelated. The total variability is shown in Figures 10.7a-f.

FIGURES 10.7A, 10.7B, 10.7C, 10.7D, 10.7E, 10.7F - NEAR HERE

As noted in Section 4, the simple model total uncertainty should provide some constraints on the total uncertainty for more complex models. In particular, the assumption that the various sources of variability are uncorrelated can be indirectly evaluated in this manner. The components of variability for a point source with event-specific  $\Delta\sigma$  is shown in figure 10.8. The total variability from the simulations is compared to the total variability from the simple point source model in figures 10.9a-f. There is reasonable agreement between the point source and more complex model total variability, indicating that sufficient variability has been accounted for (the model results may not have every source of variability in the complex models, but under the assumption that the parameters are uncorrelated, the results have accounted for enough sources of variability).

FIGURE 10.8 - NEAR HERE

FIGURES 10.9A, 10.9B, 10.9C, 10.9D, 10.9E, 10.9F - NEAR HERE

The standard error for WNA empirical attenuation relations (average of Sadigh and others, 1993; Idriss, 1994; Boore and others, 1994; and Abrahamson and Silva, 1995) is also shown in figures 10.9a-f. The standard errors for the numerical simulations are larger than the standard errors for the empirical attenuation relations by about 0.1 natural log units on average. The larger standard errors would have a large effect on a probabilistic hazard calculation.

### **Median Ground Motions**

The median ground motions for Yucca Mountain are shown in figure 10.10. As expected, the nearby normal faulting events (Bow Ridge, Solitario Canyon, and Paintbrush Canyon faults) produce the largest median ground motions due to the short distance to the site. As discussed in Section 8, these near-source ground motions are very large at high frequencies with median spectral accelerations up to 1 g at 34 Hz. The Bare Mountain and Rock Valley events produce similar ground motions with spectral accelerations of 0.2 to 0.3 g at 34 Hz. The distant Furnace Creek event produces the smallest high frequency motions (less than 0.1 g at 34 Hz), but its long period motions are similar to the Bare Mountain and Rock Valley events due to the larger magnitude of the Furnace Creek event.

**FIGURE 10.10 - NEAR HERE**

### **84th Percentile Ground Motions**

The 84th percentile ground motions are computed by combining the median ground motion shown in figure 10.10 with the total variability for each scenario (fig. 10.9a-f). The 84th percentile ground motions are shown in figure 10.11.

**FIGURE 10.11 - NEAR HERE**

## Conclusions

The scenario events considered in this study are for magnitudes that are larger than the events that dominated the hazard at the at the  $10^{-3}$  to  $10^{-4}$  annual probability level, based on the Exploratory Studies Facilities (ESF) study. The ESF study found that the dominant event for  $10^{-3}$  to  $10^{-4}$  annual probability level is M 5.5 to 6.0 at distances of 7 to 10 km. The scenario events are larger than this magnitude range. The primary use of the scenario events for the PSHA will be to constrain the large magnitude, close distance part of the attenuation relation.

The high frequency ( $T < 0.2$  sec) ground motions for the normal faulting scenario events are larger than predicted by standard California rock attenuation relations. As noted earlier, this is in part due to the lower kappa at Yucca Mountain as compared to typical California rock sites. In contrast, the extensional regime attenuation relation developed by Spudich and others (1996) based on empirical recordings from a world-wide data base produces high frequency ground motions that are lower than predicted by California rock attenuation relations. The Spudich and others model does not take the low kappa at Yucca Mountain into account, but kappa alone cannot explain all of the differences.

The lower ground motions from the Spudich study have been interpreted as lower stress drops for extensional regime events. The numerical modeling methods used in the scenario study, in general, do not use different stress drops for normal faulting events as compared to reverse events. The modeling procedures used in this study would have produced the same ground motions (with opposite polarity) if the sources had been specified as

reverse events instead of normal events. If the stress drops are lower for normal faulting events, then the scenario earthquake ground motions would be too large; however, the modeling procedures were evaluated against the 1992 Little Skull Mountain data in section 6 and generally produced unbiased results when the preferred model (SM2) was used, suggesting that the stress drops used in the modeling study were appropriate (at least for the Little Skull Mountain Earthquake). In contrast, the Spudich and others attenuation model significantly under predicts the Little Skull Mountain ground motions. (It is worth noting that in the constrained exercise (SM1), several of the models significantly overpredicted the Little Skull Mtn ground motions (Fig 6.16).) Tests with additional earthquake recordings will be needed to resolve this discrepancy between the scenario ground motions and the Spudich attenuation relation.

In addition to the median, the standard error is also important to the hazard analysis. The standard errors for the scenario events tend to be larger than those used for the WUS empirical models by about 0.1 to 0.2 natural log units and similar to the standard errors for the Spudich model. This differences could significantly increase the estimate of the hazard at the site at low annual probability levels.

## Figure Captions

Figure 10.1 Scale factors for magnitude scaling.

Figure 10.2 Comparison of modeling standard errors for LSM validation exercise.

Figure 10.3 Comparison of modeling standard errors for LSM with validations for other events.

Figure 10.4 Variability due to differences in the median predictions of the methods.

Figure 10.5 (a) Parametric variability due to multiple source realizations for Bow Ridge.

Figure 10.5 (b) Parametric variability due to multiple source realizations for Paintbrush Canyon.

Figure 10.5 (c) Parametric variability due to multiple source realizations for Bare Mountain.

Figure 10.5 (d) Parametric variability due to multiple source realizations for Solitario Canyon.

Figure 10.5 (e) Parametric variability due to multiple source realizations for Rock Valley.

**Figure 10.5 (f) Parametric variability due to multiple source realizations for Furnace Creek.**

**Figure 10.6 Parametric variability due to dip uncertainty.**

**Figure 10.7 (a) Components of variability for Bow Ridge.**

**Figure 10.7 (b) Components of variability for Paintbrush Canyon.**

**Figure 10.7 (c) Components of variability for Bare Mountain.**

**Figure 10.7 (d) Components of variability for Solitario Canyon.**

**Figure 10.7 (e) Components of variability for Rock Valley.**

**Figure 10.7 (f) Components of variability for Furnace Creek.**

**Figure 10.8 Components of variability for point source model.**

**Figure 10.9 (a) Comparison of variability for Bow Ridge.**

**Figure 10.9 (b) Comparison of variability for Paintbrush Canyon.**

**Figure 10.9 (c) Comparison of variability for Bare Mountain.**

**Figure 10.9 (d) Comparison of variability for Solitario Canyon.**

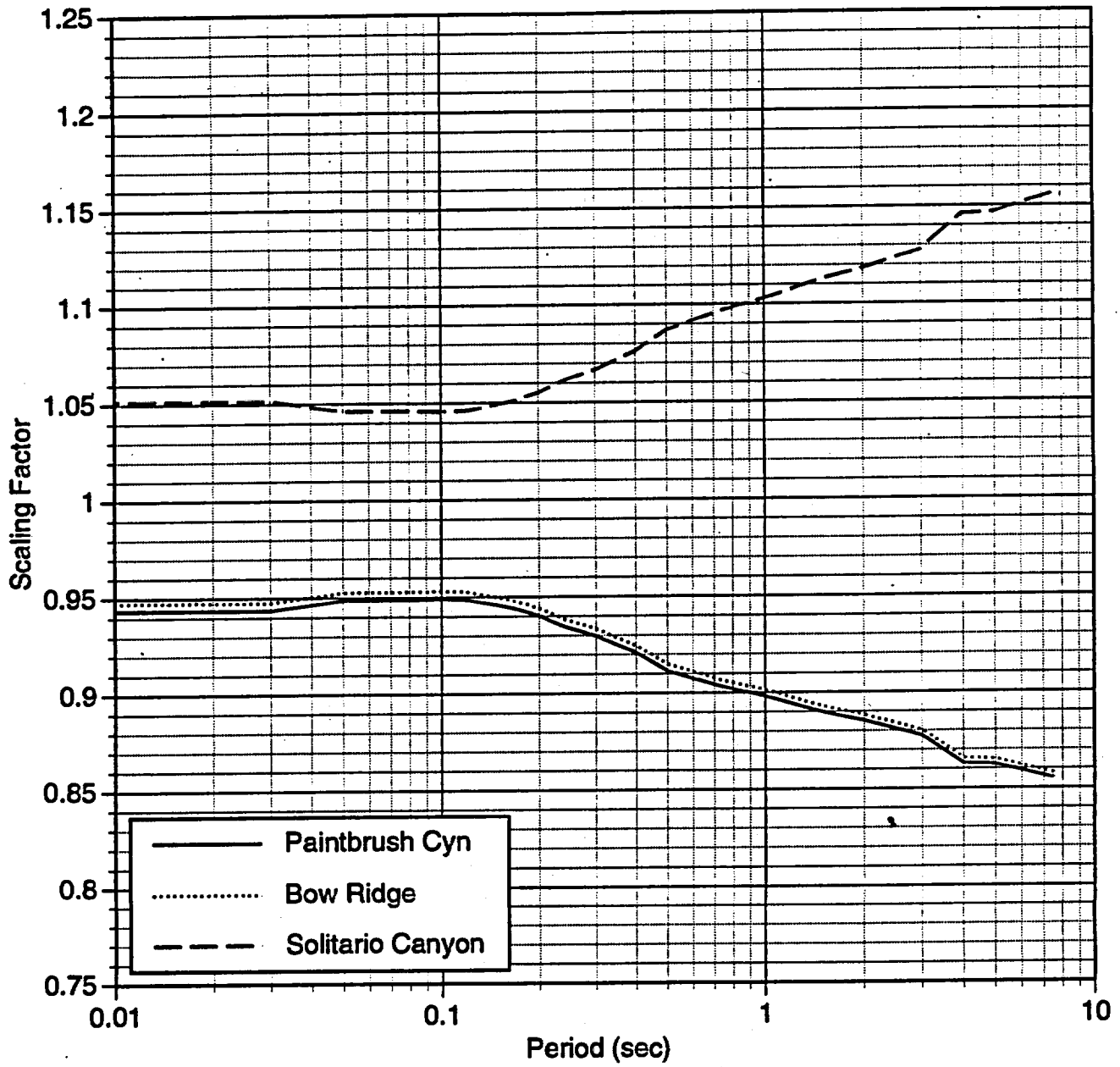
Figure 10.9 (e) Comparison of variability for Rock Valley.

Figure 10.9 (f) Comparison of variability for Furnace Creek.

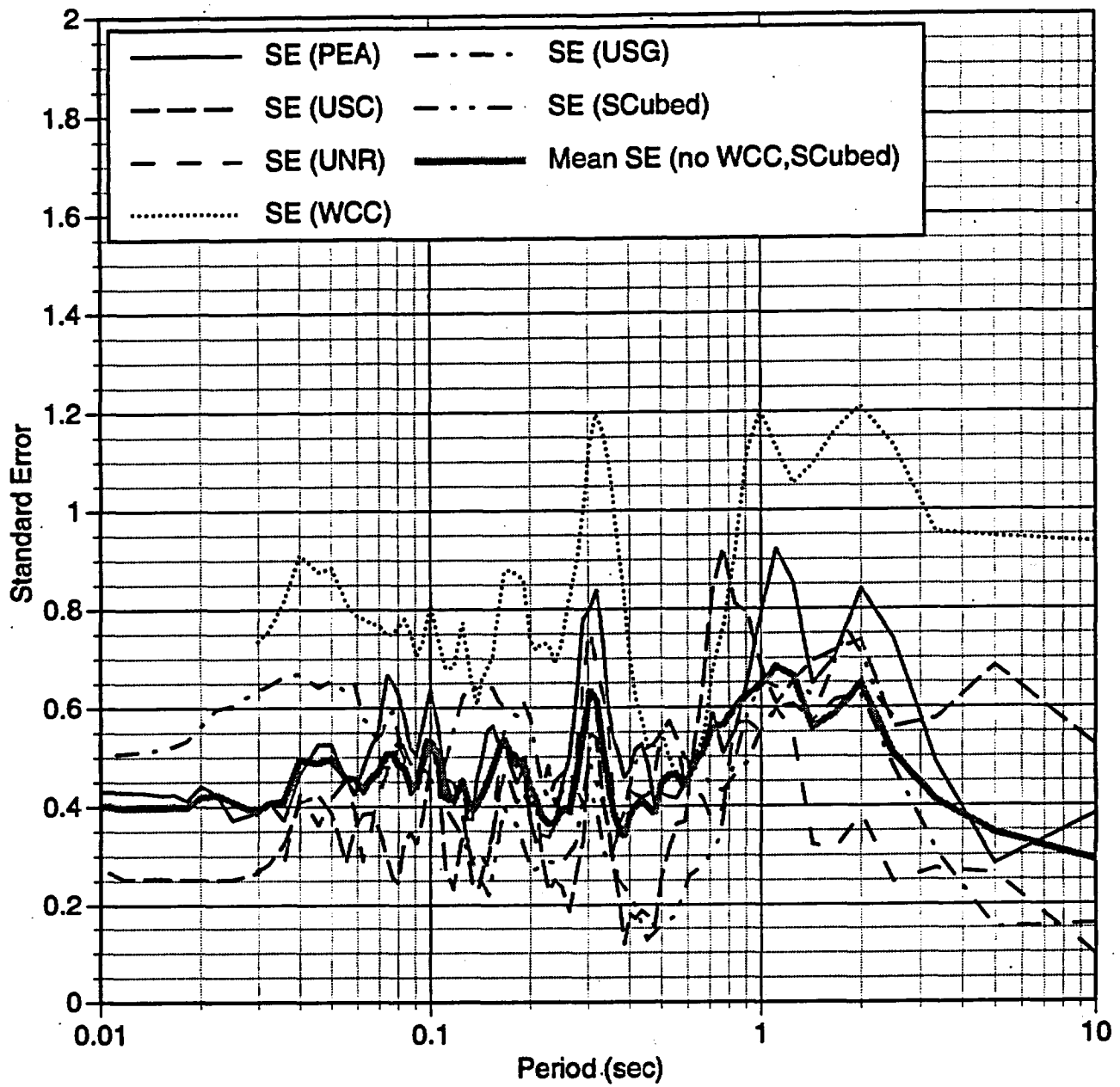
Figure 10.10 Median response spectra for scenario events.

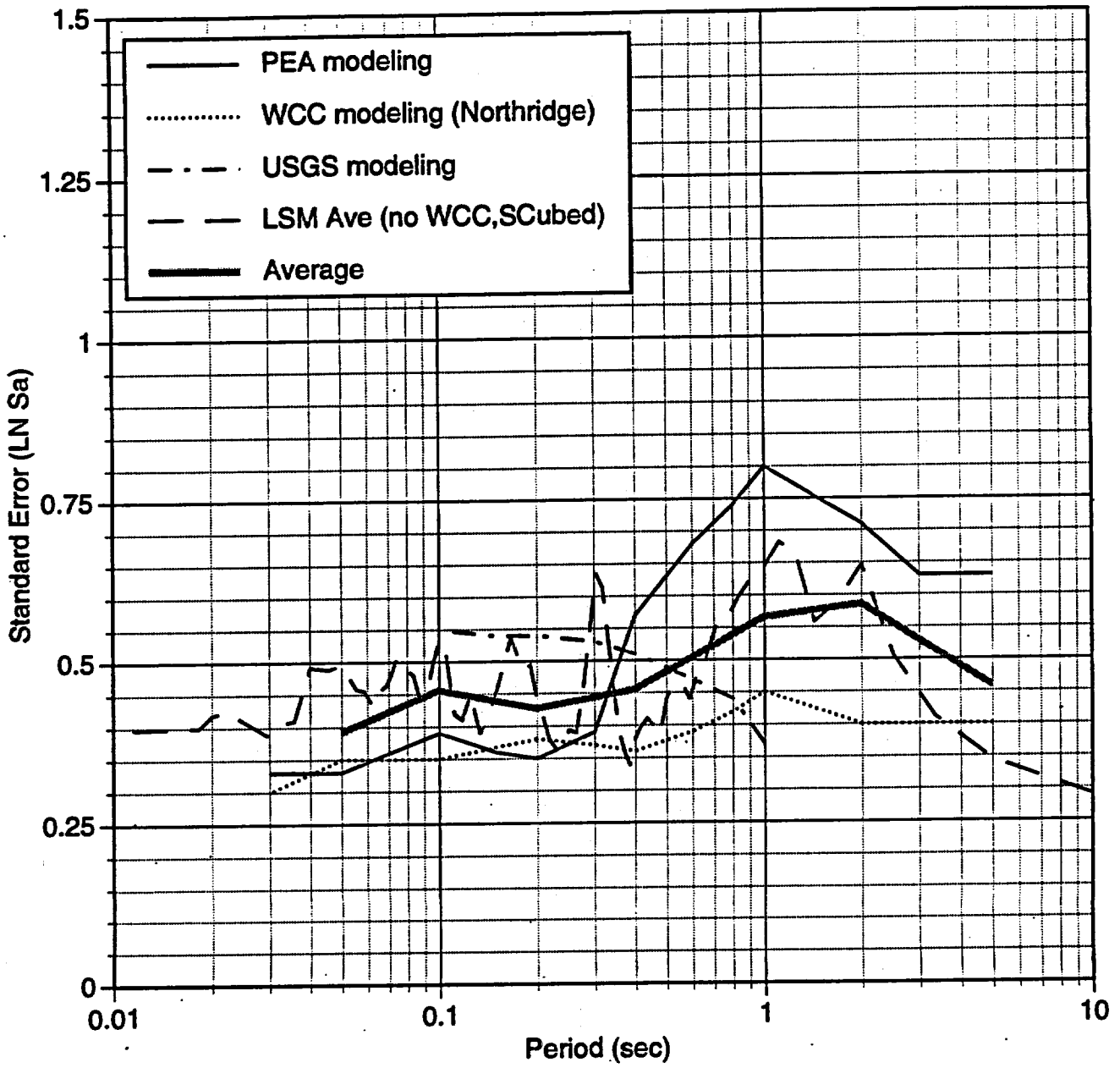
Figure 10.11 84th percentile response spectra for scenario events.

# Scaling Factors

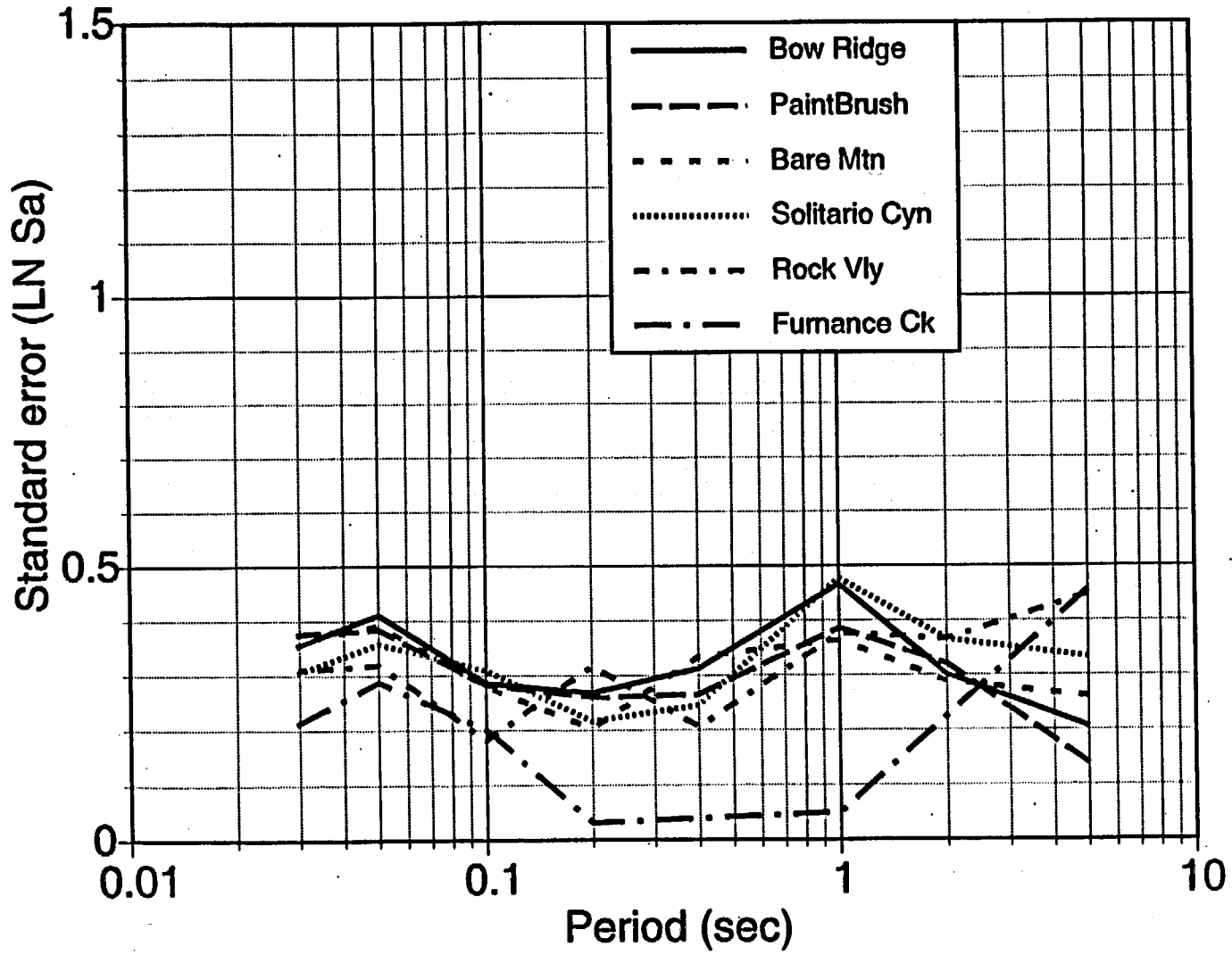


Standard Error: SM2

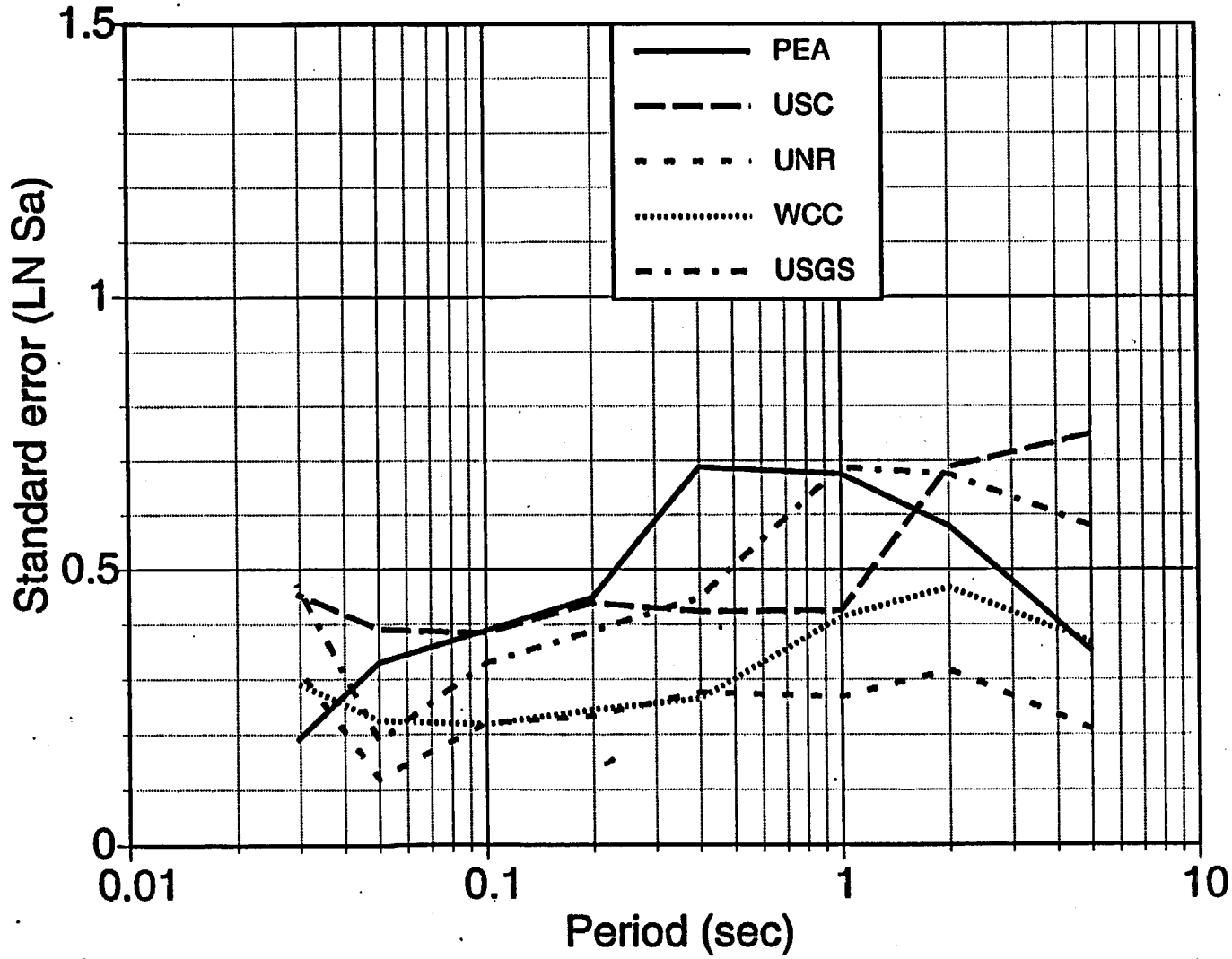




Sigma Method



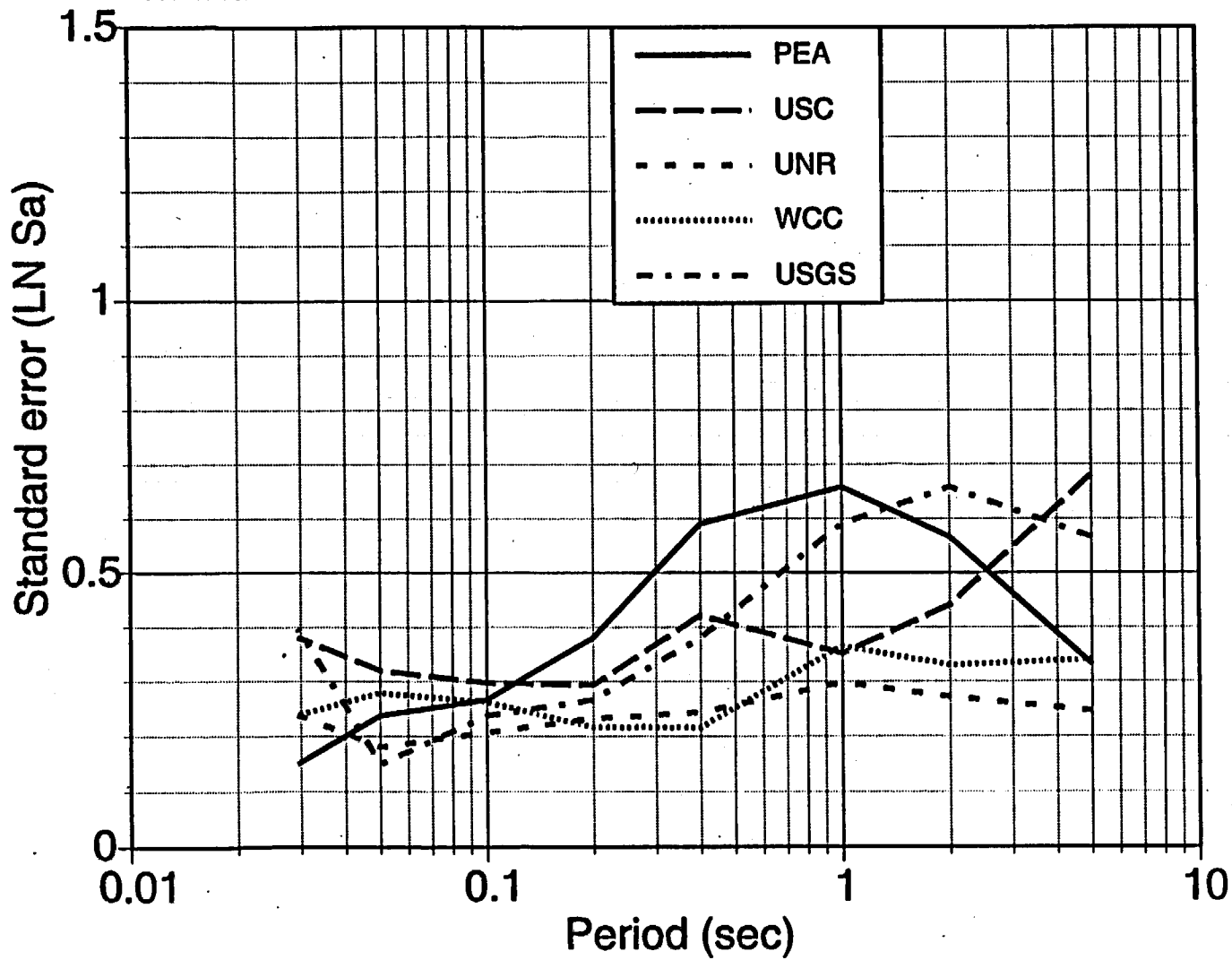
Param (source)  
Bow Ridge  
Revised

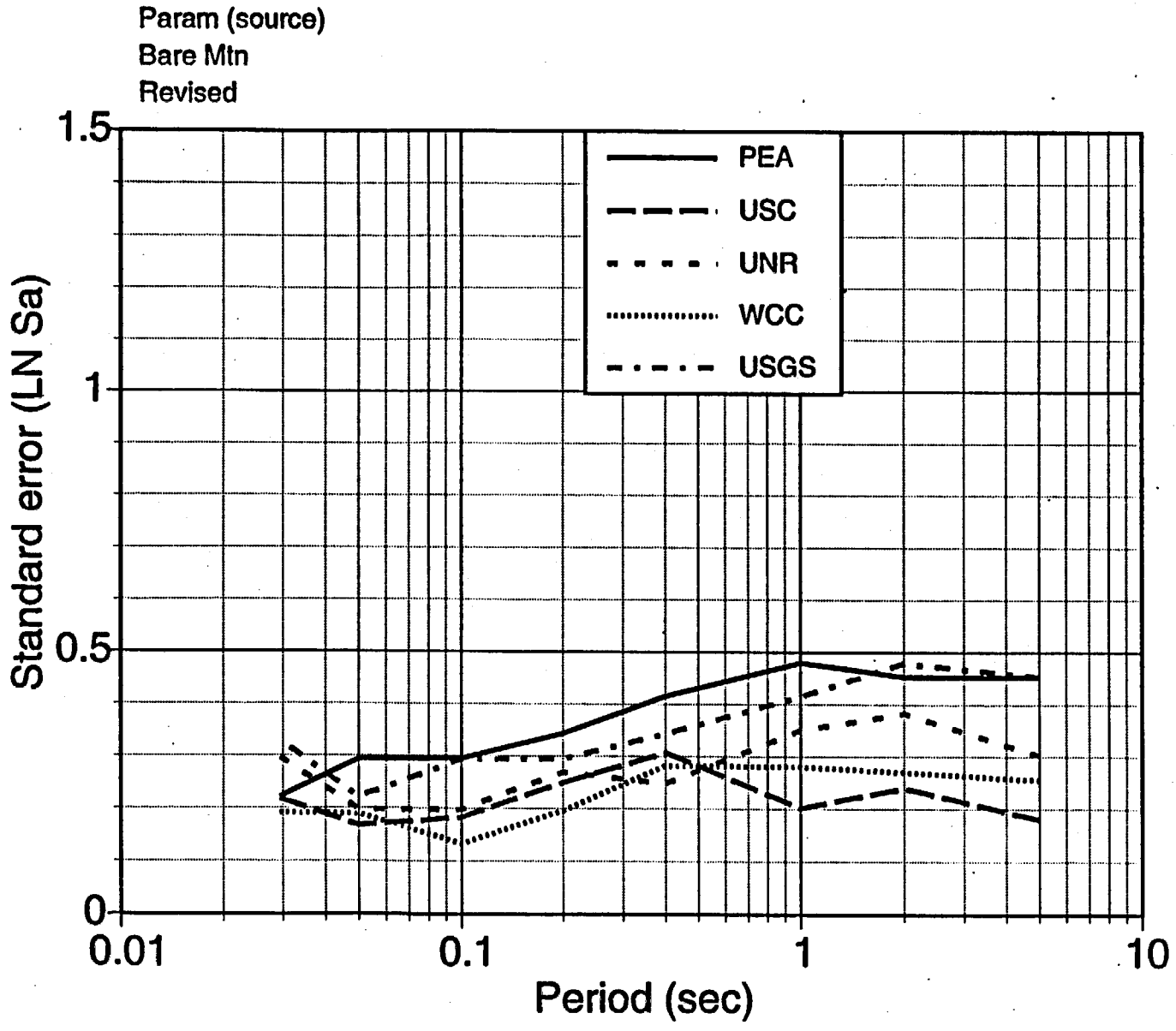


Param (source)

Paint Brush

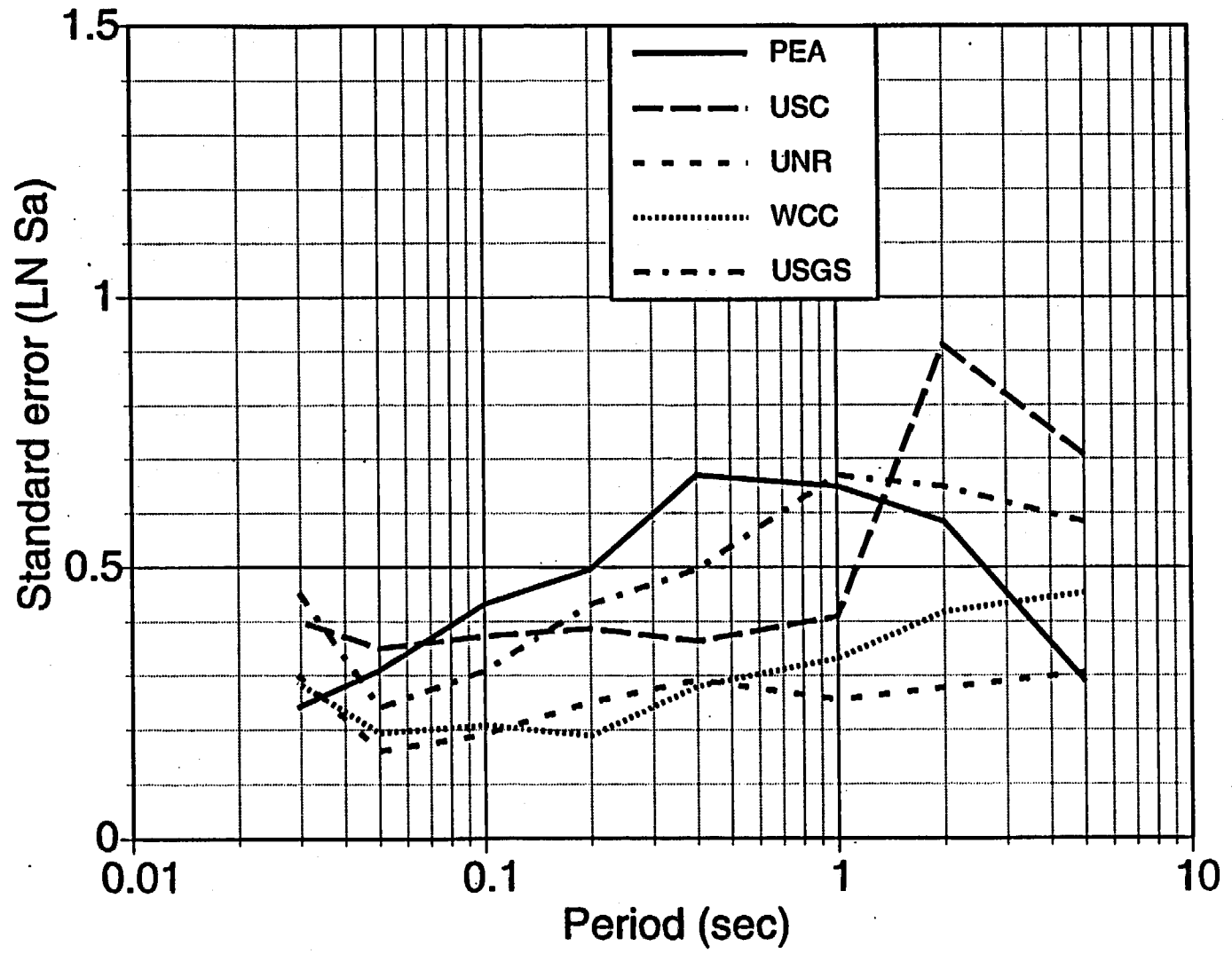
Revised



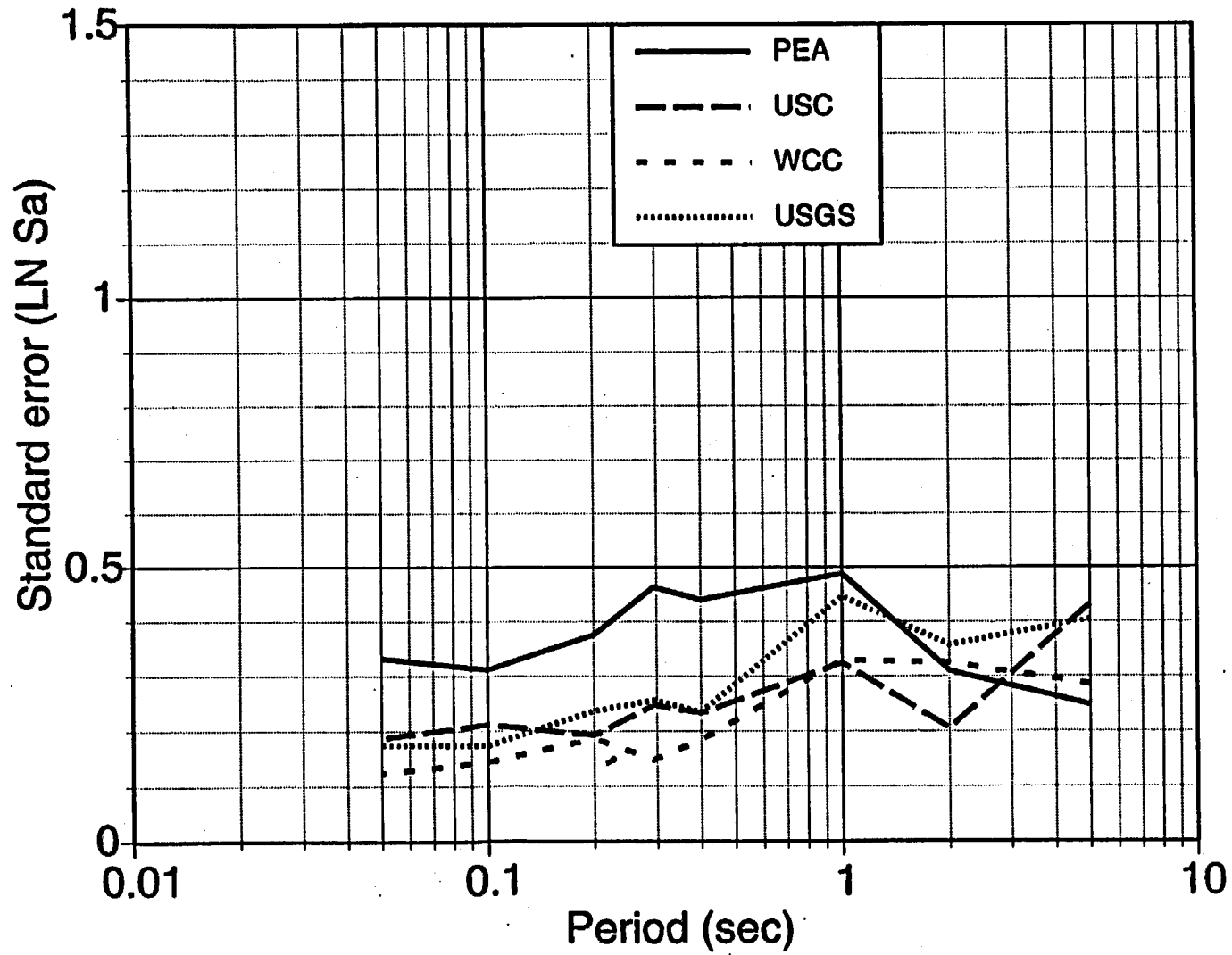


10.5 c

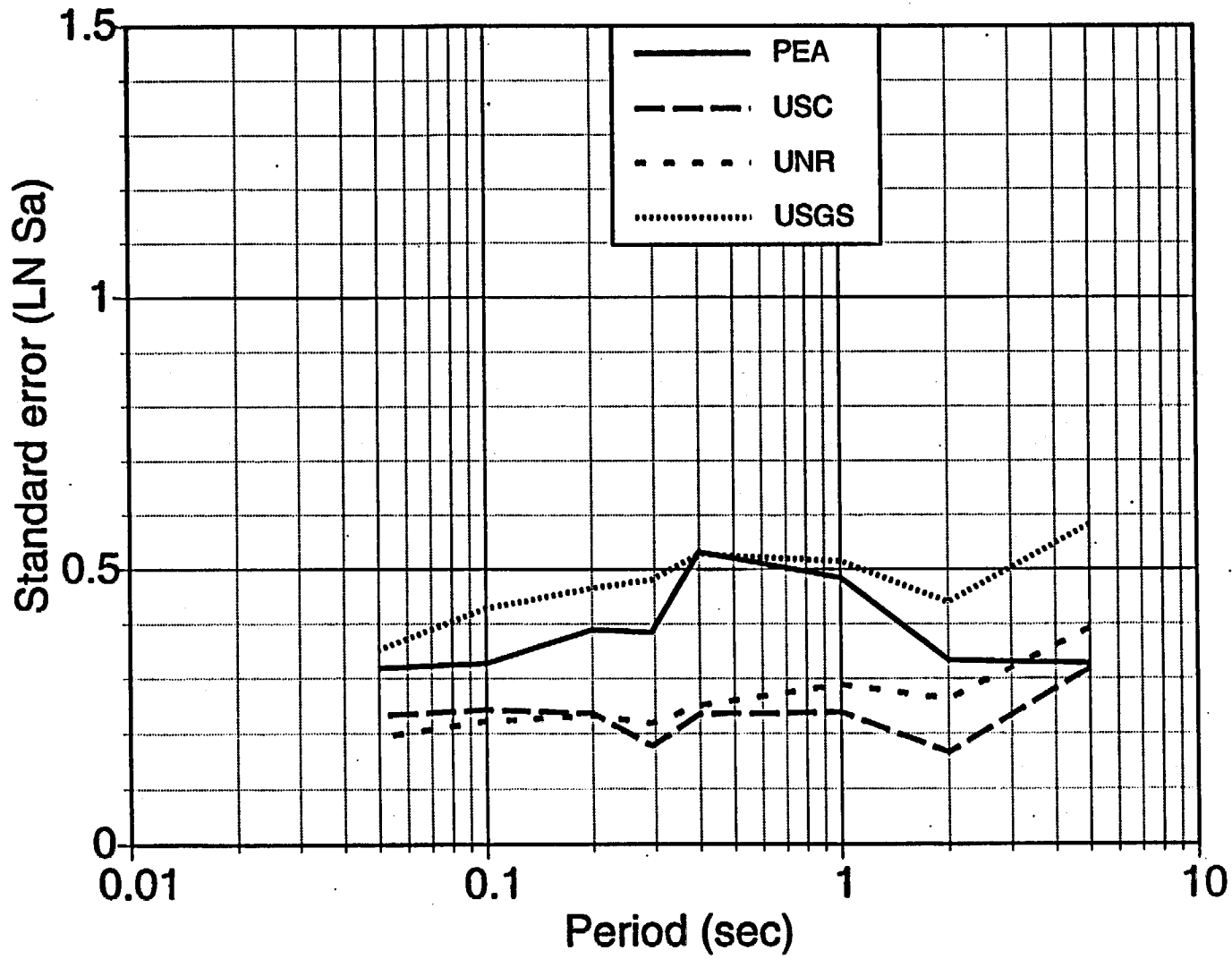
Param (Source)  
Solitario Ridge  
Revised



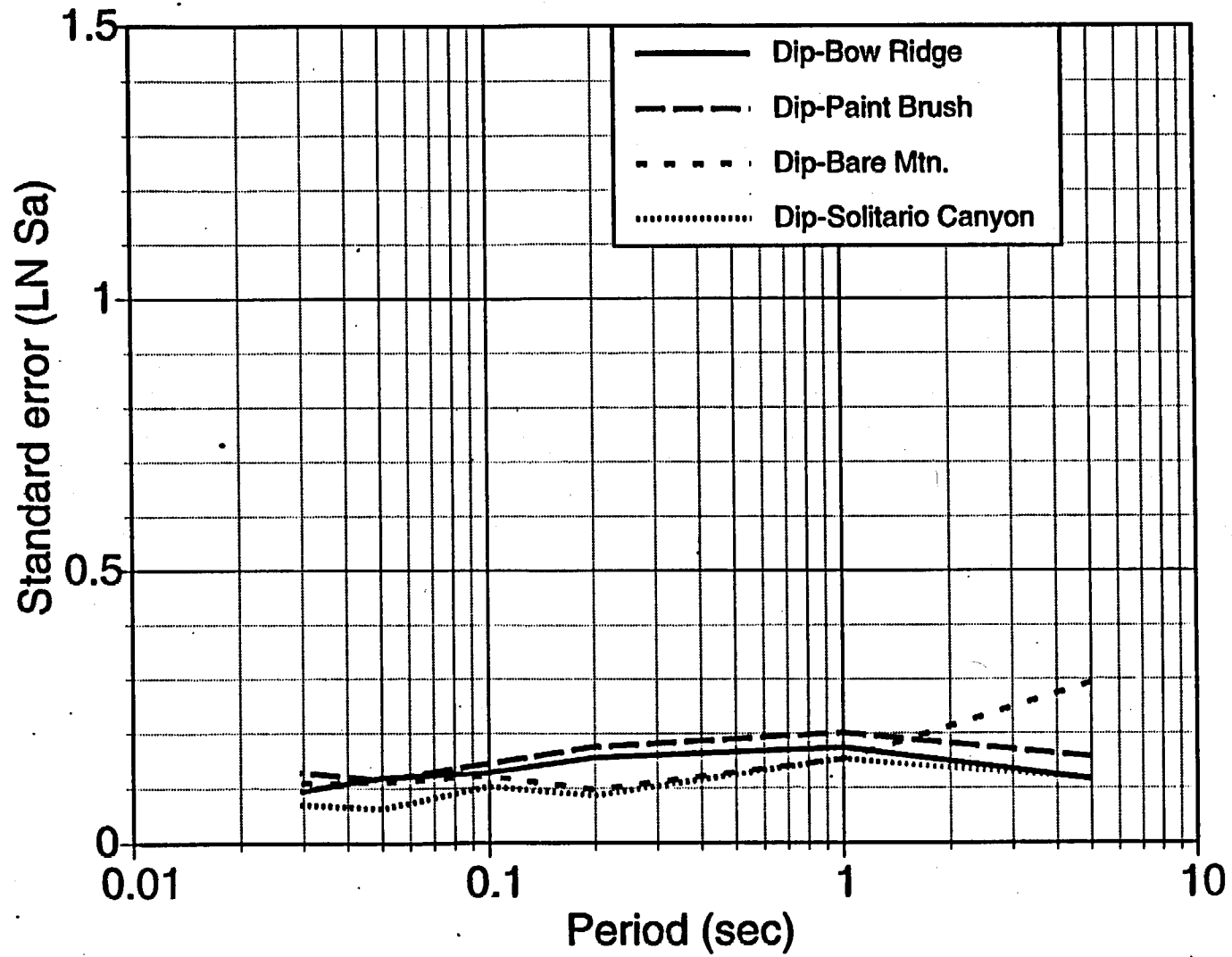
Param (Source)  
Rock Valley  
Revised



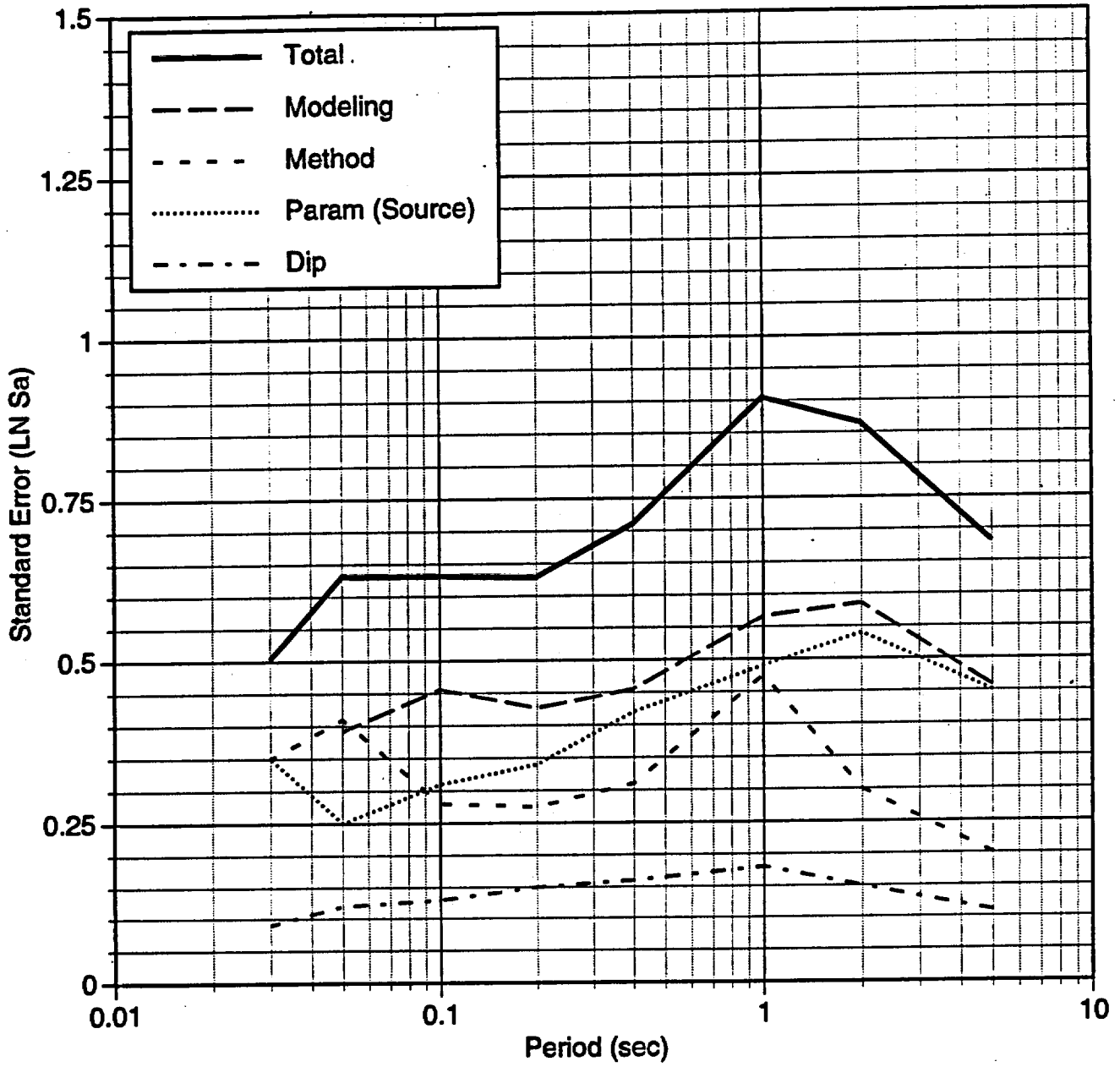
Param (Source)  
Fumance Creek  
Revised



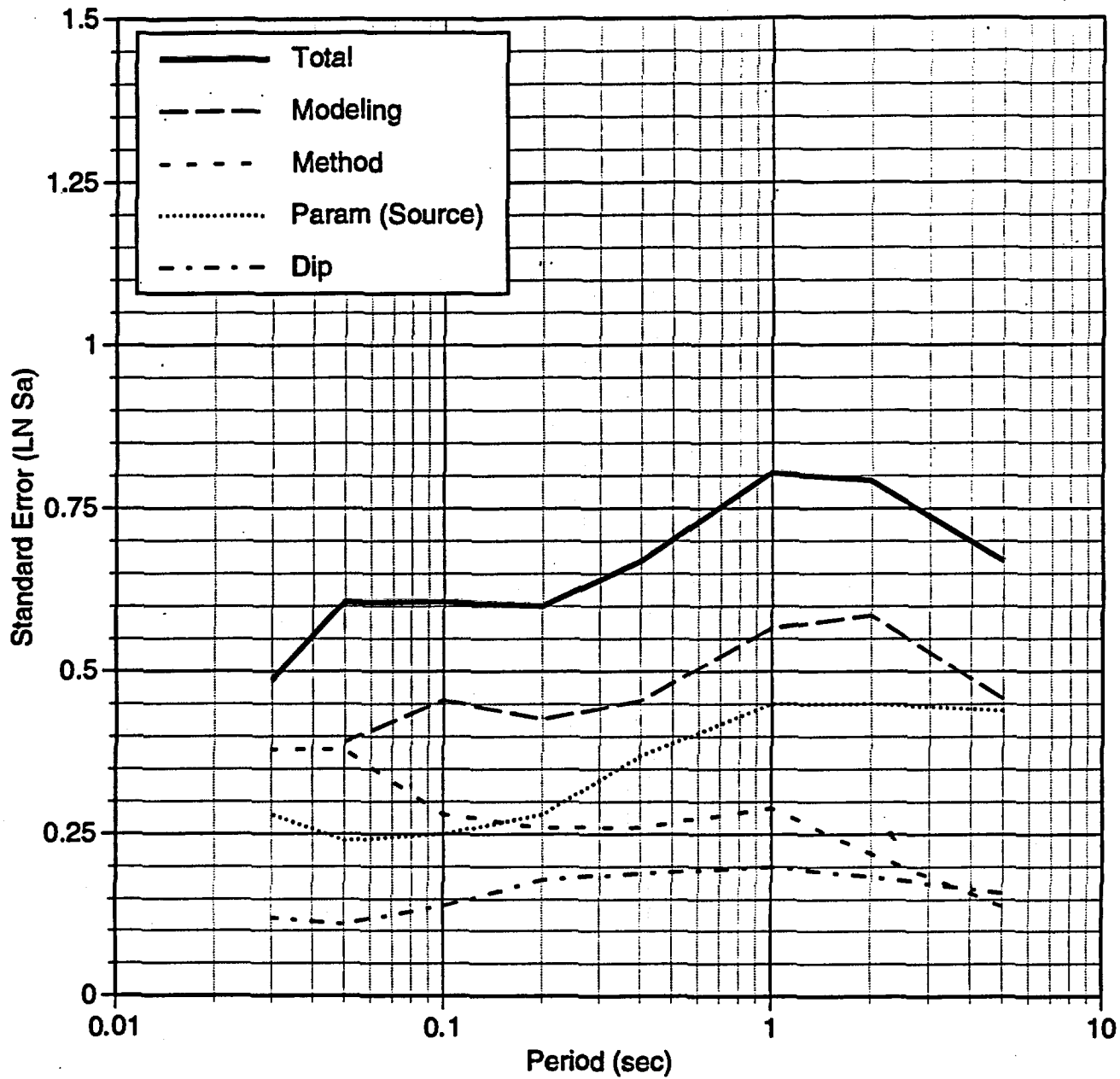
Dip  
Revised



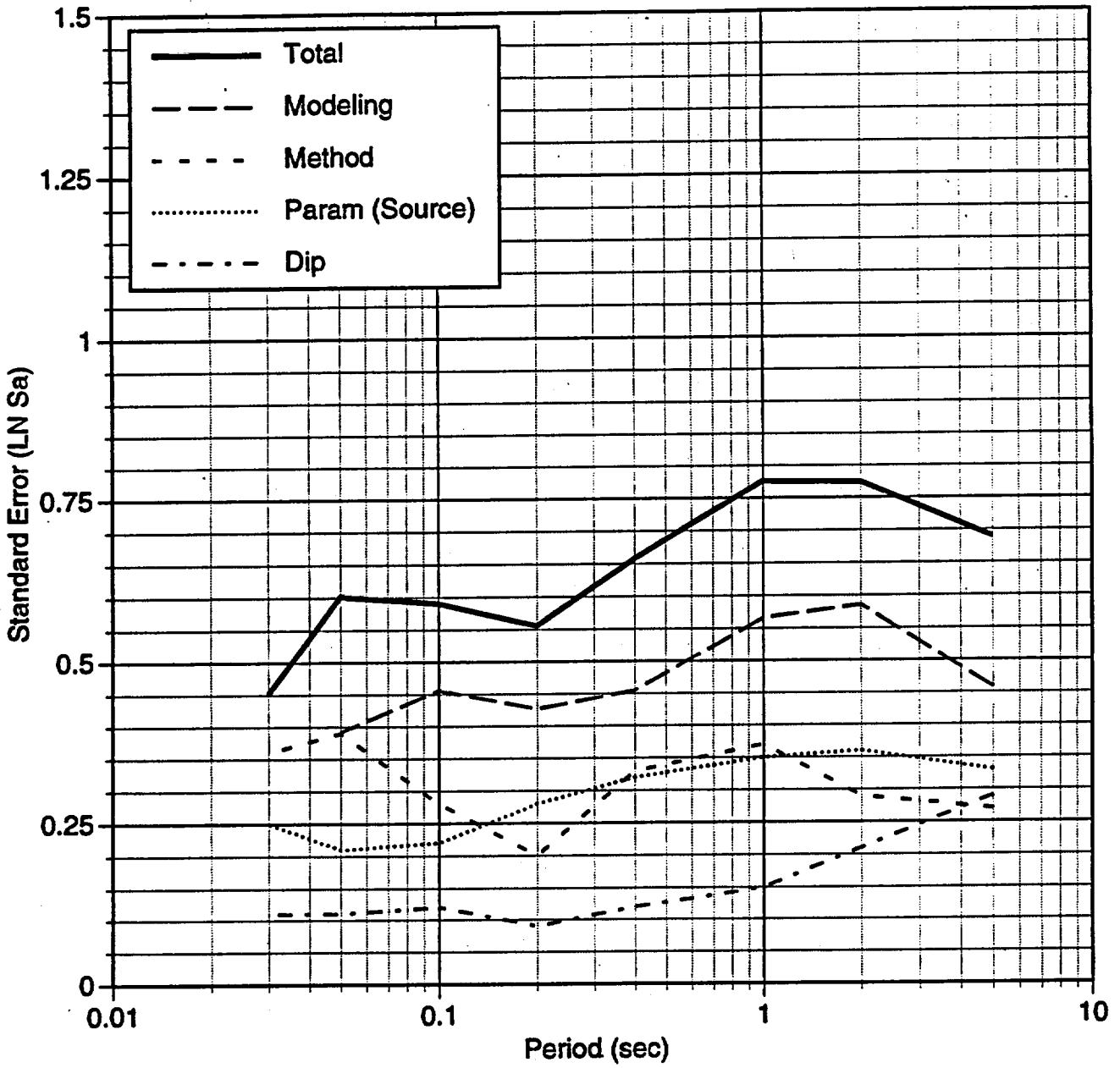
# Standard Error: Bow Ridge



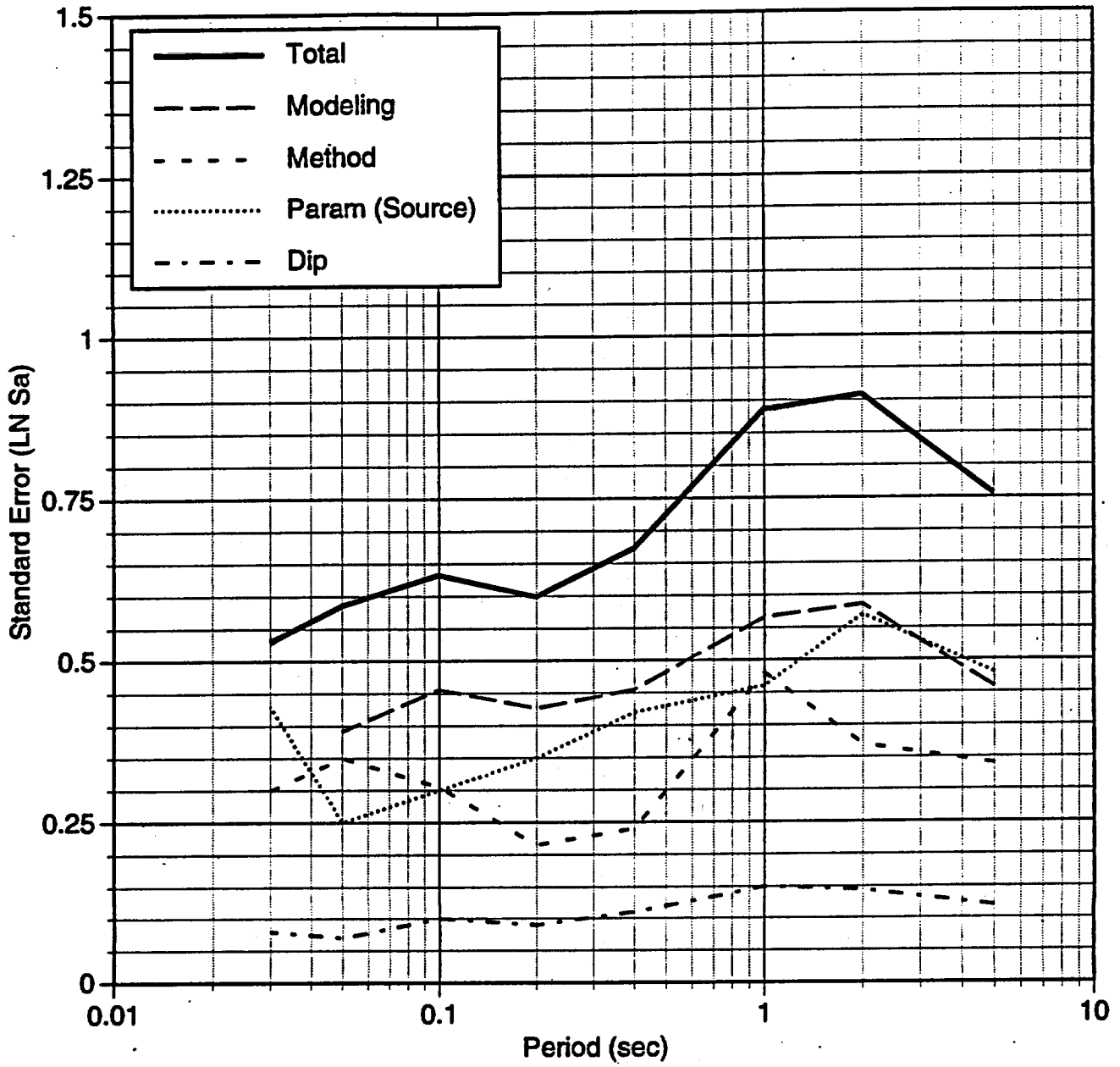
# Standard Error: Paintbrush



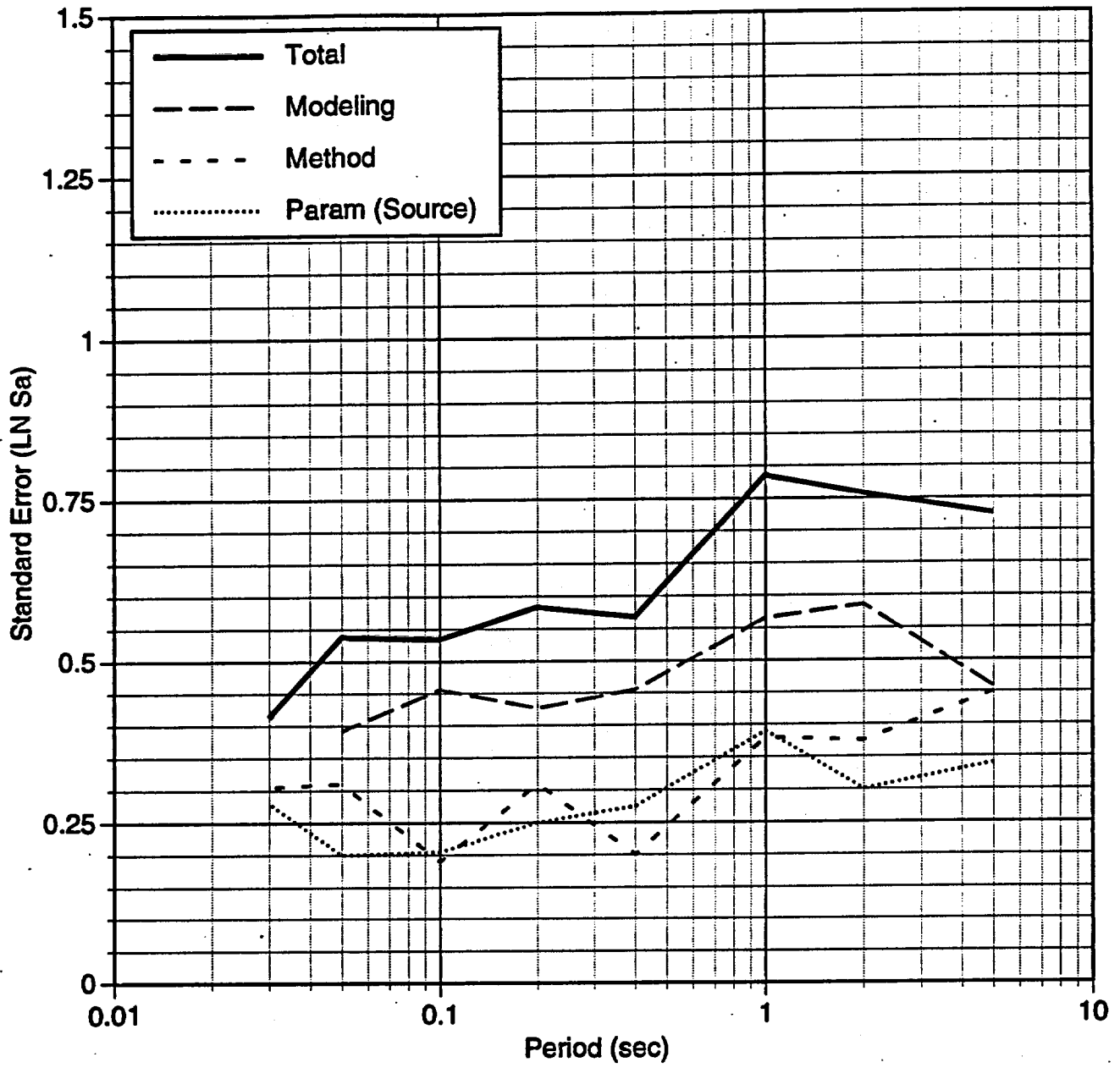
Standard Error: Bare Mtn.



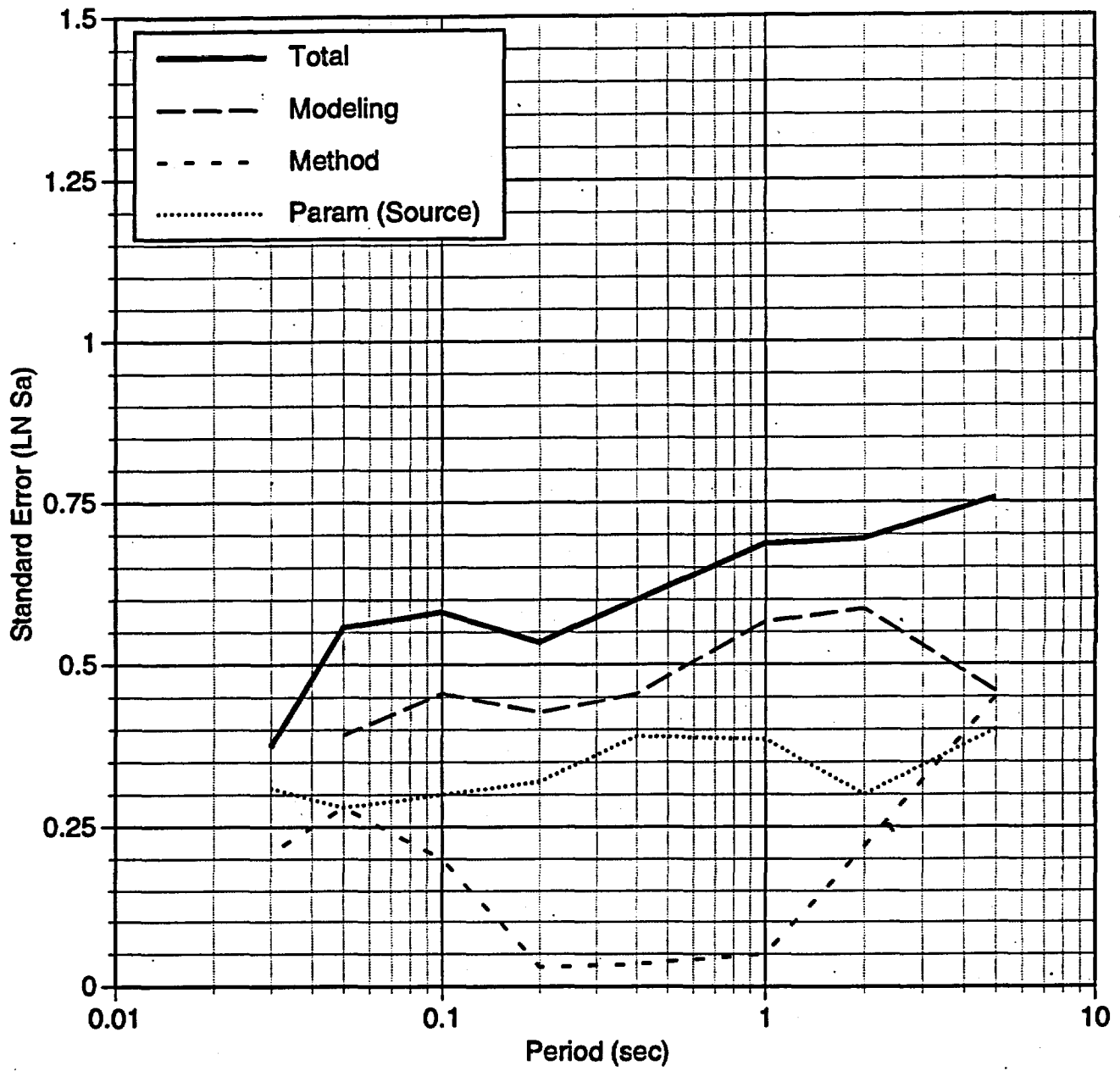
# Standard Error: Solitario Canyon

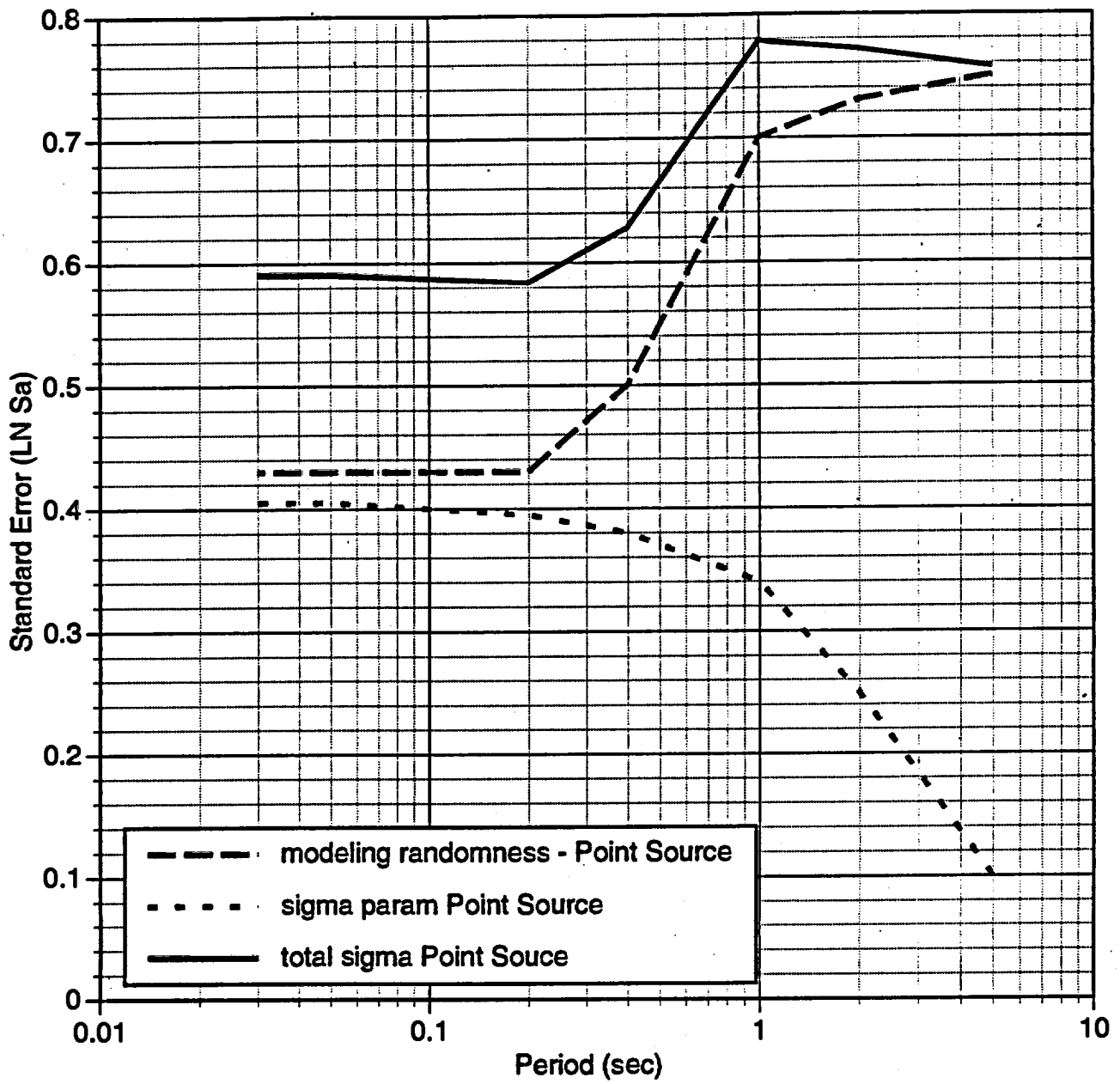


Standard Error: Rock Valley

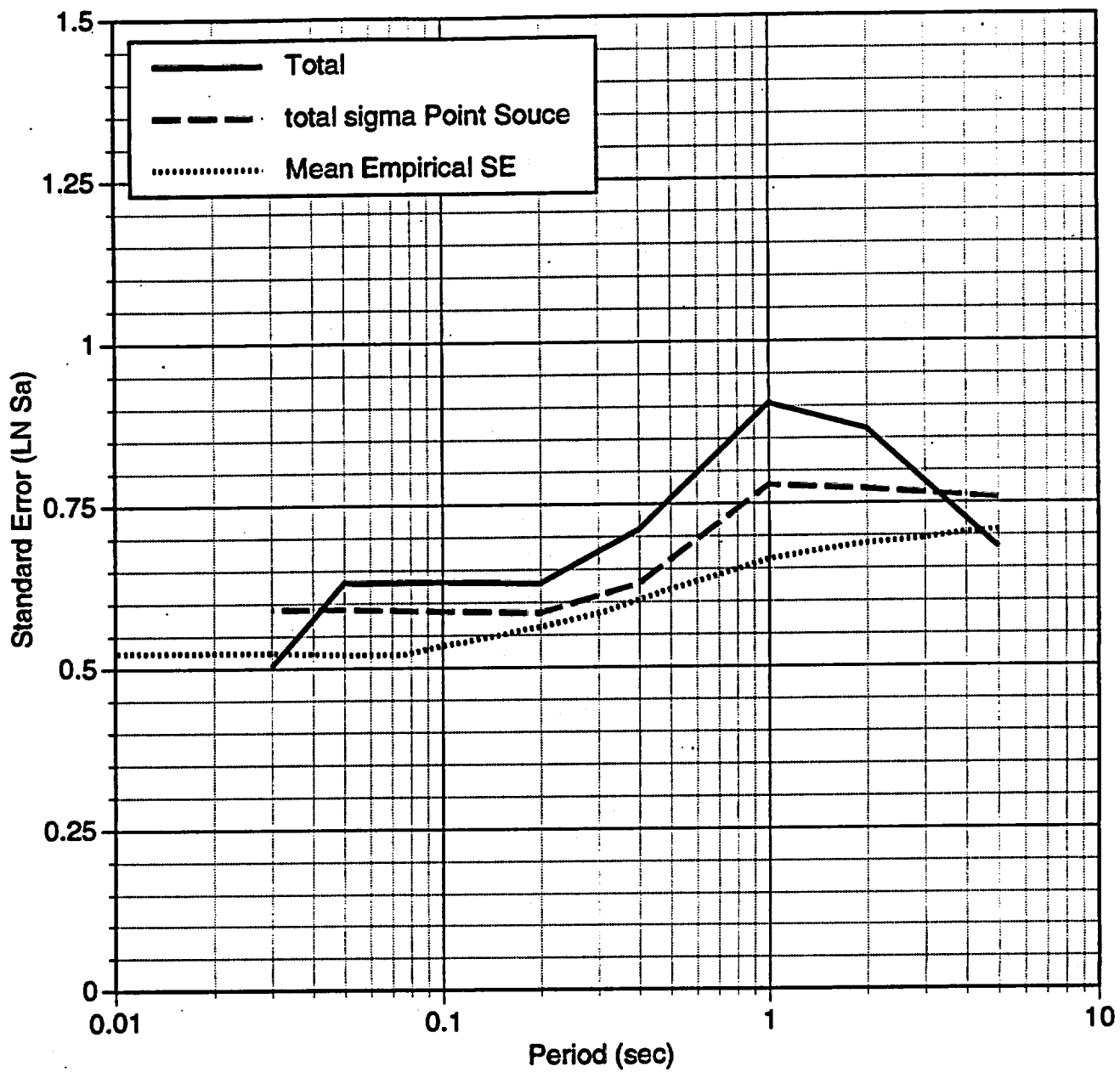


# Standard Error: Furnace Creek

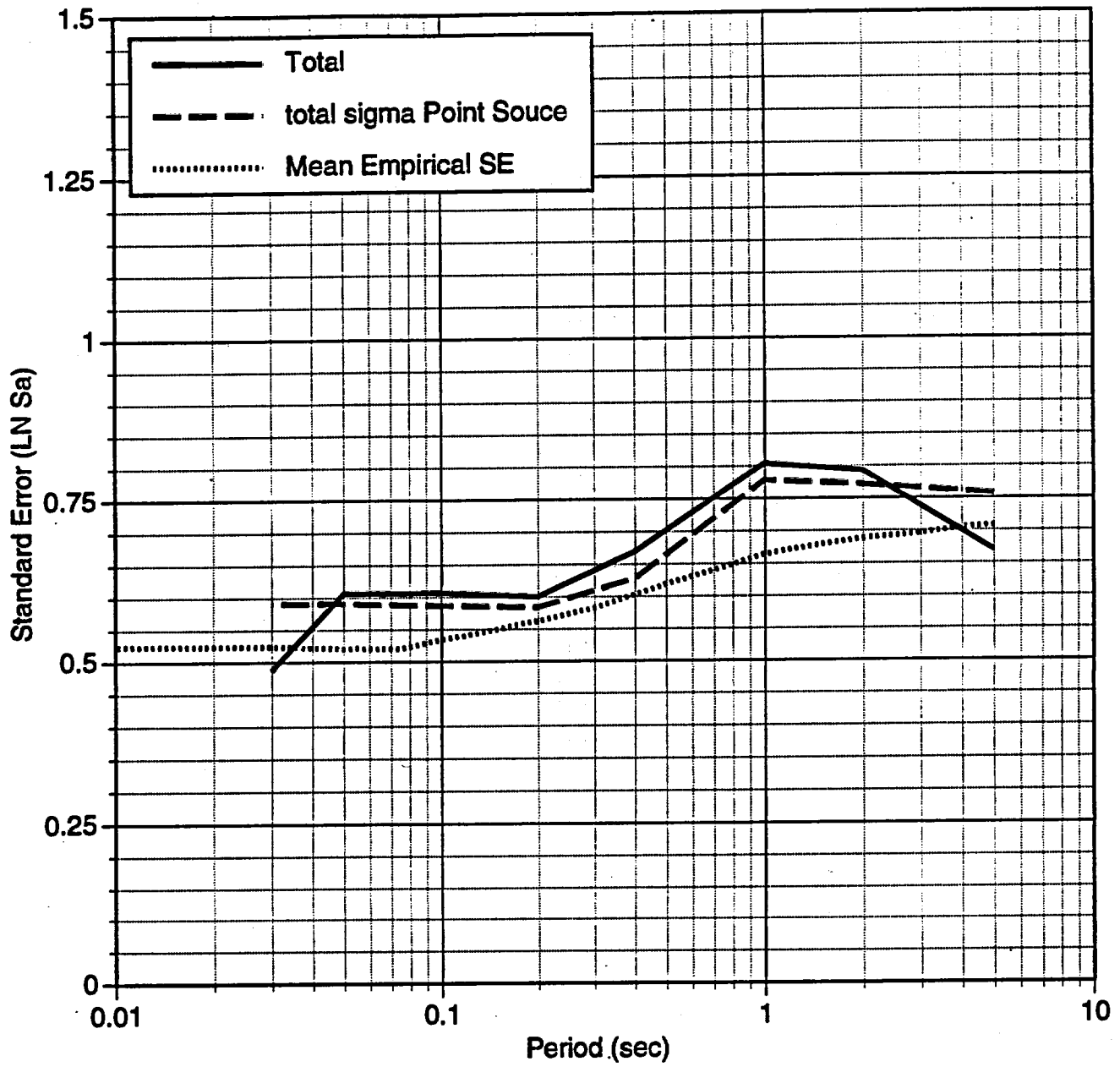




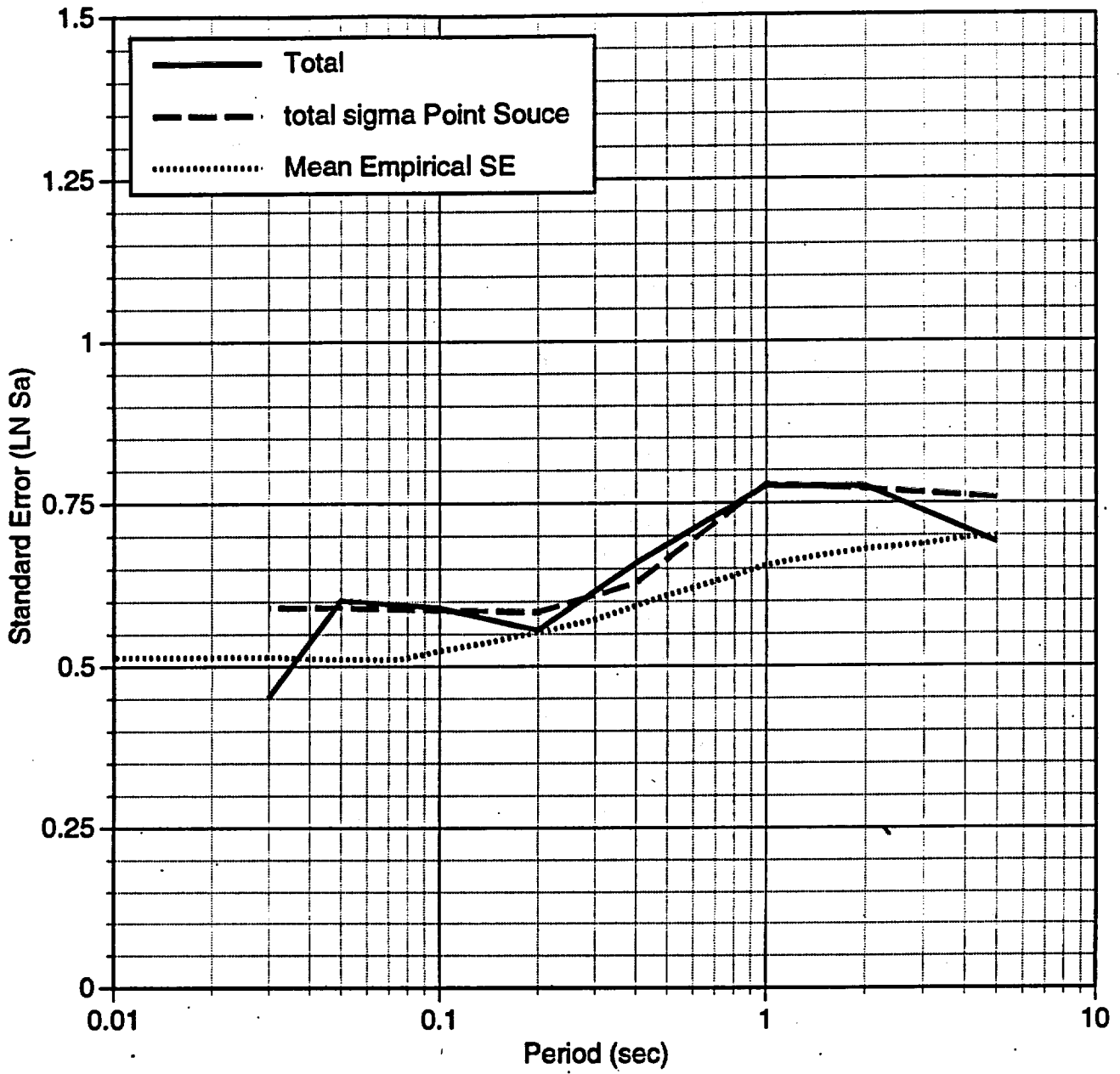
# Standard Error: Bow Ridge



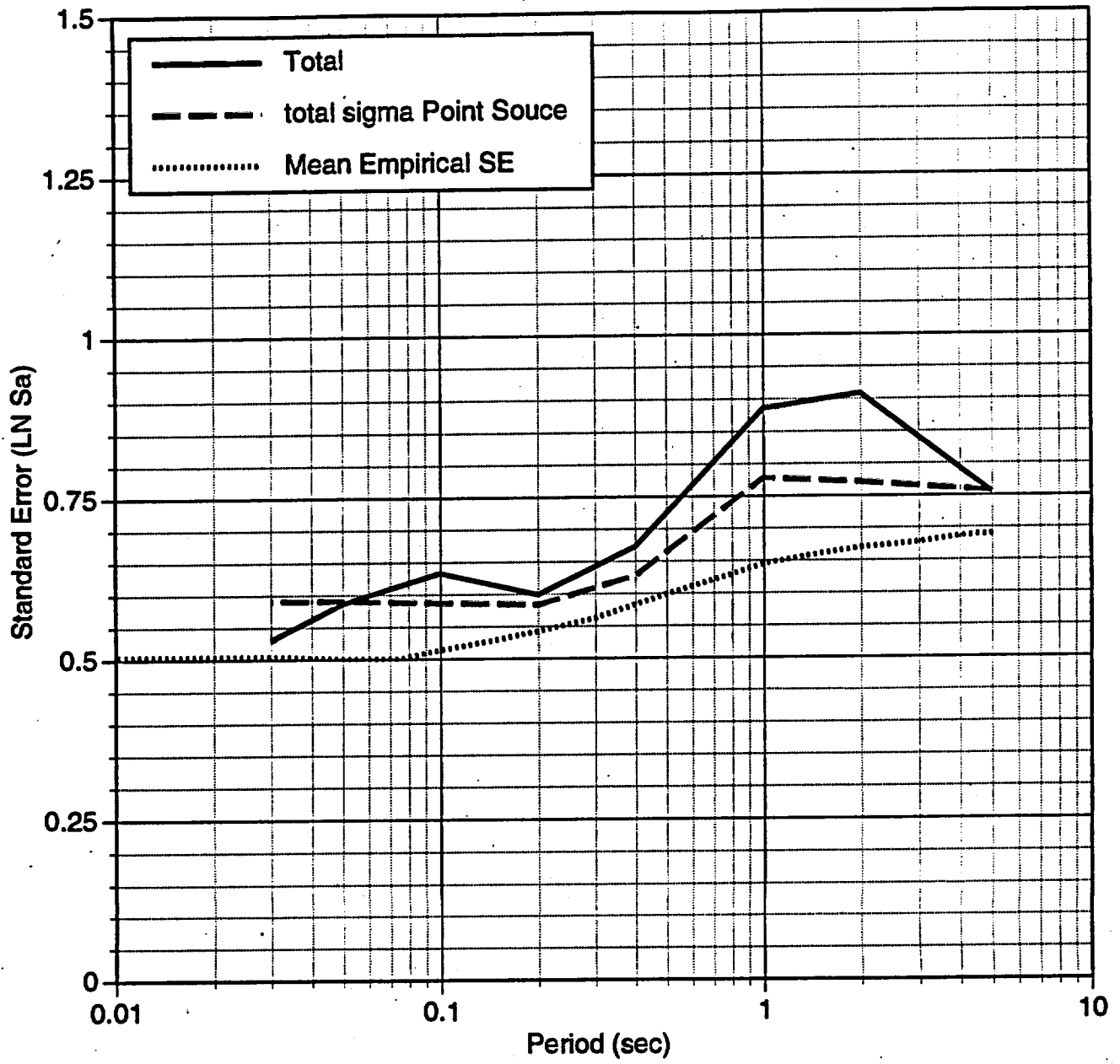
# Standard Error: Paintbrush



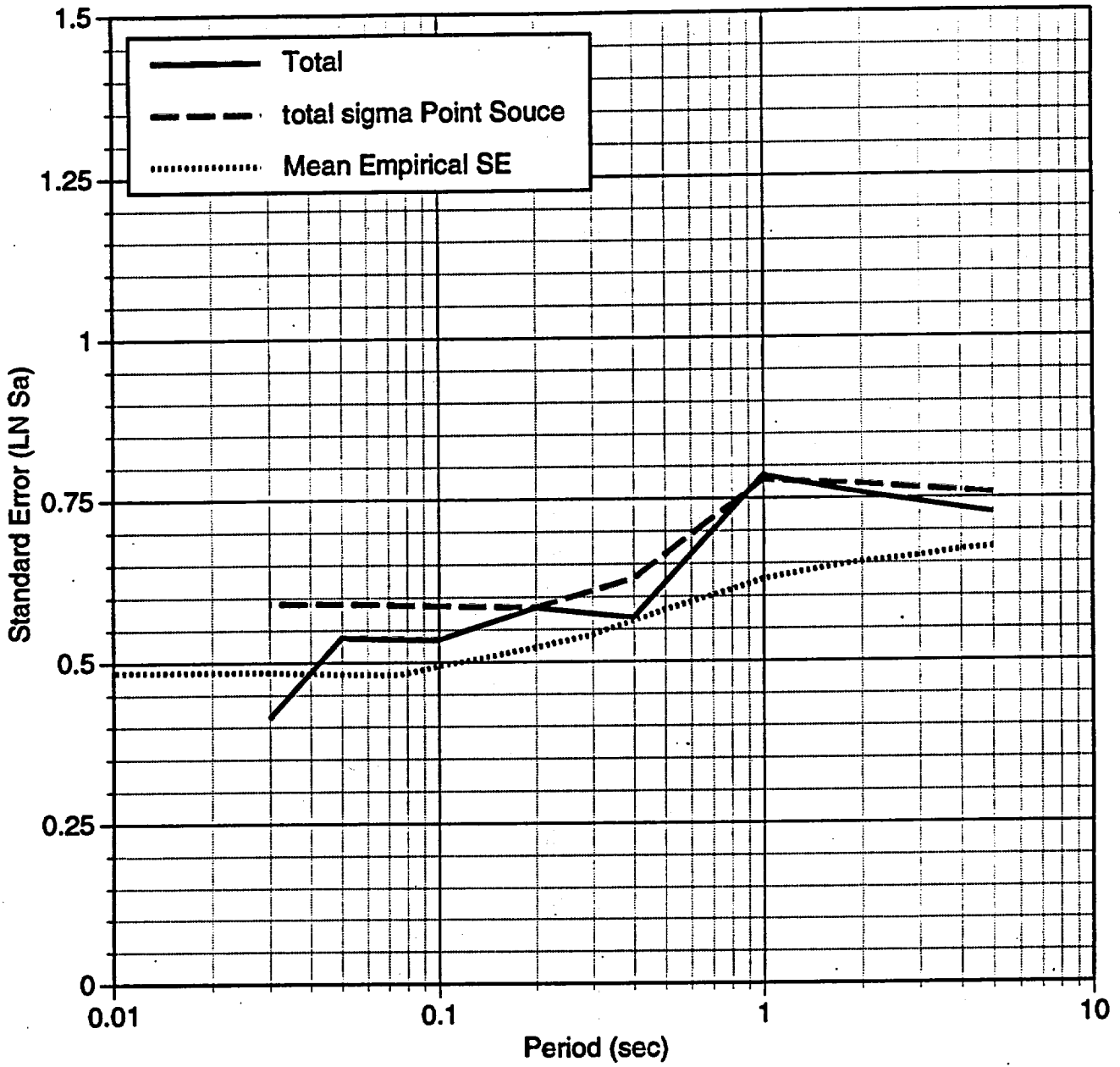
Standard Error: Bare Mtn.



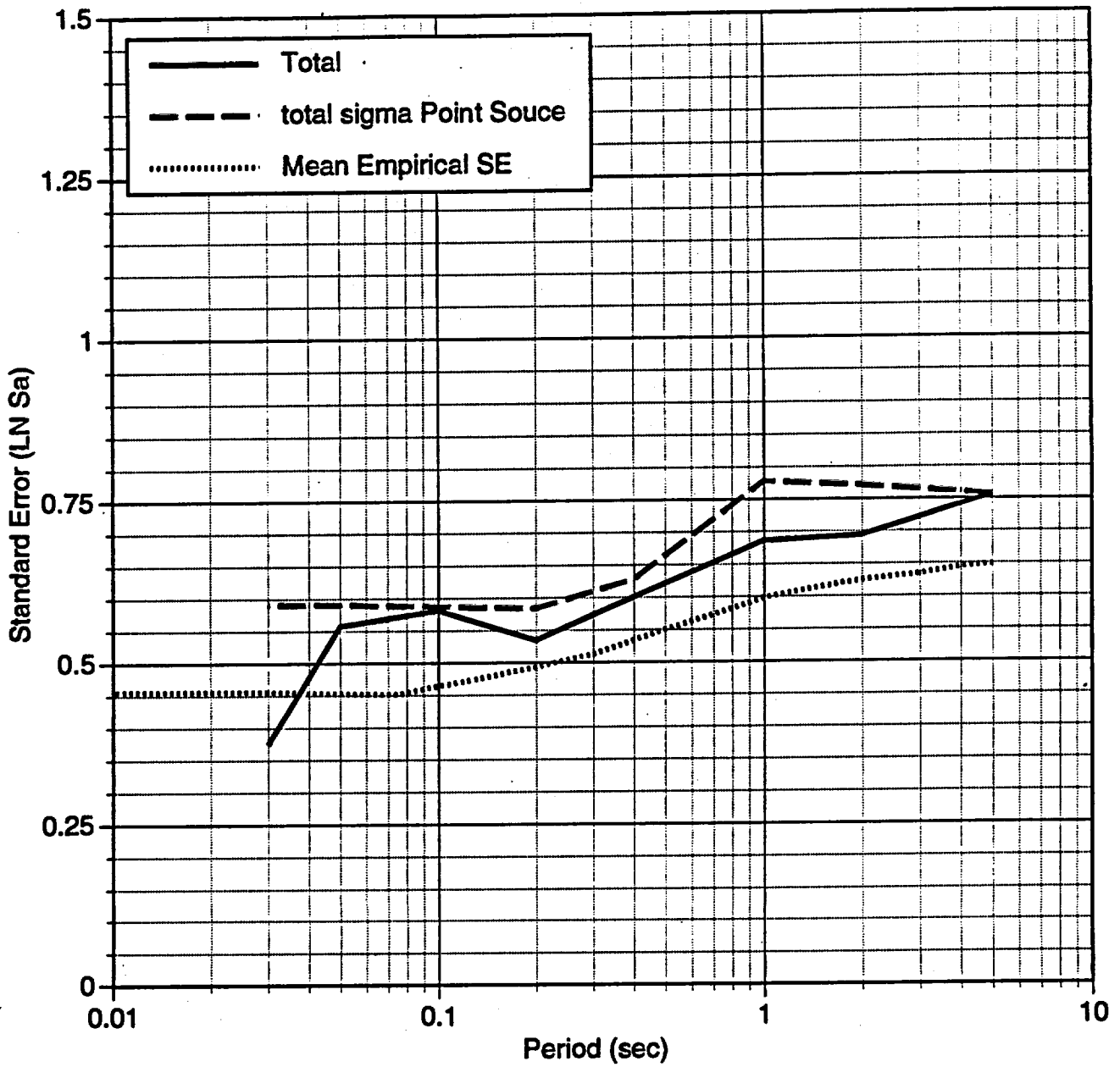
# Standard Error: Solitario Canyon



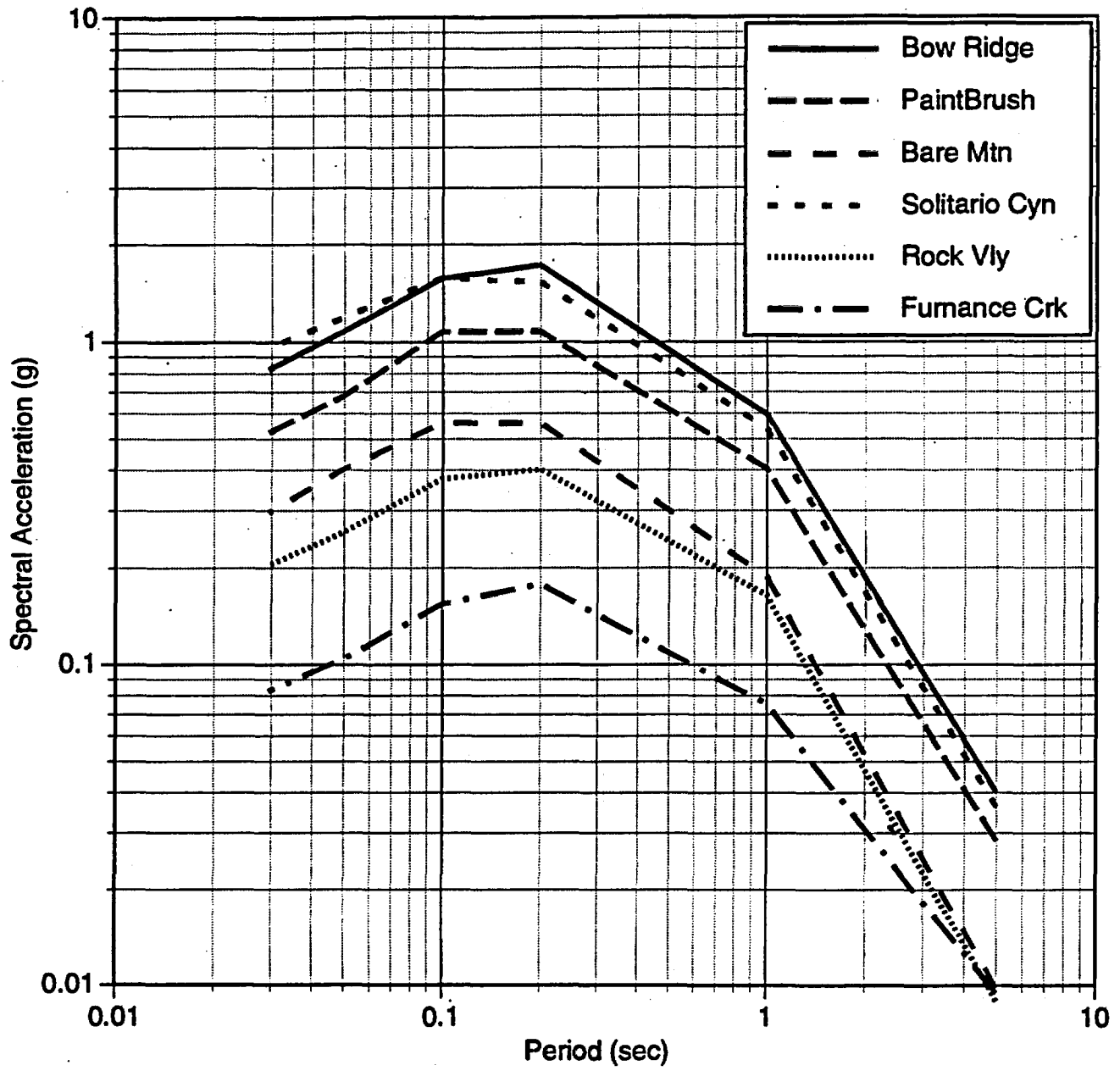
Standard Error: Rock Valley



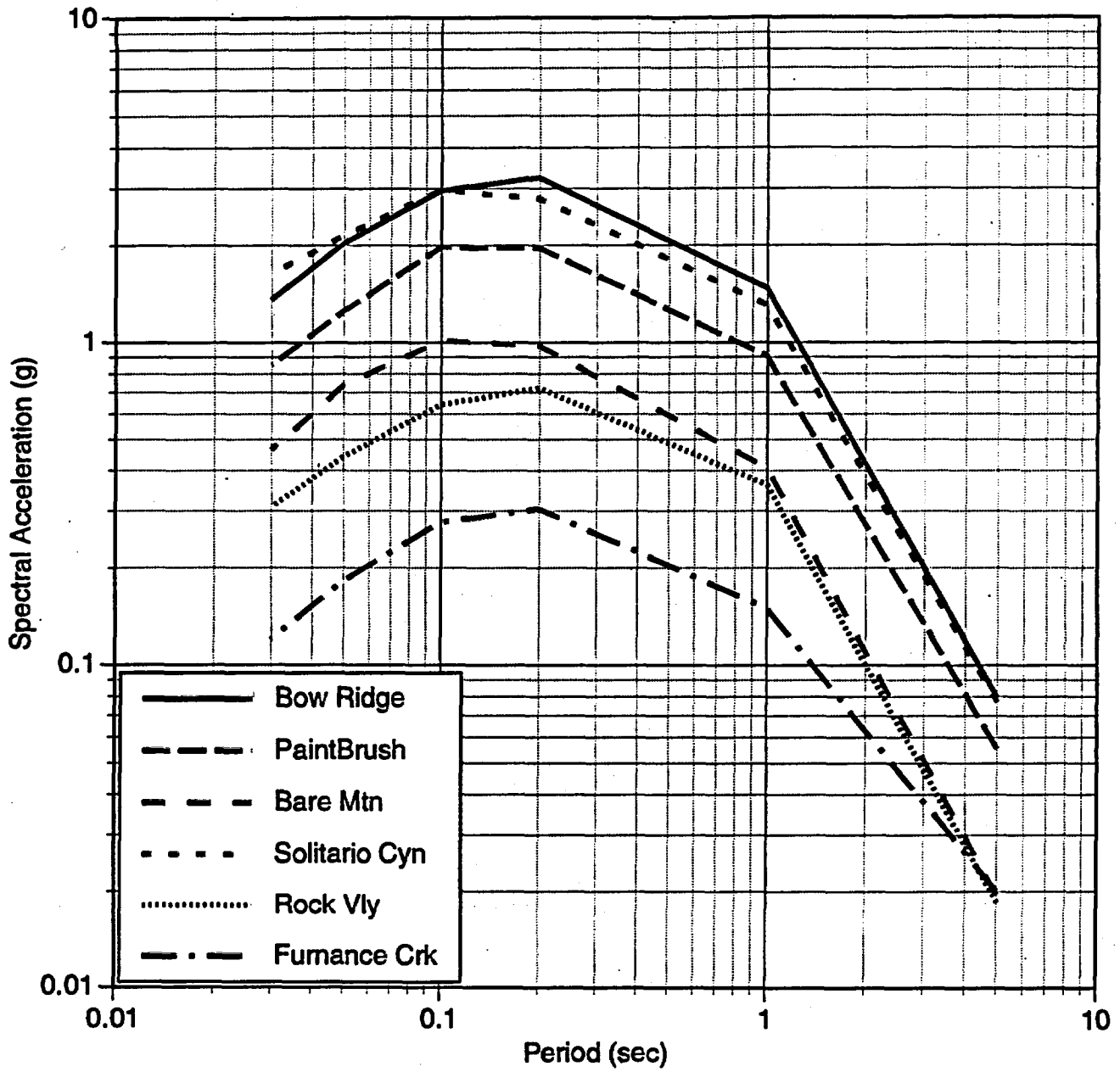
# Standard Error: Furnace Creek



Median SA values



84th Percentile SA values



## 11. References

- Abrahamson N.A. and W.J. Silva (1995). Written Communication, October 10, 1995.
- Abrahamson, N.A., P.G. Somerville, and C. A. Cornell (1990). Goodness of fit for numerical strong motion simulations and uncertainty in numerical strong motion predictions, *Proceedings of the 4th U.S. National Conference on Earthquake Engineering.*, Earthquake Engineering Research Institute.
- Ackerman, H.D., W.D. Mooney, D.B. Snyder, and V.D. Sutton (1988). Preliminary interpretation of seismic refraction and gravity studies west of Yucca Mountain, Nevada and California, in Carr, M.D. and Yount, J.C., eds., Short contributions to the geology and hydrology of a potential nuclear waste disposal site at Yucca Mountain, southern Nevada: U.S. Geological Survey Bulletin 1790.
- Anderson, J.G., and F. Su (1995). Estimates of seismic site effects in the vicinity of Yucca Mountain, Nevada, draft paper.
- Anderson, J.G., J.N. Brune, D. DePolo, J. Gomberg, S.C. Harmsen, M.K. Savage, A.F. Sheehan, and K.D. Smith (1993). Preliminary report : The Little Skull Mountain Earthquake, June 29, 1992, in *Dynamic Analysis and Design Considerations for High-Level Nuclear Waste Repositories*, Q.A. Hossain, editor, American Society of Civil Engineers, New York, pp. 162-175.

Bache, T. C. (1982). Estimating the yield of underground nuclear explosions, *Bull. Seism. Soc. Am.*, 72, S131-S168.

Balch, A.H., W. Zhuang, S. Baker, and C. Erdemir (1994). Preliminary investigation into multiple offset, three component vertical seismic profile at UE-25 UZ-16 Borehole, Yucca Mountain, Nevada, U.S. Geological Survey, Draft report, 31 March.

Bennett, T.J. and J.R. Murphy (1993). Estimation of near-regional seismic ground motion from underground nuclear explosion tests, in *Dynamic Analysis and Design Considerations for High-Level Nuclear Waste Repositories*, Q.A. Hossain, editor, American Society of Civil Engineers, New York, pp. 191-205.

Boatwright and Choy (1985) \*\*\*\*\*.

Bolt, B. A. (1976). Nuclear Explosions and Earthquakes - The Parted Veil, W. H. Freeman and Company, San Francisco, CA.

Boore, D.M. (1983). Stochastic simulation of high-frequency ground motions based on seismological models of the radiated spectra, *Bull. Seism. Soc. Am.*, 73, 1865-1894.

Boore, D.M. (1986). Short-period P- and S-wave radiation from large earthquakes: Implications for spectral scaling relations, *Bull. Seism. Soc. Am.*, 76, 43-64.

Boore, D.M., W.B. Joyner, and T.E. Fumal (1994). Estimation of response spectra and peak accelerations from western North American earthquakes: An interim report, Part 2, U.S. Geological Survey, Menlo Park, CA, Open-File Report 94-127.

Boyd, P.J., R.H. Price, J.S. Noel, and R.J. Martin (1995a). Bulk and mechanical properties of the Paintbrush tuff recovered from Boreholes UE25 NRG-4 and -5: Data report. SAND94-2138, Sandia National Laboratories, Albuquerque, NM.

Boyd, P.J., R.H. Price, J.S. Noel, and R.J. Martin (1995b). Bulk and mechanical properties of the Paintbrush tuff recovered from Boreholes UE25 NRG-2, 2A, 2B, and 3: Data report. SAND94-1902, Sandia National Laboratories, Albuquerque, NM.

Brune, J.N. (1970). Tectonic stress and the spectra of seismic shear waves from earthquakes, *J. Geophys. Res.*, **75**, 4997-5009.

Brune, J.N. (1971). Correction, *J. Geophys. Res.*, **76**, 5002.

Campbell, K.W. (1993). Empirical prediction of near-source ground motion from large earthquakes, *Int. Workshop on Earthquake Hazard and Large Dams in the Himalaya*, New Delhi, India, Jan. 15-16, 17 pp.

Campbell, K.W. and Y. Bozorgnia (1994). Near-source attenuation of peak horizontal acceleration from Worldwide Accelerograms recorded from

1957 to 1993, *Fifth U.S. Nat'l Conference on Earthquake Engineering*,  
Chicago, IL, July 10-14, 1994, Vol. III, 283-292

Carr, W.J. (1984). Regional structural setting of Yucca Mountain,  
southwestern Nevada, and late Cenozoic rates of tectonic activity in part of  
the southwestern Great Basin, Nevada and California, *U.S. Geol. Surv.*  
*Open Files Rept. 84-854*, 109 pp.

Chavez, D.E., and K.F. Priestley (1985).  $M_l$  observations in the Great Basin  
and  $M_0$  versus  $M_l$  relationships for the 1980 Mammoth Lakes, California,  
earthquake sequence, *Bull. Seism. Soc. Am.*, 75, 1583-1598.

Chavez, D.E., and K.F. Priestley (1986). Measurement of frequency-dependent  
 $L_g$  attenuation in the Great Basin, *Geophys. Res. Lett.*, 13, p. 551-554.

Daley, T. and E. Majers (1995). Preliminary report for Activity: 8.3.1.4.2.2.5  
3GGF142M analysis paper: Data reduction NRG-6/WT-2 VSP, Department  
of Energy, Yucca Mountain Site Characterization Project.

Department of Energy (1988). Site characterization plan overview: Yucca  
Mountain Site, Nevada Research and Development Area, Nevada,  
DOE/RW-0199, Washington, D.C.

Department of Energy (1994a). Methodology to assess fault displacement and  
vibratory ground motion hazards at Yucca Mountain, Technical Report  
BA0000000-01717-220-00002 Rev. 00, OCRWM M&O, March.

Department of Energy (1994b). Seismic design inputs for the Exploratory Studies Facility at Yucca Mountain, Technical Report BAB00000-01717-5705-00001 REV02, OCRWM M&O, October.

DePolo, C. (19\*\*). \*\*\*\*\*

Doser, D.I. (1986). Earthquake processes in the Rainbow Mountain-Fairview Peak-Dixie Valley, Nevada, region (1954-1959), *J. Geophys. Res.*, **91**, p. 12572-12586.

Doser, D.I. (1988). Source mechanisms of earthquakes in the Nevada seismic zone (1915-1943) and implications for deformation in the western Great Basin, *J. Geophys. Res.*, **93**, p. 120-143.

Doser, D.I., and R.B. Smith (1989). An assessment of source parameters of earthquakes in the Cordillera of the Western United States, *Bull. Seism. Soc. Am.*, **79**, 1383-1409.

Durrani, B., and M.C. Walck (1995). Near-surface velocity modeling at Yucca Mountain using borehole and surface records from underground nuclear explosions, SAND95-1606, Sandia National Laboratories, Albuquerque, NM.

Eaton, G. P. (1982). The Basin and Range province—Origin and tectonic significance. *Annual Review of Earth and Planetary Science*, **10**, 409-440.

Environmental Research Corporation (1974). Prediction of ground motion characteristics of underground nuclear detonations, U.S. Atomic Energy Commission Nevada Operations Office Report NVO-1163-239, Las Vegas, NV.

EPRI (1993). Guidelines for determining design basis ground motions, Vol. 1: Method and guidelines for estimating earthquake ground Motion in eastern North America. J.F. Schneider, editor, Electric Power Research Institute, Palo Alto, CA, Report TR-102293.

Frankel, A. (1991). High-frequency spectral fall-off for earthquakes, fractal dimension of complex rupture, b-value, and the scaling of strength on faults. *J. Geophys. Res.*, **96**, 6291-6302.

Geomatrix (1992). Seismic ground motion studies for major northern California bridges, Studies conducted in association with International Civil Engineering Consultants for Caltrans, Division of Structures, Sacramento, CA.

Gibson, J.D., F.H. Swan, J.R. Wesling, T.F. Bullard, R.C. Perman, M.M. Angell, and L.A. Disilvestro (1992). Summary and evaluation of existing geological and geophysical data near prospective surface facilities in Midway Valley, Yucca Mountain Project, Nye County, Nevada, *Sandia National Laboratories Report SAND90-2491.UC-814*.

Hanks, T.C. and R.K. McGuire (1981). The character of high-frequency strong ground motion, *Bull. Seism. Soc. Am.*, **71**, 2071-2095.

- Harmsen, S.C. (1993). Seismicity and focal mechanisms for the Southern Great Basin and California in 1991, U.S. Geological Survey, Open-File Report 92-340, 100p.
- Harmsen, S.C. (1994). The Little Skull Mountain, Nevada, Earthquake of 29 June 1992: Aftershock focal mechanisms and tectonic stress field implications, *Bull. Seism. Soc. Amer.*, 84, 1484-1505.
- Harmsen, S.C. and C.G. Bufe (1992). Seismicity and focal mechanisms for the Southern Great Basin of Nevada and California: 1987 through 1989, U.S. Geological Survey Open-File Report 91-572, Denver, CO, 208 p.
- Hartse, H., M. Fehler, and L. House (1994). Scattering and intrinsic attenuation for the southern Great Basin from near-regional earthquakes and explosions, (abs.) EOS, Transactions AGU, 75, no. 44, p. 455.
- Helmberger, D.V. and D.G. Harkrider (1978). Modeling earthquakes with generalized ray theory. In: J. Miklowitz and J. Achenbach (Editors), Proc. IUATM Symp. Modern Problems in Elastic Wave Propagation. Wiley, New York, pp. 499-518.
- Hoffman L.R., and W.D. Mooney (1983). A seismic study of Yucca Mountain and vicinity, southern Nevada: Data report and preliminary results: U.S. Geological Survey Open-File Report 83-588, 50 p.

- Hough, S.E., J.G. Anderson, and H.J. Patton (1989). Attenuation in western Nevada: preliminary results from earthquake and explosion sources, *Geophys. Res. Lett.*, **16**, 207-210.
- Houston, H., and H. Kanamori (1986). Source spectra of great Earthquakes: Teleseismic constraints on rupture process and strong motion, *Bull. Seism. Soc. Am.*, **76**, 19-42.
- Idriss, I.M. (1993). Procedures for selecting earthquake ground motions at rock sites, Report to National Institute of Standards and Technology, September 1991, revised March 1993.
- Idriss, I.M. (1994a). Updated standard errors, personal communication, April 17, 1994.
- Idriss, I.M. (1994b). Attenuation relationship for peak horizontal accelerations at rock sites, personal communication, September 1, 1994.
- King, Geoffrey C. P. (1994). Written communication.
- King, Geoffrey C. P., and R. Janssen (1994). Tectonic Modelling of Yucca Mountain, report prepared for the U.S. Geological Survey, Yucca Mountain Project Branch, April 1994, 24 pp.
- Luco, J.E. and R.J. Apsel (1983). On the Green's functions for a layered half space. Part I., *Bull. Seism. Soc. Am.*, **73**, 909-929.

Lum, P.K., and K.K. Honda (1993a). Processed seismic motion records from Little Skull Mountain, Nevada earthquake of June 29, 1992 recorded at seismic stations in southern Nevada. DOE Report JAB-10733-TM6.

Lum, P.K., and K.K. Honda (1993b). Processed seismic motion records from Little Skull Mountain aftershocks, Nevada earthquakes of July 5 and September 13, 1992 recorded at seismic stations in southern Nevada. DOE Report JAB-10733-TM8.

Marshall, P.D., A. Douglas, and J.A. Hudson (1971). Surface waves from underground nuclear explosions," *Nature*, 234, 8-9.

Martin, R.J., R.H. Price, P.J. Boyd, and J.S. Noel (1994). Bulk and mechanical properties of the Paintbrush tuff recovered from Borehole USW NRG-6: Data report. SAND93-4020, Sandia National Laboratories, Albuquerque, NM.

Martin, R.J., R.H. Price, P.J. Boyd, and J.S. Noel (1995). Bulk and mechanical properties of the Paintbrush tuff recovered from Borehole USW NRG-7/7A: Data report. SAND94-1996, Sandia National Laboratories, Albuquerque, NM.

McGarr, A. (1984). Scaling of ground motion parameters, state of stress, and focal depth, *J. Geophys. Res.*, 89, 6969-6979.

Meremonte, Mark, J. Gomberg, and E. Cranswick (1995). Constraints on the June 29, 1992, Little Skull Mountain, Nevada, earthquake sequence